Copper-Mediated Radiosynthesis of ^{18}F- and ^{123}I-Radiolabelled PARP Inhibitors

A thesis submitted to the Board of the Faculty of Physical Sciences, in partial fulfilment of the requirements for the degree of Doctor of Philosophy at the University of Oxford

Zijun Chen

Merton College

University of Oxford

Hilary 2022

Author's Declaration

The work presented in this thesis was conducted under the supervision of Prof. Véronique Gouverneur at the Department of Chemistry, University of Oxford. All of the work is my own, unless otherwise stated, and has not been submitted for any other degree at this or any other university.

Zijun Chen
February 2022

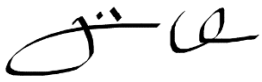

Acknowledgement

First, I would like to thank Prof. Véronique Gouverneur for all her support since the first day in Oxford, 2013. It has been a fantastic journey and Véronique is always so inspiring and. It is my honour and pleasure to be supervised by her and work in this brilliant group.

I would like to thank the members of the VG group. Special thanks go to Dr. Gregor S. Cremosnik for teaching me all the techniques when I started my PhD, Dr. Florian Guibbal for supervising me in the radio-lab, and Dr. Gianluca Destro for the most enjoyable collaboration. My special mentions go to Dr. Francesco Ibba and Dr. Osman Tack for sharing music, Dr. Robert Szpera and Dr. Sandrine Hell for the cheerful office time and Konstantinos Afratis who is an amazing chef.

Thanks to all the staff in the Chemistry Research Lab and at Merton College.

Finally, I want to thank my parents for all the encouragement and support in every aspect of my life.

Abstract

This thesis aims to develop copper-mediated radiosynthesis to incorporate fluorine-18 and iodine-123 into FDA-approved poly(ADP-ribose) polymerase (PARP) inhibitors for cancer diagnosis and treatment, consisting the development of ^{18}F-radiolabelled rucaparib for positron emission tomography (PET) application in cancer diagnosis and development of ^{123}I-radiolabelled rucaparib and olaparib analogues as potential theragnostic agents for Auger therapy.

Chapter I presents a general introduction of DNA damage, PARP and PARP inhibitors.

Chapter II starts with a brief overview of PET, and ^{18}F-fluorination of (hetero)arenes, and discusses two copper-mediated radiosynthesis approaches of ^{18}F-radiolabelled rucaparib from pinacol boronic ester precursors. Full radiosynthesis of the most successful approach is demonstrated. *In vitro* data, *in vivo* dynamic PET imaging and *ex vivo* biodistribution of [^{18}F]rucaparib are presented subsequently.

Chapter III provides a summary of Auger therapy and current methodologies to access ^{123}I-radiolabelled (hetero)arenes. Development of ^{123}I-rucaparib analogue and ^{123}I-olaparib analogue via copper-mediated ^{123}I-iodination from pinacol boronic ester precursors are discussed separately.

Chapter IV provides experimental data for compounds and procedures of radiosynthesis discussed in this thesis.

Abbreviations

[^{18}F]	Enriched in fluorine-18
[^{18}F]AcOF	Acetyl [^{18}F]hypofluorite
[^{18}F]FDG	2-[^{18}F]Fluoro-2-deoxy-D-glucose
[^{18}F]FDOPA	6-$_{L}$-[^{18}F]Fluoro-3,4-dihydroxyphenylalanine
[^{18}F]NFSI	[^{18}F]Fluorobenzenesulfonimide
[^{18}F]Selectfluor bis(triflate)	1-Chloromethyl-4-[^{18}F]fluoro-1,4-diazoniabicyclo[2.2.2]octane bis(triflate)
[^{18}F]TBAF	Tetra-*n*-butylammonium [^{18}F]fluoride
[^{123}I]	Enriched in iodine-123
[^{125}I]	Enriched in iodine-125
[^{131}I]	Enriched in iodine-131
[^{123}I]MIBG	*meta*-[^{123}I]Iodobenzylguanidine
[^{125}I]MIBG	*meta*-[^{125}I]Iodobenzylguanidine
[^{125}I]NIS	*N*-[^{125}I]Iodosuccinimide
Å	Angstrom
AE	Auger electron
Ala	Alanine
A_m	Molar activity
AP	Apurinic/apyrimidinic
APE1	Apurinic/apyrimidinic endonuclease 1
APLF	Aprataxin-and-PNK-like factor
ATM	Ataxia-telangiectasia mutated
β^+	Positron
BDE	Bond dissociation energy
Boc	*Tert*-Butoxycarbonyl
BRCA1	Breast cancer type 1 susceptibility protein
CRPC	Castration-resistant prostate cancer

CS_NAr	Concerted nucleophilic aromatic substitution
Da	Dalton
DDR	DNA damage response
DFT	Density functional theory
DMC	Dimethyl carbonate
DNA	Deoxyribonucleic acid
DSB	Double-strand break
EC	Electron capture
equiv	Equivalent
FWHM	Full width at half maximum
gBRCAm	Germline BRCA-mutated
Glu	Glutamic acid
Gly	Glycine
HBTU	3-[Bis(dimethylamino)methyliumyl]-3*H*-benzotriazol-1-oxide hexafluorophosphate
HJ	Holiday junction
HR	Homologous recombination
HRR	Homologous recombination repair
IC	Internal conversion
IR	Ionising radiation
K_i	Inhibitor constant
Krytofix® 222	4,7,13,16,21,24-Hexaoxa-1,10-diazabicyclo[8.8.8]hexacosane
LET	Linear energy transfer
Lig1	DNA ligase I
Lys	Lysine
M	Mega
m	Milli
MIBG	*meta*-Iodobenzylguanidine

MRN	MRE11-RAD50-NBS1 (complex)
NAD^+	Nicotinamide adenine dinucleotide
NCS	*N*-Chlorosuccinimide
NHEJ	Non-homologous end joining
OIA	Oxidised iodoarene
p	Para
P450s	Cytochrome P450 enzymes
PAR	Poly(ADP-ribose)
PARG	Poly(ADP-ribose) glycohydrolase
PARP	Poly(ADP-ribose) polymerase
PARylation	Poly(ADP-ribosyl)ation
PCNA	Proliferating cell nuclear antigen
PEEK	Polyether ether ketone
PET	Positron emission tomography
PhenoFluor™	1,3-*Bis*(2,6-diisopropylphenyl)-2,2-difluoro-2,3-dihydro-1*H*-imidazole
PNK	Polynucleotide Kinase
Polβ	Polymerase beta
PP	Polypropylene
ppb	Parts per billion
PTFE	Polytetrafluoroethylene
RCP	Radiochemical purity
RCY	Radiochemical yield
ROI	Region of interest
ROS	Reactive oxygen species
RPA	Replication protein A
SAM	S-Adenosylmethionine
SEM	2-(Trimethylsilyl)ethoxymethyl

Ser	Serine
S_EAr	Electrophilic aromatic substitution
S_NAr	Nucleophilic aromatic substitution
SSA	Single-strand annealing
SSB	Single-strand break
ssDNA	Single-stranded DNA
SUV	Standardised uptake value
T	Tera
t	Tert
TBAF	Tetra-*n*-butylammonium fluoride
TEMPO	(2,2,6,6-Tetramethylpiperidin-1-yl)oxyl
TFA	Trifluoroacetic acid
TIPS	Triisopropylsilyl
Tyr	Tyrosine
µ	Micro
UV	Ultraviolet
XLF	XRCC4-like factor
XRCC	X-ray repair cross-complementing protein
ZnF1	Zinc finger 1

Contents

Chapter 1. Introduction to PARP and PARP Inhibitors

1.1 DNA Damage

Tens of thousands of DNA lesions occur in human cells every day.[1,2] The causes of DNA damage are divided into two categories, endogenous and exogenous.[3] Endogenous DNA damage is due to replication stress, lack of nucleotides during replication, and genotoxic products generated during spontaneous DNA metabolism and normal cellular process, such as DNA depurination, hydrolytic cytosine deamination, cytotoxic alkylation induced by S-adenosylmethionine (SAM) and reactive oxygen species (ROS) generated during cell metabolism.[4-6] Such spontaneous pathway is accountable for most of the DNA lesions in human cells, estimated to happen 10^5 times per cell per day.[4] Exogenous DNA damage is induced by external sources including ultraviolet (UV) radiation from sunlight, ionising radiation (IR) in radiotherapy and chemicals agents used in chemotherapy.[3]

Table 1.1: Common DNA damaging agents, induced lesions and most relevant repair pathways. UV: ultraviolet; *cis*-Pt: cisplatin; MMC: Mitomycin C; (6-4)PP: pyrimidine-6-4-pyrimidone photoproducts; CPD: cyclobutane pyrimidine dimers; A-G: adenine-guanine; T-C: thymine-cytocine; HR: homologous recombination; NHEJ: non-homologous end joining.

Damaging Agents	Sites/Types of Lesions	Repair Pathways
X-rays Oxygen radicals Alkylating agents Spontaneous reactions	Uracil A-basic site 8-Oxoguanine Single-strand break	Base-excision repair
UV light Polycyclic aromatic hydrocarbons	(6-4)PP Bulky adduct CPD	Nucleotide-excision repair
X-rays Anti-tumour agents (*cis*-Pt, MMC)	Interstrand cross-link Double-strand break	Recombinational repair (HR, NHEJ)
Replication errors	A-G mismatch T-C mismatch Insertion Deletion	Mismatch repair

Among the different types of damage, DNA single-strand breaks (SSBs) and double-strand breaks (DBSs) are paramount, the former being the most common type of lesion and the latter being the most cytotoxic lesions. Other types of DNA lesions caused by common DNA

damaging agents are listed in Table 1.1.[8] Accumulated DNA damage is closely linked to genomic instability, which is a key feature of cancer and tumour development.[2,8-11]

1.2 DNA Damage Response

To maintain genomic stability, in other words, to keep a faithful transmission of genetic information, the cells have developed a series of DNA damage response (DDR) events that sense, signal and repair DNA lesions. Four main, partially overlapping, pathways are responsible for repairing DNA damages in mammals: base-excision repair (BER), nucleotide-excision repair (NER), homologous recombination (HR) and non-homologous end joining (NHEJ).[8] Both BER and NER repair DNA lesions in one of the DNA strands; whereas HR and NHEJ pathways are responsible for the more problematic DSBs (Table 1.1).

1.2.1 SSB Repair Pathway (BER)

BER pathway is responsible for most of endogenous DNA damage, encompassing SSBs, apurinic/apyrimidinic (AP) sites, and bases derived from deamination, alkylation and oxidation.[12] Despite variations in the detailed mechanism, BER shares five common steps, referred as the short-patch BER. The repairing process starts with DNA glycosylase detection and removal of the damaged base to create an AP site. Next, apurinic/apyrimidinic endonuclease incises the DNA strand at the a-basic site. DNA polymerase beta (Polβ) then removes the baseless sugar residue and subsequently performs a one-nucleotide gap-filling reaction. Lastly, the DNA repair protein, X-ray repair cross-complementing protein 1 (XRCC1), complexed with DNA ligase I or III (Lig1/Lig3), seals the remaining nick (Scheme 1.1).[8,12] The other minor repair pathway, referred as the long-patch BER, differs from the short-patch BER mainly in the gap-filling stage. Instead of a one-nucleotide gap-filling, the long-patch BER incorporates 2 to 12 nucleotides and recruits more proteins, including Polβ, Polδ, Polε and proliferating cell nuclear antigen (PCNA).[13,14] SSB repair is considered as a sub-pathway

under BER. Both poly(ADPribose) polymerase 1 (PARP1) and 2 (PARP2) recognise SSBs and are recruited at the DNA damaged sites. Upon binding with DNA, PARP1/2 takes NAD^+ as a substrate, and enzymatically catalyses conversion of NAD into PAR (poly(ADP ribose)). PARP1/2 PARylates itself and other proteins around, including histones H1 and H2B. These elements altogether form a platform for DNA repair.[15] PARP1 and the scaffold protein XRCC1 are both responsible for stabilisation of DNA strand breaks until the repair and ligation steps.[16,17]

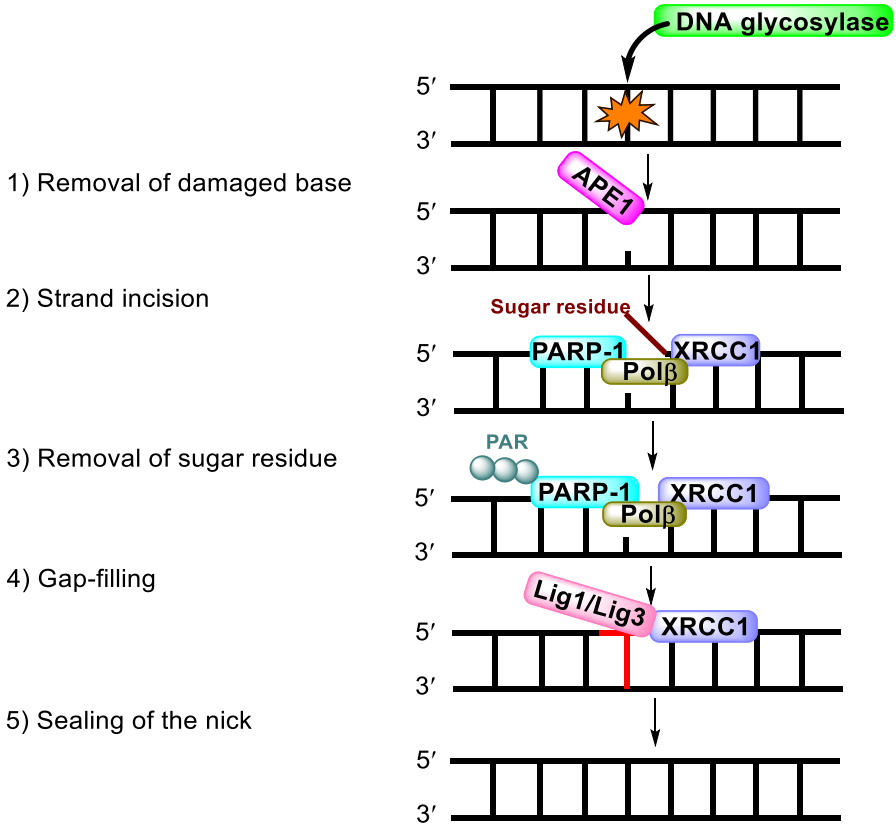

Scheme 1.1: Simplified scheme of the short-patch base-excision repair (BER). APE1: apurinic/ apyrimidinic endonuclease 1; XRCC1: X-ray repair cross-complementing protein 1; Polβ: DNA polymerase beta; PAR: Poly(ADP-ribose); Lig1: DNA ligase I; Lig3: DNA ligase III;

1.2.2 DSB Repair Pathway (HR and NHEJ)

DSBs are induced by various sources, including ionising radiation, such as X-rays and UV, anti-tumour agents and during replication of SSB. When a DSB is detected, at least three independent repair pathways can be induced, including HR, NHEJ, and alternative-NHEJ (alt-

NHEJ). These three pathways differ mainly by the DNA end processing.[18] DNA end resection is not required by NHEJ, limited for alt-NHEJ and to a greater extent for HR.

NHEJ encompasses direct ligation of DNA ends without the need for a template (Scheme 1.2). Ku hetero-dimer (Ku70-Ku80) binds with the DNA ends to initiate NHEJ by recruiting the DNA-protein dependent kinase, catalytic subunit (DNA-PK_{CS}).[19] DNA-PK_{CS} stabilises and protects DSB ends followed by access of end processing enzymes, such as Artemis and Aprataxin-and-PNK-Like Factor (APLF).[20,21] The XRCC4/DNA ligase IV (Lig4) complexes are recruited, with the assistance of XRCC4-like factor (XLF), altogether promoting the ligation of the broken DNA ends.[22]

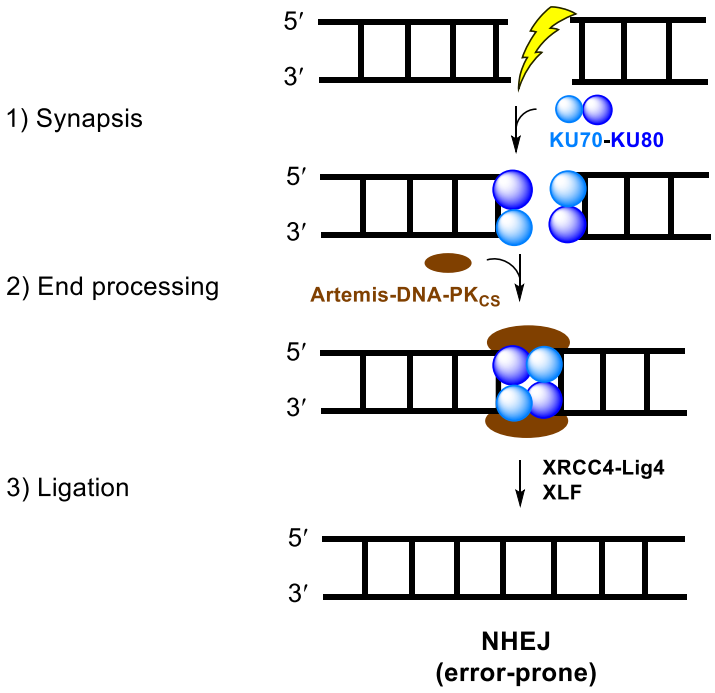

Scheme 1.2: Simplified scheme of the non-homologous end joining NHEJ. Ku70-Ku80: Ku hetero-dimer; DNA-PK_{CS}: DNA-protein dependent kinase, catalytic subunit; XRCC4: X-ray repair cross-complementing protein; Lig4: DNA ligase IV; XLF: XRCC4-like factor.

NHEJ is an error-prone mechanism, resulting in loss of nucleotides, and thus have a greater probability of mutations.[23] On the other hand, HR is an error-free mechanism, but restricted to S and G2 phases, because it requires a sister chromatid as a template for accurate repair (Scheme 1.3).

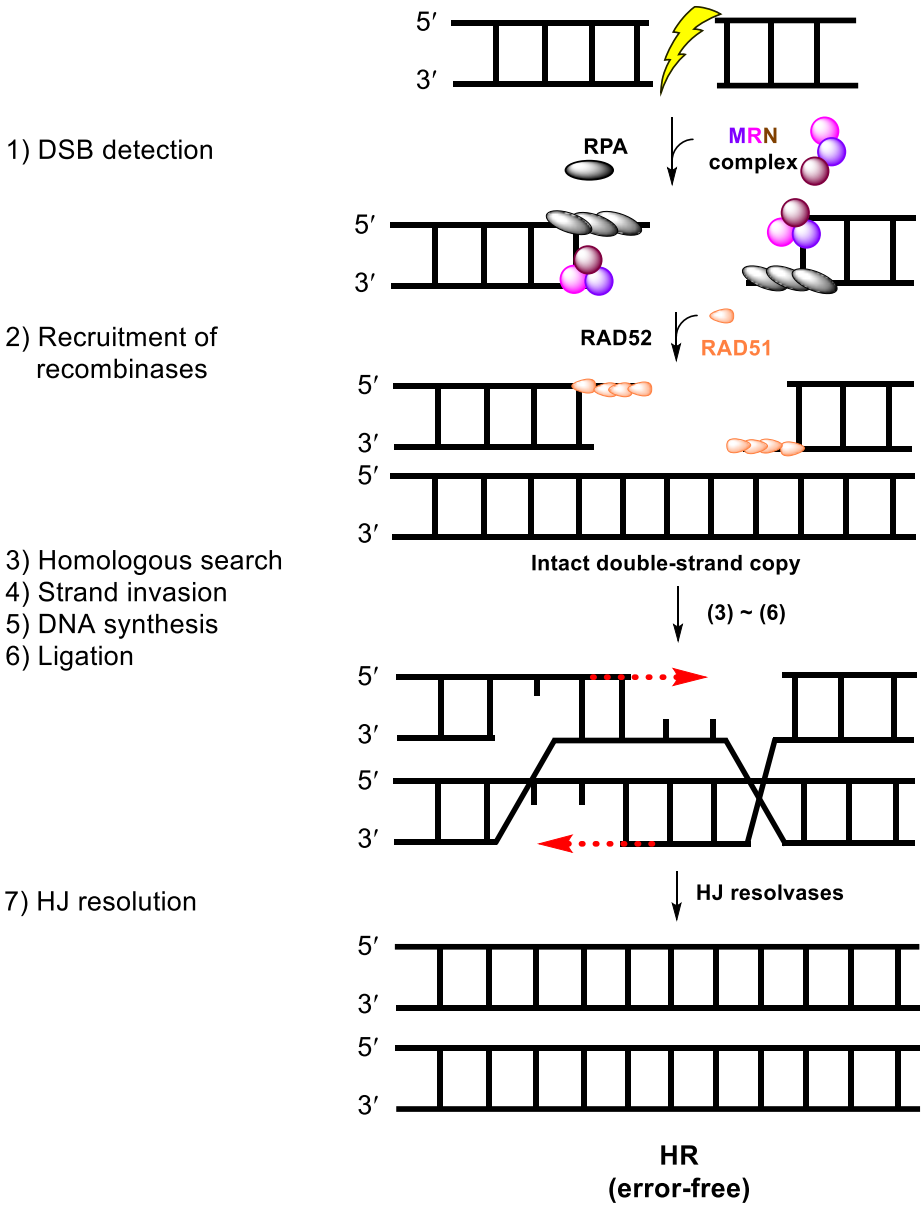

Scheme 1.3: Simplified scheme of the homologous recombination (HR). RPA: Replication protein A; MRN: MRE11-RAD50-NBS1 complex; RAD51: RAD51 recombinase; HJ: Holiday conjunction.

MRE11-RAD50-NBS1 (MRN) complex detects DSBs and binds to both 3' ends, which recruits the ataxia-telangiectasia mutated (ATM) kinase to initiate the HR pathway.[24-26] Replication protein A (RPA) stabilises the DSB and facilitates formation of RAD51 nucleoprotein filaments, which is accelerated by RAD52.[27] RAD51 is structurally related to E. coli RecA protein, possessing a recombinase activity.[28] RAD51 binds to the single-stranded DNA and catches an intact double-stranded copy for a homologous search. Upon finding the homologous sequence, the RAD51 filaments mediate strand exchange,[29-31] promoted by breast cancer type

1 and 2 susceptibility proteins (BRCA1 and BRCA2).[28,32] Finally, the resultant key DNA intermediate, so-called Holliday junctions (HJs) are resolved into two DNA duplexes by HJ resolvases.[33,34]

In a comparative study of HR and NHEJ, Gorbunova *et al.* reported a general 3:1 ratio between NHEJ and HR in mammalian cells. NHEJ was also kinetically faster than HR. For cell samples that could be repaired via NHEJ within 30 minutes, the time course of completion for HR was 7 hours.[35] Balance between these two pathways is essential for maintaining genomic stability. Choice of the pathways might be governed by the intrinsic genomic composition.[36] The genomes in mammalian cells consist of a substantial amount of repetitive DNA. Unlike HR, which is limited to late S phase and G2 phase where a sister chromatin template is physically positioned, NHEJ is viable throughout the whole cell cycle. Homology partners for NHEJ in the repetitive regions could be chosen from any of the chromosomes. In evolution, mammalian cells might avoid overly efficient HR which might lead to deleterious genomic rearrangements in the presence of large amount of repetitive DNA. As a trade-off, error-prone NHEJ might accumulate small mutations that contribute to aging and carcinogenesis.

1.2.3 Roles of BRCA1 and BRCA2 in DSB Repair

Inappropriate DSB repair can lead to increased likelihood of cancer development. Targeting at mutations in genes involved in DNA damage repair has drawn increasing attention in cancer research. *BRCA1* and *BRCA2* were identified as two of the most prominent tumour suppressor genes in 1994 and 1995 respectively.[37,38]

Cancer Type	General Population Risk	Risk for Malignancy	
		BRCA1	*BRCA2*
Breast	12%	46%-87%	38%-84%
Ovarian	1%-2%	39%-63%	16.5%-27%
Prostate	6% by age 69	8.6% by age 65	15% by age 65
Pancreatic	0.5%	1%-3%	2%-7%

Table 1.2: Risk of malignancy in individuals with *BRCA1* or *BRCA2* pathogenic variants.

Inheritance of defects in either of the two genes predisposes individuals to familial forms of breast and ovarian cancers. Individuals with *BRCA1* or *BRCA2* pathogenic variants are associated with increased risk of breast, ovarian cancers and to a lesser extent in other cancers, including prostate and pancreatic cancers (Table 1.2).[39] Roles of BRCA1/2 in DSB repair are explained in this section.

The product of human *BRCA1* gene, the BRCA1 protein comprises 1863 amino acids and is characterised by the BRCT domain, an amino-acid sequence motif at the C-terminus for protein-protein interaction, a serine-glutamine (SQ) cluster region in the middle for phosphorylation, and the ring domain at the N-terminus for protein-protein interaction. BRCA1 is critical to the DSB pathway choice. Chromatin recruitment of 53BP1 mediated NHEJ pathway. BRCA1 antagonises 53BP1 by forming a complex with phosphorylated DDR protein CtIP and MRN, which displaces 53BP1 in the S/G2 phases.[40] This BRCA1-CtIP-MRN complex also facilitates DSB resection to generate single-stranded DNA which is essential for initiating the HR pathway (Figure 1.1). [41]

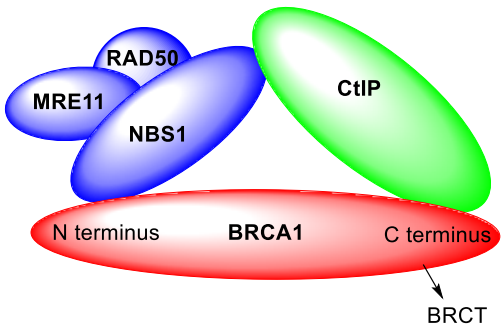

Figure 1.1: Proposed structure of the BRCA1-CtIP-MRN complex based on immunoprecipitation and Western blot analysis.[41] CtIP bridges the interaction of MRN with BRCA1. CtIP interacts with the BRCT domain at the C terminus of BRCA1, MRN interacts with BRCA1 at the N terminus of BRCA1.

The BRCA2 protein contains 3418 amino acids, including eight conserved BRC peptide motifs and a single-strand DNA binding domain at the C-terminus. The BRC repeat is a unique structural motif of approximate 35 residues, that has not been observed in other proteins to date.[42,43] BRCA2 plays a key role in the HR pathway by directly interacting with RAD51 recombinase at the BRC repeat, and promoting the formation of the RAD51 nucleoprotein

filament to initiate the homologous DNA repair. Two classes of BRC repeats in BRCA2 have been identified to promote the RAD51 nucleoprotein filament function. [43,44] Electrophoretic mobility-shift assays revealed BRC1, -2, -3, and -4 stimulated the binding of RAD51 to single-stranded DNA (ssDNA), whereas BRC5 to 8 bind to the RAD51-ssDNA filament rather than to free RAD51.[44] 3D models reconstructed from high resolution cryo-electron microscopy further brought insights into the role of BRCA2 in driving RAD51 filament formation (Figure 1.2).[45] Zhang and co-workers proposed that ssDNA binds across the BRCA2 dimer (Figure 1.2e). Two sets of RAD51 bind to BRCA2, but only one set is productive in ssDNA binding due to the inherent polarity of this ssDNA (Figure 1.2f). The RAD51 elongates in the 3'-5' direction. BRCA2 dissociates during the filament growth and can be subsequently used to initiate another filament formation.

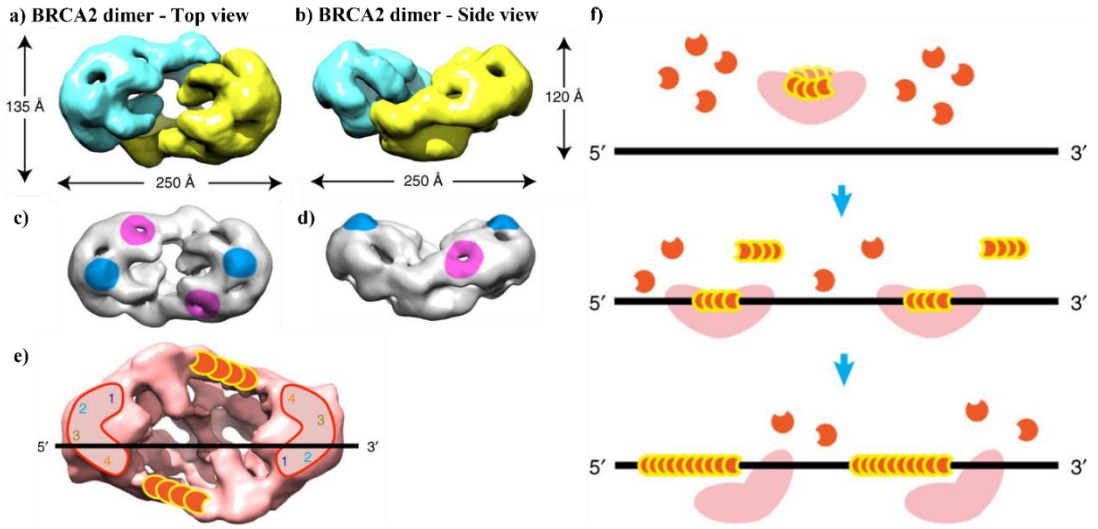

Figure 1.2: Figures adapted from the work of X. Zhang et al.45 a,b) 3D reconstruction of the BRCA2 dimer. Two monomers are coloured in yellow and cyan, although the exact boundary is unknown. c,d) Antibody labelling against the C-terminal (blue) and BRC repeats (magenta) of the BRCA2 dimer. e) Numbers 1-4 represent four DNA-binding domains of BRCA2, such that ssDNA could simultaneously bind to both BRCA2 monomers. Two sets of RAD51 (red crescents) bind to the BRCA2 dimer in opposite direction. f) Mechanism of action of the BRCA2 protein (pink) in RAD51 (red crescents) filament formation and elongation. A BRCA2 dimer binds to two sets of RAD51 molecules. Only one set is productive in ssDNA binding due to the inherent polarity of the bound ssDNA. The RAD51 elongates in the 3'-5' direction, due to its molecular architecture.

To summarise, BRCA1 and BRCA2 proteins are essential to HR pathway for DNA double-strand break repair. Mutations in *BRCA1* or *BRCA2* gene impair DSB repair and can lead to

increased risk of cancer development. In the next section, a protein that acts as a DNA damage sensor and has equally important roles in DNA damage repair is introduced.

1.3 The PARP Family

Poly(ADP-ribose) (PAR) was not discovered until 1963 in the pioneering work "Nicotinamide mononucleotide activation of new DNA-dependent polyadenylic acid synthesising nuclear enzyme" by Mandel and co-workers.[46] Poly(ADP-ribosyl)ation (PARylation) is now universally endorsed as an important post-translational modification of proteins involved in multiple cellular activities including DNA repair, apoptosis, carcinogenesis. The enzymes that catalyse this process are called Poly(ADP-ribose) polymerases or PARPs. PARPs form a superfamily of 17 known members in human cells, based on their sequence homology with the founding member PARP1. Among them, PARP1, PARP2, PARP5a (also known as tankyrase 1 or TNKS1) and PARP5b (tankyrase 2 or TNKS2) have poly(ADP-ribosyl)ation activity, transferring ADP-ribose sequentially from nicotinamide adenine dinucleotide (NAD^+) to acceptor protein residues, including glutamate, aspartate and lysine, but not limited to these, to synthesise PAR chains that are essential for efficient SSB repair.[47,48] Other catalytically active PARPs transfer only one ADP-ribose unit from NAD^+. PARP1, PARP2, and PARP3 are DNA-dependent enzymes.[49] PARP1 is the largest among the three and is approximately 116 kDa. Being the most extensively studied PARP enzyme, PARP 1 is responsible for 90% of PARylation.[50,51] In the absence of PARP1, despite having lower activity, PARP2 can take up to 25% of the normal DNA damage-induced PAR synthesis.[52]

1.3.1 PARP1

PARP1 consists multiple domains joined by a "beads-on-a-string" assembly, including an N-terminal DNA-binding domain, a BRCA1 C-terminus (BRCT) domain, a tryptophan-glycine-arginine-rich (WGR) domain and a C-terminal catalytic (CAT) domain (Figure 1.3).

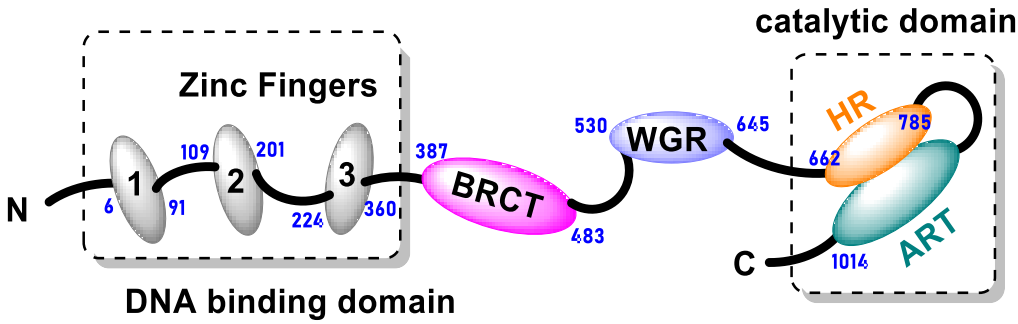

Figure 1.3: Domain structure of PARP1.

The N-terminal domain contains three zinc fingers. Zinc fingers are a large family of metalloproteins, where a zinc ion (Zn^{2+}) coordinates with protein residues, including cysteine and histidine. Zinc fingers 1 and 2 (ZnF1 and ZnF2) do not bind to specific DNA sequence but are capable of recognising unique DNA structures.[53] Oliver *et al.* demonstrated that ZnF1 and ZnF2 domains act together as a functional unit that binds specifically at a single strand-double strand transition of a DNA break (Figure 1.4). Further DNA binding studies revealed that the major contribution of this binding interaction arises from the phosphate backbone grip of both ZnF1 and ZnF2.[54]

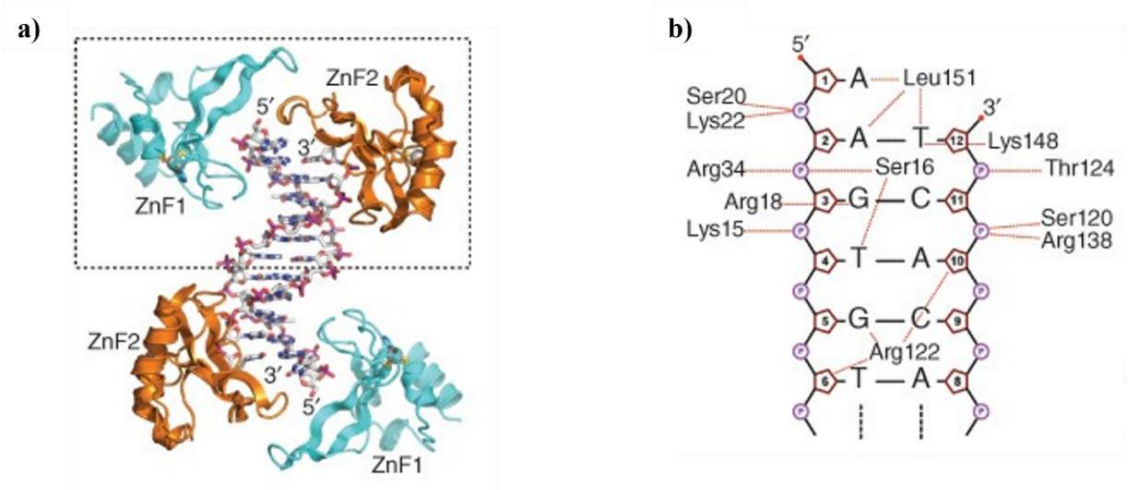

Figure 1.4: Figures from the work of A. W. Oliver *et al.*[53] a) Crystal structure of ZnF1 and ZnF2 domains bound to the end of a DNA duplex with a 5′ overhang. b) Schematic interaction of the zinc finger domains with the DNA duplex within the dashed box in a). Orange lines indicate interactions with phosphates (circled P), deoxyriboses (pentagons) or bases (letters).

X-ray crystallography of the ZnF3 domain conducted by Pascal *et al.* disclosed a novel zinc-ribbon fold and a homodimeric structure of ZnF3. These two structural features serve two distinct roles. The zinc-ribbon fold facilitates interdomain contact of the DNA-activated

PARP1 and contributes to the PAR synthesis activity (Figure 1.5a). The dimer interface of ZnF3 is crucial to the chromatin compaction activity of PARP1 (Figure 1.5b).[55]

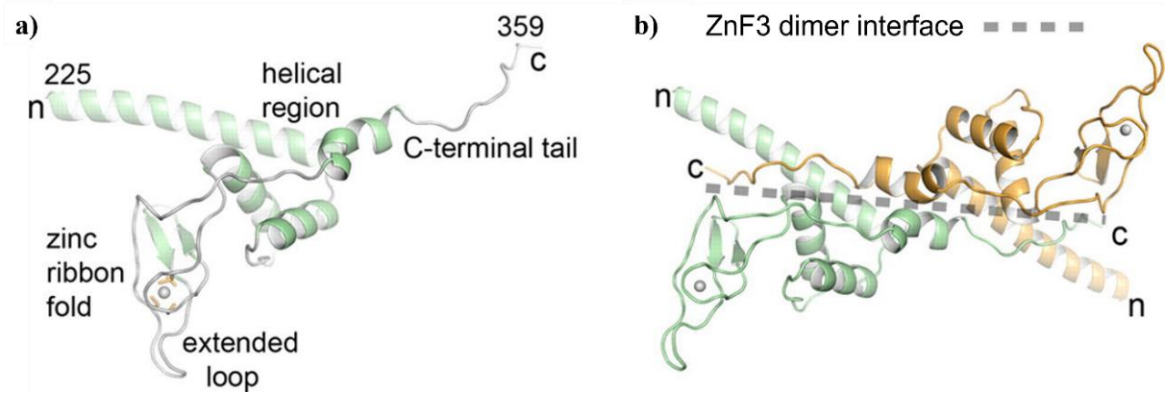

Figure 1.5: Figures adapted from the work of J. M. Pascal *et al*.[55a] Crystal structures of the ZnF3 domain, featuring a) a zinc-ribbon fold and b) a homodimeric structure.

The BRCT domain has a weight of 11.67 kDa and mediates protein-protein interactions. Upon activation, PARP1 auto-(ADP-ribosyl)ates its BRCT domain forming interaction site for the scaffold protein XRCC1, required for SSB repair.[56] The WGR domain interacts with ZnF1, ZnF3, the CAT domain and the DNA (Figure 1.6). It transfers activation signals between them and is important for DNA-dependent activity of the catalytic domain.[57,58]

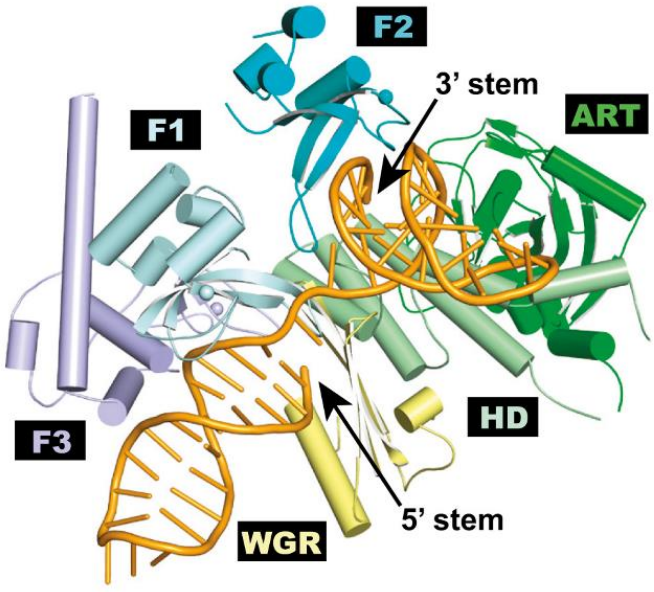

Figure 1.6: Figures adapted from the work of J. M. Pascal *et al*.[58] Model crystal structure of the PARP1-DNA complex, including ZnF1, ZnF2, ZnF3, WGR and CAT domains. The DNA duplex bears an SSB. ART and HD domains are subdomains of the catalytic domain. HD: helical domain; ART: ADP-ribosyltransferase domain.

The catalytic domain is most conserved across the PARP family and consists of two subdomains.[54] One is an autoinhibitory region, namely the helical domain (HD) and the other contains the active site that binds to NAD^+, called the ADP-ribosyltransferase (ART) domain.[59] The helical domain adopts a folded conformation that blocks productive NAD^+ binding to the active site when PARP1 is inactivated.

Upon encountering an DNA break, PARP1 zinc fingers induces PARP1 self-assembly. Inter-domain communications, including BRCT and WGR domains reduces the conformational space of the system. A series of interdomain contacts are formed with the helical domain, destabilising its folded conformation. The helical domain rapidly unfolds and relieves autoinhibition. Thus NAD^+ is allowed to bind with the ART domain in a productive conformation, leading to efficient PAR synthesis (Scheme 1.4).[58]

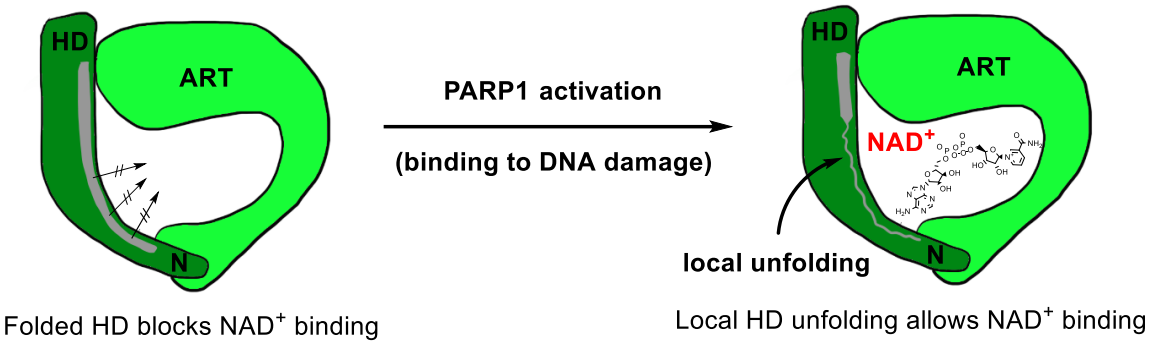

Scheme 1.4: Simplified illustration showing relief of autoinhibitory activity in the helical domain upon PARP1 activation. HD: helical domain; ART: ADP-ribosyltransferase domain; N: N-terminal of PARP1.

The ART domain contains the catalytic core of PARP and is crucial to PAR synthesis. It consists of a donor site that positions NAD^+ in the nicotinamide-binding pocket for the transferase reaction, and an acceptor site that binds to the PARylation target. The nicotinamide-binding pocket features a His-Tyr-Glu (H-Y-E) triad, the so-called "ART signature", that is required for NAD^+ positioning and is conserved across PARPs1-6 (Figure 1.7).

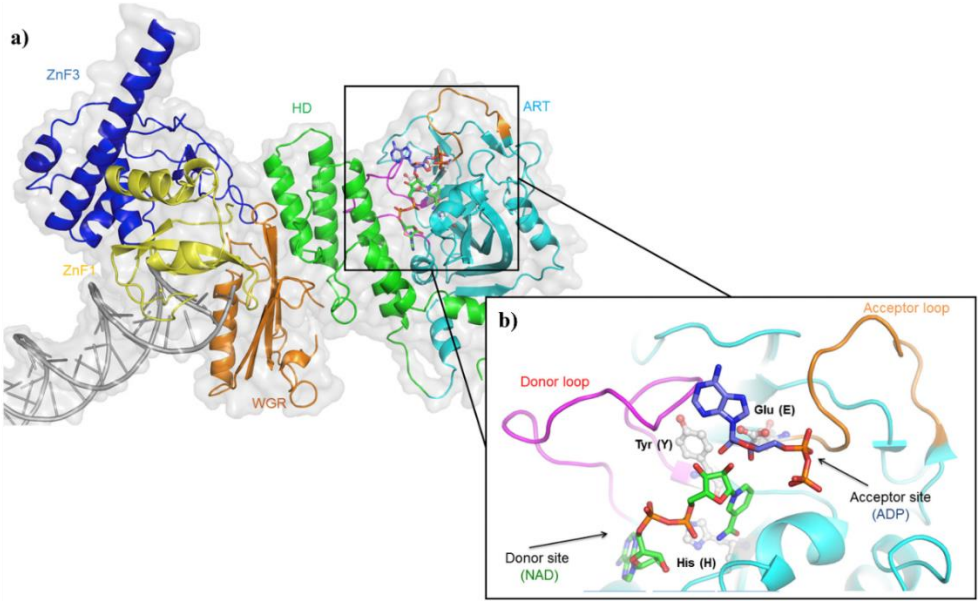

Figure 1.7: Figures adapted from the work of I. Ahel *et al*.[49] a) The crystal structure of essential domains in PARP1 bind to a DNA double-strand break. b) The triad residues, His(H)862, Tyr(Y)896, and Glu(E)988 in the ART domain are illustrated as atom colored sticks.

His862 forms a hydrogen bond with the 2′-OH of the adenine-ribose. Tyr896 forms π-π interaction with the nicotinamide ring. Apart from NAD^+ positioning, Glu988 binds to the 2'-OH of the nicotinamide ribose that positions NAD^+ for nucleophilic attack by the acceptor substrate. Besides the binding pocket, the donor site is formed by a phosphate-binding site and an adenine-ribose-binding site (Scheme 1.5).[54b]

The ART domain catalyses three distinct enzymatic reactions in PAR synthesis: initiation, elongation and branching. The initiation reaction is the attachment of an ADP-ribose monomer to a glutamate residue in the acceptor site. Multiple amino acid acceptors can be PARylated, including Lys, Arg, Glu, Asp, Cys, Ser, Thr, His and Tyr residues. The elongation reaction, as depicted in Figure 1.5, involves a 2'-1" ribose-ribose glycosidic bond formation and the branching reaction takes place at the branching point to form a 2"-1" ribose-ribose glycosidic bond (Scheme 1.6).

As a result of the PARylation, the PAR chain serves as a platform for recruitment of DNA repair factors, including XRCC1, Polβ and Lig3 in SSB repair and MRN complex, Ku, and DNA-PK in DSB repair (Figure 1.8).[51]

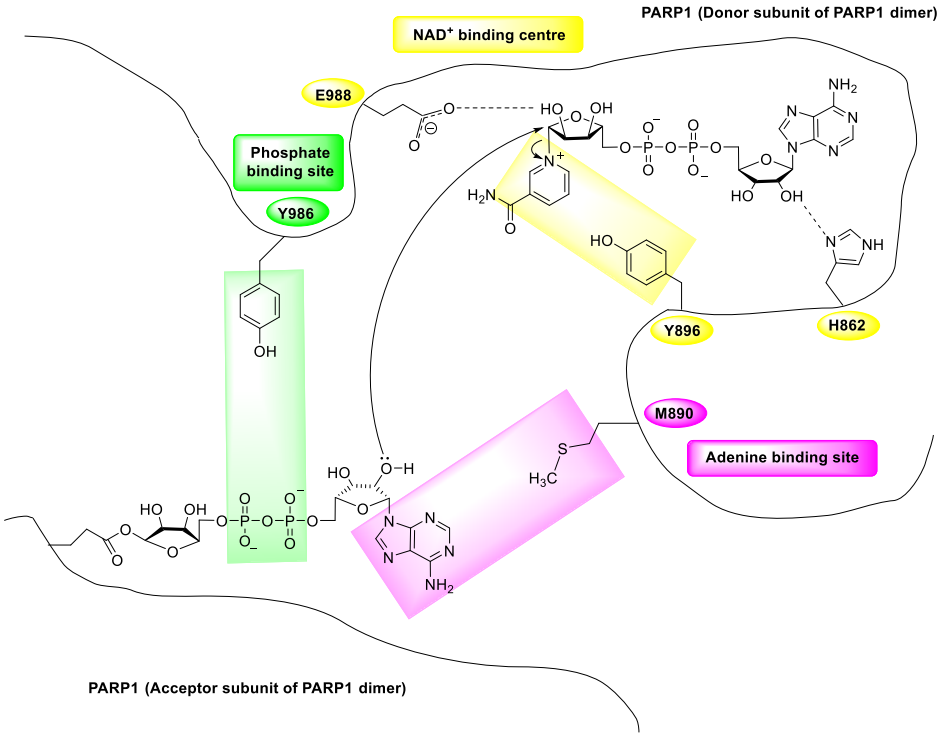

Scheme 1.5: Mechanism of elongation in PAR synthesis. H-Y-E triad are labelled in yellow. Key amino acid residues for the acceptor site, Met(M)890 and Tyr(Y)896 are labelled in purple and green, respectively. A glutamate residue (E988) in the acceptor site of PARP1 catalytic domain facilitates the release of nicotinamide from NAD^+, followed by transferring of the ADP-ribose motif to the acceptor subunit at the PARP1 catalytic domain.

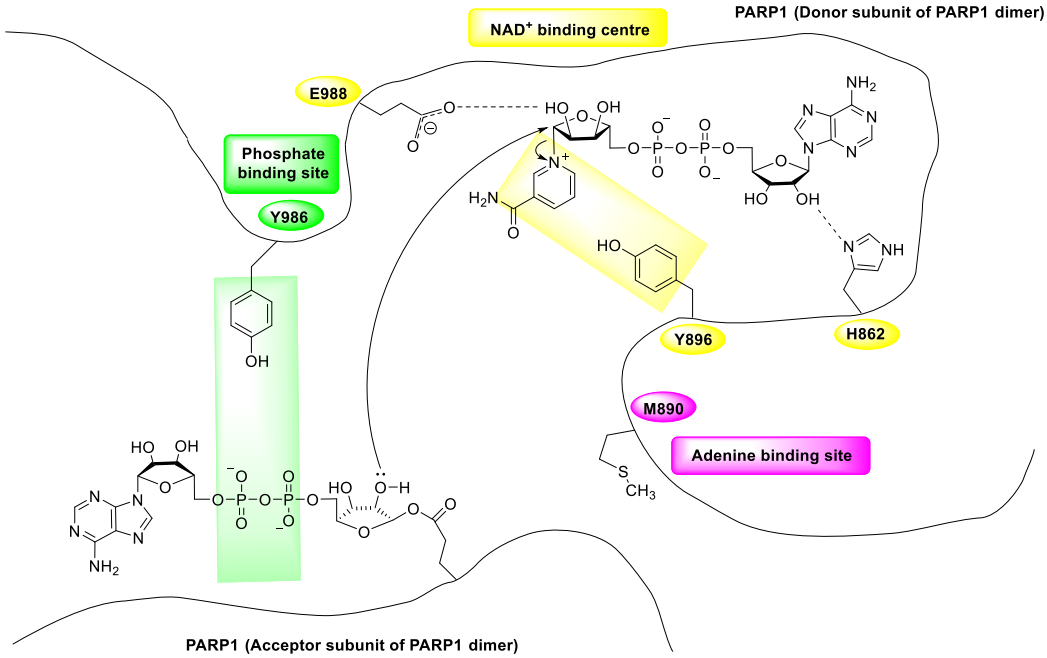

Scheme 1.6: Mechanism of branching in PAR synthesis. H-Y-E triad are labelled in yellow. Key amino acid residues, Met(M)890 and Tyr(Y)896 are labelled in purple and green, respectively.

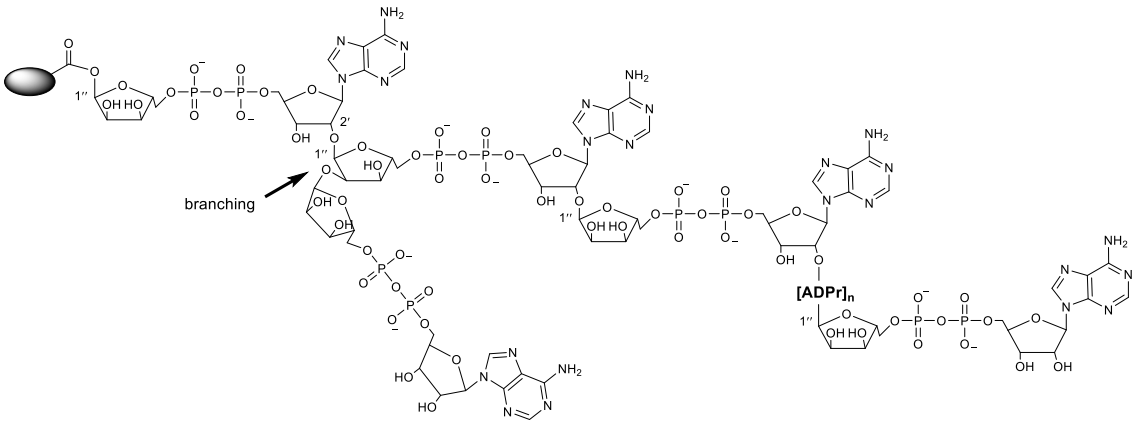

Figure 1.8: Structure of poly(ADP-ribosyl)ated protein.

1.4 PARP Inhibitors

1.4.1 Design of PARP inhibitors

Understanding the roles of DDR could potentially facilitate targeting a broader range of cancers. One or more DDRs have loss or impaired capabilities through cancer development. Targeted DDR inhibitors can be employed as a potential strategy to maximise DNA damage and selectively kill cancer cells. In this section, a novel class of cancer drugs that target at PARP proteins will be introduced.

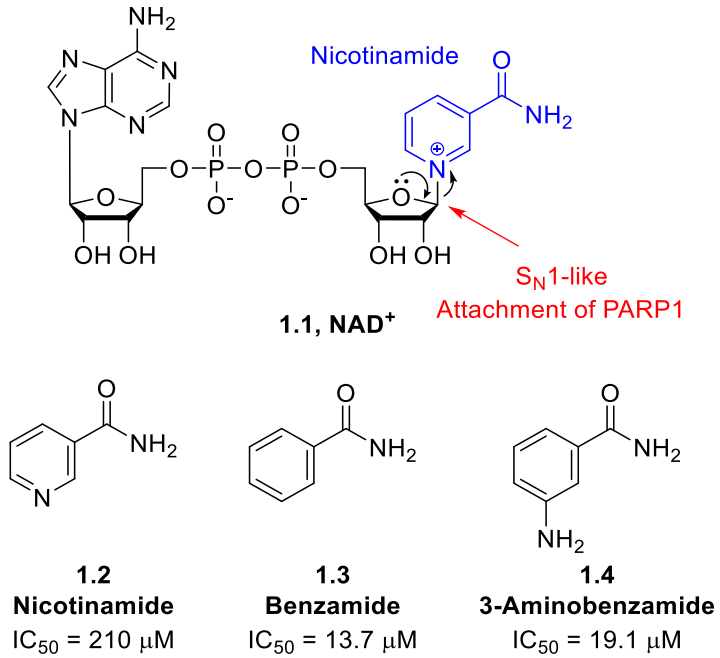

Figure 1.9: Structures of NAD^+ and nicotinamide based PARP inhibitors.

Since the PARP enzymes play crucial roles in the DNA damage response, especially PARP1 (and PARP2), substantial efforts have been driven to develop small molecules that inhibit

PARP1/2. The journey toward the development of the PARP inhibitors started in the 1970s when nicotinamide was found to have modest inhibitory activity toward PARP1.[60] The underlying concept of this potential anticancer activity was to compete with NAD^+ at the catalytically active site of PARP1 (Figure 1.9).

Due to its relatively low potency (**1.2**, IC_{50} = 210 µM) and variety of cellular functions, a more specific PARP1 inhibitor based on this fruitful lead **1.2** was needed.[61] The next candidates that drew attention were benzamide (**1.3**, IC_{50} = 13.7 µM) and 3-aminobenzamide (**1.4**, IC_{50} = 19.1 µM).[62-65] Since then, intensive studies were conducted to design and optimise the pharmacophore of PARP inhibitors. In 1998, the first co-crystal structure of some first generation PARP inhibitors and chicken PARP was generated, bringing insights to the inhibitor-PARP1 binding interaction at its active site (Figure 1.10a).[66] The emergency of more PARP inhibitors further refined the pharmacophore (Figure 1.10b).

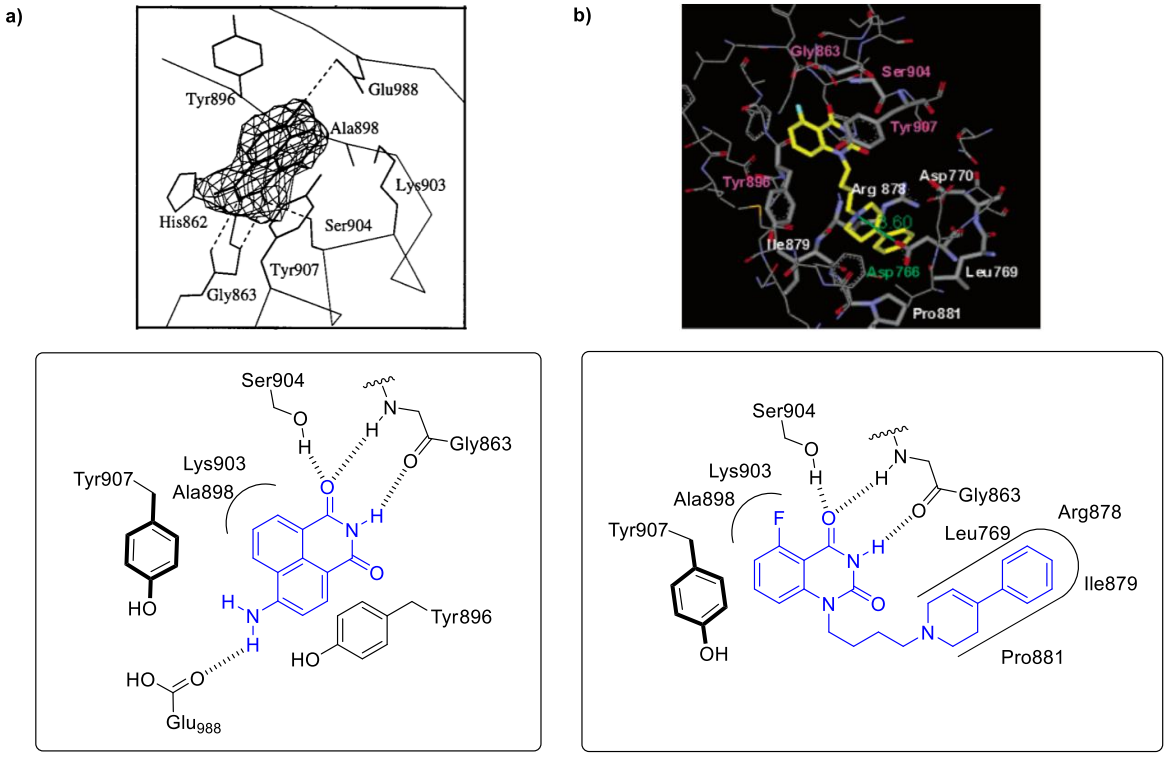

Figure 1.10: a) Co-crystal structure of a first generation PARP inhibitor, 4ANI, and PARP1 derived from chicken. [66] b) A quinazolinone-based PARP inhibitor binds to the active site of the human PARP1.[92]

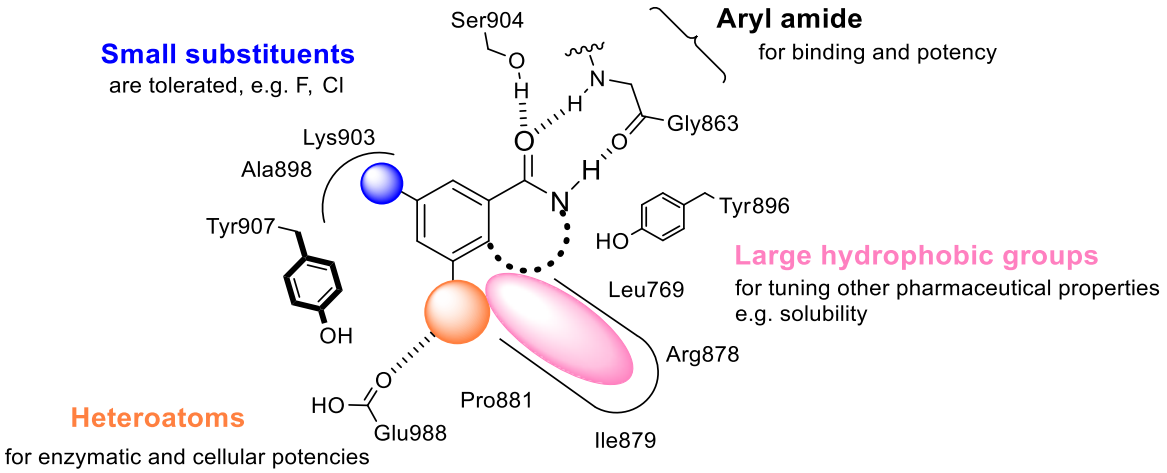

Figure 1.11: The pharmacophore of PARP inhibitors

So far, it is widely recognised that an effective PARP-1 inhibitor includes the following moieties: 1) an aryl amide (Figure 1.11 in black) in which the amide is hydrogen bonded with Ser904 and Gly863 and (multicyclic) aryl moiety is π-π interacted with Tyr896 and Tyr907 in human PARP1 to improve binding and potency,[68] 2) heteroatoms opposite to the amide, usually nitrogen or oxygen atoms as hydrogen bond donors and/or acceptors to interact with Glu988 (Figure 1.11 in orange), 3) small substituents adjacent to the amide which just sits inside the tight pocket formed by Ala898 and Lys903 (Figure 1.11 in blue), and 4) large hydrophobic groups to fill the adenine-ribose binding site next to the nicotinamide (Figure 1.11 in pink) for improving cellular potency, solubility and oral bioavailability.[69]

1.4.2 Synthetic Lethality

PARP inhibitors have gained increasing attraction in therapeutic cancer research mainly in two areas. They are used as part of combination therapies, or used in monotherapy by employing synthetic lethality.[70] The genetic concept of synthetic lethality was first introduced by Calvin Bridges in 1922.[71] He described that certain mutations conferred lethality in *Drosophila melanogaster* (a species in fruit fly), if and only if these genes were perturbed simultaneously. This phenomenon was not named until 1946 by his colleague Theodore Dobzhansky who noted the same effect in *Drosophila pseudoobscura* (another species in fruit fly).[72] The classical

synthetic lethality defines a situation where simultaneous alteration of two genes or proteins leads to cell death, yet altering either of them individually is not lethal. Now this terminology can also applied to cases in which a combination of a gene mutation and the action of a cancer drug leads to lethality, whereas the presence of either alone is non-lethal.

PARP inhibitors are the first class of clinically approved drugs that exploit synthetic lethality. As explained in previous sections, PARP1 functions as an DNA damage sensors and is essential for SSB repair (Scheme 1.7). Upon recognising SSBs, PARPs are recruited at the damaged sites, which will be activated and start PARylation to initiate SSB repairing, and eventually lead to cell survival.

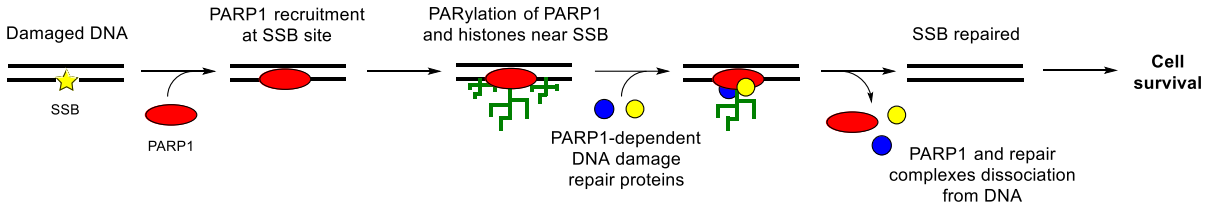

Scheme 1.7: Simplified scheme of DNA damage detection and SSB repair promoted by PARP1.

In the presence of PARP inhibitors, normal cells and *BRCA1/2*-mutated cancer cells respond differently. PARPs are either catalytically inhibited by PARP inhibitors or directly trapped onto DNA. Thus, SSBs cannot be repaired. This PARP-PARP inhibitor complex further causes collapse of replication fork (RF) during DNA replication and lead to DSBs (Scheme 1.8).

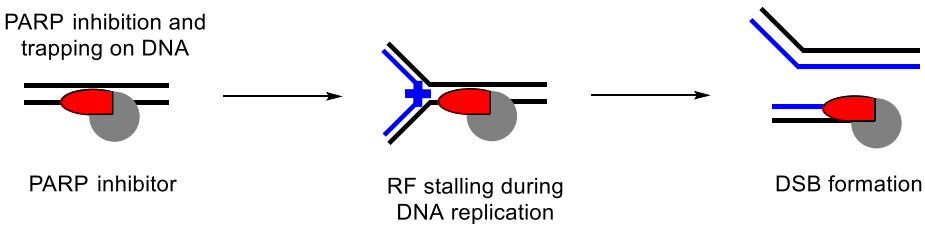

Scheme 1.8: Simplified scheme of DSB formation caused by PARP inhibition.

In normal cells, where BRCA1/2 proteins have intact functions, DSBs can be repaired via the HR pathway. Subsequently, the replication fork can be installed and leads to cell survival. In cancer cells, where *BRCA1/2* are mutated, the HR repair pathway is impaired. DSBs are either

accumulated or repaired by the error-prone NHEJ pathway and eventually cause cell death (Scheme 1.9).[73]

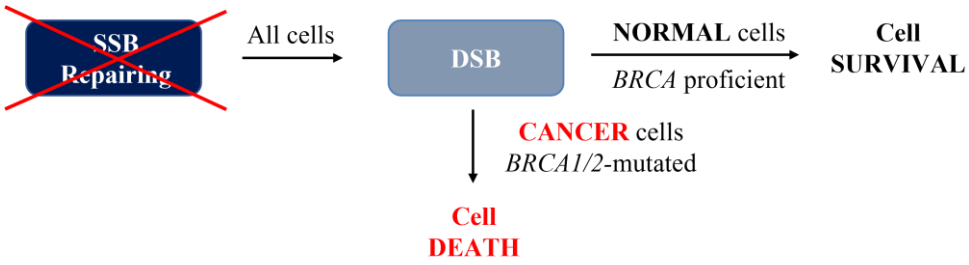

Scheme 1.9: Simplified scheme of PARP inhibition and synthetic lethality using PARP inhibitors.

1.4.3 Overview of PARP Inhibitors in the Clinic

Four PARP inhibitors, olaparib (Lynparza, AstraZeneca), rucaparib (Rubraca, Clovis Oncology), niraparib (Zejula, Tesaro, Inc.), and talazoparib (Talzenna, Pfizer), have obtained approval from US Food and Drug Administration (FDA) and/or European Medicines Agency (EMA) for various clinical uses. A further PARP inhibitor, veliparib (ABT-888) is currently undergoing phase III clinical trials for treatment of *BRCA*-mutant breast cancer and ovarian cancer.[70,74,75] Recently, five more candidates, stenoparib (2X-121), pamiparib (BGB-290), fluzoparib (SHR-3162), amelparib (JPI-289), and AZD-5305 have entered clinical trials (Table 1.3).[76-79]

Name	PARP1 IC_{50}	Structure	Comments[a]
Olaparib (Lynparza)	1 nM	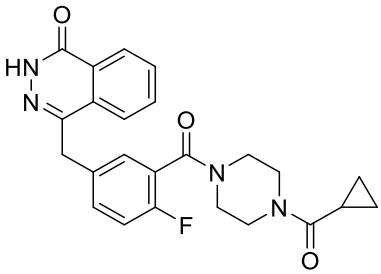	FDA Approved (First Approved in 2014) Ovarian, Breast, Pancreatic, and Prostate Cancer
Rucaparib (Rubraca)	1 nM	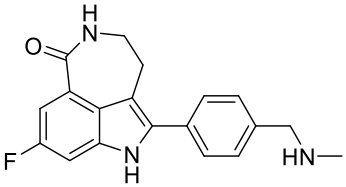	FDA Approved (First Approved in 2016) Ovarian and Prostate Cancer

Niraparib (Zejula)	4 nM	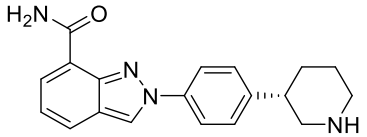	FDA Approved (First Approved in 2017) Ovarian Cancer
Talazoparib (Talzenna)	0.6 nM	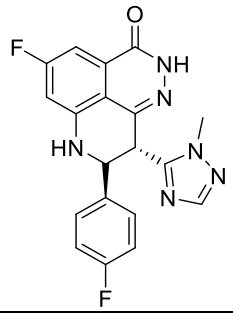	FDA Approved (2018) Breast Cancer
Veliparib (ABT-888)	2 nM	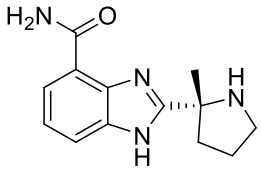	Phase I/II/III Breast Cancer, Ovarian Cancer, Neoplasms, and Other Solid Tumours
Stenoparib (2X-121)	1 nM	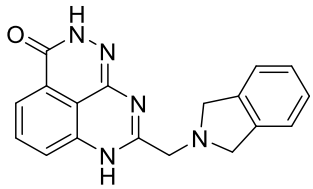	Phase II Breast and Ovarian Cancer
Pamiparib (BGB-290)	0.83 nM	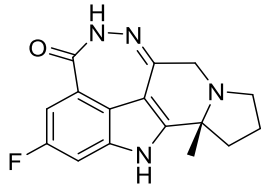	Phase I/II Ovarian Cancer, Breast Cancer, and other Solid Tumours
Fluzoparib (SHR-3162)	1.5 nM	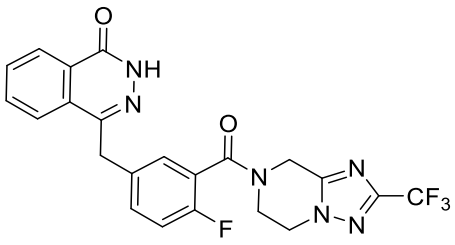	Phase I/II/III Ovarian Cancer
Amelparib (JPI-289)	18 nM	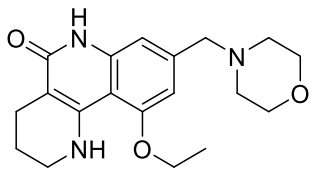	Phase II Acute Ischemic Stroke

AZD5305	3 nM	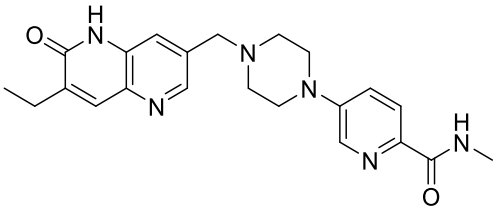	Phase I Ovarian, Breast, Pancreatic, and Prostate Cancer

Table 1.3: PARP inhibitors in clinics or under clinical trials. [a]Treatments with PARP inhibitors either as monotherapy or as part of combination are not specified.

The cytotoxicity of PARP inhibitors in monotherapy does not correlate with their ability to inhibit PARylation, but their potency to trap PARP.[80,81] All PARP inhibitors in the clinic are catalytic inhibitors, but their ability to trap PARP onto DNA differs enormously in the following decreasing order: talazoparib, niraparib, olaparib, rucaparib, veliparib.[80,82,83]

One major complication in PARP inhibitors as single agents is the acquired resistance in tumours, mainly due to four reasons: the restored HR pathway, the increased drug efflux, the restoration of RF stability, and the down-regulation of poly(ADP-ribose) glycohydrolase (PARG) protein expression.[70,84] This expands the application of PARP inhibitors to combination treatments. Combination treatments are notable for minimising dosage requirement, increasing drug efficacy and slow down DNA damage repair. Effective combinations with PARP inhibitors include alkylating agents, metal complexes, radiation, and immunotherapy.[72,85-89] Overall, PARP inhibitors are showing promising results both in monotherapy and in combination treatments.[90]

1.4.4 Rucaparib

In the late 1990, a collaboration searching for new PARP inhibitors was initiated between the Northern Institute for Cancer Research (Newcastle) and Agouron Pharmaceuticals (Pfizer).[91,92] Based on the structure of benzimidazole carboxamide **1.5** (K_i = 95 nM against PARP1), the two groups designed the novel tricyclic indole scaffold **1.6** (AG014344, K_i = 5.6 nM) mimicking the intramolecular hydrogen bonding in **1.5** (Figure 1.12).

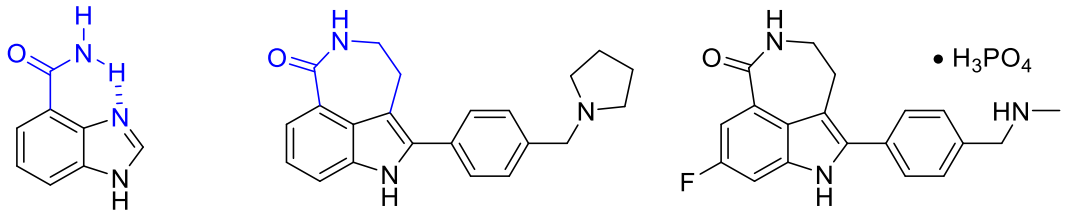

1.5
benzimidazole carboxamide
K_i = 95 nM

1.6
AG014344
K_i = 5.6 nM

1.7
rucaparib phosphate
AG014699
K_i = 1.4 nM

Figure 1.12: Selected PARP inhibitors designed by Newcastle/Agouron.

With further optimisation, rucaparib phosphate **1.7** (AG014699 phosphate, K_i = 1.4 nM) stood out from a list of tricyclic indole lactams. The co-crystal structure refined the interaction between rucaparib and PARP1 catalytic domain (Figure 1.13).[93,94] Besides the conventional triad hydrogen bonding network (lactam/Gly863/Ser904) and π-π interaction (indole/Tyr907), the additional indole C-2 aryl side chain allows π-stacking with Tyr889, pseudo-edge-to-face interaction with Tyr896, and hydrogen bonding between *p*-(*N*-methylamino)methyl group and Asp766.

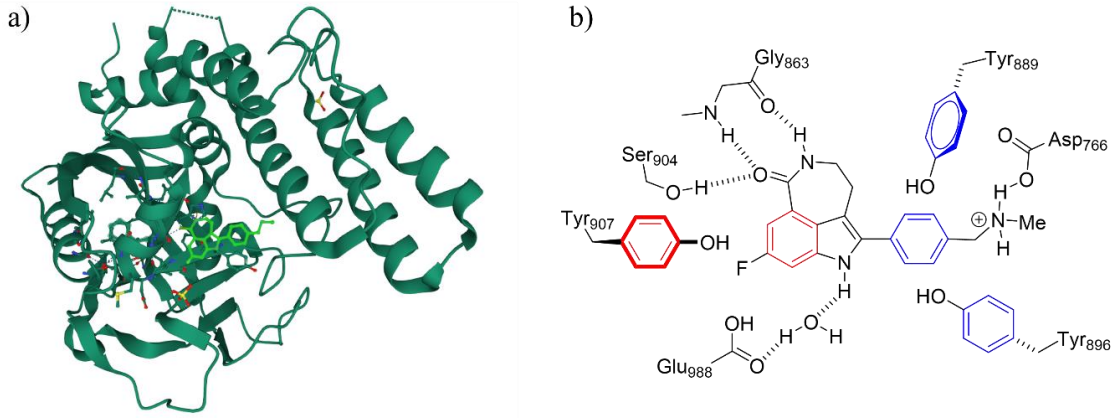

Figure 1.13: a) Co-crystal structure of Rucaprib (grass green) and the CAT domain of human PARP1. b) Rucaparib binding mode in PARP1 catalytic domain.

The Clovis Oncology group licensed rucaparib from Pfizer after phase II clinical trial in 2011 and took over further global development. The active ingredient found in a rucaparib tablet (Rubraca) in the current market is rucaparib camsylate. Among all the counter anions investigated, including chloride, phosphate and maleate, camsylate was the least hygroscopic,

"making it particularly suitable in the preparation of solid dosage forms".[95] Rucaparib was granted FDA accelerated approval for advanced ovarian cancer in 2016, FDA approval for treatment of recurrent ovarian cancer in 2018, and accelerated approval for treatment of *BRCA1/2*-mutant, metastatic castration-resistant prostate cancer (mCRPC) in 2020.[96,97]

1.4.5 Olaparib

Olaparib is the first FDA approved PARP inhibitor, developed by Kudos Pharmaceuticals and Maybridge from the early 2000s.[98] Benzyl phthalazinone **1.8** (PARP1 IC_{50} = 770 nM) stood out from a high throughput screening. Further modification on the benzyl substituents resulted in a 100-fold improvement of potency with the homopiperazine analogue **1.9** (PARP1 IC_{50} = 7 nM). However, this analogue was limited by low oral bioavailability, mainly due to the high pKa (calculated value of 9.87) of the homopiperazine motif. The limitation of oral administration was alleviated when olaparib **1.10** (PARP1 IC_{50} = 5 nM) was synthesised with a cyclopropyl amide installed at the distant end of piperazine. Shortly after olaparib entered clinical trials, it was acquired by AstraZeneca who purchased KuDOS pharmaceutical in 2005, and underwent further clinical development by AstraZeneca and Merck & Co. Olaparib was granted FDA approval for treatment of germline *BRCA*-mutated (g*BRCA*m) advanced ovarian cancer in 2014, g*BRCA*m metastatic breast cancer in 2018, g*BRCA*m metastatic pancreatic cancer in 2019, homologous recombination repair (HRR) gene-mutated mCRPC in 2020, and first-line treatment with bevacizumab for homologous recombination defictive (HRD) advanced ovarian cancer in 2020.[99-101]

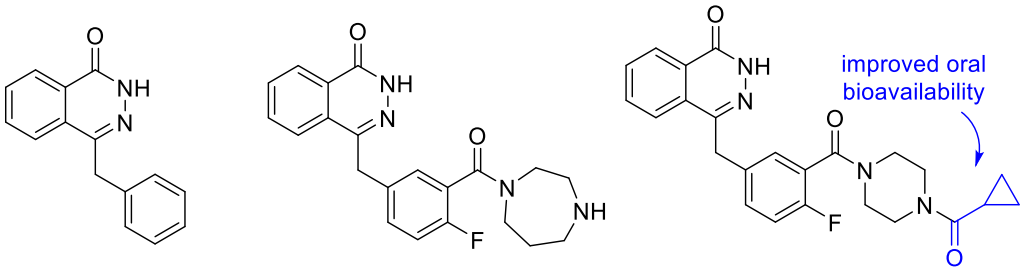

1.8
Benzyl phthalazinone
PARP1 IC_{50} = 770 nM

1.9
Homopiperazine analogue
PARP1 IC_{50} = 7 nM

1.10
Olaparib
PARP1 IC_{50} = 5 nM

Figure 1.6: Selected PARP inhibitors designed by Kudos/Maybridge.

1.5 Conclusions and Thesis Outline

This chapter introduced DNA damage, the corresponding DNA damage response and the fundamental role of PARPs in DNA repairing. PARP inhibitors, emerged as a novel class of cancer drugs that could selectively block PARPs during DNA repairing and selectively target cancer cells by employing synthetic lethality.

To date, PARP inhibitors have reached the first milestone of exhibiting prominent anti-cancer activity. However, questions still remain. Firstly, the mechanism of action of PARP inhibitors in cancer therapy is not fully understood. PARP1 is a multifunctional protein and is associated with a range of cellular activities. Various cellular responses are triggered by DNA damage depending on the type of damage and the stage of cell cycle. All these processes could be affected by PARP inhibitors and thus influence the outcome of cancer treatment. Secondly, apart from the extensively studied PARP1 (and PARP2 to 5 from this century), functions of other members from the PARP family are less well-understood. To what extent PARP inhibitors could interact with other proteins in the PARP family remain in question. Thirdly, expansion of potential targets of PARP inhibitors are still under investigation. Whether PARP inhibitors can be used for treatment of other cancers draws increasing attention. Development a more selective PARP inhibitor is ongoing. Lastly, poor patients' responses with PARP treatment draws the need to establish a method for more accurate patient selection and fast

therapy evaluation. This project aims to employ a radiolabelling strategy to facilitate the understanding of these unsolved questions from both diagnostic and therapeutic aspects.

In Chapter 2, Positron emission tomography (PET) will be introduced as a useful imaging technique to visualise metabolism and other biological processes. Fluorine-18 incorporated PARP inhibitors can function as diagnostic radiotracers to estimate PARP expression levels, PARP inhibitor accumulation in tissues and may benefit for patients with PARP inhibitor treatment. Beyond this, these tracers may also bring insights to the mechanism and binding interaction of PARP inhibitors with PARP proteins or other cellular components. Methods of fluorine-18 production and incorporation will be discussed. An ^{18}F-isotopologue of an FDA-approved PARP inhibitor, rucaparib is access via Cu(II)-mediated ^{18}F-fluorodeboronation from two boronic ester precursors. Full radiosynthesis of the most successful route toward [^{18}F]rucaparib is demonstrated. *In vitro* data, *in vivo* dynamic PET imaging and *ex vivo* biodistribution of [^{18}F]rucaparib are presented subsequently. Biological results reveal the potential of [^{18}F]rucaparib as a potential diagnostic radiotracer for *BRCA*-mutated pancreatic cancer. The future aim of this project includes establishing [^{18}F]rucaparib as a commercial radiotracer through clinical trials for patient stratification.

In Chapter 3, Auger therapy will be introduced as a new emerged treatment for cancer. Iodine-123 incorporated PARP inhibitors are potential radiopharmaceutical therapy agents. A ^{123}I-olaparib analogue and a ^{123}I-rucaparib analogue will be fully radiosynthesised via Cu(II)-mediated ^{123}I-iododeboronation, demonstrating a divergent radiohalogenation approach to access ^{18}F- and ^{123}I-incorporation from common boronic ester precursors. Future aim of this project will be a full biological evaluation of these radiolabelled target as potential Auger therapy agents for cancer treatment.

1.6 Reference

[1] Jackson, S. P.; Bartek, J., The DNA-Damage Response in Human Biology and Disease. *Nature* **2009**, *461* (7267), 1071−1078.

[2] O'Connor, Mark J., Targeting the DNA Damage Response in Cancer. *Mol. Cell* **2015**, *60* (4), 547−560.

[3] Ciccia, A.; Elledge, S. J., The DNA Damage Response: Making It Safe to Play with Knives. *Mol. Cell* **2010**, *40* (2), 179−204.

[4] Hoeijmakers, J. H., DNA Damage, Aging, and Cancer. *N. Engl. J. Med.* **2009**, *361* (15), 1475−1485.

[5] Lindahl, T.; Barnes, D. E., Repair of Endogenous DNA Damage. *Cold Spring Harb. Symp. Quant. Biol.* **2000**, *65*, 127−133.

[6] Klungland, A.; Rosewell, I.; Hollenbach, S.; Larsen, E.; Daly, G.; Epe, B.; Seeberg, E.; Lindahl, T.; Barnes, D. E., Accumulation of Premutagenic DNA Lesions in Mice Defective in Removal of Oxidative Base Damage. *Proc. Natl. Acad. Sci.* **1999**, *96* (23), 13300−13305.

[7] Caldecott, K. W., Single-Strand Break Repair and Genetic Disease. *Nat. Rev. Genet.* **2008**, *9* (8), 619−631.

[8] Hoeijmakers, J. H. J., Genome Maintenance Mechanisms for Preventing Cancer. *Nature* **2001**, *411* (6835), 366−374.

[9] Tubbs, A.; Nussenzweig, A., Endogenous DNA Damage as a Source of Genomic Instability in Cancer. *Cell* **2017**, *168* (4), 644−656.

[10] Lindahl, T., Instability and Decay of the Primary Structure of DNA. *Nature* **1993**, *362* (6422), 709−715.

[11] Friedberg, E. C., A Brief History of the DNA Repair Field. *Cell Res.* **2008**, *18* (1), 3−7.

[12] Kim, Y. J.; Wilson, D. M., 3rd, Overview of Base Excision Repair Biochemistry. *Curr. Mol. Pharmacol.* **2012**, *5* (1), 3−13.

[13] Robertson, A. B.; Klungland, A.; Rognes, T.; Leiros, I., DNA Repair in Mammalian Cells: Base Excision Repair: The Long and Short of It. *Cell Mol. Life Sci.* **2009**, *66* (6), 981−993.

[14] Zharkov, D. O., Base Excision DNA Repair. *Cell Mol. Life Sci.* **2008**, *65* (10), 1544−1565.

[15] Schreiber, V.; Dantzer, F.; Ame, J. C.; de Murcia, G., Poly(ADP-ribose): Novel Functions for an Old Molecule. *Nat. Rev. Mol. Cell Biol.* **2006**, *7* (7), 517−528.

[16] Caldecott, K. W., Single-Strand Break Repair and Genetic Disease. *Nat. Rev. Genet.* **2008**, *9* (8), 619−631.

[17] Beard, W. A.; Horton, J. K.; Prasad, R.; Wilson, S. H., Eukaryotic Base Excision Repair: New Approaches Shine Light on Mechanism. *Annu. Rev. Biochem.* **2019**, *88* (1), 137−162.

[18] Hartlerode, A. J.; Scully, R., Mechanisms of Double-Strand Break Repair in Somatic Mammalian Cells. *Biochem. J.* **2009**, *423* (2), 157−168.

[19] Mahaney, B. L.; Meek, K.; Lees-Miller, S. P., Repair of Ionizing Radiation-Induced DNA Double-Strand Breaks by Non-Homologous End-Joining. *Biochem. J.* **2009**, *417* (3), 639−650.

[20] Meek, K.; Dang, V.; Lees-Miller, S. P., DNA-PK: the Means to Justify the Ends? *Adv. Immunol.* **2008**, *99*, 33−58.

[21] Grundy, G. J.; Rulten, S. L.; Zeng, Z.; Arribas-Bosacoma, R.; Iles, N.; Manley, K.; Oliver, A.; Caldecott, K. W., APLF Promotes the Assembly and Activity of Non-Homologous End Joining Protein Complexes. *EMBO J.* **2013,** *32* (1), 112−125.

[22] Weterings, E.; Chen, D. J., The Endless Tale of Non-Homologous End-Joining. *Cell Res.* **2008**, *18* (1), 114−124.

[23] Bassing, C. H.; Alt, F. W., The Cellular Response to General and Programmed DNA Double Strand Breaks. *DNA Repair (Amst)* **2004**, *3* (8-9), 781−796.

[24] Maréchal, A.; Zou, L., DNA Damage Sensing by the ATM and ATR Kinases. *Cold Spring Harb. Perspect. Biol.* **2013**, *5* (9), a012716.

[25] Jin, M. H.; Oh, D.-Y., ATM in DNA Repair in Cancer. *Pharmacol. Ther.* **2019**, *203*, 107391.

[26] Williams, R. S.; Williams, J. S.; Tainer, J. A., Mre11-Rad50-Nbs1 Is a Keystone Complex Connecting DNA Repair Machinery, Double-Strand Break Signaling, and the Chromatin Template. *Biochem. Cell Biol.* **2007**, *85* (4), 509−520.

[27] Sugiyama, T.; Kowalczykowski, S. C., Rad52 Protein Associates with Replication Protein A (RPA)-Single-Stranded DNA to Accelerate Rad51-Mediated Displacement of RPA and Presynaptic Complex Formation. *J. Biol. Chem.* **2002**, *277* (35), 31663−31672.

[28] Sung, P.; Klein, H., Mechanism of Homologous Recombination: Mediators and Helicases Take on Regulatory Functions. *Nat. Rev. Mol. Cell Biol.* **2006**, *7* (10), 739−750.

[29] Bianco, P. R.; Tracy, R. B.; Kowalczykowski, S. C., DNA Strand Exchange Proteins: A Biochemical and Physical Comparison. *Front Biosci.* **1998**, *3*, D570−603.

[30] Renkawitz, J.; Lademann, C. A.; Jentsch, S., Mechanisms and Principles of Homology Search during Recombination. *Nat. Rev. Mol. Cell Biol.* **2014**, *15* (6), 369−383.

[31] Greene, E. C., DNA Sequence Alignment during Homologous Recombination. *J. Biol. Chem.* **2016**, *291* (22), 11572−11580.

[32] Prakash, R.; Zhang, Y.; Feng, W.; Jasin, M., Homologous Recombination and Human Health: The Roles of BRCA1, BRCA2, and Associated Proteins. *Cold Spring Harb. Perspect. Biol.* **2015**, *7* (4), a016600.

[33] Wyatt, H. D.; West, S. C., Holliday Junction Resolvases. *Cold Spring Harb. Perspect. Biol.* **2014**, *6* (9), a023192.

[34] Constantinou, A.; Chen, X. B.; McGowan, C. H.; West, S. C., Holliday Junction Resolution in Human Cells: Two Junction Endonucleases with Distinct Substrate Specificities. *EMBO J.* **2002**, *21* (20), 5577−5585.

[35] a) Mao, Z.; Bozzella, M.; Seluanov, A.; Gorbunova, V., Comparison of Nonhomologous End Joining and Homologous Recombination in Human Cells. *DNA Repair* **2008,** *7* (10), 1765−1771. b) Lieber, M. R., The biochemistry and biological significance of nonhomologous DNA end joining: an essential repair process in multicellular eukaryotes. *Genes to Cells* **1999,** *4* (2), 77−85.

[36] Lieber, M. R.; Karanjawala, Z. E., Ageing, repetitive genomes and DNA damage. *Nat. Rev. Mol. Cell Biol.* **2004,** *5* (1), 69−75.

[37] Miki, Y.; Swensen, J.; Shattuck-Eidens, D.; Futreal, P. A.; Harshman, K.; Tavtigian, S.; Liu, Q.; Cochran, C.; Bennett, L. M.; Ding, W.; Bell, R.; Rosenthal, J.; Hussey, C.; Tran, T.; McClure, M.; Frye, C.; Hattier, T.; Phelps, R.; Haugen-Strano, A.; Katcher, H.; Yakumo, K.; Gholami, Z.; Shaffer, D.; Stone, S.; Bayer, S.; Wray, C.; Bogden, R.; Dayananth, P.; Ward, J.; Tonin, P.; Narod, S.; Bristow Pam, K.; Norris Frank, H.; Helvering, L.; Morrison, P.; Rosteck, P.; Lai, M.; Barrett, J. C.; Lewis, C.; Neuhausen, S.; Cannon-Albright, L.; Goldgar, D.; Wiseman, R.; Kamb, A.; Skolnick Mark, H., A Strong Candidate for the Breast and Ovarian Cancer Susceptibility Gene BRCA1. *Science* **1994,** *266* (5182), 66−71.

[38] Wooster, R.; Bignell, G.; Lancaster, J.; Swift, S.; Seal, S.; Mangion, J.; Collins, N.; Gregory, S.; Gumbs, C.; Micklem, G.; Barfoot, R.; Hamoudi, R.; Patel, S.; Rices, C.; Biggs, P.; Hashim, Y.; Smith, A.; Connor, F.; Arason, A.; Gudmundsson, J.; Ficenec, D.; Kelsell, D.; Ford, D.; Tonin, P.; Timothy Bishop, D.; Spurr, N. K.; Ponder, B. A. J.; Eeles, R.; Peto, J.; Devilee, P.; Cornelisse, C.; Lynch, H.; Narod, S.; Lenoir, G.; Egilsson, V.; Bjork Barkadottir, R.; Easton, D. F.; Bentley, D. R.; Futreal, P. A.; Ashworth, A.; Stratton, M. R., Identification of the breast cancer susceptibility gene BRCA2. *Nature* **1995,** *378* (6559), 789−792.

[39] Petrucelli, N.; Daly, M.B.; Pal, T.; BRCA1- and BRCA2-Associated Hereditary Breast and Ovarian Cancer. In *GeneReviews*®, University of Washington, Seattle; 1998. [Updated 2016 Dec 15]

[40] Daley James, M.; Sung, P., 53BP1, BRCA1, and the Choice between Recombination and End Joining at DNA Double-Strand Breaks. *Mol. Cell. Biol.* **2014,** *34* (8), 1380−1388.

[41] Chen, L.; Nievera, C. J.; Lee, A. Y.-L.; Wu, X., Cell Cycle-dependent Complex Formation of BRCA1-CtIP-MRN Is Important for DNA Double-strand Break Repair. *J. Biol. Chem.* **2008,** *283* (12), 7713−7720.

[42] Islam, M. N.; Paquet, N.; Fox, D., III; Dray, E.; Zheng, X.-F.; Klein, H.; Sung, P.; Wang, W., A Variant of the Breast Cancer Type 2 Susceptibility Protein (BRC) Repeat Is Essential for the RECQL5 Helicase to Interact with RAD51 Recombinase for Genome Stabilization. *J. Biol. Chem.* **2012,** *287* (28), 23808−23818.

[43] Rajendra, E.; Venkitaraman, A. R., Two Modules in the BRC Repeats of BRCA2 Mediate Structural and Functional Interactions with the RAD51 Recombinase. *Nucleic Acids Res.* **2009,** *38* (1), 82−96.

[44] Carreira, A.; Kowalczykowski, S. C., Two Classes of BRC Repeats in BRCA2 Promote RAD51 Nucleoprotein Filament Function by Distinct Mechanisms. *Proc. Natl. Acad. Sci.* **2011,** *108* (26), 10448.

[45] Shahid, T.; Soroka, J.; Kong, E. H.; Malivert, L.; McIlwraith, M. J.; Pape, T.; West, S. C.; Zhang, X., Structure and Mechanism of Action of the BRCA2 Breast Cancer Tumor Suppressor. *Nat. Struct. Mol. Biol.* **2014,** *21* (11), 962−968.

[46] Chambon, P.; Weill, J. D.; Mandel, P., Nicotinamide Mononucleotide Activation of New DNA-Dependent Polyadenylic Acid Synthesizing Nuclear Enzyme. *Biochem. Biophys. Res. Commun.* **1963**, *11*, 39−43.

[47] Wang, Z.; Wang, F.; Tang, T.; Guo, C., The Role of PARP1 in the DNA Damage Response and Its Application in Tumor Therapy. *Front. Med.* **2012**, *6* (2), 156−164.

[48] Helleday, T., The Underlying Mechanism for the PARP and BRCA Synthetic Lethality: Clearing up the Misunderstandings. *Mol. Oncol.* **2011**, *5* (4), 387−393.

[49] Barkauskaite, E.; Jankevicius, G.; Ahel, I., Structures and Mechanisms of Enzymes Employed in the Synthesis and Degradation of PARP-Dependent Protein ADP-Ribosylation. *Mol. Cell* **2015**, *58* (6), 935−946.

[50] Schiewer, M. J.; Knudsen, K. E., Transcriptional Roles of PARP1 in Cancer. *Mol. Cancer Res.* **2014**, *12* (8), 1069−1080.

[51] Tallis, M.; Morra, R.; Barkauskaite, E.; Ahel, I., Poly(ADP-ribosyl)ation in Regulation of Chromatin Structure and the DNA Damage Response. *Chromosoma* **2014,** *123* (1), 79−90.

[52] Fisher, A. E.; Hochegger, H.; Takeda, S.; Caldecott, K. W., Poly(ADP-Ribose) Polymerase 1 Accelerates Single-Strand Break Repair in Concert with Poly(ADP-Ribose) Glycohydrolase. *Mol. Cell Biol.* **2007**, *27* (15), 5597−5605.

[53] Ali, A. A. E.; Timinszky, G.; Arribas-Bosacoma, R.; Kozlowski, M.; Hassa, P. O.; Hassler, M.; Ladurner, A. G.; Pearl, L. H.; Oliver, A. W., The Zinc-Finger Domains of PARP1 Cooperate to Recognize DNA Strand Breaks. *Nat. Struct. Mol. Biol.* **2012,** *19* (7), 685−692.

[54] (a) van Beek, L.; McClay, É.; Patel, S.; Schimpl, M.; Spagnolo, L.; Maia de Oliveira, T., PARP Power: A Structural Perspective on PARP1, PARP2, and PARP3 in DNA Damage Repair and Nucleosome Remodelling. *Int. J. Mol. Sci.* **2021**, *22* (10), 5112. (b) Alemasova, E. E.; Lavrik, O. I., Poly(ADP-ribosyl)ation by PARP1: reaction mechanism and regulatory proteins. *Nucleic Acids Res.* **2019,** *47* (8), 3811−3827.

[55] a) Langelier, M.-F.; Ruhl, D. D.; Planck, J. L.; Kraus, W. L.; Pascal, J. M., The Zn3 Domain of Human Poly(ADP-ribose) Polymerase-1 (PARP-1) Functions in Both DNA-dependent Poly(ADP-ribose) Synthesis Activity and Chromatin Compaction. *J. Biol. Chem.*

2010, *285* (24), 18877−18887. b) Langelier, M.-F.; Planck, J. L.; Roy, S.; Pascal, J. M., Crystal Structures of Poly(ADP-ribose) Polymerase-1 (PARP-1) Zinc Fingers Bound to DNA. *J. Biol. Chem.* **2011,** *286* (12), 10690−10701. c) Steffen, J. D.; McCauley, M. M.; Pascal, J. M., Fluorescent Sensors of PARP-1 Structural Dynamics and Allosteric Regulation in Response to DNA Damage. *Nucleic Acids Res.* **2016,** *44* (20), 9771−9783.

[56] Loeffler, P. A.; Cuneo, M. J.; Mueller, G. A.; DeRose, E. F.; Gabel, S. A.; London, R. E., Structural Studies of the PARP-1 BRCT Domain. *BMC Struct. Biol.* **2011,** *11* (1), 37.

[57] Kamaletdinova, T.; Fanaei-Kahrani, Z.; Wang, Z.-Q., The Enigmatic Function of PARP1: From PARylation Activity to PAR Readers. *Cells* **2019,** *8* (12).

[58] Dawicki-McKenna, Jennine M.; Langelier, M.-F.; DeNizio, Jamie E.; Riccio, Amanda A.; Cao, Connie D.; Karch, Kelly R.; McCauley, M.; Steffen, Jamin D.; Black, Ben E.; Pascal, John M., PARP-1 Activation Requires Local Unfolding of an Autoinhibitory Domain. *Mol. Cell* **2015,** *60* (5), 755−768.

[59] Lord, C. J.; Ashworth, A., PARP Inhibitors: Synthetic Lethality in the Clinic. *Science* **2017**, *355* (6330), 1152−1158.

[60] Clark, J. B.; Ferris, G. M.; Pinder, S., Inhibition of Nuclear NAD Nucleosidase and Poly ADP-Ribose Polymerase Activity from Rat Liver by Nicotinamide and 5′-Methyl Nicotinamide. *Biochim. Biophys. Acta* **1971**, *238* (1), 82−85.

[61] Banasik, M.; Komura, H.; Shimoyama, M.; Ueda, K., Specific Inhibitors of Poly(ADP-Ribose) Synthetase and Mono(ADP-Ribosyl)Transferase. *J. Biol. Chem.* **1992**, *267* (3), 1569−1575.

[62] Shall, S., Proceedings: Experimental Manipulation of the Specific Activity of Poly(ADP-Ribose) Polymerase. *J. Biochem.* **1975**, *77* (1), 2p.

[63] Rankin, P. W.; Jacobson, E. L.; Benjamin, R. C.; Moss, J.; Jacobson, M. K., Quantitative Studies of Inhibitors of ADP-Ribosylation *In Vitro* and *In Vivo*. *J. Biol. Chem.* **1989**, *264* (8), 4312−4317.

[64] Purnell, M. R.; Whish, W. J., Novel Inhibitors of Poly(ADP-Ribose) Synthetase. *Biochem. J.* **1980**, *185* (3), 775−777.

[65] Boulton, S.; Pemberton, L. C.; Porteous, J. K.; Curtin, N. J.; Griffin, R. J.; Golding, B. T.; Durkacz, B. W., Potentiation of Temozolomide-Induced Cytotoxicity: A Comparative Study of the Biological Effects of Poly(ADP-Ribose) Polymerase Inhibitors. *Br. J. Cancer* **1995**, *72* (4), 849−856.

[66] Ruf, A.; de Murcia, G.; Schulz, G. E., Inhibitor and NAD+ Binding to Poly(ADP-ribose) Polymerase As Derived from Crystal Structures and Homology Modeling. *Biochemistry* **1998,** *37* (11), 3893−3900.

[67] Hattori, K.; Kido, Y.; Yamamoto, H.; Ishida, J.; Kamijo, K.; Murano, K.; Ohkubo, M.; Kinoshita, T.; Iwashita, A.; Mihara, K.; Yamazaki, S.; Matsuoka, N.; Teramura, Y.; Miyake, H., Rational Approaches to Discovery of Orally Active and Brain-Penetrable Quinazolinone Inhibitors of Poly(ADP-ribose)polymerase. *J. Med. Chem.* **2004,** *47* (17), 4151−4154.

[68] Skalitzky, D. J.; Marakovits, J. T.; Maegley, K. A.; Ekker, A.; Yu, X.-H.; Hostomsky, Z.; Webber, S. E.; Eastman, B. W.; Almassy, R.; Li, J.; Curtin, N. J.; Newell, D. R.; Calvert, A. H.; Griffin, R. J.; Golding, B. T., Tricyclic Benzimidazoles as Potent Poly(ADP-ribose) Polymerase-1 Inhibitors. *J. Med. Chem.* **2003**, *46* (2), 210−213.

[69] Ferraris, D. Overview of PARP Inhibitor Design and Optimization.In *PARP Inhibitors for Cancer Therapy*; Cancer Drug Discovery and Development, Vol. 83. Humana Press, 2015; pp 183−203.

[70] Rose, M.; Burgess, J. T.; O'Byrne, K.; Richard, D. J.; Bolderson, E., PARP Inhibitors: Clinical Relevance, Mechanisms of Action and Tumor Resistance. *Front. Cell Dev. Biol.* **2020**, *8* (879), 564601.

[71] Bridges, C. B., The Origin of Variations in Sexual and Sex-Limited Characters. *Am. Nat.* **1922**, *56* (642), 51−63.

[72] Dobzhansky, T., Genetics of Natural Populations; Recombination and Variability in Populations of Drosophila Pseudoobscura. *Genetics* **1946**, *31* (3), 269−290.

[73] Livraghi, L.; Garber, J. E., PARP Inhibitors in the Management of Breast Cancer: Current Data and Future Prospects. *BMC Med.* **2015**, *13* (1), 188.

[74] Boussios, S.; Karihtala, P.; Moschetta, M.; Abson, C.; Karathanasi, A.; Zakynthinakis-Kyriakou, N.; Ryan, J. E.; Sheriff, M.; Rassy, E.; Pavlidis, N., Veliparib in Ovarian Cancer: A New Synthetically Lethal Therapeutic Approach. *Invest. New Drugs* **2020**, *38* (1), 181−193.

[75] Stodtmann, S.; Nuthalapati, S.; Eckert, D.; Kasichayanula, S.; Joshi, R.; Bach, B. A.; Mensing, S.; Menon, R.; Xiong, H., A Population Pharmacokinetic Meta-Analysis of Veliparib, a PARP Inhibitor, Across Phase 1/2/3 Trials in Cancer Patients. *J. Clin. Pharmacol.* **2021**, *61* (9), 1195−1205.

[76] Curtin, N. J.; Szabo, C., Poly(ADP-Ribose) Polymerase Inhibition: Past, Present and Future. *Nat. Rev. Drug Discov.* **2020**, *19* (10), 711−736.

[77] Plummer, R.; Dua, D.; Cresti, N.; Drew, Y.; Stephens, P.; Foegh, M.; Knudsen, S.; Sachdev, P.; Mistry, B. M.; Dixit, V.; McGonigle, S.; Hall, N.; Matijevic, M.; McGrath, S.; Sarker, D., First-in-Human Study of the PARP/Tankyrase Inhibitor E7449 in Patients with Advanced Solid Tumours and Evaluation of a Novel Drug-Response Predictor. *Br. J. Cancer* **2020**, *123* (4), 525−533.

[78] Leo, E.; Johannes, J., Abstract ND05: Discovery and First Structural Disclosure of AZD5305: A Next Generation, Highly Selective PARP1 Inhibitor and Trapper. *Cancer Res.* **2021**, *81* (13 Supplement), ND05.

[79] Staniszewska, A. D.; Jwt, J. W. Y.; Pike, A.; Fazenbaker, C.; Cook, K.; Bosco, E.; Smith, A.; Wilson, J.; Leo, E., Abstract 1270: The Novel PARP1-Selective Inhibitor, AZD5305, Is Efficacious as Monotherapy and in Combination with Standard of Care Chemotherapy in the *In Vivo* Preclinical Models. *Cancer Res.* **2021**, *81* (13 Supplement), 1270.

[80] Murai, J.; Huang, S.-y. N.; Das, B. B.; Renaud, A.; Zhang, Y.; Doroshow, J. H.; Ji, J.; Takeda, S.; Pommier, Y., Trapping of PARP1 and PARP2 by Clinical PARP Inhibitors. *Cancer Res.* **2012**, *72* (21), 5588−5599.

[81] Murai, J.; Marchand, C.; Shahane, S. A.; Sun, H.; Huang, R.; Zhang, Y.; Chergui, A.; Ji, J.; Doroshow, J. H.; Jadhav, A.; Takeda, S.; Xia, M.; Pommier, Y., Identification of Novel PARP Inhibitors Using a Cell-Based TDP1 Inhibitory Assay in a Quantitative High-Throughput Screening Platform. *DNA Repair (Amst)* **2014**, *21*, 177−182.

[82] Murai, J.; Huang, S.-Y. N.; Renaud, A.; Zhang, Y.; Ji, J.; Takeda, S.; Morris, J.; Teicher, B.; Doroshow, J. H.; Pommier, Y., Stereospecific PARP Trapping by BMN 673 and Comparison with Olaparib and Rucaparib. *Mol. Cancer Ther.* **2014**, *13* (2), 433−443.

[83] Pommier, Y.; O'Connor, M. J.; de Bono, J., Laying a Trap to Kill Cancer Cells: PARP Inhibitors and Their Mechanisms of Action. *Sci. Transl. Med.* **2016**, *8* (362), 362ps17.

[84] Dias, M. P.; Moser, S. C.; Ganesan, S.; Jonkers, J., Understanding and Overcoming Resistance to PARP Inhibitors in Cancer Therapy. *Nat. Rev. Clin. Oncol.* **2021**, online ahead of print.

[85] Vikas, P.; Borcherding, N.; Chennamadhavuni, A.; Garje, R., Therapeutic Potential of Combining PARP Inhibitor and Immunotherapy in Solid Tumors. *Front. Oncol.* **2020**, *10*, 570.

[86] Matulonis, U. A.; Monk, B. J., PARP Inhibitor and Chemotherapy Combination Trials for the Treatment of Advanced Malignancies: Does a Development Pathway Forward Exist? *Ann. Oncol.* **2017**, *28* (3), 443−447.

[87] Nacev, B. A.; Tap, W. D., TOMAS: Revisiting PARP Inhibitor Combination Therapy. *Lancet Oncol.* **2018**, *19* (10), 1269−1270.

[88] Yusoh, N. A.; Ahmad, H.; Gill, M. R., Combining PARP Inhibition with Platinum, Ruthenium or Gold Complexes for Cancer Therapy. *ChemMedChem* **2020**, *15* (22), 2121−2135.

[89] Jannetti, S. A.; Zeglis, B. M.; Zalutsky, M. R.; Reiner, T., Poly(ADP-Ribose) Polymerase (PARP) Inhibitors and Radiation Therapy. *Front Pharmacol.* **2020**, *11*, 170.

[90] Chan, C. Y.; Tan, K. V.; Cornelissen, B., PARP Inhibitors in Cancer Diagnosis and Therapy. *Clin. Cancer Res.* **2021**, *27* (6), 1585−1594.

[91] Curtin, N. J., The Development of Rucaparib/Rubraca®: A Story of the Synergy Between Science and Serendipity. *Cancers (Basel)* **2020**, *12* (3), 564.

[92] Golding, B. T., The Story of Rucaparib (Rubraca). In *Successful Drug Discovery*, Vol. 4. John Wiley & Sons, 2019; pp 201−223.

[93] Canan Koch, S. S.; Thoresen, L. H.; Tikhe, J. G.; Maegley, K. A.; Almassy, R. J.; Li, J.; Yu, X.-H.; Zook, S. E.; Kumpf, R. A.; Zhang, C.; Boritzki, T. J.; Mansour, R. N.; Zhang, K. E.; Ekker, A.; Calabrese, C. R.; Curtin, N. J.; Kyle, S.; Thomas, H. D.; Wang, L.-Z.; Calvert, A. H.; Golding, B. T.; Griffin, R. J.; Newell, D. R.; Webber, S. E.; Hostomsky, Z., Novel Tricyclic Poly(ADP-ribose) Polymerase-1 Inhibitors with Potent Anticancer Chemopotentiating Activity: Design, Synthesis, and X-ray Cocrystal Structure. *J. Med. Chem.* **2002**, *45* (23), 4961−4974.

[94] Zandarashvili, L.; Langelier, M.-F.; Velagapudi, U. K.; Hancock, M. A.; Steffen, J. D.; Billur, R.; Hannan, Z. M.; Wicks, A. J.; Krastev, D. B.; Pettitt, S. J.; Lord, C. J.; Talele, T.

T.; Pascal, J. M.; Black, B. E., Structural Basis for Allosteric PARP-1 Retention on DNA Breaks. *Science* **2020,** *368* (6486), eaax6367.

[95] Basford P. A.; Campeta A. M.; Gillmore A.; Jones M. C.; Kougoulos E.; Luthra S.; Walton R., Salts and Polymorphs of 8-Fluoro-2-{4-[(methylamino)methyl]phenyl}-1,3,4,5-tetrahydro-6*H*-azepino[5,4,3-*cd*]indol-6-one. U. S. Patent US 8754072B2, June 17, 2014.

[96] Balasubramaniam, S.; Beaver, J. A.; Horton, S.; Fernandes, L. L.; Tang, S.; Horne, H. N.; Liu, J.; Liu, C.; Schrieber, S. J.; Yu, J.; Song, P.; Pierce, W.; Robertson, K. J.; Palmby, T. R.; Chiu, H. J.; Lee, E. Y.; Philip, R.; Schuck, R.; Charlab, R.; Banerjee, A.; Chen, X. H.; Wang, X.; Goldberg, K. B.; Sridhara, R.; Kim, G.; Pazdur, R., FDA Approval Summary: Rucaparib for the Treatment of Patients with Deleterious BRCA Mutation-Associated Advanced Ovarian Cancer. *Clin. Cancer Res.* **2017**, *23* (23), 7165−7170.

[97] Anscher, M. S.; Chang, E.; Gao, X.; Gong, Y.; Weinstock, C.; Bloomquist, E.; Adeniyi, O.; Charlab, R.; Zimmerman, S.; Serlemitsos-Day, M.; Ning, Y. M.; Mayrosh, R.; Fuller, B.; Trentacosti, A. M.; Gallagher, P.; Bijwaard, K.; Philip, R.; Ghosh, S.; Fahnbulleh, F.; Diggs, F.; Arora, S.; Goldberg, K. B.; Tang, S.; Amiri-Kordestani, L.; Pazdur, R.; Ibrahim, A.; Beaver, J. A., FDA Approval Summary: Rucaparib for the Treatment of Patients with Deleterious BRCA-Mutated Metastatic Castrate-Resistant Prostate Cancer. *Oncologist* **2021**, *26* (2), 139−146.

[98] Menear, K. A.; Adcock, C.; Boulter, R.; Cockcroft, X.-l.; Copsey, L.; Cranston, A.; Dillon, K. J.; Drzewiecki, J.; Garman, S.; Gomez, S.; Javaid, H.; Kerrigan, F.; Knights, C.; Lau, A.; Loh, V. M.; Matthews, I. T. W.; Moore, S.; O'Connor, M. J.; Smith, G. C. M.; Martin, N. M. B., 4-[3-(4-Cyclopropanecarbonylpiperazine-1-carbonyl)-4-fluorobenzyl]-2*H*-phthalazin-1-one: A Novel Bioavailable Inhibitor of Poly(ADP-ribose) Polymerase-1. *J. Med. Chem.* **2008,** *51* (20), 6581−6591.

[99] Kim, G.; Ison, G.; McKee, A. E.; Zhang, H.; Tang, S.; Gwise, T.; Sridhara, R.; Lee, E.; Tzou, A.; Philip, R.; Chiu, H. J.; Ricks, T. K.; Palmby, T.; Russell, A. M.; Ladouceur, G.; Pfuma, E.; Li, H.; Zhao, L.; Liu, Q.; Venugopal, R.; Ibrahim, A.; Pazdur, R., FDA Approval Summary: Olaparib Monotherapy in Patients with Deleterious Germline BRCA-Mutated Advanced Ovarian Cancer Treated with Three or More Lines of Chemotherapy. *Clin. Cancer Res.* **2015,** *21* (19), 4257−4261.

[100] Arora, S.; Balasubramaniam, S.; Zhang, H.; Berman, T.; Narayan, P.; Suzman, D.; Bloomquist, E.; Tang, S.; Gong, Y.; Sridhara, R.; Turcu, F. R.; Chatterjee, D.; Saritas-Yildirim, B.; Ghosh, S.; Philip, R.; Pathak, A.; Gao, J. J.; Amiri-Kordestani, L.; Pazdur, R.; Beaver, J. A., FDA Approval Summary: Olaparib Monotherapy or in Combination with Bevacizumab for the Maintenance Treatment of Patients with Advanced Ovarian Cancer. *Oncologist* **2021,** *26* (1), e164−e172.

[101] Now available online:

https://www.accessdata.fda.gov/drugsatfda_docs/label/2020/208558s014lbl.pdf

Chapter 2. Development of [^{18}F]Rucaparib as a Potential Diagnostic Radiotracer

2.1 Positron Emission Tomography

Medical imaging plays a crucial rule in diagnosis and therapeutic treatment of diseases. Techniques such as magnetic resonance imaging (MRI), computed tomography (CT), X-ray and ultrasound, focus on anatomical imaging. In contrast, positron emission tomography (PET) provides valuable information to study metabolism and visualise biological processes.[1-4] The development of PET can be traced back to the late 1920s, with the discovery of the positron by Carl David Anderson at the California Institute of Technology, and the invention of the cyclotron by Ernest Orlando Lawrence at the University of California, Berkeley. In the mid-1950s, the first cyclotron was installed in a medical centre at Hammersmith Hospital in London (1955) and oxygen-15 was used in biochemical studies. In the mid-1970s, the prototype of modern PET system was developed and the now common PET probe, 2-[^{18}F]fluoro-2-deoxy-D-glucose ([^{18}F]FDG) **[^{18}F]2.1** was made available at the Brookhaven National Laboratory in 1976 (Figure 2.1).[5-7] PET imaging with radiolabelled probes has acquired increased attention, especially in cancer research and clinical applications. Furthermore, combined imaging techniques, such as PET/CT, renders both anatomic and molecular information, thereby improving disease management.[8]

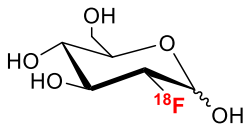

[^{18}F]2.1

Figure 2.1: Structure of 2-[^{18}F]fluoro-2-deoxy-D-glucose ([^{18}F]FDG).

2.1.1 Principles of PET

PET requires the injection, or sometimes inhalation of a biologically-active molecule labelled with a positron-emitting radionuclide. Frequently used non-metal radionuclides including carbon-11, nitrogen-13, oxygen-15, fluorine-18, are mostly, but not exclusively, generated in a cyclotron (Table 2.1). Charged particles, e.g. protons, are accelerated along a spiral path

under a constant magnetic field and a high frequency alternating voltage to create bombardment towards stable nuclide targets, generating radioactive nuclides in the process.[9] A compact notation of these nuclear reactions are denoted in Table 2.1. The symbols *p*, *α*, *d*, *n* represent proton, alpha particle, deuteron and neutron, respectively. In the notation $^{18}O(p,n)^{18}F$, oxygen-18 represents the target nucleus bombarded by a beam of protons. The neutron is generated as the side product and the radionuclide fluoride-18 is produced in this process. Other examples of radionuclides for human PET imaging studies, including gallium-68 and rubidium-82, are produced by a generator, although gallium-68 can also be produced with a cyclotron from zinc-68 ($^{68}Zn(p,n)^{68}Ga$). Radionuclide generators are devices which produce short-lived radionuclide (referred to as the "daughter") from a relatively long-lived radionuclide (referred to as the "parent").[10] In a $^{68}Ge/^{68}Ga$ (parent/daughter) radionuclide generator, the parent radionuclide germanium-68 is produced from the nuclear reaction $^{69}Ga(p,2n)^{68}Ge$, which spontaneously decays to gallium-68 via an electron capture reaction. Gallium-68 is eluted with dilute hydrochloric acid and separated from germanium-68 through a solid-phase column packed with inorganic oxides, such as TiO_2, SnO_2 and ZrO_2, which selectively absorb the parent germanium-68.

Radio-nuclide	Main method of production	Half-life $t_{1/2}$/ (min)	Target	Product	Maximum β^+ energy (MeV)	Decay product
^{11}C	$^{14}N(p,\alpha)^{11}C$	20.2	$N_2(+O_2)$ $N_2(+H_2)$	$[^{11}C]CO_2$ $[^{11}C]CH_4$	0.97	^{11}B
^{13}N	$^{16}O(p,\alpha)^{13}N$	9.97	H_2O H_2O+EtOH	$[^{13}N]NO_x$ $[^{13}N]NH_3$	1.20	^{13}C
^{15}O	$^{15}N(d,n)^{15}O$	2.04	$N_2(+O_2)$	$[^{15}O]O_2$	1.74	^{15}N
^{18}F	$^{20}Ne(d,\alpha)^{18}F$ $^{18}O(p,n)^{18}F$	110	$Ne(+F_2)$ $[^{18}O]H_2O$	$[^{18}F]F_2$ $^{18}F^-$	0.64	^{18}O

Table 2.1: Physical properties of common radionuclides used in PET imaging.

PET radionuclides undergo decay by emitting a positron (β^+), which is not detected directly, but travels a short distance and dissipates its kinetic energy through multiple collisions with electrons in the neighbouring tissues. Upon almost loss of its energy, the positron combines with an electron to form a positronium (Figure 2.2).[11] This short-lived composition eventually

annihilates and emits simultaneously two gamma (γ) quanta of 511 keV that travel at 180° to each other which will then be detected by surrounding detectors. The approximate location of the annihilation event can be deducted, which localises along the line between two parallel opposite detectors. A cross-sectional 2D image of the radiotracer distribution under region of interest can then be reconstructed into a 3D image.[12]

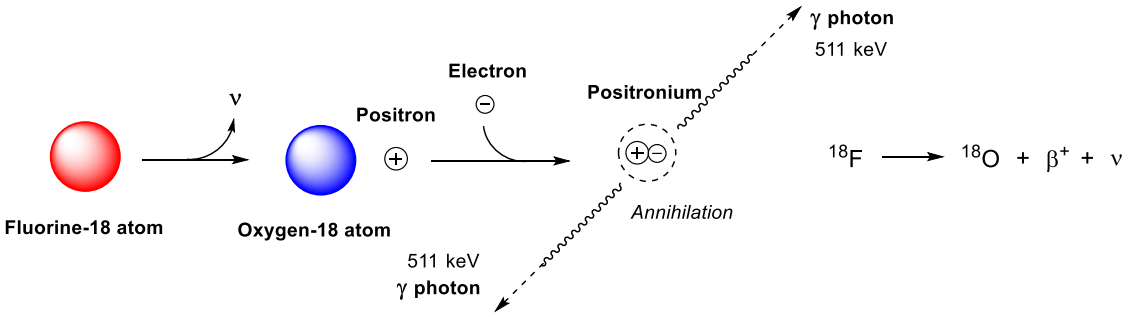

Figure 2.2: Decay profile of a positron emitting radionuclide.

2.1.2 Fundamental Limit of Spatial Resolution in PET Imaging

The spatial resolution of PET imaging is limited by multiple factors, including detector size, positron range, and non-collinearity (Figure 2.3).[13,14]

Detector size

The detector elements are usually made of scintillator crystals. The limitation caused by the detector size originates from the fact that the position of detection within the detector element is not determined. The coincidence rate of an opposite detection pair reaches maximum when the positron source is at half way of their widths.

Positron range

The positron emitted from the nucleus travels a short distance before it captures an electron to form a positronium and subsequently decays into a pair of photons. Fluorine-18, for example, has the lowest endpoint energy of 0.64 MeV among common PET radionuclides and its positron travels about 2.4 mm in water.[15] This distance between the annihilation event and the

position of its parent nucleus creates image blurring, ranging from 0.54 mm full width at half maximum (FWHM) for fluorine-18, and 6.14 mm FWHM for rubidium-86.

Non-collinearity

The kinetic energy of the short-lived positronium doesn't fall to zero when it annihilates, so the direction of the photon pairs is slightly tilted from 180°. The mean angle of this deviation is 0.2° FWHM and results in a blurring effect proportional to the radius of the detector ring.

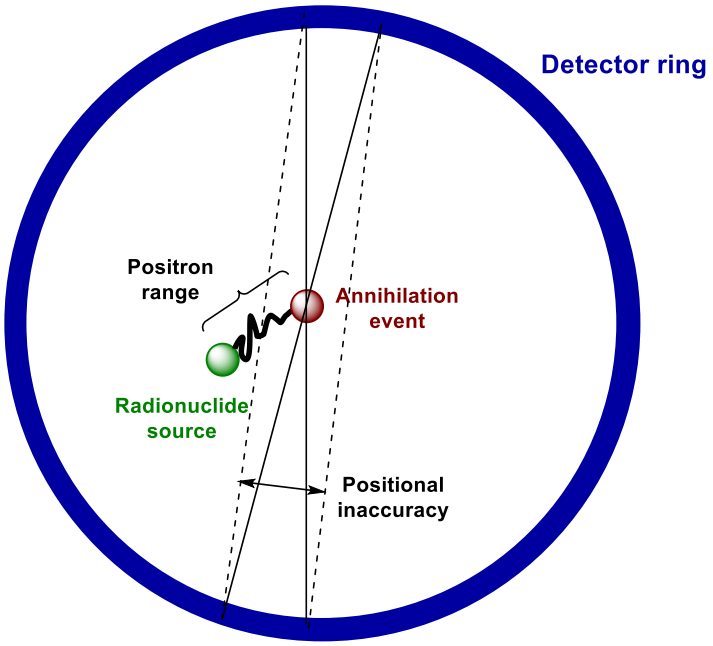

Figure 2.3: Positional inaccuracy caused by positron range, non-collinearity, and detector diameter.

The overall spatial resolution is a convolution of all the components.. Methods have been developed to ameliorate the underlying physical limitations posed by different factors. Positron range blurring can be alleviated by Fourier deconvolution. This method uses a previously obtained positron range spread function to retain the information in higher spatial frequency and improves the estimation of positron activity in each region of quantitation.[16] Better detector design with light-sharing properties using small cross-section crystals also improves spatial resolution.[17] Another essential factor is the choice of radionuclide. The positron that emits from fluorine-18 typically travels a range of 2−3 mm in the tissue. The positional inaccuracy is the

lowest among the PET radionuclides, and hence PET imaging with fluorine-18 incorporated probes tends to have the highest spatial resolution, if other variables are assumed constant.

2.2 Fluorine-18

Positron energy is not the only criterion that dominates the design and selection of radiopharmaceuticals and fluorine-18 has advantages in several other aspects. Fluorine-18 has a half-life of 109.77 minutes, enabling radiosynthesis of complex molecules (up to 6 hours, i.e. $3 \times t_{1/2}$, being considered acceptable),[18] distribution of radiotracers to remote sites and longer *in vitro* and *in vivo* experiments.[19,20] The clean decay profile (97% positron decay and 3% electron capture) of fluorine-18 also contributes to its high demand in nuclear medicine (Equation 2.1 and 2.2).

$$^{18}F \rightarrow {}^{18}O + \beta^{+} + \nu \quad (97\%) \qquad (2.1)$$

$$^{18}F + e^{-} \rightarrow {}^{18}O + \nu \quad (3\%) \qquad (2.2)$$

2.2.1 Fluorine in Medicinal Chemistry

Fluorine plays a significant role in medicinal chemistry. In the last two decades, approximately 25% of registered synthetic marketed drugs contain at least one fluorine atom[21,22] and the number has increased to 40-50% from 2018 onwards.[23] Fluorine is the most electronegative element and C-F is one of the strongest single bonds (Table 2.2).[24]

Element	Van der Waals radius [Å]	C-X bond length [Å]	C-X BDE [kJ·mol^{-1}]
H	1.20	1.09	421[a], 466[b]
F	1.47	1.41	467[a], 532[b]
O	1.52	1.43	391[a], 471[b]

Table 2.2: Properties of H, O, and F substituents.[24-26] [a]Bond dissociation energies of C_2H_5-**H**, C_2H_5-**F** and C_2H_5-**OH**. [b]Bond dissociation energies of C_6H_5-**H**, C_6H_5-**F** and C_6H_5-**OH**.

Bioisosterism is a key concept in medicinal chemistry. It refers to the capacity of interchanging substituents with similar chemical and physical properties, without significantly altering the biological properties of the drug molecule, such as binding affinity. Fluorine is often used to

replace an H atom, but their radii and stereoelectronic effects are quite different.[25,26] C-C single bonds adjacent to F are strengthened and C=C double bonds with allylic fluoro-substituents are weakened. Such substitution could lead to change in conformational preference. Instead, due to the similarities in atomic radii and bond lengths, C-F is a good bioisostere of C-OH, C=O and in some cases C-OMe groups.[27,28]

Fluorine atoms are also introduced to improve metabolic stability. One notable example is the cytochrome P450 enzymes (P450s), which are involved in the metabolism of most pharmaceutical compounds, including hydroxylation, dealkylation and epoxidation.[29] Impact of P450s metabolism is profound and sometimes may result in deactivation of the drug to increase its clearance from the body.[30] Installing a fluorine substituent at the metabolically labile site may block this catalytic pathway without significantly altering binding affinity.[31]

Another major challenge in drug development is the balance between oral bioavailability and binding affinity. Strongly basic amine groups are sometimes required for binding but may result in low bioavailability due to poor ability to pass through membranes. Introducing a fluorine atom close to the amine reduces its basicity and impacts membrane permeability, thereby improving bioavailability.

The significance of fluorine-19 in the pharmaceutical industry and fluorine-18 in PET imaging applications accentuates the need for the development of simple and efficient procedures for fluorine-18 production and ^{18}F-radiosynthesis. A recent study shows that the most prevalent motif by far in fluorinated pharmaceuticals is (hetero)aryl fluoride (C_{sp2}-F, 45.3%).[32,33]

2.2.2 Production of Fluorine-18

Fluorine-18 is produced with cyclotrons either as $[^{18}F]F_2$ for electrophilic and/or radical fluorination, or as nucleophilic $[^{18}F]F^-$ (Table 2.3). Two prevalent methods have been developed for the production of $[^{18}F]F_2$. In the first approach, $[^{18}F]F_2$ is produced by the nuclear

reaction $^{18}O(p,n)^{18}F$ using a "two-bombardment" method.[34,35] A passivated nickel target is charged with $[^{18}O]O_2$ and irradiated with 10−16 MeV protons to give ^{18}F affixed to the target wall. The target is then emptied and refilled with an inert gas (neon or krypton) carrying 1% F_2 (in micromoles), and irradiated again to induce isotopic exchange between ^{18}F absorbed on the wall and the molecule F_2. Nickel was later replaced by aluminium as the target body to achieve consistent activity yields of up to 34 GBq, with molar activities (A_m) in the range of 350−600 MBq/μmol.[36-38] In the second approach, $[^{18}F]F_2$ was obtained from $^{20}Ne(d,\alpha)^{18}F$ by deuteron irradiation of neon-20 gas carrying 0.1−2% of F_2 (in micromoles).[39,40] In the 1980s, there was a high demand of fluorine-18 labelled fluorine gas for electrophilic radiosynthesis of important radiopharmaceuticals, including $[^{18}F]$FDG. $[^{18}F]F_2$ is a highly reactive reagent, which leads to poor regioselectivity and mixtures of undesired products which are usually difficult to separate.[41] In addition, carrier-added $[^{18}F]F_2$, generally results in low A_m (100−600 MBq/μmol), which is an important limitation for PET tracers and their applications in biological systems.

Nuclear Reaction	Target	Energy Range (MeV)	Product
$^{18}O(p,n)^{18}F$	$[^{18}O]O_2$	18−4	$[^{18}F]F_2$
$^{20}Ne(d,\alpha)^{18}F$	Ne, then Ne + 0.1% F_2	15−0	$[^{18}F]F_2$
$^{18}O(p,n)^{18}F$	$[^{18}O]H_2O$	18−4	$[^{18}F]F^-$
$^{6}Li(n,\alpha)^{3}H$, $^{16}O(^{3}H,n)^{18}F$	H_2O	15−1	$[^{18}F]F^-$
$^{16}O(^{3}H,n)^{18}Ne$: ^{18}F	H_2O	40−15	$[^{18}F]F^-$
$^{16}O(\alpha,np)^{18}F$	H_2O	40−20	$[^{18}F]F^-$
$^{16}O(\alpha,2n)^{18}Ne$: ^{18}F	H_2O	52−10	$[^{18}F]F^-$
$^{20}Ne(^{3}H,\alpha p)^{18}F$	Ne	40−10	$[^{18}F]F^-$
$^{20}Ne(p,2pn)^{18}F$	Ne	40−30	$[^{18}F]F^-$

Table 2.3: Nuclear reactions used for the cyclotron production of fluorine-18.

In the 1960s, $[^{18}F]$fluoride was produced from nuclear reactions $^{6}Li(n,\alpha)^{3}H$ and $^{16}O(^{3}H,n)^{18}F$ by irradiating Li_2CO_3 powder with the neutron flux from a nuclear reactor.[42] The earliest cyclotron produced $[^{18}F]$fluoride was obtained by bombardment of large-volume (10 mL)

water targets with a 30 MeV α-particle beam from the nuclear reaction $^{16}O(\alpha,np)^{18}F$.[43] The protocol used at present for clinical PET studies is from the nuclear reaction $^{18}O(p,n)^{18}F$ by 4−18MeV proton irradiation of small-volume (< 3 mL) [^{18}O]water targets to yield oxygen-18 enriched aqueous solutions of [^{18}F]fluoride.[44-47] Nucleophilic [^{18}F]fluoride is produced in much higher molar activity, in the range of 10^2 GBq/µmol. Although the general procedure has not been changed significantly since first reported, improvement was achieved by optimising the production equipment. Optimising the material of the target body and the foil reduced ionic impurities.[48,49] A high target current of 160 µA was achieved by adopting desired target properties, such as target body thickness, foil composition and beam profile. Production of 1 TBq of [^{18}F]F^- was reported.[50] By replacing fluorine-containing components such as polytetrafluoroethylene (PTFE) with polypropylene (PP) or polyether ether ketone (PEEK) in tubing led to increased A_m up to 2−6 TBq/µmol.[51-53]

2.3 ^{18}F-Fluorination of (Hetero)arenes

2.3.1 Electrophilic ^{18}F-Fluorination of (Hetero)arenes

Before the advent of small-volume [^{18}O]H_2O target, the nuclear reaction $^{20}Ne(d,\alpha)^{18}F$ was more often used to produce carrier-added [^{18}F]F_2. [^{18}F]Fluoroarenes were accessed from this fluorine-18 source via electrophilic aromatic substitution (S_EAr) reactions.

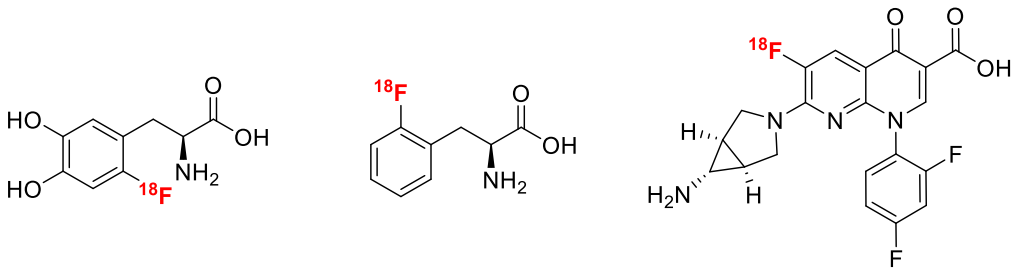

[^{18}F]2.2 **[^{18}F]2.3** **[^{18}F]2.5**

Figure 2.4: Structures of [^{18}F]FDOPA, 2-L-[^{18}F]fluorophenylalanine, and [^{18}F]Trovafloxacin.

Classic fluorine-18 labelled radiopharmaceuticals includes 6-L-[^{18}F]fluoro-3,4-dihydroxyphenylalanine ([^{18}F]FDOPA) **[^{18}F]2.2** via electrophilic ^{18}F-fluorodemetallation in

the research of dopamine metabolism,[54,55] 2-$_L$-[^{18}F]fluorophenylalanine **[^{18}F]2.3** via electrophilic fluorination with acetyl [^{18}F]hypofluorite ([^{18}F]AcOF) **[^{18}F]2.4** to study neutral amino acid transport,[56,57] and [^{18}F]Trovafloxacin **[^{18}F]2.5** via electrophilic isotopic exchange between fluorine-18 and fluorine-19 used for understanding antibiotic pharmacokinetics (Figure 2.4).[58]

Whilst electrophilic ^{18}F-fluorination facilitates ^{18}F-incorporation into sites that are difficult to functionalize via nucleophilic reactions, [^{18}F]F_2 is too reactive to achieve high chemo- and/or regioselectivity. A widely applied solution is to convert the vigorous [^{18}F]F_2 into less reactive but more selective electrophiles. One example was [^{18}F]AcOF developed in 1980, a reagent prepared by passing [^{18}F]F_2 through a $CH_3COONa{\cdot}3H_2O$ column. [^{18}F]AcOF was bubbled into a mixture containing the precursor and acid (TFA) to induce radiofluorination.[59] Since then, additional ^{18}F-electrophiles were developed and applied in the synthesis of radio-pharmaceuticals,[60] including [^{18}F]XeF_2 **[^{18}F]2.6**, *O*-^{18}F-fluorination reagents, and more recently a series of *N*-^{18}F-fluorination reagents. [^{18}F]XeF_2 **[^{18}F]2.6** was accessed via [^{18}F]F_2 reacting with excess of xenon in a high pressure nickel vessel at 390 °C for 40 minutes.[61] Another method of production is the isotopic exchange between XeF_2 and [^{18}F]HF, [^{18}F]SiF_4, and [^{18}F]AsF_5.[62] Classic *O*-^{18}F-fluorination reagents include [^{18}F]AcOF **[^{18}F]2.4**, trifluoromethyl [^{18}F]hypofluorite **[^{18}F]2.7**,[63] and perchloryl [^{18}F]fluoride **[^{18}F]2.8**.[64,65] *N*-^{18}F-fluorination reagents include *N*-[^{18}F]fluoro-*N*-alkylsulfonamide **[^{18}F]2.9**,[66] 1-[^{18}F]fluoro-2-pyridone **[^{18}F]2.10**,[67] *N*-[^{18}F]fluoropyridinium triflate **[^{18}F]2.11**,[68] 1-chloromethyl-4-[^{18}F]fluoro-1,4-diazoniabicyclo[2.2.2]octane bis(triflate) ([^{18}F]Selectfluor bis(triflate)) **[^{18}F]2.12,**[69] and *N*-[^{18}F]fluorobenzenesulfonimide ([^{18}F]NFSI) **[^{18}F]2.13** (Scheme 2.1).[70] [^{18}F]NFSI **[^{18}F]2.13** was first introduced in 2007, prepared from sodium dibenzenesulfonimide. Selectfluor® is commercially available and reacts via either a two-electron pathway as an electrophilic fluoride source or a single-electron pathway in radical fluorination processes.

[^{18}F]Selectfluor bis(triflate)) was ^{18}F-radiolabelled from triethylenediamine (TEDA) and [^{18}F]F_2 in 2010. It is noteworthy that [^{18}F]Selectfluor bis(triflate) was selected instead of [^{18}F]Selectfluor bis(tetrafluoroborate), to avoid undesired ^{18}F/^{19}F isotopic exchange, that would result in low A_m. *O*-^{18}F-Fluorination reagents are very reactive, and are less safe and less stable. The new emerged *N*-^{18}F-fluorinated reagents are generally safer, easier to handle, and more selective as electrophilic and radical fluoride sources.[71]

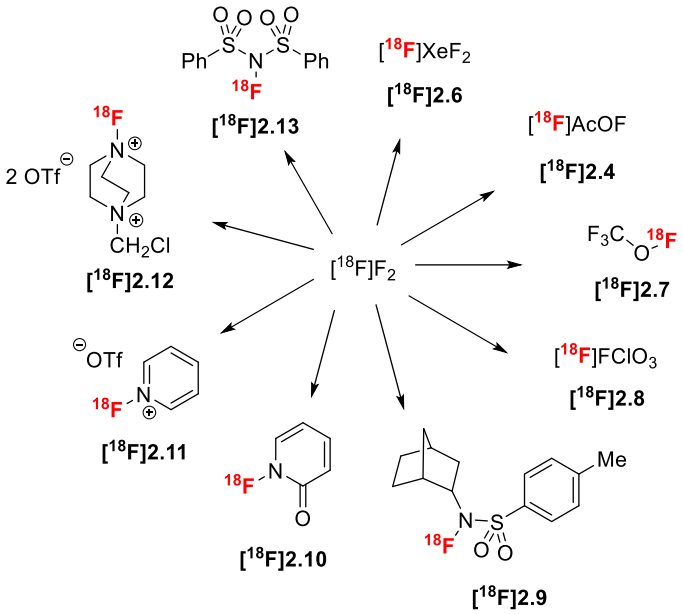

Scheme 2.1: Examples of electrophilic ^{18}F-fluorination reagents derived from [^{18}F]F_2.

Early attempts of direct electrophilic radiofluorination of L-DOPA with reagents such as [^{18}F]XeF_2,[72] and [^{18}F]AcOF,[56,73-75] resulted in poor regioselectivity and low RCYs. The desired 6-[^{18}F]FDOPA was afforded as the minor product, whilst 2- and 5-regioisomers were predominantly formed (Scheme 2.2).

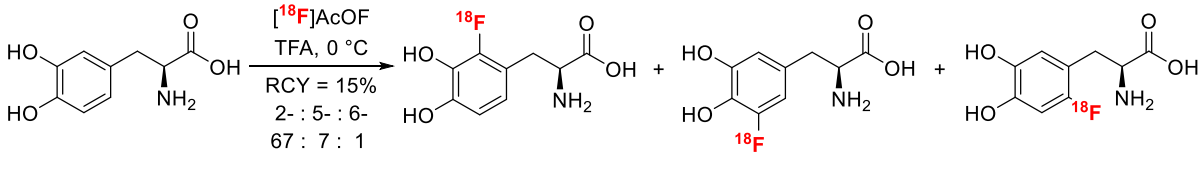

Scheme 2.2: Direct electrophilic ^{18}F-fluorination towards [^{18}F]FDOPA.

^{18}F-Fluorodemetallation is an effective strategy to allow for regioselectivity. Two ^{18}F-Fluorodemetallation methodologies were developed to achieve regioselective radiolabelling of

[^{18}F]FDOPA. In the first approach, a protected mercury derivative **2.17** was subjected to ^{18}F-fluorodemercuration with [^{18}F]AcOF, followed by deprotection in hydroiodic acid (Scheme 2.2a).[76,77] [^{18}F]FDOPA was obtained in high radiochemical purity (RCP) (> 99%), with a radiochemical yield (RCY) of 12% (decay corrected). In the second approach, [^{18}F]FDOPA was prepared in a fully automated fashion, with a RCP > 99% and a RCY of 33% ± 4% via ^{18}F-fluorodestannylation of the fully protected stannylated precursor **2.19**, namely 4,5-di-[(1,1-dimethylethoxycarbonyl)oxy]-*N*-formyl-2-trimethylstannyl-L-phenylalanine ethyl ester precursor with [^{18}F]F_2, followed by deprotection in excess of aqueous hydrobromic acid (Scheme 2.2b).[78] Knowing the versatility of Selectfluor in electrophilic fluorination with aryl stannane and arylboronic esters in the presence of silver,[79,80] Gouverneur and co-workers subjected a protected arylboronic ester precursor **2.21** to a Ag(I)-mediated electrophilic ^{18}F-fluorination with [^{18}F]Selectfluor bis(triflate) in A_m of 3.4 ± 0.1 GBq/µmol from [^{18}F]F_2.[81] Deprotection in hydroiodic acid led to the final [^{18}F]FDOPA, with an RCY of 19% ± 12% and A_m of 2.6 ± 0.3 GBq/µmol (Scheme 2.2c).[82]

Early [^{18}F]F_2 production relying on isotopic exchange leads to limited A_m. To overcome this limitation, Bergman and Solin reported a "post-target" method that produces [^{18}F]F_2 with A_m up to 55 GBq/µmol, by use of a fluoromethane electrical discharge chamber.[73] [^{18}F]F^- produced from nuclear reaction ^{18}O(p,n)^{18}F was azeotropically dried and reacted with CH_3I to form [^{18}F]CH_3F purified by gas chromatography, which was then transferred to a quartz chamber and mixed with 0.5% F_2 (~ 1 µmol) in neon to induce ^{18}F/^{19}F isotopic exchange, promoted by high-voltage electrical discharge.[81,83]

Despite all the improvements, [^{18}F]F_2 is now used less commonly, mainly due to the inherently halved RCY, use of F_2 as carrier, low selectivity and the innovation of modern nucleophilic ^{18}F-fluorination methods.

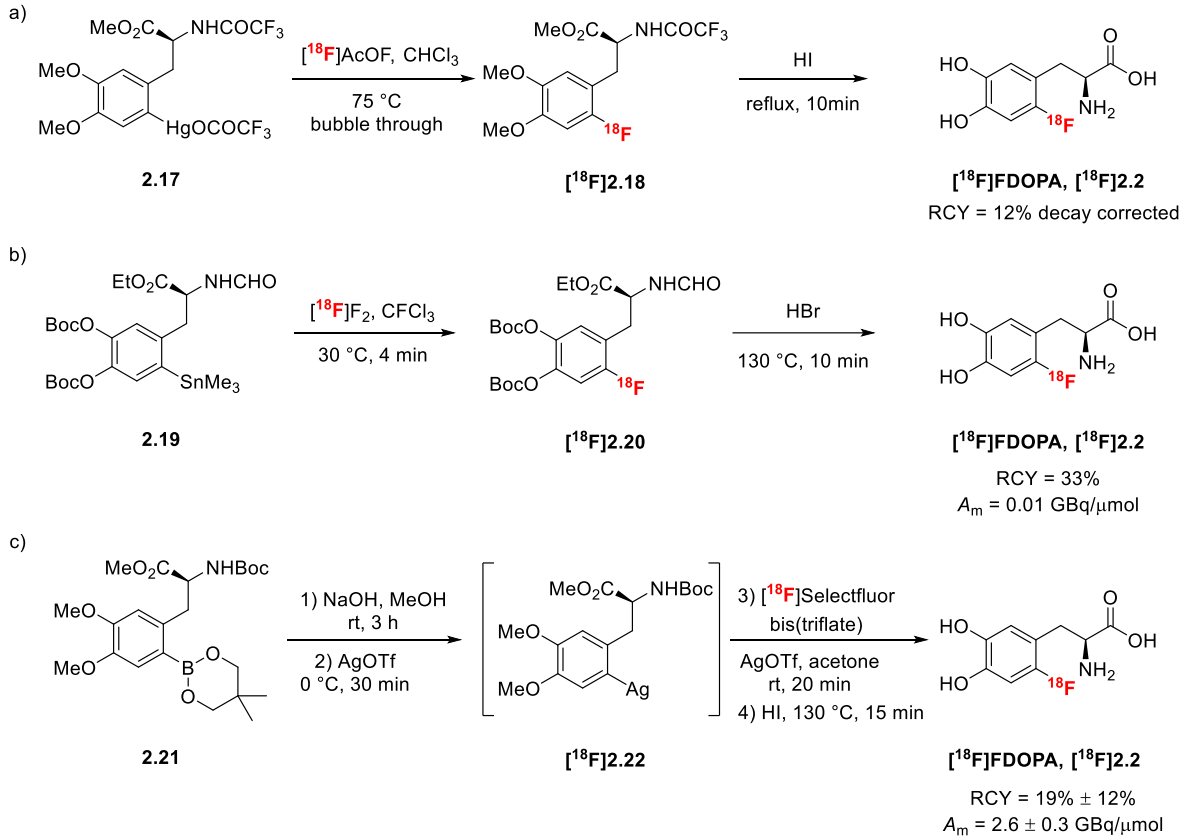

Scheme 2.2: Regioselective electrophilic ^{18}F-fluorination toward [^{18}F]FDOPA.

2.3.2 Nucleophilic ^{18}F-Fluorination of (Hetero)arenes

Classic S_NAr Methodologies in Last Century

For nucleophilic aromatic substitution (S_NAr), classical approaches subject activated arene precursors, such as (hetero)aryl halides,[84] nitroarenes,[85] and trimethylammonium salts [86] to ^{18}F-fluorination with cyclotron produced [^{18}F]F$^-$. (Scheme 2.3a). These reactions are usually limited to electron-deficient aryl precursors which bear electron withdrawing groups at *ortho* and/or *para* position relative to the group to be displaced. Halide precursors usually has slower rate than nitro and trimethylammonium groups in terms of displacement by [^{18}F]F$^-$.[87] In addition, it is impractical to use aryl fluoride precursors, since the ^{18}F-labelled products are inseparable from their precursors. Two other less commonly adopted methodologies are the Balz-Schiemann and the Wallach reactions, which are limited by harsh conditions and narrow substrate scopes (Scheme 2.3b and c). The original Balz-Schiemann approach suffered from

maximum theoretical RCY of 25% and low molar activity due to competing ^{18}F-incorporation of the unlabelled fluoride in the monolabelled [^{18}F]tetrafluoroborate.[88] The alternative counterion BCl_4^- was introduced to solve the problem. However, undesired gaseous [^{18}F]$BFCl_2$ led to drastic loss of RCY up to 75%.[89,90] Similar to the concept of thermal ^{18}F-fluorodediazonation in the Balz-Schiemann reaction, the Wallach reaction forms a aryldiazonium salt in situ from its triazene precursor in the presence of strong acids, such as trifluoromethanesulfonic acid.[91,92] Although triazenes are relatively more stable than diazonium salts, both methods are becoming less common, especially since the 21st century, when the development of novel nucleophilic aromatic radiofluorination methodologies with wider scope, more stable precursors, and milder conditions have surfaced.

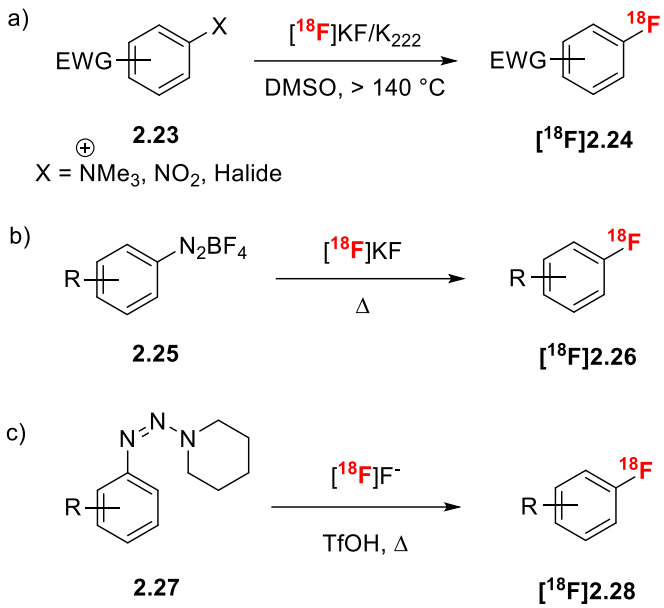

Scheme 2.3: Classic S_NAr methodologies of [^{18}F]arenes synthesis in the 20th century.

New Leaving Groups Developed in This Century

Several new leaving groups were introduced to S_NAr, expanding the scope outside electron-deficient (hetero)arenes, such as triarylsulfonium salts,[93] *N*-arylsydnones,[94] and hypervalent iodines including iodonium salts, [95,96] iodonium ylides,[97] and oxidised iodoarenes (OIAs).[98]

Triarylsulfonium triflate bearing electron-deficient or electron-neutral arenes underwent S_NAr with [^{18}F]KF in the presence of 4,7,13,16,21,24-hexaoxa-1,10-diazabicyclo[8.8.8]hexacosane (Kryptofix® 222) to afford corresponding [^{18}F]fluoroarenes. Density functional theory (DFT) calculations revealed that attack of the fluoride at C_{ipso} of the substituted ring favours the electron poor ring system. Consistent with the calculations, the observed experimental data showed that nucleophilic attack by [^{18}F]fluoride occurred at the most electron-deficient arene as predicted from Hammett σ_P constants (Scheme 2.4a). Installing electron-donating ancillary arenes on triarylsulfonium triflate expanded the substrate scope to nonactivated aromatics (Scheme 2.4b).[93]

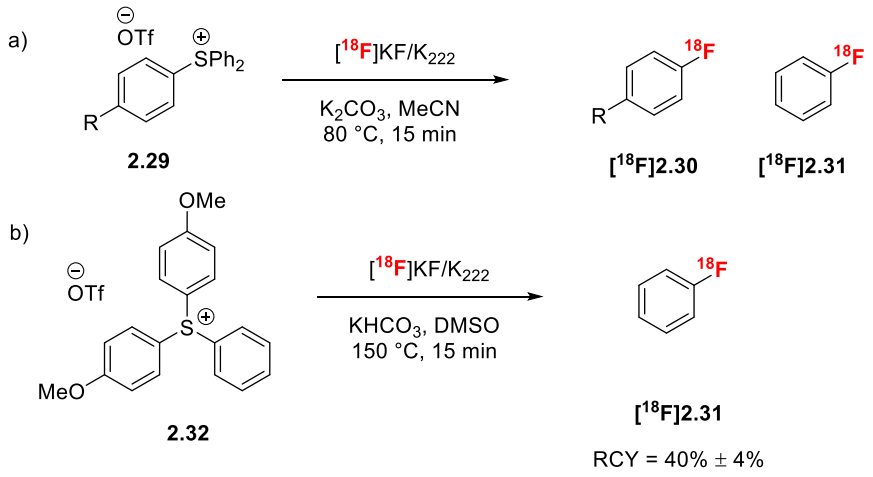

Scheme 2.4: Nucleophilic synthesis of [^{18}F]arenes from triarylsulfonium triflates.

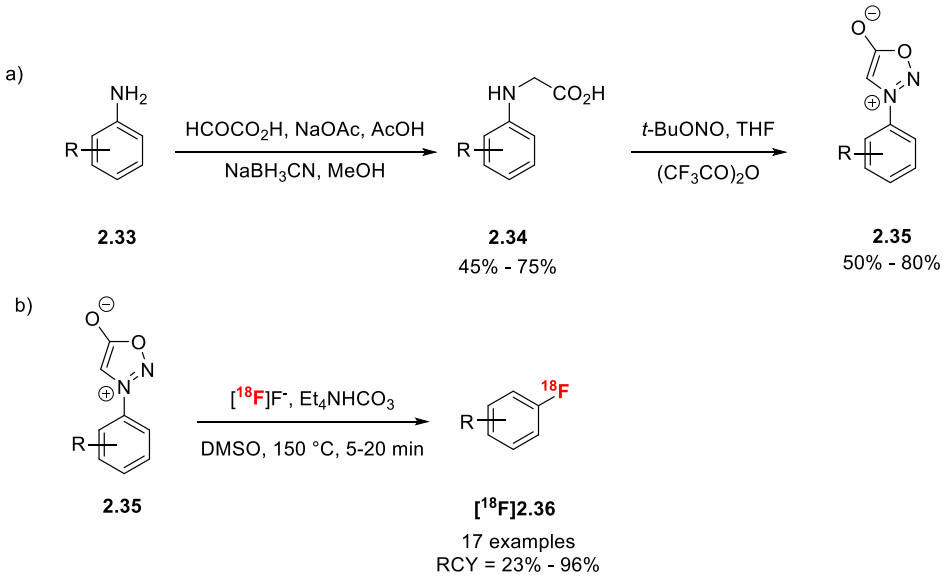

Scheme 2.5: Synthesis and radiofluorination of *N*-arylsydnones.

N-Arylsydnones are bench-stable heterocycles that can be accessed in two steps from their corresponding anilines. On the formation of N-arylglycine **2.34**, a one-pot N-nitrosation and cyclodehydration afforded the *N*-arylsdynones **2.35** (Scheme 2.5a). ^{18}F-fluorination enabled formation of corresponding [^{18}F]fluoroarenes, with a diverse substrate scope, including ester, nitro, amino, sulfone and sulfonamide. Heteroarenes are also tolerated, including thiophene, benzofuran and pyridine (Scheme 2.5b).

Diaryliodonium salts emerged as alternative precursors in 1990s. Both electron-rich and electron-poor arenes can be ^{18}F-labelled. For unsymmetric substrates, the more electron-deficient arene undergoes selective ^{18}F-fluorination (Scheme 2.6a).

Heteroarene-bearing iodonium salts allow ^{18}F-incorporation into electron-rich aromatics for asymmetric arene extrusion. Thiophene is more electron-rich than *para*-methoxybenzene and thereby **[^{18}F]2.38** was afforded as the single product (Scheme 2.6b).[99]

Sanford and Scott reported a Cu-mediated radiofluorination to access a diverse range of [^{18}F]fluoroarenes from electron-deficient to electron-rich (mesityl)(aryl)iodonium tetrafluoroborate salts (Scheme 2.6c).[100] The high regioselectivity was achieved by strong steric bias for the small aryl group on the iodine and was found to be insensitive to the electronic nature of the arene.

Computational studies revealed this sterically biased selectivity of unsymmetric diaryliodonium salts arises from the so-called "*ortho*-effect" (Scheme 2.7). [^{18}F]Fluoride displaces the axial counterion in the diaryliodonium salt, forming a trigonal bipyramidal complex. Subsequently, ipso attack of the nucleophilic [^{18}F]fluoride at the equatorial arene results in formation of [^{18}F]fluoride-aryl bond. For unsymmetric diaryliodonium salts, arenes bearing sterically bulky *ortho*-substituent occupy the equatorial position to minimise the steric repulsion, leading to the corresponding [^{18}F]fluoroarenes.

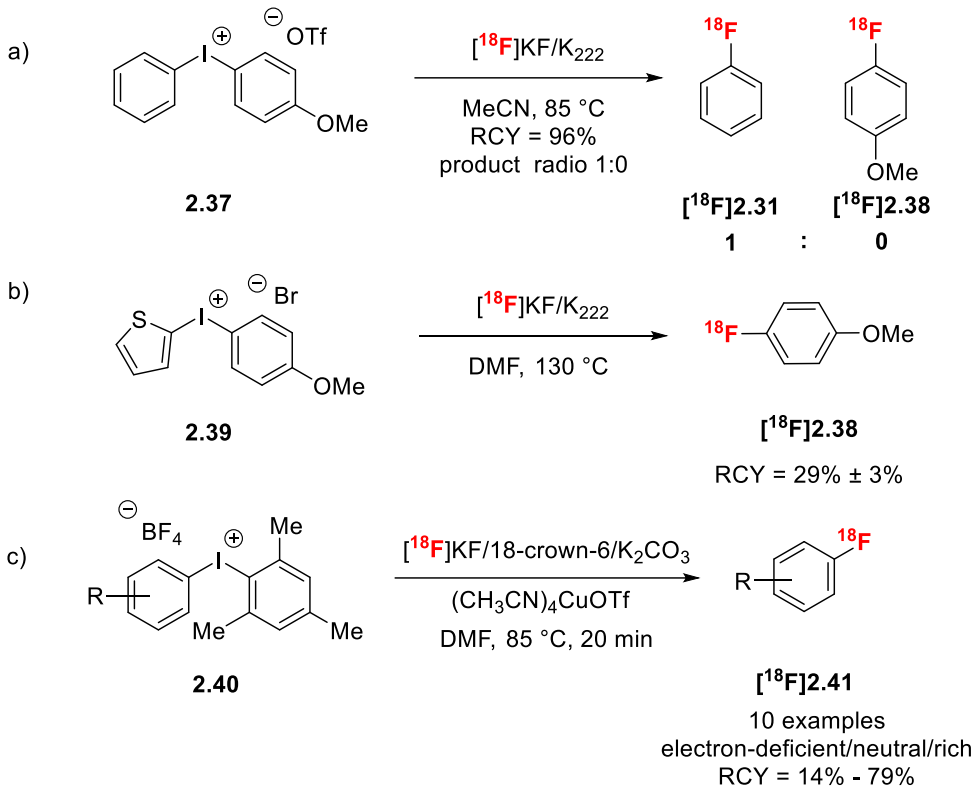

Scheme 2.6: a) Regioselective ^{18}F-incorportion of diaryliodonium salt. b) Access of electron-rich [^{18}F]arene from diaryliodonium salt. c) Cu-mediated radiofluorination of diaryliodonium salt.

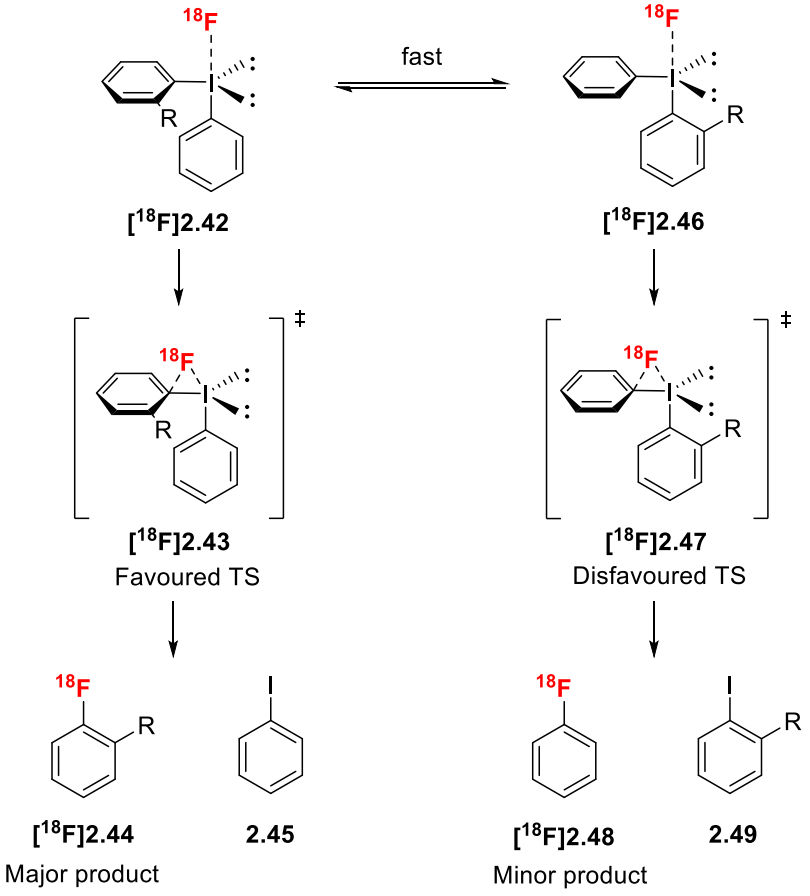

Scheme 2.7: Mechanistic insights of the selectivity of unsymmetric diaryliodonium salts.

Electron-rich iodonium salts are prone to decomposition.[101] Spirocyclic iodonium ylides, in the form of crystalline solids, are promising alternatives to iodonium salts and are more stable.[102] Successful ^{18}F-incorporation of radiopharmaceuticals from spirocyclic iodonium precursors includes [^{18}F]fluoroestrone **[^{18}F]2.52**, 5-[^{18}F]fluorouracil **[^{18}F]2.53**, and a *N*,*O*-protected 4-[^{18}F]fluorophenylalanine **[^{18}F]2.54** with RCYs of 23%, 11%, and 55%, respectively (Scheme 2.8).

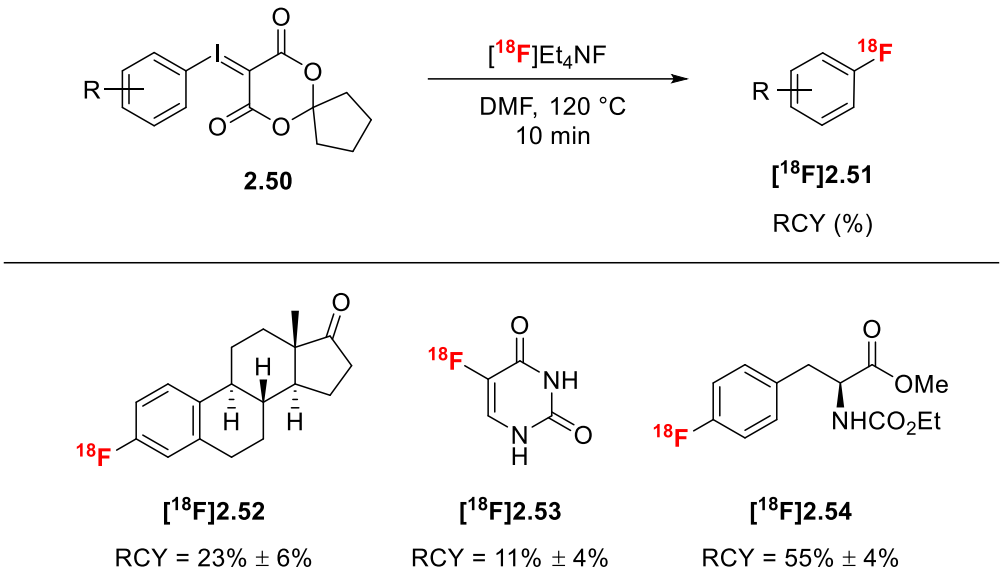

Scheme 2.8: examples of ^{18}F-radiopharmaceuticals accessed from spirocyclic iodonium ylides.

Radiofluorination of Phenols via Concerted S_NAr

In the classic S_NAr approach, ^{18}F-incorporation occurs via a negatively charged Meisenheimer complex intermediate, which is sufficiently stabilised for arenes bearing electron-withdrawing substituents, and hence limits the scope of S_NAr. Ritter and co-workers have reported a direct radiofluorination of phenols using 1,3-*bis*(2,6-diisopropylphenyl)-2-chloro-2,3-dihydro-1*H*-imidazolium chloride **2.56**.[103] Role of the chloride **2.56** is to activate the phenol to prepare an uronium intermediate, which could be directly ^{18}F-labelled by elution of 18F-fluoride from the anion exchange cartridge. The mechanism was proposed to proceed via an unusual concerted S_NAr (CS_NAr) through the π-orbital framework, making nucleophilic displacement feasible even on electron-rich arenes (Scheme 2.9).

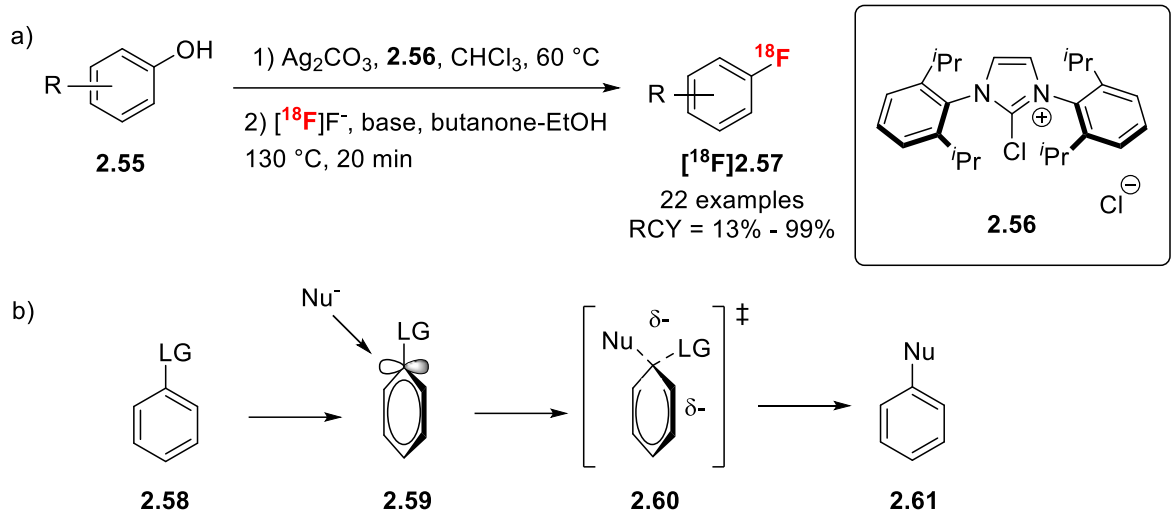

Scheme 2.9: a) Radiofluorination of phenols using 1,3-*bis*(2,6-diisopropylphenyl)-2-chloro-2,3-dihydro-1*H*-imidazolium chloride. b) Proposed CS_NAr pathway through π-framework.

Late Stage Transition-Metal-Mediated Aromatic Radiofluorination Using [^{18}F]Fluoride

Palladium has been widely used in ligand-directed functionalisations.[104] In 2011, Ritter, Hooker and co-workers reported a novel electrophilic [^{18}F]fluorination of palladium aryl complexes to afford aryl [^{18}F]fluorides. The nucleophilic [^{18}F]fluoride was transformed into an electrophilic [^{18}F]Pd(IV)-F complex, which could in turn react with the aryl palladium(II) precursor to generate the desired ^{18}F-labelled product (Scheme 2.10).[105]

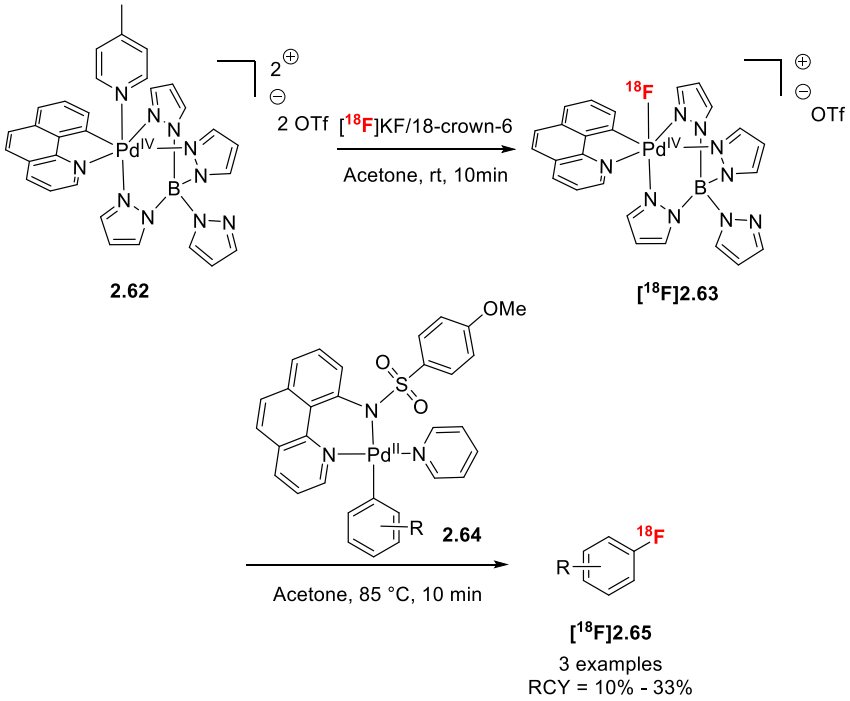

Scheme 2.10: Aromatic ^{18}F-fluorination via an electrophilic Pd(IV) intermediate using [^{18}F]fluoride.

A year later, in 2012, the Ritter group established a procedure for direct oxidative ^{18}F-fluorination of aryl nickel(II) complexes using nucleophilic [^{18}F]F$^-$, mediated by hypervalent iodine oxidant in one step (Scheme 2.11).[106-108]

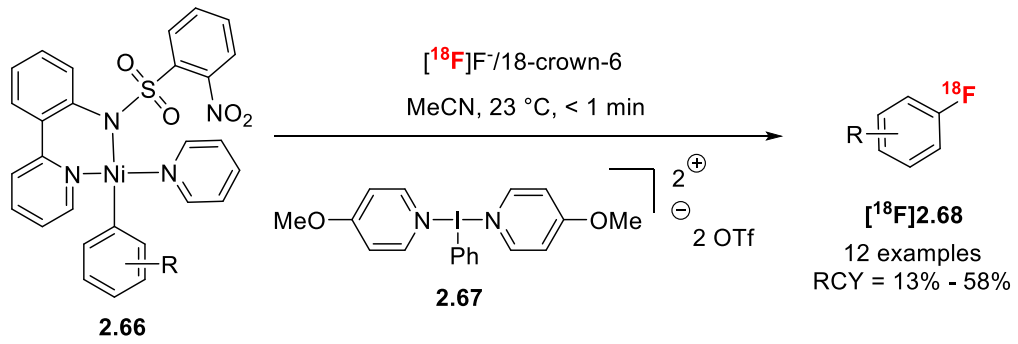

Scheme 2.11: ^{18}F-Fluorination of aryl nickel(II) complex.

In 2011, Ribas disclosed the first Cu(I)-mediated fluorination of aryl halide substrates, using nucleophilic fluoride sources, including KF and AgF. Stoichiometric C-F bond was formed at room temperature in acetonitrile under nitrogen (Scheme 2.12).[109]

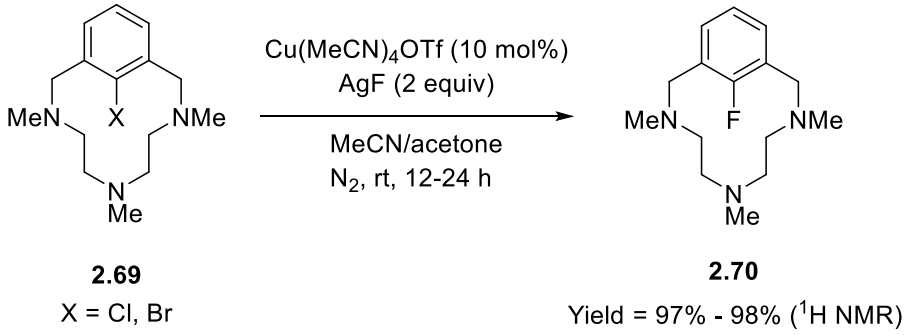

Scheme 2.12: Cu(I)-mediated fluorination of aryl halides.

The proposed mechanism was via a Cu^{I}/Cu^{III} catalytic cycle. Aryl-X (X = Cl, Br) was oxidatively added to Cu^{I}, followed by halide exchange to form the key complex aryl-Cu^{III}-F **2.71**, which undergoes reductive elimination to regenerate Cu^{I} and release the desired aryl fluoride **2.70** (Scheme 2.13).

In 2012, Wang and co-workers isolated a fluorinated Cu(III) complex derived from $Cu(ClO_4)_2$-mediated aerobic C–H activation of the macrocyclic host (Scheme 2.14).[110] This Cu(III)-F complex underwent reductive elimination to form an aryl-F bond.

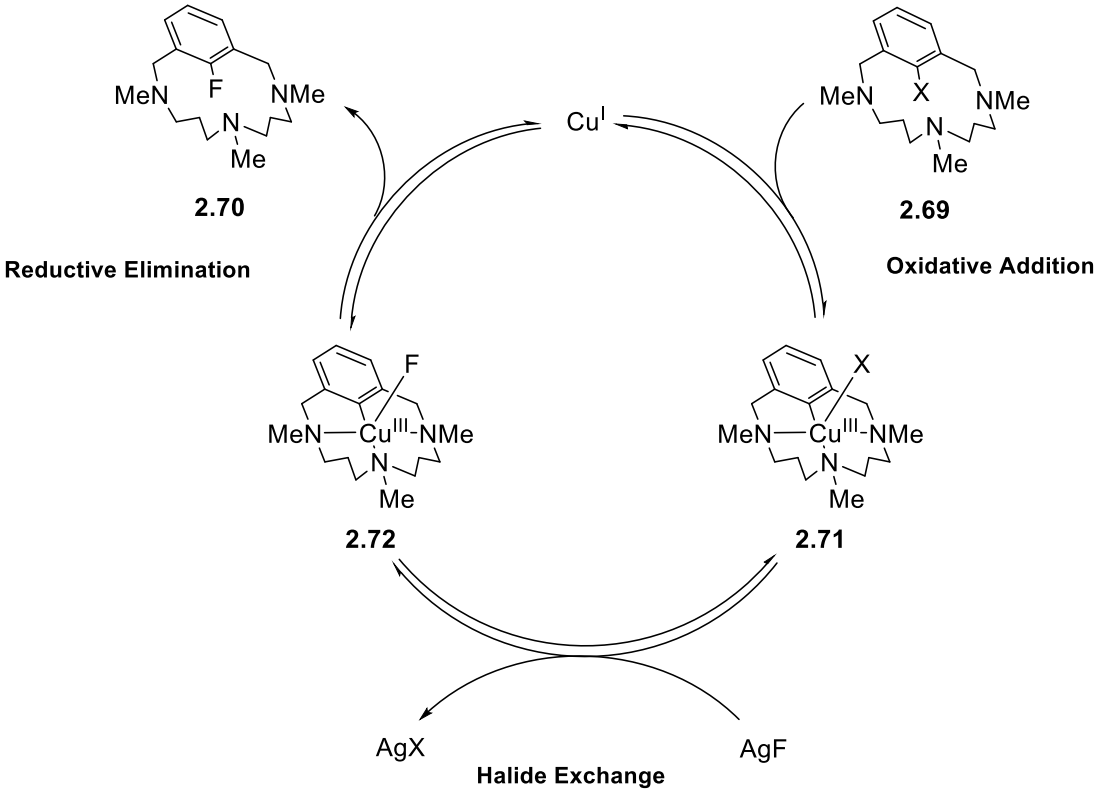

Scheme 2.13: Proposed catalytic cycle of Cu(I)-mediated aryl halide exchange.

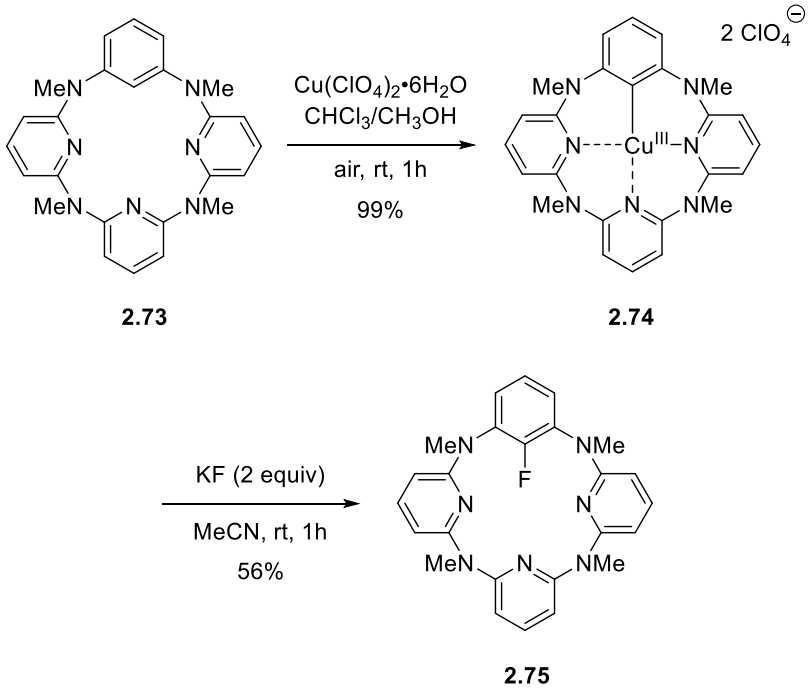

Scheme 2.14: Fluorination of isolated macrocyclic aryl Cu(III) complex.

Subsequent to these mechanistic studies, the Hartwig group reported a Cu(I)-mediated direct formation of aryl fluorides from arylboronic esters, and electrophilic F^+ sources, tolerating a range of functional groups such as esters, amides, halides, protected indoles. (Scheme 2.15).[111]

Although an excess of Cu(I) was needed, the proposed mechanism is suggested to proceed through a similar Ar-Cu(III)-F reductive elimination pathway to afford fluoroarenes.

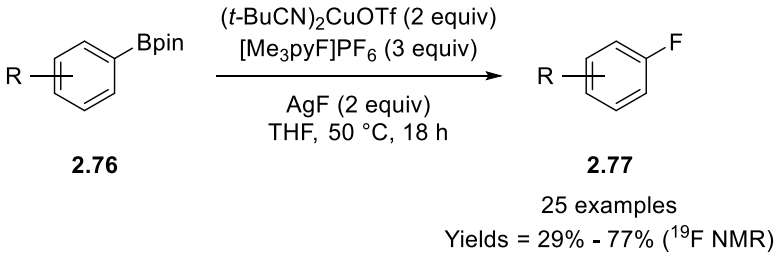

Scheme 2.15: Copper(I)-mediated fluorination of arylboronic esters.

A breakthrough in the field came in 2013 when Sanford and co-workers revealed that aryltrifluoroborates and arylboronic esters could undergo carbon-fluorine bond formation with a nucleophilic F^- source, 4 equiv of KF and 4 equiv of $Cu(OTf)_2$ (Scheme 2.16).[112]

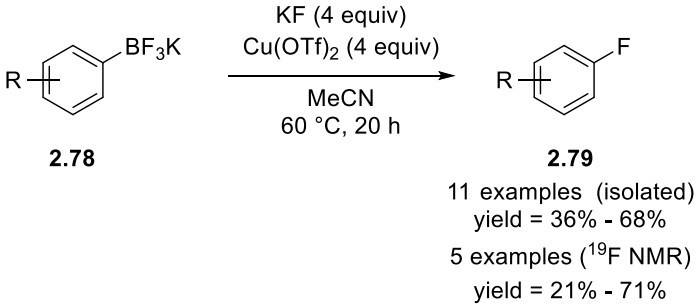

Scheme 2.16: Cu(II)-mediated fluorination of aryltrifluoroborates.

Whilst aryltrifluoroborates **2.82** were shown to be the most reactive towards this type of fluorination, the pinacol boronic ester **2.83** was also reactive. The MIDA borate **2.84** and the boronic acid **2.85** led to the desired aryl fluoride **2.81** in much lower yields (Scheme 2.17).

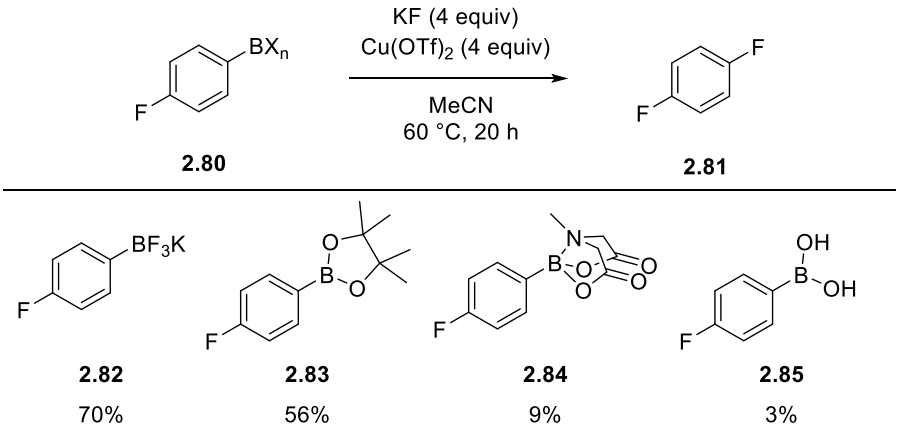

Scheme 2.17: Cu(II)-mediated fluorination of aryltrifluoroborates and arylboronic esters.

A Cu(III) intermediate **2.89** was proposed, resulting from a disproportionation reaction, in which 1 equiv of aryl Cu(II) intermediate **2.88** was oxidised by 1 equiv of $Cu(OTf)_2$ (Scheme 2.18).

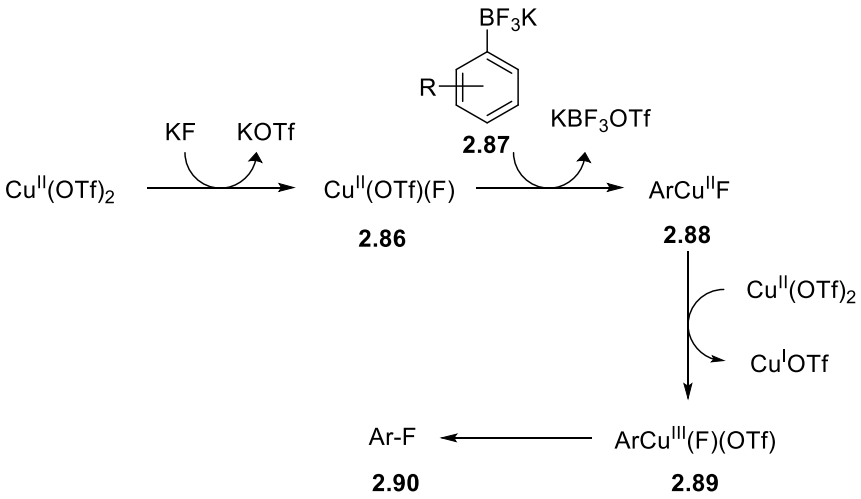

Scheme 2.18: Proposed mechanism of Cu(II)-mediated fluorination of aryltrifluoroborates.

Bridging the gap between copper-mediated ^{19}F- and ^{18}F-fluorination, the Gouverneur group demonstrated the pre-formed Cu(III) complex **2.91** could be a viable intermediate for ^{18}F-fluorination of arenes. Non-radiolabelled TBAF·2pin was added to increase the concentration of fluoride in a "carrier-added" manner. ^{18}F-fluorinated **[^{18}F]2.92** was afforded with an RCY of 16% (Scheme 2.19).[113]

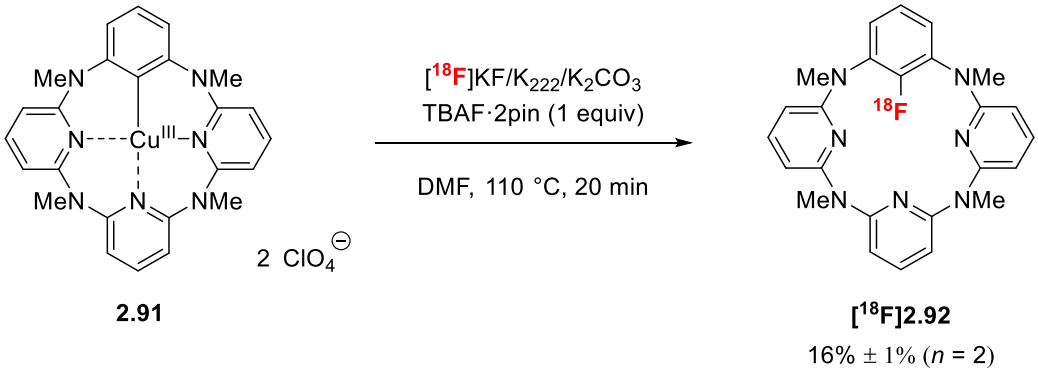

Scheme 2.19: ^{18}F-Fluorination of macrocyclic Cu(III) complex.

In 2014, the Gouverneur group revealed the Cu(II)-mediated nucleophilic ^{18}F-fluorination of (hetero)aryl pinacol-derived boronic esters, upon treatment with $[^{18}F]KF/K_{222}$ and commercially available $Cu(OTf)_2(py)_4$ to access [^{18}F]fluoro(hetero)arenes (Scheme 2.20).[114]

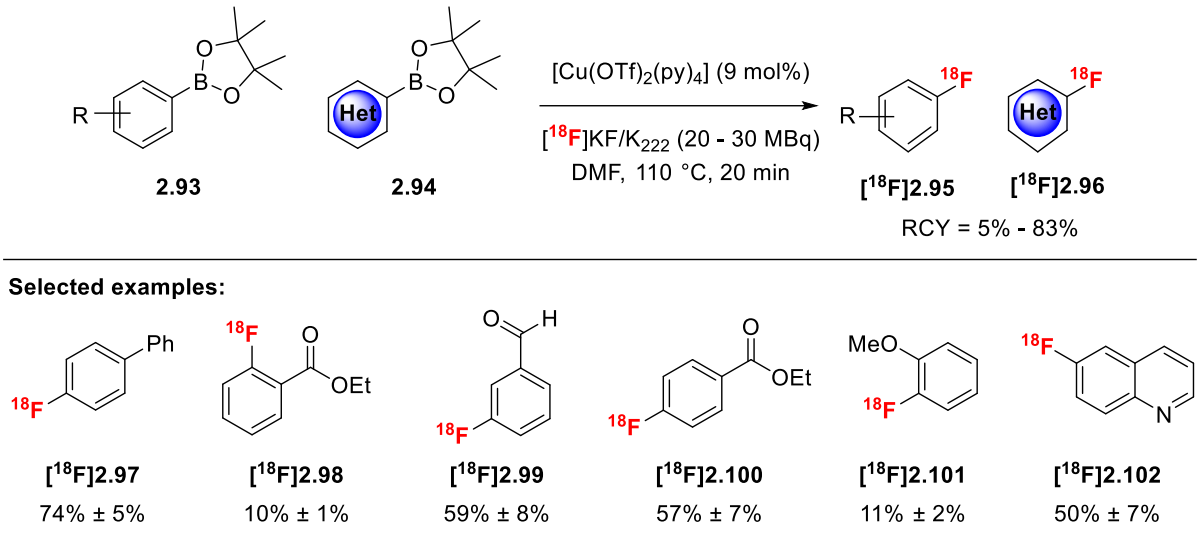

Scheme 2.20: Cu(II)-mediated nucleophilic ^{18}F-fluorination of (hetero)aryl boronic esters.

This method tolerated electron-poor and electron-rich arenes and various functional groups. Starting with 13 GBq of [^{18}F]fluoride at full automation, a dose of 609 MBq of [^{18}F]FDOPA was prepared, with a decay-corrected RCY of 12%. Both of the radiochemical and the enantiomeric purities exceeded 98% (Scheme 2.21).

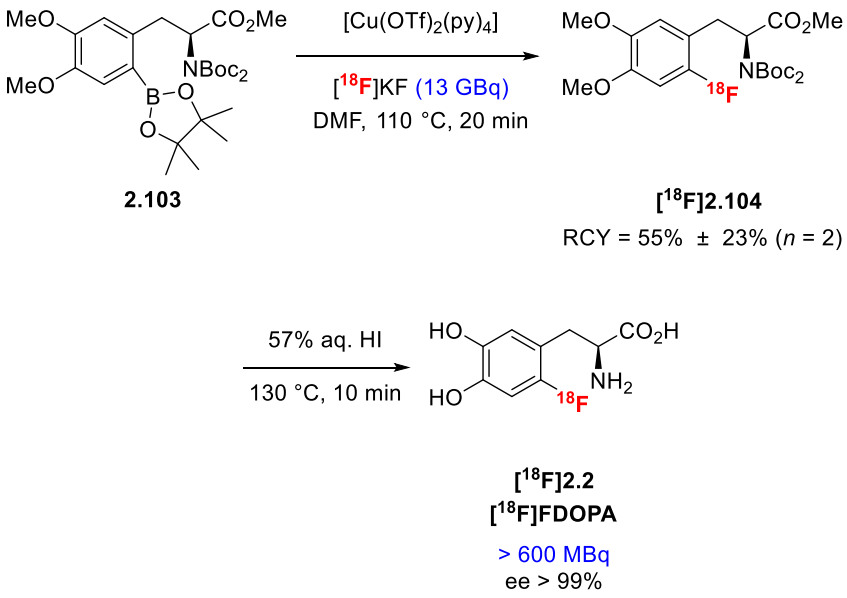

Scheme 2.21: Radiosynthesis of [^{18}F]FDOPA from [^{18}F]fluoride.

In 2015 and 2016, Sanford and Scott disclosed two further Cu(II)-mediated nucleophilic ^{18}F-fluorination methodologies, using stoichiometric amount of $Cu(OTf)_2$, from arylboronic acids and arylstannanes respectively, both tolerating electron-poor and electron-rich arenes, with a range of functional groups (Scheme 2.22).[115,116]

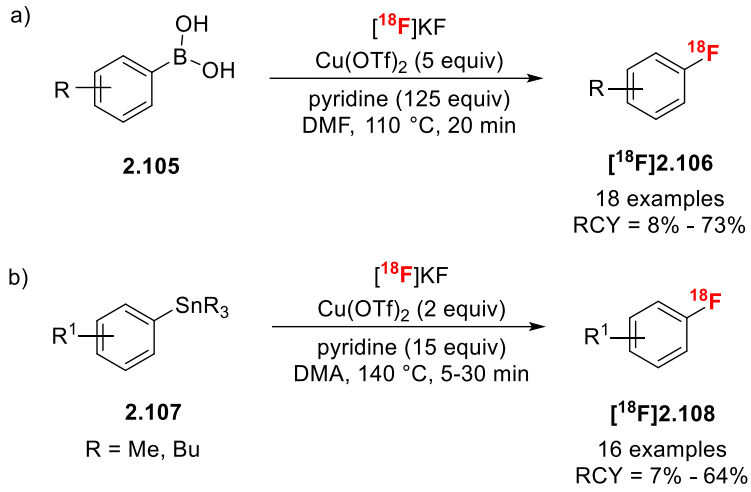

Scheme 2.22: Cu(II)-mediated ^{18}F-fluorination of a) arylboronic acids, and b) arylstannanes.

"Late-stage" ^{18}F-incorporation is ideal, due to the half-life of fluorine-18, and to avoid unproductive radioactive decay before injection *in vivo* for PET applications. However, such strategy often carries risk especially for functionalised ^{18}F-radiotracers containing one or more *N*-heterocycles. In 2017, the Gouverneur group described a robust screening approach for the rapid evaluation of functional group compatibility, tolerance of heterocycles and selection of reaction conditions to determine whether ^{18}F-fluorodeboronation as the last step in the synthesis would be viable.[117] If not possible, this screening approach could also suggest which step(s) if any should follow ^{18}F-fluorination. In practice, a model aryl boronic ester responding well to ^{18}F-labelling, such as 2-(4-cyanophenyl)-4,4,5,5-tetramethyl-1,3,2-dioxaborolane **2.109** (RCY = 34% ± 15%, *n* = 122), was subjected to Cu-mediated ^{18}F-fluorodeboronation in the presence of one equivalent of heterocycle contained in the complex molecule of interest (Scheme 2.23).

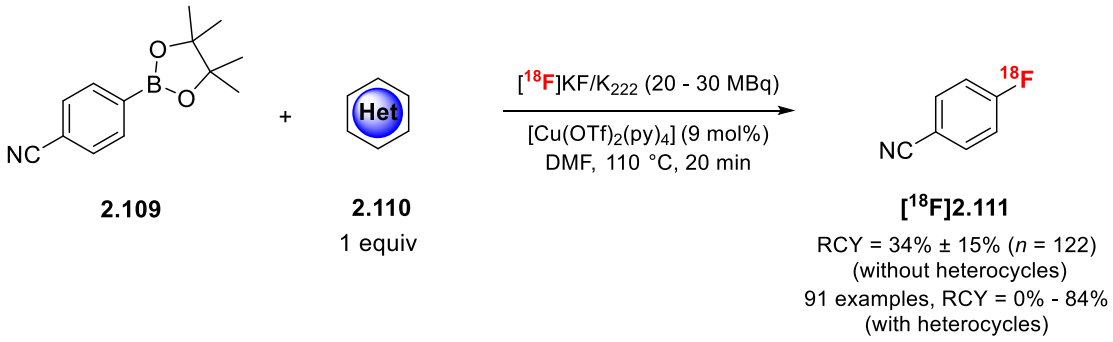

Scheme 2.23: The spiking experiments to de-risking the copper mediated ^{18}F-fluorination.

If the presence of this additive did not affect the RCY, a last step ^{18}F-fluorination of the complex target molecule may be viable (Scheme 2.24).

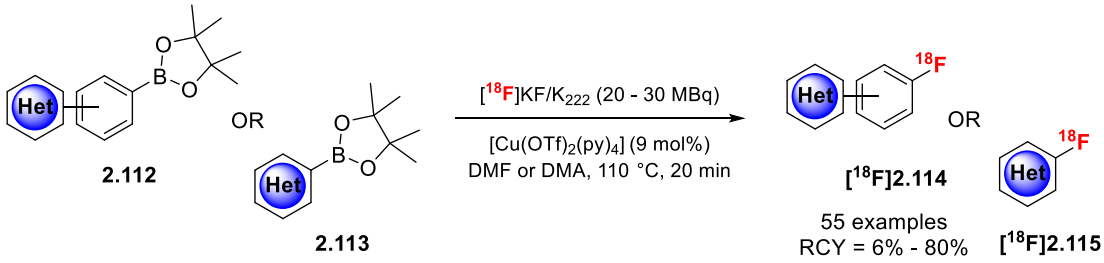

Scheme 2.24: The de-risking approach for Cu-mediated ^{18}F-fluorination of heterocyclic PET tracers.

Adding 1 equiv of *N*-benzyl protected morpholine **2.116** or 1 equiv of quinazoline **2.117** did affect the RCY (Scheme 2.25a). Thus, a direct final-stage ^{18}F-fluorination was proposed to access [^{18}F]Gefitinib **[^{18}F]2.97** from the boronic ester precursor 2.118. As expected [^{18}F]Gefitinib **[^{18}F]2.97** was prepared with an RCY of 22% (Scheme 2.25b)..

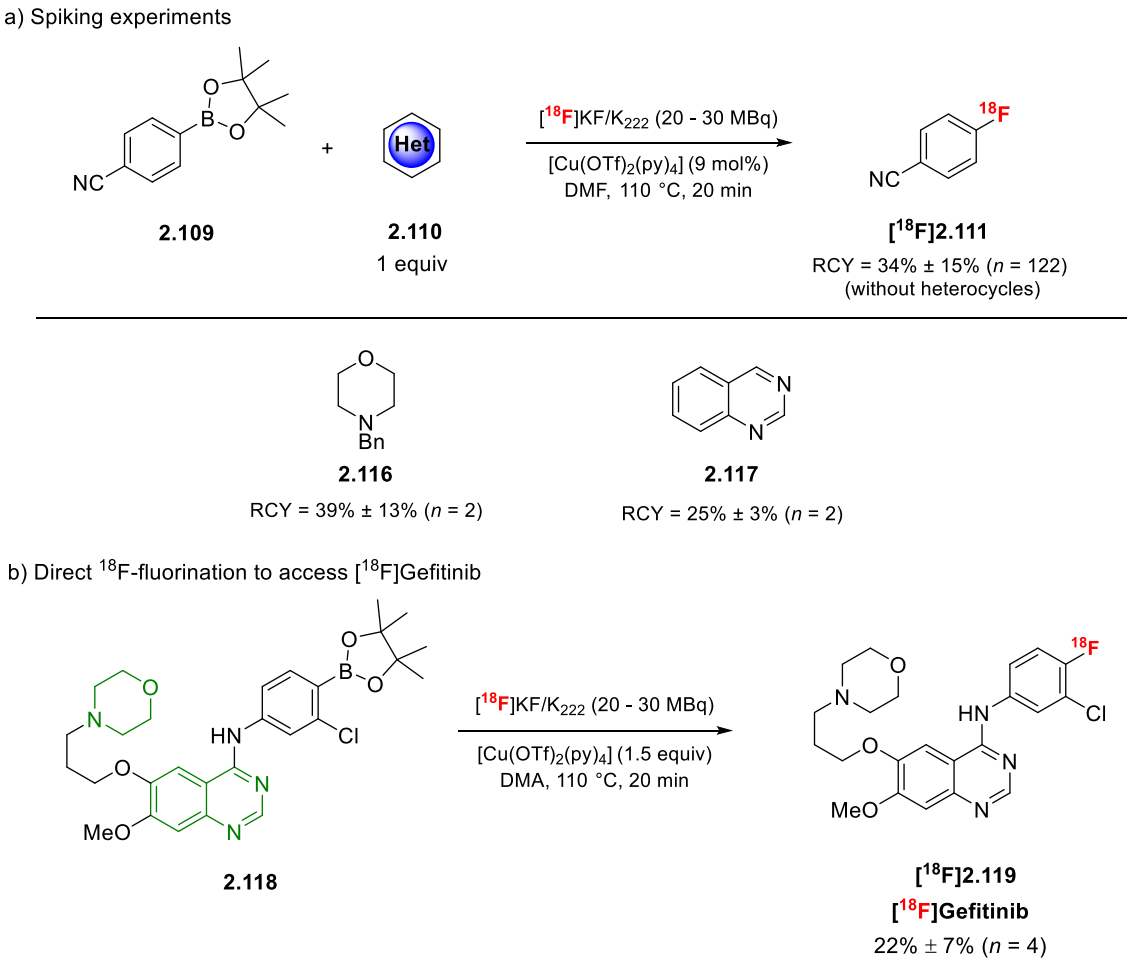

Scheme 2.25: Direct final-stage ^{18}F-fluorination to access [^{18}F]gefitinib.

However, if the RCY was markedly decreased, or no ^{18}F-incorporation was observed (RCY < 5%), it is necessary to identify which group or sub-motif affected detrimentally ^{18}F-radiofluorination. One strategy is to protect the heterocycle that affected the radiolabelling. In the case of rufinamide, spiking with amide **2.120**, no ^{18}F-incorporation was observed. With *N*-trityl protected amide **2.121**, the efficiency of ^{18}F-incorporation was recovered, indicating this protected group was no longer detrimental to the reaction. Thereby, the synthesis of [^{18}F]rufinamide **[^{18}F]2.124** required precursor **2.122** protected at the amide group. The radiofluorination was followed by a subsequent deprotection of the triphenyl methyl group to obtain the final product **[^{18}F]2.124** (Scheme 2.26).

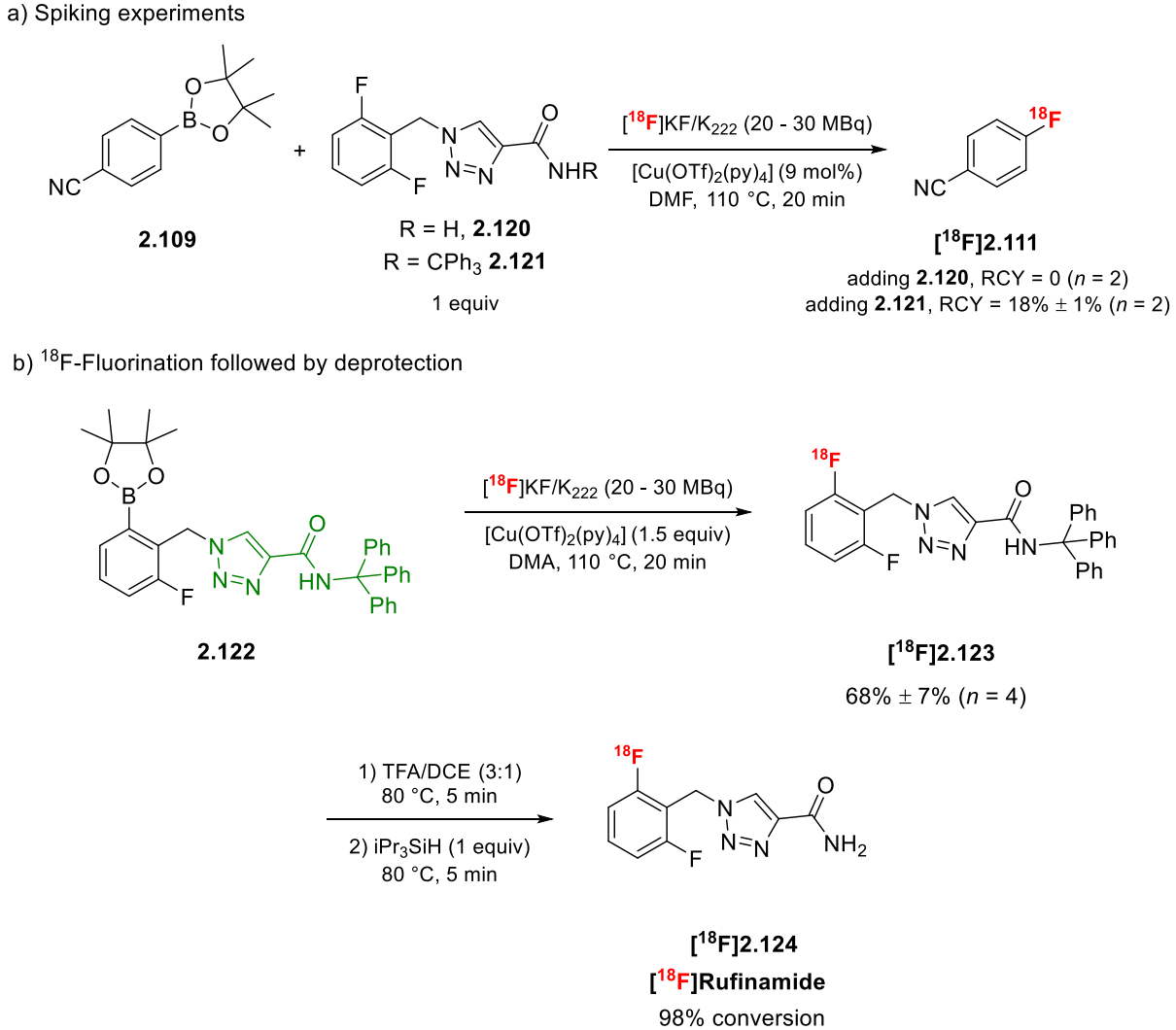

Scheme 2.26: The protection-deprotection strategy to access [^{18}F]rufinamide.

Another common post-labelling strategy is a coupling step of the radiolabelled (hetero)arene to afford the final radiolabelled molecule. In the case of [^{18}F]risperidone **[^{18}F]2.127**, initial spiking experiment suggested that pyrimidone **2.125** might inhibit ^{18}F-incorporation (Scheme 2.27a). This was proved to be true when boronic ester **2.126** was subjected to the final-stage ^{18}F-fluorination. No ^{18}F-incorporation was observed (Scheme 2.27b). Thus, a post-labelling coupling step was envisaged. An *N*Boc-protected benzo[*d*]isoxazole **2.128** was radiolabelled in 42% RCY. In situ *N*-deprotection of **[^{18}F]2.129** with TFA was followed by alkylation with pyrimidone **2.130** to afford the final product [^{18}F]Risperidone **[^{18}F]2.127** (Scheme 2.27c).

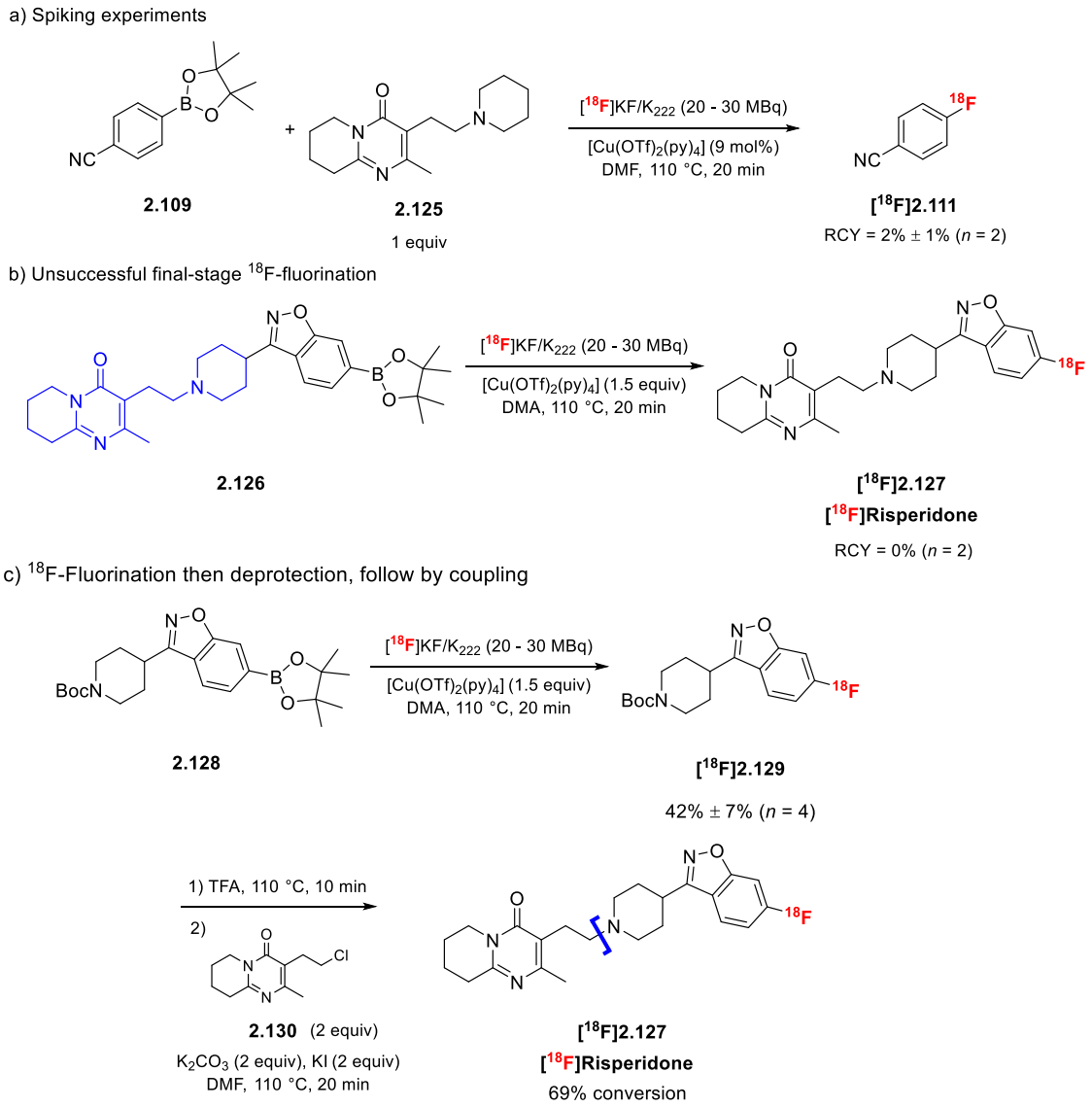

Scheme 2.27: The coupling strategy to access [^{18}F]risperidone.

Photoredox-Catalysed ^{18}F-Fluorination

In 2019, Nicewicz and co-workers reported a direct C-H ^{18}F-fluorination via photoredox catalysis (Scheme 2.28a).[118] The Nicewicz lab developed an acridinium-based single-electron photooxidant **2.132** to catalytically generate arene radical cations as reactive intermediates. The photooxidant **2.132** and 2,2,6,6-tetramethyl-1-piperidine-1-oxyl (TEMPO) as a redox co-mediator were subjected to direct C-H to C-^{18}F bond conversion under aerobic conditions, without the need for pre-functionalisation of arenes. In the following year, the Nicewicz group applied the same photocatalyst in ^{18}F-deoxyfluorination via cation-radical-accelerated S_NAr, enabling access to electron-rich [^{18}F]fluoroarenes (Scheme 2.28b).[119]

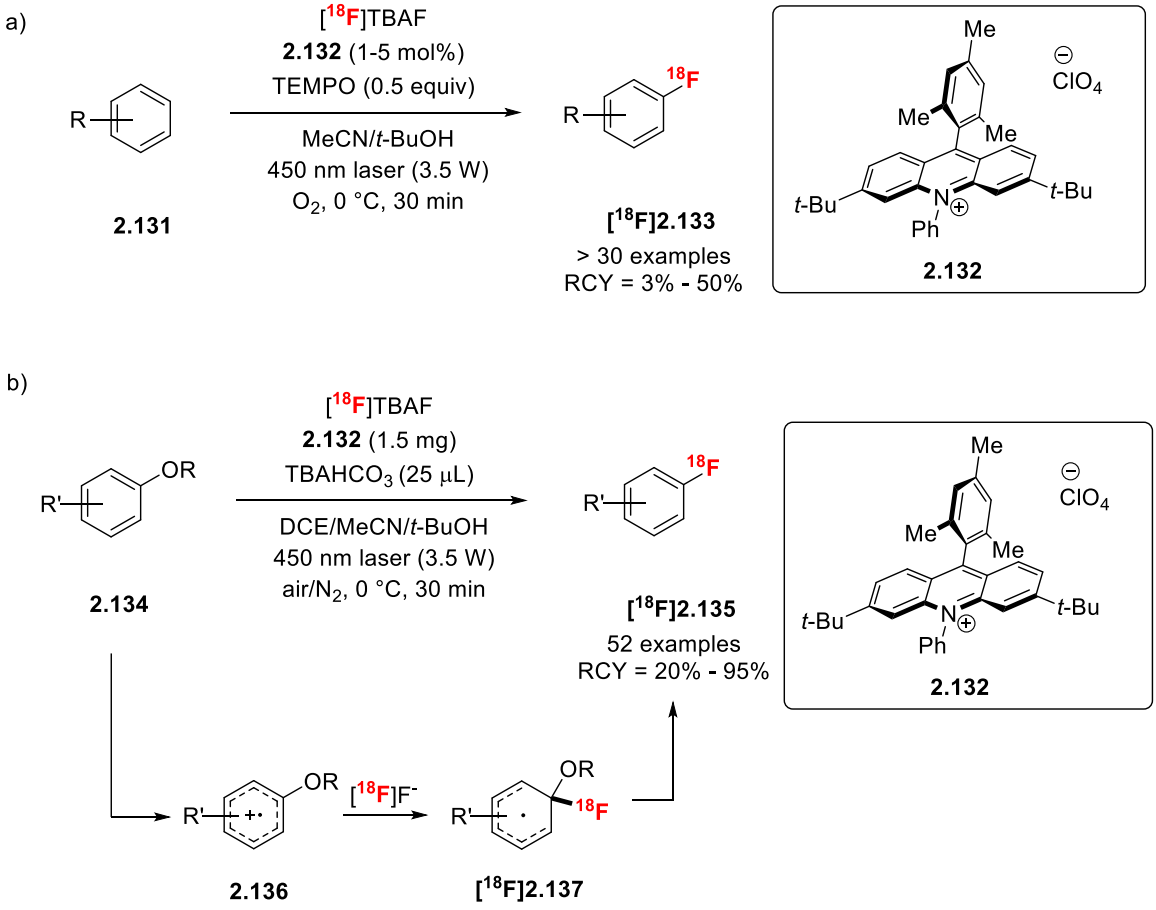

Scheme 2.28: a) Direct C-H ^{18}F-fluorination and b) ^{18}F-deoxyfluorination via photoredox catalysis.

2.4 Radiosynthesis of [^{18}F]Rucaparib

A review of the recent development in the nucleophilic aromatic ^{18}F-fluorination was delivered in the previous section. In this section, a Cu(II)-mediated ^{18}F-fluorination will be demonstrated to access a novel potential radiotracer, [^{18}F]rucaparib.

2.4.1 Labelled PARP Inhibitors and Analogues

For *BRCA1/2*-mutated cancer treatment with PARP inhibitors, poor response for some patients is observed, which may be caused by a lack of drug accumulation in the tumour, active drug efflux, or other resistance mechanisms, as explained in Chapter 1. A method that estimates PARP expression levels, PARP inhibitor accumulation in tumour tissue, and target occupancy of PARP enzyme binding pockets, will allow more accurate selection and fast therapy evaluation of patients who may benefit from PARP inhibitor treatment. An optimal PET radiotracer should have high selectivity toward the targeted receptor and low nonspecific binding. In this context, ^{18}F-radiolabelled PARP inhibitors for PET imaging stand out for clinical standard of care.

In 2019, the Gouverneur and Cornelissen groups reported a radiosynthesis of the first ^{18}F-isotopogue of PARP inhibitor, [^{18}F]olaparib **[^{18}F]2.139** from a pinacol boronic ester precursor. This radiotracer was taken up in PARP-1 expressing cell lines and tumour cells in a mouse xenograft model, with increased uptake upon tumour irradiation (Scheme 2.29).[120,121]

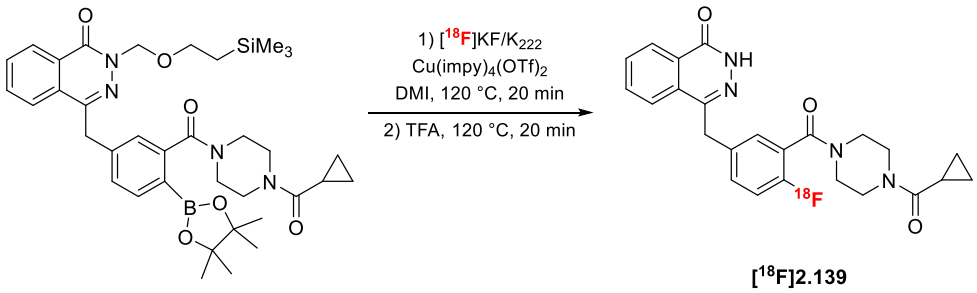

2.138

[^{18}F]2.139
[^{18}F]Olaparib
Manual: AY = 17% ± 5% (*n* = 15), A_m up to 34.6 GBq/μmol
Automated: AY = 6% ± 5% (*n* = 3), A_m up to 319 GBq/μmol
Gouverneur & Cornelissen (2019)

Scheme 2.29: Radiosynthesis of [^{18}F]olaparib.

In 2021, Maurer and Xu disclosed independently the radiosynthesis of [^{18}F]talazoparib **[^{18}F]2.141** from a pinacol boronic ester precursor and a trimethylammonium precursor respectively (Scheme 2.27).[122,123] The Maurer group demonstrated that [^{18}F]talazoparib was taken up in breast cancer cell lines and showed an excellent tumour-to-blood ratio in xenograft-bearing mice. The Xu group revealed that [^{18}F]talazoparib had a good level of tumour uptake in the murine prostate cancer (PC-3) tumour model.

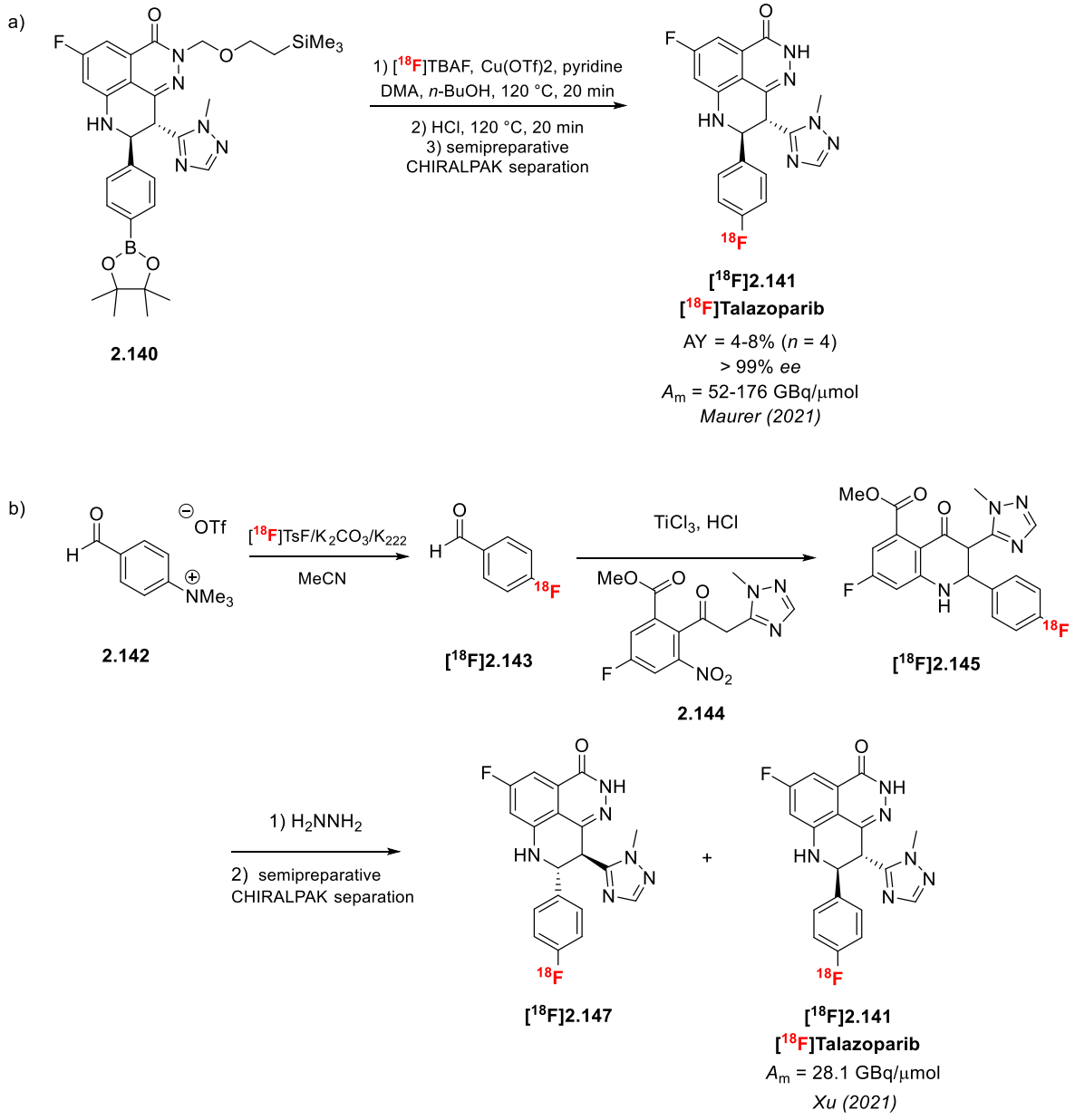

Scheme 2.30: Radiosynthesis [^{18}F]talazoparib.

In 2018, Domchek and co-workers reported promising efficacy of rucaparib treatment with an acceptable safety profile for patients with advanced pancreatic cancer.[124] However, not all patients receive the same benefit from rucaparib-maintenance therapy. We envisaged that an ^{18}F-isotopologue of rucaparib might act as a predictive biomarker to help with patient selection for rucaparib treatment and predict clinical benefit. The aim of this work is to develop the first radiosynthesis of [^{18}F]rucaparib **[^{18}F]2.147** (Figure 2.5).

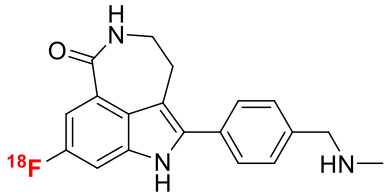

[^{18}F]2.147
[^{18}F]Rucaparib
This work

Figure 2.5: Structure of [^{18}F]rucaparib.

Radiolabelled analogues of rucaparib have been prepared by Mach and co-workers. The radiotracer [^{18}F]WC-DZ-F **[^{18}F]2.113** was applied for the preliminary evaluation of PARP expression in prostate cancer,[125] and [^{18}F]FluorThanatrace **[^{18}F]2.114** developed by Mach *et al.* is being evaluated as a PET imaging agent for clinical use.[126] The structurally related analogue ^{123}I/^{125}I-radiolabelled KX-1 **[$^{123/125}$I]2.115**, will be discussed in Chapter 3 (Figure 2.6).[127]

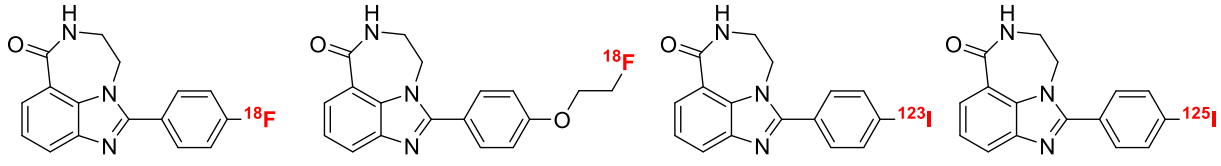

[^{18}F]2.148
[^{18}F]WC-DZ-F

[^{18}F]2.149
[^{18}F]FluorThanatrace

[^{123}I]2.150
[^{123}I]KX-1

[^{125}I]2.150
[^{125}I]KX-1

Figure 2.6: Radiolabelled analogues of rucaparib.

Using structurally identical ^{18}F-isotopologues of PARP inhibitors presents several advantages as these allow direct visualization of PARP expression in patients with PET imaging, as well as enable quantification of PARP inhibitor biodistribution, tumour delivery and target

engagement; as such stratification of patients becomes possible and response to DNA damaging cancer treatment can be monitored.[128] [^{3}H]rucaparib and [^{14}C]rucaparib were prepared to study their metabolism using *ex vivo* autoradiography and radio-HPLC (Figure 2.7).[129,130]

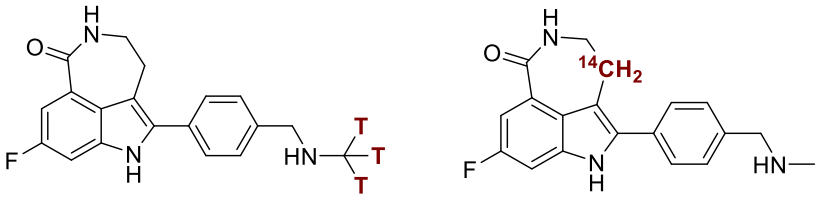

Figure 2.7: Labelled isotopologues of rucaparib.

2.4.2 Project Overview

To access [^{18}F]rucaparib, the Cu(II)-mediated ^{18}F-fluorination was selected for multiple reasons. Firstly, the boronic ester precursor is readily accessible and bench stable. Secondly, the procedure is amenable for automation. Thirdly, the reaction is generally high in A_m, activity yield (AY), RCP and chemical purity as reviewed in Section 2.3.2. Following the recently reported radiosynthesis of [^{18}F]olaparib,[120,121] this work focused on the development of a method to access [^{18}F]rucaparib, applying the key step, the Cu(II)-mediated radiofluorination of an aryl boronic ester with cyclotron-produced nucleophilic [^{18}F]fluoride (Scheme 2.31).

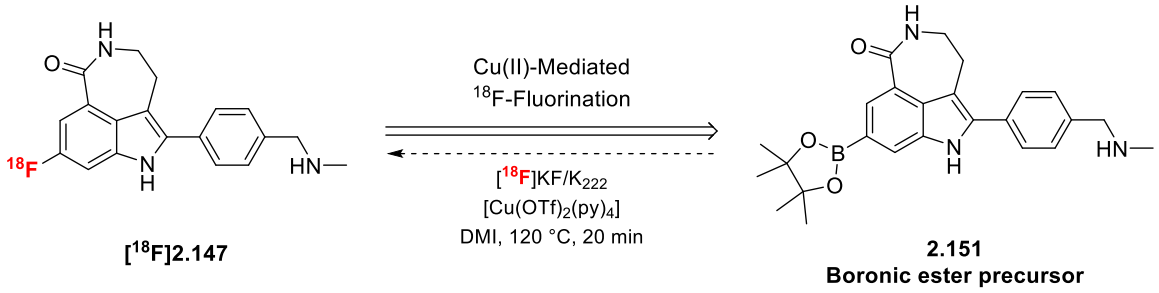

Scheme 2.31: Retro-radiosynthesis for [^{18}F]rucaparib.

2.4.3 Screening Experiments for [^{18}F]Rucaparib

The de-risking strategy for the Cu(II)-mediated radiofluorination developed by the Gouverneur group was reviewed in Section 2.3.2. We applied the same approach to this project with initial

screening experiments, investigating the compatibility of rucaparib and its sub-motifs towards Cu-mediated ^{18}F-fluorination. To prepare the additive **2.158** for screening, the synthesis started with the reaction of commercially available methyl 4-indolecarboxylate **2.152** with 2-nitroethylacetate **2.153**, made available by esterification of nitroethanol, to afford (2-nitroethyl)indole **2.154** which was required for ring closure (Scheme 2.32).

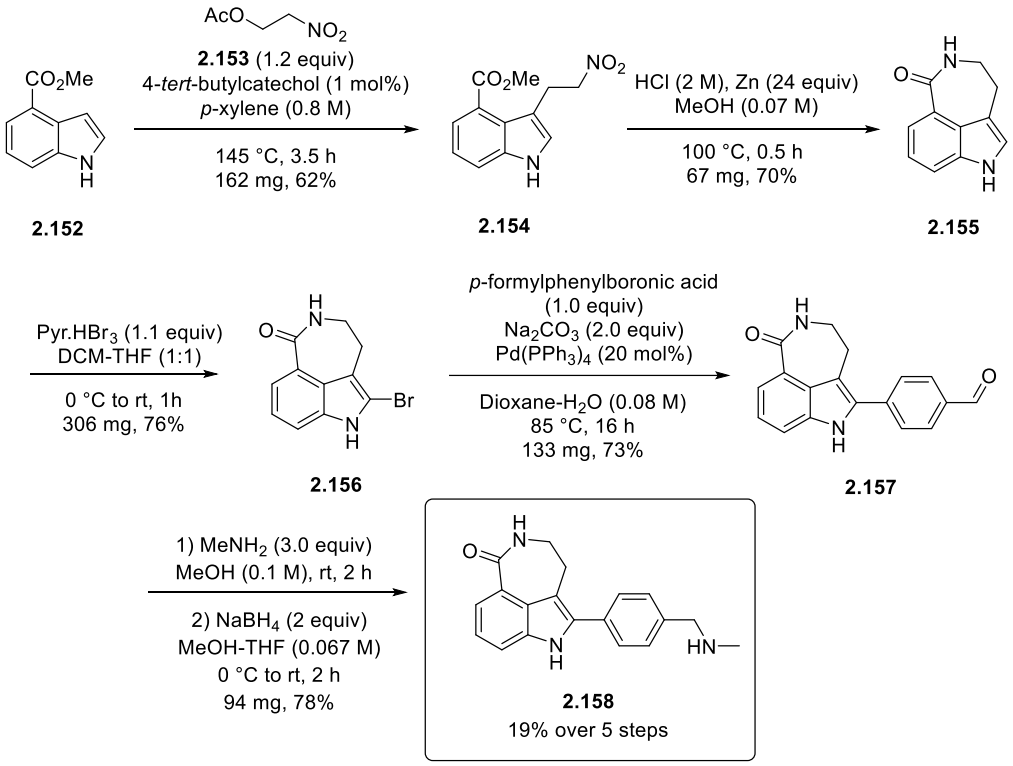

Scheme 2.32: Synthesis of non-fluorinated rucaparib analogue **2.158**.

Upon reduction with zinc in methanolic hydrochloric acid, lactonization led to the tricyclic indole **2.155** in 70% yield. Regioselective bromination at the C2-indole with pyridinium tribromide took place within an hour and led to the bromide **2.156** in 76% yield. Superimposing the ^{1}H NMR spectra of the starting material **2.155** and the brominated product **2.156** confirmed that the bromination was regioselective at C-2 (Figure 2.8). The peak corresponds to the proton (H_e) at C-2 in **2.155** (highlighted in grey) disappeared after bromination. ^{1}H-^{1}H Correlation Spectroscopy (COSY) showed the expected coupling between 3 protons at C-5, C-6 and C-7 of bromide **2.156** (Figure 2.9). Proton H_b at C-6 couples with both H_a at C-5 and H_c at C-7. Suzuki-Miyaura coupling between **2.157** and *p*-formylphenyl boronic acid followed by a

reductive amination led to the final non-fluorinated rucaparib analogue **2.158** with an overall yield of 19% (chemical purity > 95%) from commercially available indole **2.152** (Scheme 2.32).[131,132]

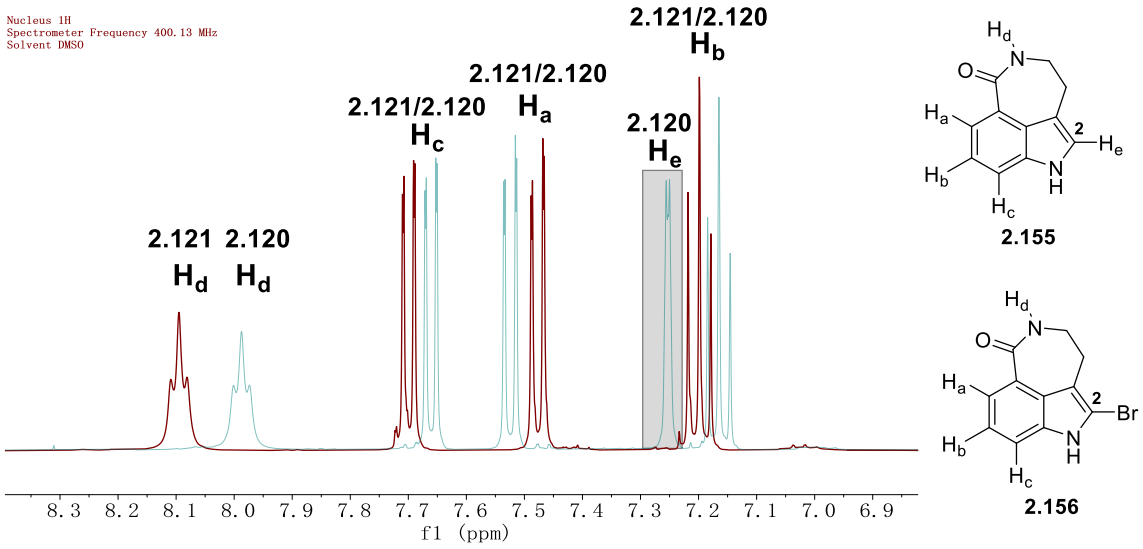

Figure 2.8: ^{1}H NMR spectra of **2.155** (indigo) and **2.156** (maroon).

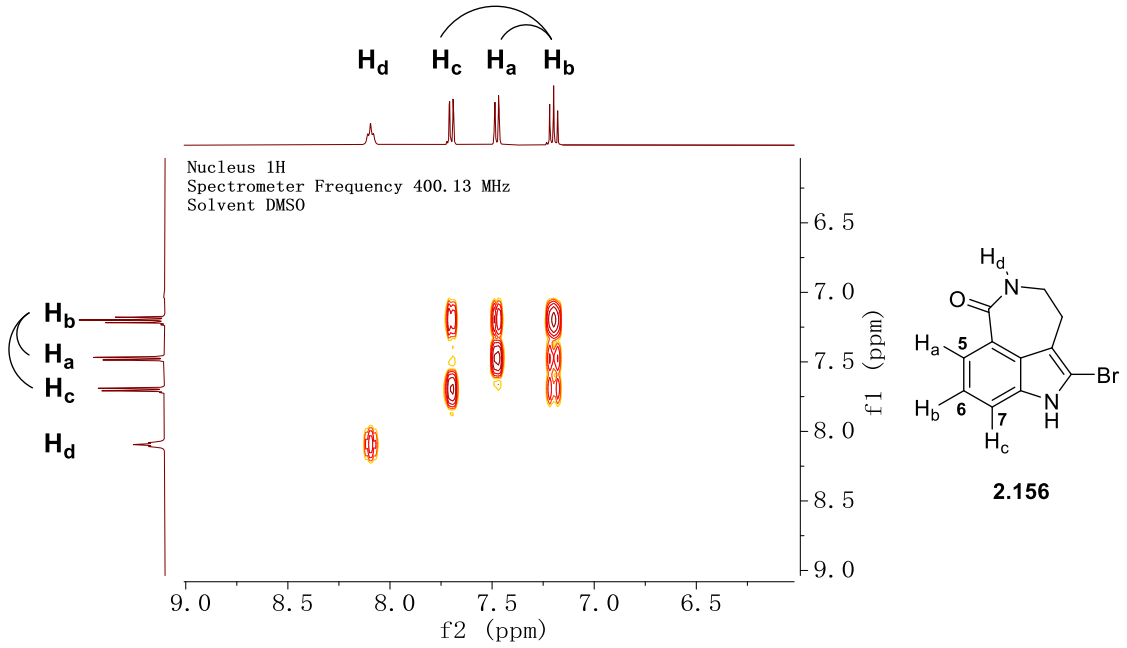

Figure 2.9: ^{1}H-^{1}H COSY of bromide **2.156**.

Subsequently the non-fluorinated analogue of rucaparib **2.158**, the tricyclic indole **2.155**, the aldehydic analogue of rucaparib **2.157** and an *N*Boc protected non-fluorinated analogue **2.159** were added as additives to the robustness screening experiments (Scheme 2.33). As expected, the model aryl boronic ester **2.109** responded well to Cu(II)-mediated ^{18}F-fluorination (RCY =

39% ± 2%, *n* = 4). "+/-" refers to standard deviation. However, when 1 equivalent of non-fluorinated rucaparib **2.158** was added, only trace amount of [^{18}F]4-fluorobenzonitrile **[^{18}F]2.111** (RCY < 5%) was observed. This result discouraged ^{18}F-incorporation as the last step. We assumed that the secondary amine of non-fluorinated rucaparib **2.158** might prevent ^{18}F-fluorination. This assumption was confirmed upon spiking with the tricyclic indole **2.155**. The RCY of the benchmark reaction was not affected (~ 43%). Knowing the secondary amine is detrimental to ^{18}F-incorporation, we spiked the model reaction with two other analogues bearing an *N*Boc protecting group and an aldehyde, respectively. Adding the *N*Boc protected non-fluorinated analogue **2.159** (preparation of **2.159** see Chapter 4) did not hamper the efficiency of ^{18}F-incorporation (RCY = 34% ± 5%, *n* = 2), suggesting that a post-labelling deprotection strategy might be viable. Spiking the model reaction with aldehyde **2.157** did not affect the RCY of 4-[^{18}F]fluorobenzonitrile (RCY = 42% ± 8%, *n* = 2). Thus we considered a second strategy, which is a reductive amination. It has been used as a potential post-labelling step with ample examples to support its feasibility. [133-136]

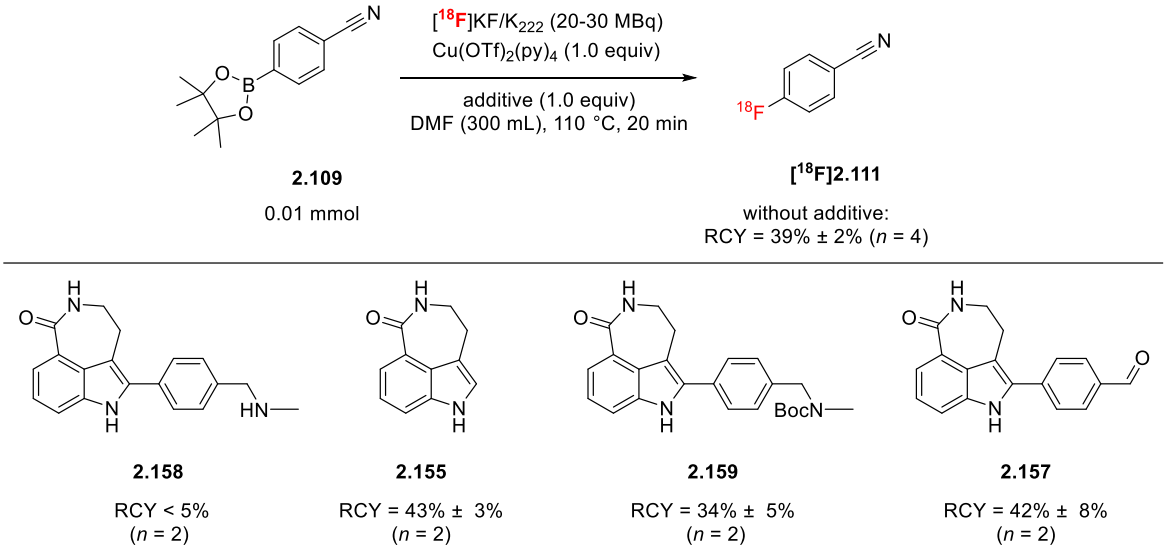

Scheme 2.33: Screening experiments informing suitable radiosynthetic routes towards [^{18}F]rucaparib.

Based on the screening results, we envisaged two retrosynthesis routes for [^{18}F]rucaparib. In the first route, [^{18}F]rucaparib **[^{18}F]2.147** could be afforded from deprotection of *N*Boc protected [^{18}F]rucaparib **[^{18}F]2.160** which might be accessed from the *N*Boc protected boronic ester

precursor **2.161** via Cu(II)-mediated ^{18}F-fluorination (Scheme 2.34, left route). In the second route, a reductive amination would be applied as the post-labelling step from aldehyde [^{18}F]2.162 and the corresponding precursor is an aldehydic boronic ester **2.163** (Scheme 2.34, right route).

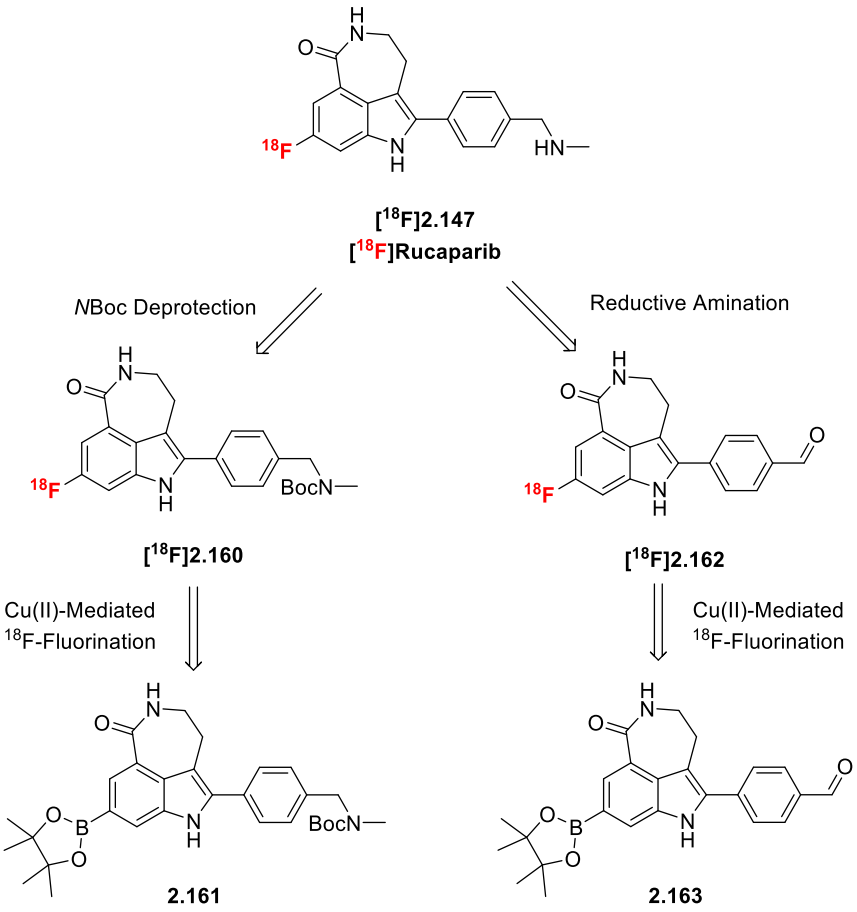

Scheme 2.34: Two possible retro-radiosynthesis routes for [^{18}F]rucaparib.

2.4.4 Retrosynthesis approaches to Boronic Ester Precursors

Having identified two potential borylated rucaparib precursors **2.161** and **2.163**, initial investigation focused on their synthesis, applying a method that would enable selective functionalisation at C-2 and C-6 indole (Scheme 2.35).

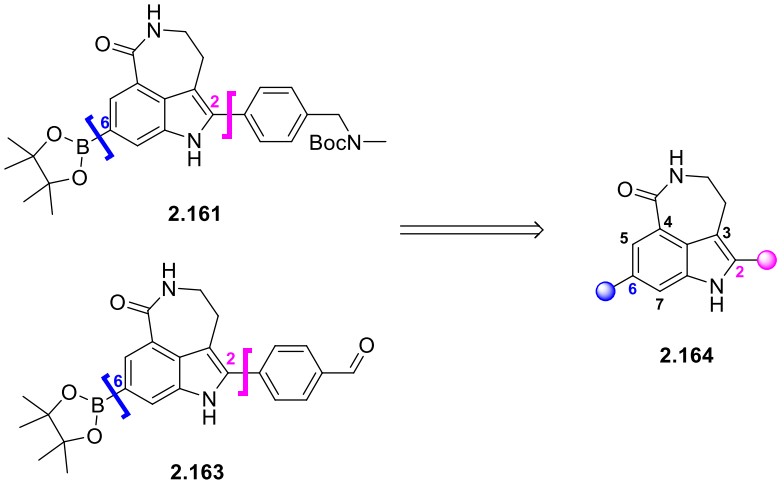

Scheme 2.35: C-2 and C-6 of tricyclic indole to be selectively functionalised.

Two retrosynthesis approaches of the *N*Boc protected boronic ester precursor **2.161** were envisaged. The first approach aimed to access the *bis*-borylated tricyclic indole **2.162** (Scheme 2.36). Baran and co-workers reported an iridium catalysed regioselective C-H borylation at C-6 indole (Scheme 2.37).[137] A bulky protecting group, such as triisopropylsilyl (TIPS) effectively blocked C-2 and C-7 which are known to react preferentially. The regioselectivity of the Suzuki-Miyaura coupling could be a potential limitation of this approach.

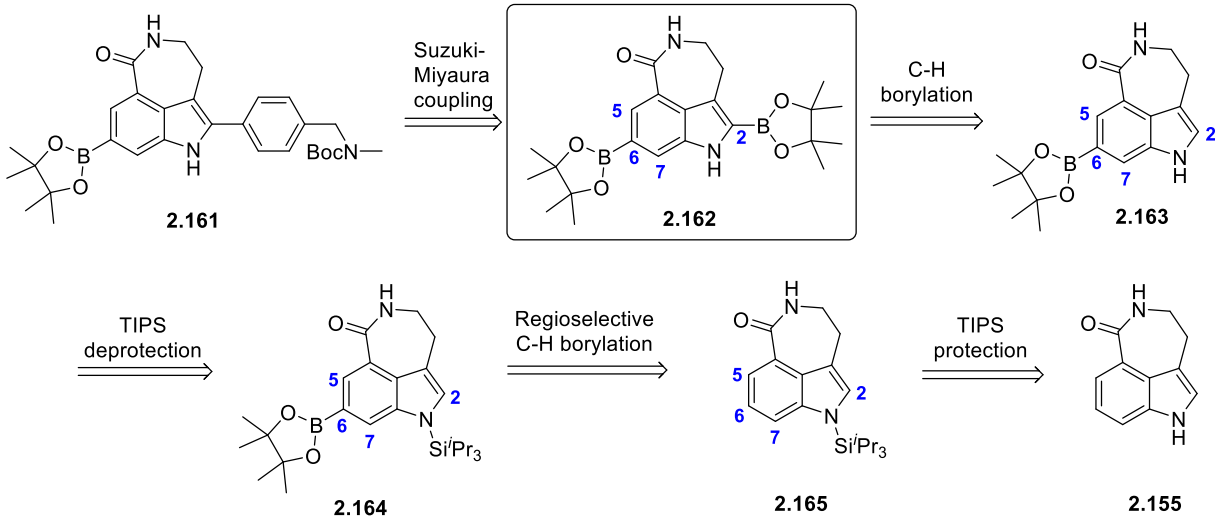

Scheme 2.36: Retrosynthesis analysis for the synthesis of boronic ester precursor **2.161**, featuring a *bis*-borylated tricyclic indole as the key intermediate.

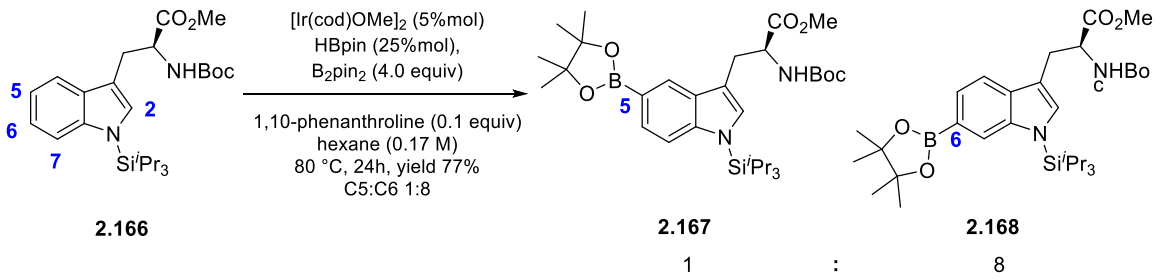

Scheme 2.37: Iridium catalysed regioselective C-H borylation developed by Baran and co-workers.

The second approach featured a last-step Miyaura borylation. A *bis*-halogenated tricyclic indole **2.170** was proposed as the key intermediate for a chemoselective Suzuki-Miyaura coupling to access **2.169** (Scheme 2.38). Since C-3 position of the tricyclic indole **2.171** is inhibited, electrophilic iodination with **2.171** should undergo regioselectively at C-2 indole to afford the *bis*-halogenated substrate **2.170**.

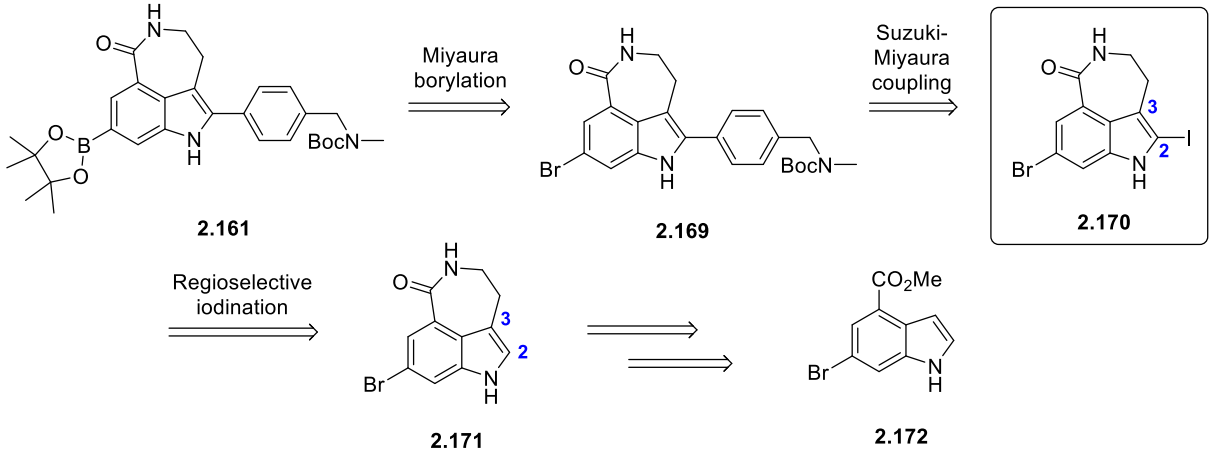

Scheme 2.38: Retrosynthesis analysis for the synthesis of boronic ester precursor **2.161**, featuring a *bis*-halogenated tricyclic indole as the key intermediate.

2.4.5 Synthesis of Boronic Ester Precursors for ^{18}F-Fluorination

In the first approach to access the *N*Boc protected boronic ester precursor **2.161**, a TIPS-protected tricyclic indole **2.165** was subjected to iridium-catalysed C-H borylation. Boronic ester **2.164** functionalised at C-6 indole was afforded as the single product. C-2 and C-7 are sterically hindered by the TIPS protecting group as expected. The C-5 borylated regioisomer was not observed, possibly due to the steric hindrance impaired by the lactam at C-4.The regioselectivity at C-6 indole was confirmed by ^{1}H-^{1}H COSY (Scheme 2.39 and Figure 2.10).

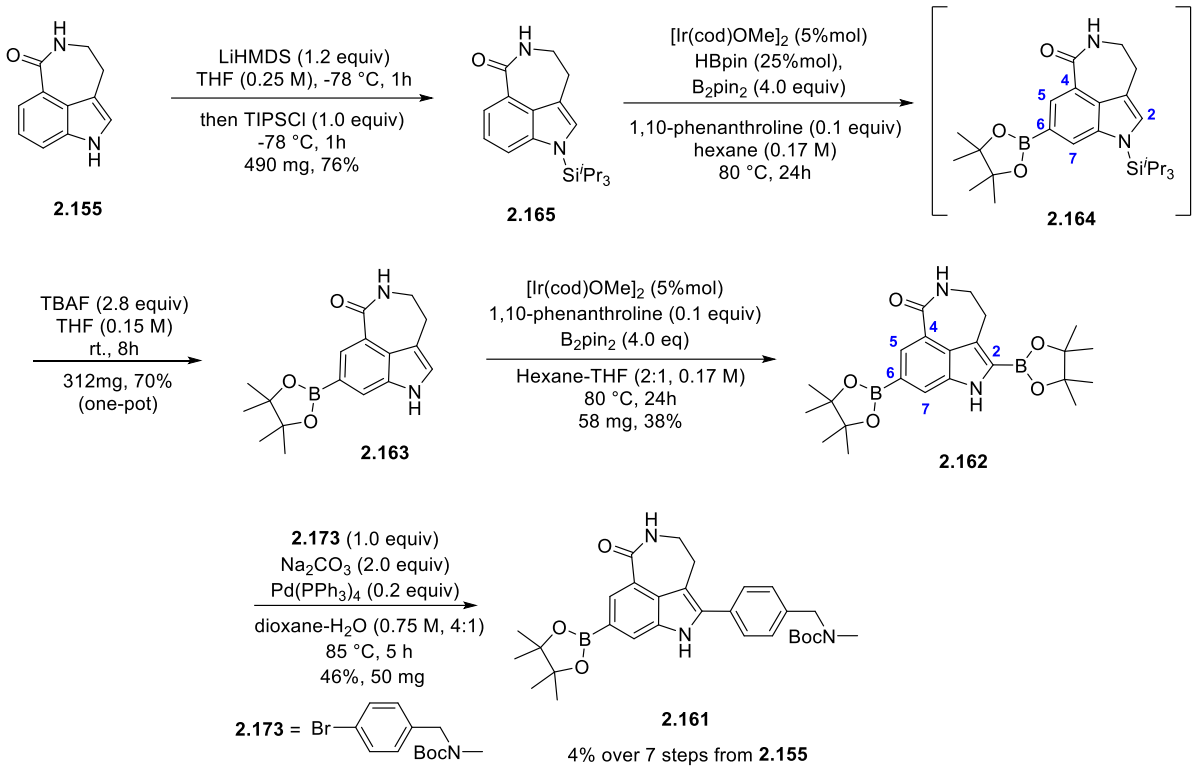

Scheme 2.39: Synthesis of boronic ester precursor **2.161** via bis-borylated intermediate **2.162**.

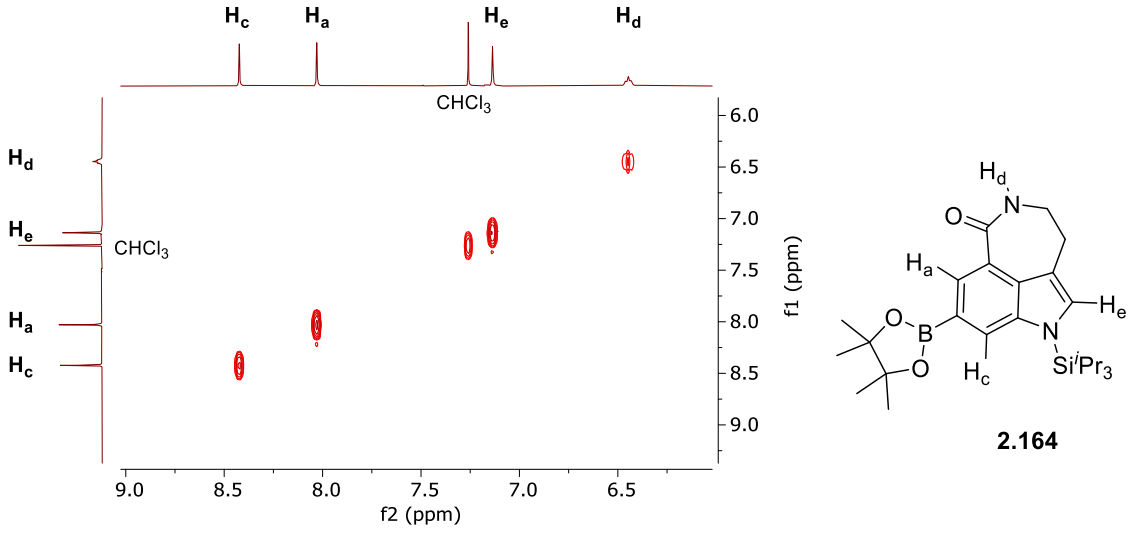

Figure 2.10: ^{1}H-^{1}H COSY of boronic ester **2.164**.

All three proton signals at the aromatic region exhibited as singlets. The lack of vicinal proton-proton coupling ($^{3}J_{HH}$) suggested that no proton is adjacent to each other on the indole motif, leaving the C-6 position the only possibility to be borylated. Boronic ester **2.164** was then deprotected in TBAF under room temperature for 8 hours. The C-H borylation and the deprotection could be done as a one-pot procedure in 70% yield. The resulting boronic ester

2.163 was subjected to a second iridium-catalysed C-H borylation. Without steric hindrance, C-2 indole was functionalised regioselectively due to the inherent reactivity of the pyrrole ring. Protodeboronation at C-2 indole was observed during isolation of boronic ester **2.162** via silicon gel column chromatography, indicating the lability of the boronic ester at this position. When *bis*-borylated tricyclic indole **2.162** was subjected to Suzuki-Miyaura reaction with bromide **2.173**, the desired boronic ester **2.161** was obtained as the single product. This bold move was based on the assumption that the C-2 position in the pyrrole-like ring is inherently more reactive and thus more prone to transmetallation in the Suzuki-Miyaura coupling.[138] The overall yield of the precursor **2.161** was 4% from methyl 4-indolecarboxylate **2.155** (Scheme 2.39).

In the second approach to access the same *N*Boc protected boronic ester precursor **2.161**, the *bis*-halogenated tricyclic indole **1.170** was prepared by modifying the sequence disclosed in the literature.[131,132] Similar to the synthesis of non-fluorinated rucaparib, this synthesis started with the reaction of commercially available methyl 6-bromo-4-indolecarboxylate **2.172** with 2-nitroethylacetate **2.153**, to afford (2-nitroethyl)indole **2.174**. Upon reduction with zinc in methanolic hydrochloric acid, lactonization led to the tricyclic indole **2.171** in 71% yield (Scheme 2.40).

Iodination with PIFA/I_2 (PIFA = [bis(trifluoroacetoxy)iodo]benzene) led to the *bis*-halogenated **2.170** in a yield of 46%. Subjecting to a Suzuki-Miyaura reaction, the C2-indole was selectively coupled with the *N*-protected boronic ester fragment **2.175** to yield bromide **2.169** as a single product, leaving the C6-indole bromide intact for further functionalization. Isolation of bromide **2.169** was challenging. The crude mixture was immediately subjected to Miyaura borylation to afford the desired boronic ester **2.161** as the best yield. After preparative HPLC purification, **2.161** required for ^{18}F-incorporation was obtained with an overall yield of 8% (chemical purity > 95%) from commercially available indole **2.172**.

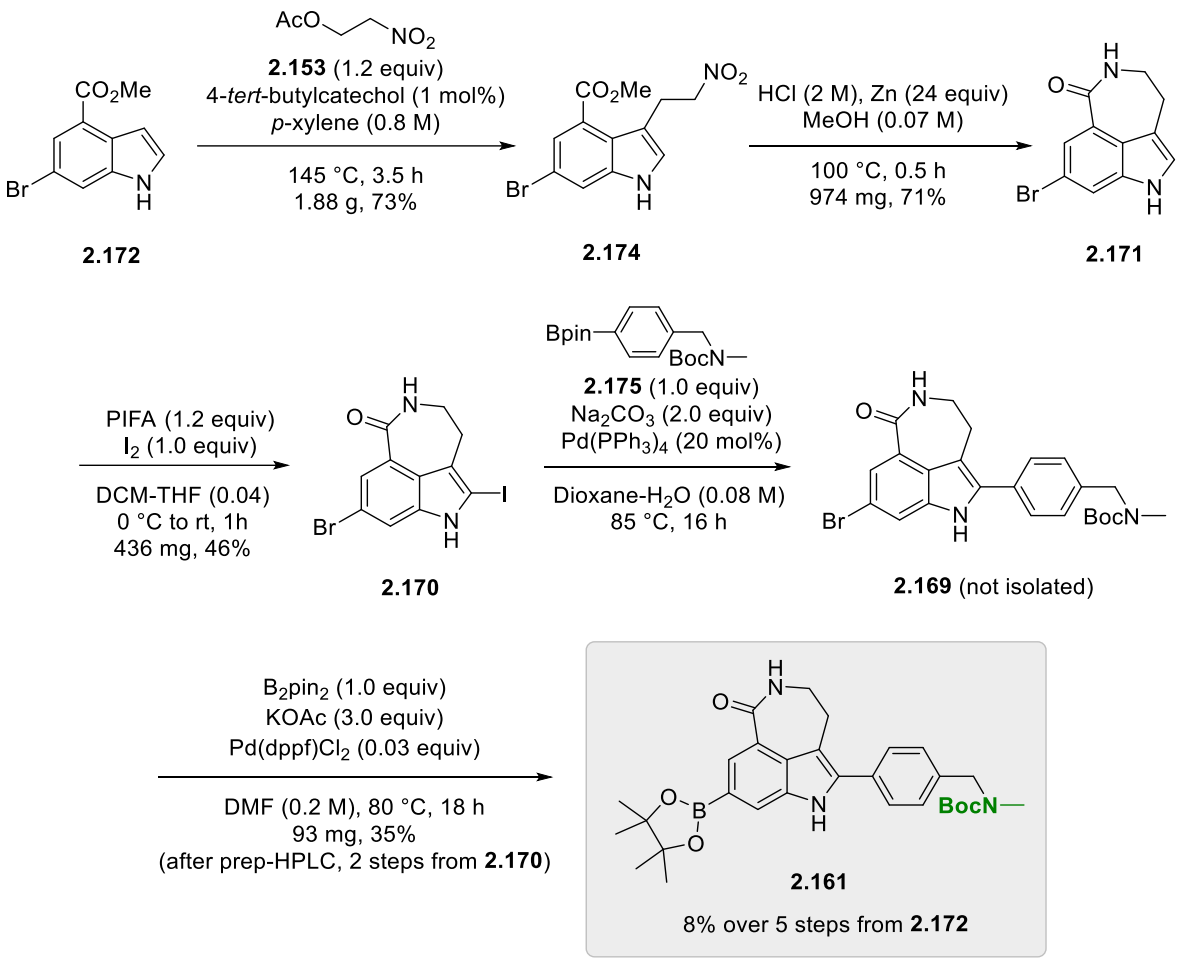

Scheme 2.40: Synthesis of *N*Boc protected boronic ester precursor **2.161**.

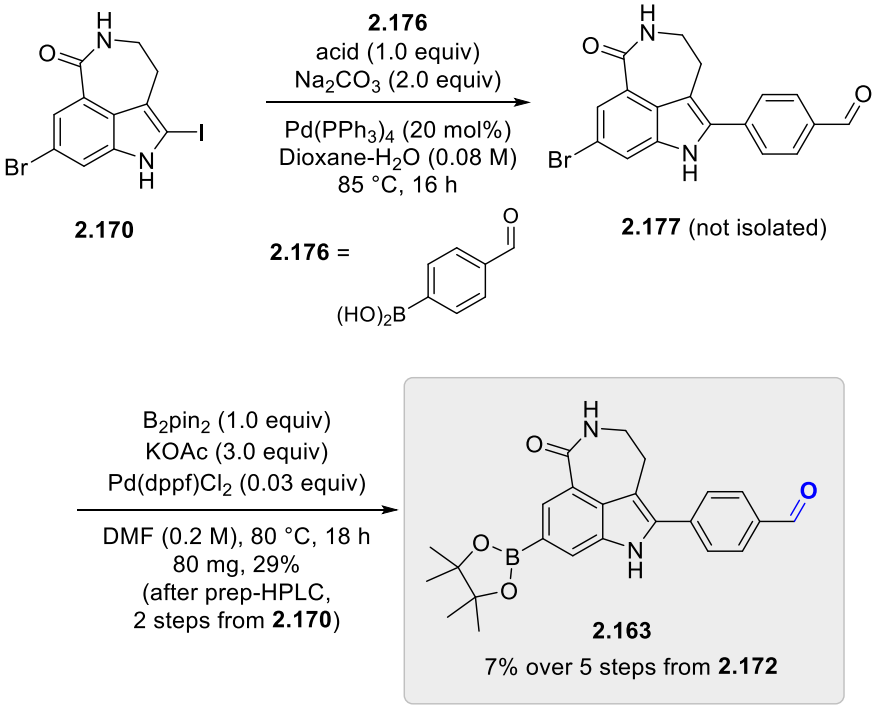

Scheme 2.41: Synthesis of aldehydic boronic ester precursor **2.163**.

The aldehydic boronic ester precursor **2.163** was also accessed via this strategy. Coupling between the *bis*-halogenated **2.170** and *p*-formylphenyl boronic acid afforded aldehyde **2.177** which was not isolated for the same reason as for **2.169**. The crude mixture was directly subjected to a borylative coupling leading to the aldehydic boronic ester **2.163** with an overall yield of 7% (chemical purity > 95%) from commercially available indole **2.172** (Scheme 2.41).

2.4.6 Synthesis of ^{19}F-Rucaparib as Verification for Radiolabelling

In radiochemistry, the ^{18}F-radiolabelled product is usually yielded in nanomolar or picomolar scale. Due to its limited quantity and safety in handling radioactivity, the identity of the ^{18}F-radiolabelled product is confirmed by comparing the retention time of the peak with its corresponding ^{19}F-reference via HPLC. To prepare the fluorinated references for the precursors, we expected the reactivity of each step in the synthetic sequence would be similar to the non-fluorinated and brominated analogues.

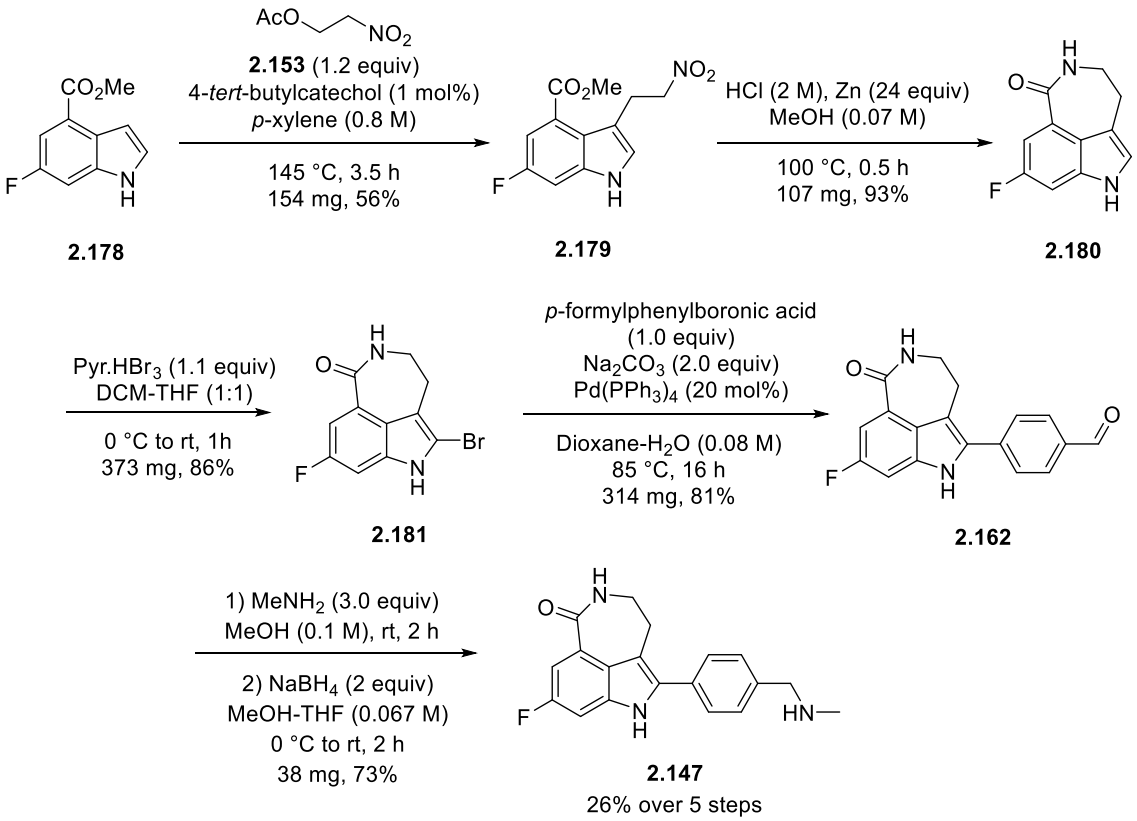

Scheme 2.42: Synthesis of rucaparib as standard reference.

With the synthesis routes to access the boronic ester precursors in hand, the similar approach was applied to prepare rucaparib **2.147** subsequently, starting from the commercially available methyl 6-fluoro-4-indolecarboxylate **2.178**, with an overall yield of 26% (Scheme 2.42) .

2.4.7 Optimisation Study for ^{18}F-Fluorination of Boronic Ester Precursors

Next, both *N*Boc and aldehydic precursors **2.161** and **2.163** were subjected to radiofluorination subsequently. Upon delivery of [^{18}F]fluoride to the radiolab, [^{18}F]Fluoride (3.0-4.0 GBq) was trapped onto a quaternary methylammonium (QMA) cartridge and separated from the ^{18}O-enriched-water. It was then released with a solution of K_{222}/ $K_2C_2O_4$/K_2CO_3 in MeCN/H_2O. We applied the same elution method as in the radiosynthesis of [^{18}F]olaparib which was proved to be the most efficient elution method (~ 80%).[120] The solution was azeotropically dried with MeCN under constant N_2 flow at 105 °C. The dried [^{18}F]KF/K_{222} residue was redissolved in anhydrous MeCN. A solution of [^{18}F]KF/K_{222} in MeCN (20 - 30 MBq, 10-50 µL) was dispensed into a V-vial. A solution containing $Cu(OTf)_2(py)_4$ and the *N*Boc protected precursor **2.161** was added to the vial, followed by injection of air via a syringe to maintain aerobic condition. The sealed vial was heated at 120 °C for 20 min. An aliquot was removed for analysis by radio-HPLC to calculate the RCY and to confirm the product identity.

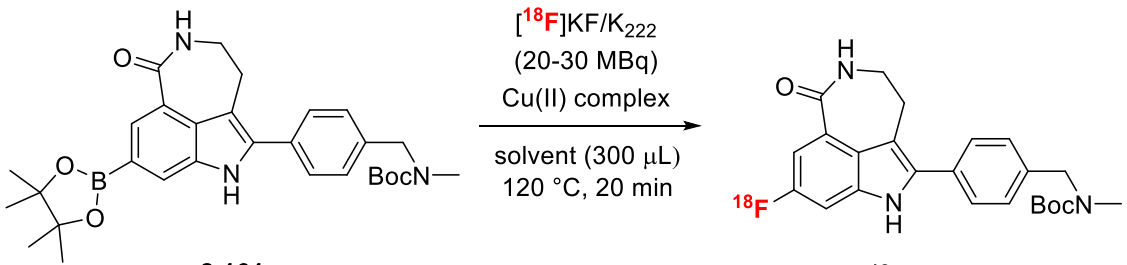

2.161
0.01 mmol, 5 mg

[^{18}F]2.160

Entry	Solvent	$Cu(OTf)_2(py)_4$	RCY (n = 2)[a]
1	**DMI**	**1 equiv**	42% ± 5%
2	DMI	2 equiv	39% ± 1%
3	DMI	3 equiv	25% ± 3%

4	DMA	2 equiv	29% ± 2%
5	DMF	2 equiv	7% ± 0%

Table 2.4: Optimization study for the ^{18}F-radiolabeling of the *N*-protected boronic ester precursor **2.126**. [a]RCY = radiochemical yield, determined by analytical HPLC. K_{222} = 4,7,13,16,21,24-hexaoxa-1,10-diazabicyclo[8.8.8]hexacosane or Kryptofix 222. DMI = 1,3-dimethyl-2-imidazolidinone. DMF = *N*,*N*-dimethylformamide.

The labelling of the *N*Boc protected precursor **2.161** with 1 equivalent of $Cu(OTf)_2(py)_4$ in DMI afforded [^{18}F]**2.160** in 42% RCY (Table 1, entry 1). Slight modification of these labelling conditions did not improve the RCY, including changing the solvent and adding more Cu(II) (Table 2.4, entry 2-5). Deprotection of [^{18}F]**2.160** with TFA at 120 °C for 20 minutes was quantitative (Scheme 2.43).

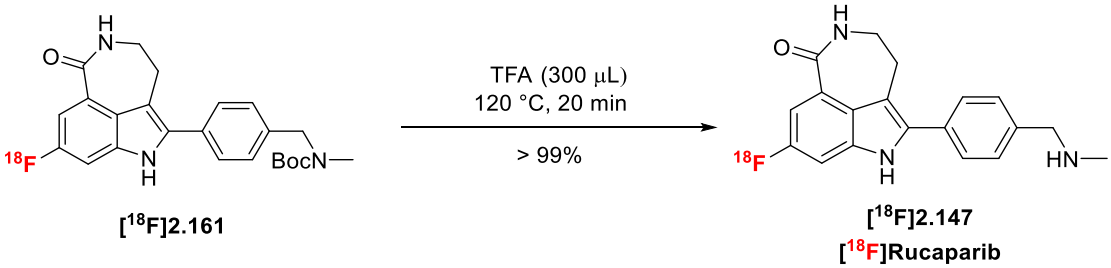

Scheme 2.43: Quantitative deprotection to access [^{18}F]rucaparib.

When the aldehydic precursor **2.163** was subjected to the reaction condition found optimal for **2.161**, the RCY of [^{18}F]**2.162** was significantly higher (73% RCY, Table 2.5, entry 1). Further optimization by modifying the stoichiometry of the copper complex with respect to the boronic ester precursor and the solvent indicated that the best result was obtained by increasing the $Cu(OTf)_2(py)_4$:**2.163** ratio from 1:1 to 2:1. These ^{18}F-labeling conditions gave [^{18}F]**2.162** in 80% RCY (Table 2.5, entries 2–5).

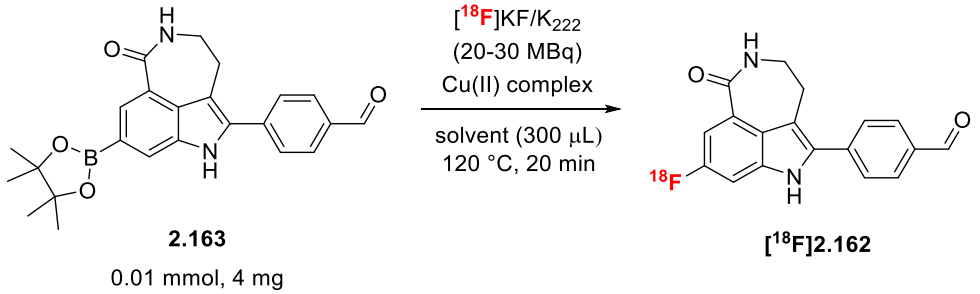

Entry	Solvent	$Cu(OTf)_2(py)_4$	RCY (n = 2)[a]

1	DMI	1 equiv	73% ± 7%
2	**DMI**	**2 equiv**	**80% ± 3%**
3	DMI	3 equiv	56% ± 1%
4	DMA	2 equiv	50% ± 5%
5	DMF	2 equiv	13% ± 3%

Table 2.5: Optimization study for the ^{18}F-radiolabeling of the *N*-protected boronic ester precursor **2.128**. [a]RCY = radiochemical yield, determined by analytical HPLC. K_{222} = 4,7,13,16,21,24-hexaoxa-1,10-diazabicyclo[8.8.8]hexacosane or Kryptofix 222. DMI = 1,3-dimethyl-2-imidazolidinone. DMF = *N*,*N*-dimethylformamide.

Aldehyde **[^{18}F]2.162** was then subjected to the reductive amination, in excess of methylamine and $NaBH_3CN$ in EtOH for 20 minutes at 120 °C. The conversion was quantitative and the identity of the product [^{18}F]rucaparib was confirmed by analytical radio-HPLC (Scheme 2.44).

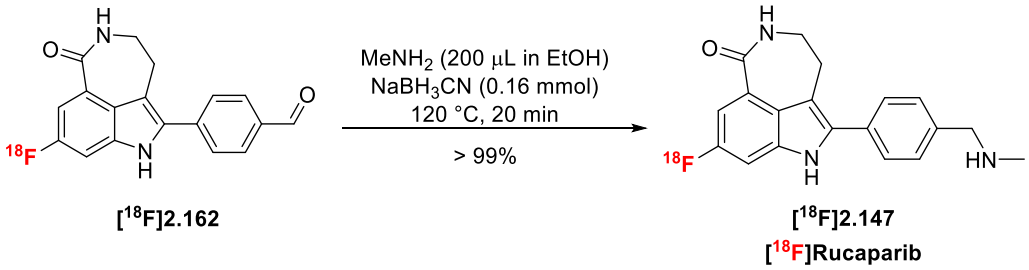

Scheme 2.44: Quantitative conversion of reductive amination to access [^{18}F]rucaparib.

The aldehydic boronic ester precursor **2.163** was selected for radiosynthesis and isolation of [^{18}F]rucaparib.

2.4.8 Large Scale Radiosynthesis and Isolation of [^{18}F]Rucaparib

The aldehydic precursor **2.163** was subjected to the optimised condition for radiofluorination, starting from 2 to 3 GBq of [^{18}F]fluoride. The crude mixture after reductive amination was loaded onto a semi-preparative HPLC in reverse phase for separation. The [^{18}F]rucaparib **[^{18}F]2.147** was collected from the HPLC and trapped onto a C18 cartridge. It was then released with 3 mL of EtOH. After drying, [^{18}F]rucaparib was reformulated in 10% DMSO/PBS solution with a non-decay corrected AY of 11% ± 3% (n = 3), a radiochemical purity (RCP) superior to 95%, and A_m up to 30 GBq/µmol (n = 3); the total synthesis time was 2.5 h (Scheme 2.45 and Figure 2.8).

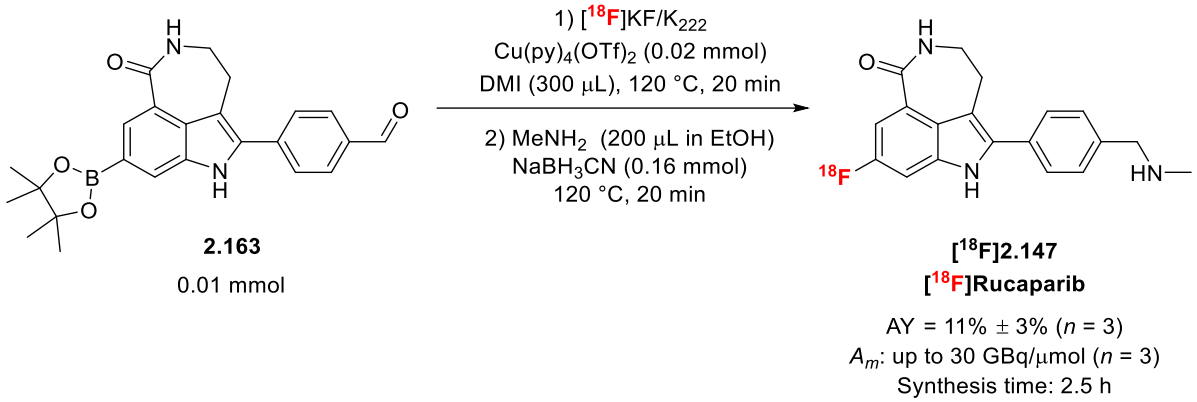

Scheme 2.45: Radiosynthesis and isolation of [^{18}F]rucaparib.

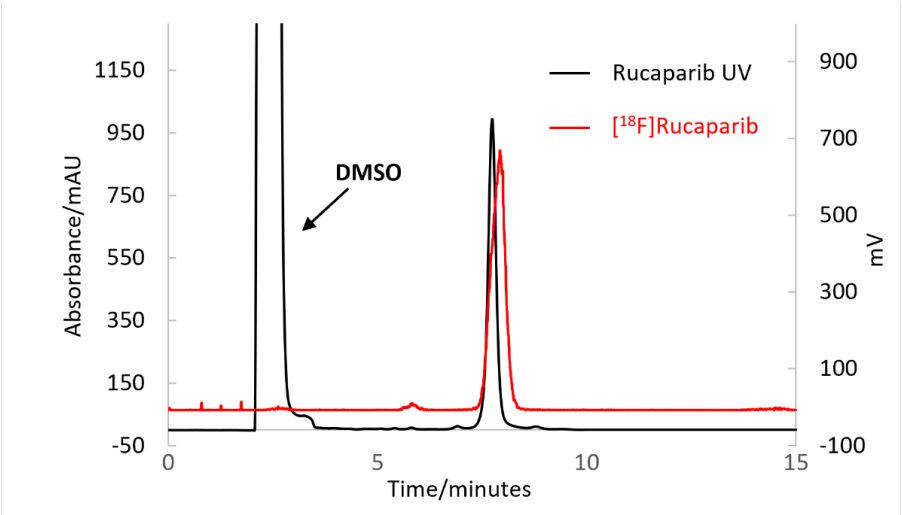

Figure 2.8: Radiochromatogram obtained during the HPLC analysis of [^{18}F]rucaparib (red) overlayed with UV chromatogram of non-radiolabelled reference standard rucaparib (λ = 220 nm, black).

2.5 In vitro and In Vivo Evaluations of [^{18}F]Rucaparib[a]

Pancreatic cancer is one of the hard-to-treat diseases and is associated with germline (5%) or somatic (12%) mutations in BRCA1/*2*.[138] BRCA1/*2* mutations are also the most common causes of familial pancreatic cancer, which makes PARP inhibition a promising strategy to treat pancreatic cancer.[140] Recent clinical studies showed promising therapeutic efficacy of rucaparib as monotherapy in the treatment of advanced pancreatic cancer patients with BRCA1/*2* mutation,[141] as well as in the maintenance therapy for patients with advanced pancreatic cancer and BRCA1/*2* pathogenic variant, expanding the patient scope that may

[a] The following work was carried out by Dr. Chung Ying Chan (Department of Oncology, University of Oxford).

benefit from treatment with PARP inhibitors. Two human pancreatic adenocarcinoma (PDAC) models: AsPC1 and PSN1 were used for biological evaluations of [^{18}F]rucaparib. [^{18}F]Rucaparib was delivered as a solution in 10% DMSO in PBS at pH 7.4, with a dilution ~ 600 MBq/mL. All biological data were obtained at least in triplicate.

2.5.1 *In Vitro* [^{18}F]Rucaparib Uptake in PDAC Cell Lines

In vitro [^{18}F]rucaparib uptake was evaluated in pancreatic cancer models: AsPC1 and PSN1 cell lines. PSN1 was previously reported to inherently express higher PARP1 level than AsPC1 cells.[142] Upon treatment with [^{18}F]rucaparib for 30 min, the uptake of [^{18}F]rucaparib in AsPC1 and PSN1 cells was observed, and the amount of overall [^{18}F+^{19}F]rucaparib uptake was calculated based on the radioactivity signal (cpm) (Equation 2.1). PSN1 cells retained rucaparib more effectively than AsPC1, indicating the correlation between rucaparib uptake and PARP1 expression in these cells.

$$\text{Overall } [^{18}\text{F}+^{19}\text{F}]\text{rucaparib pmol/cell} = \frac{\left(\frac{\text{Radioactivity from lysate (cpm)}}{\text{Radioactivity from 100 kBq (cpm)}} \times \text{Total amount of } [^{18}\text{F}+^{19}\text{F}]\text{rucaparib (pmol/well)}\right)}{\text{Number of cells/well}} \quad (2.1)$$

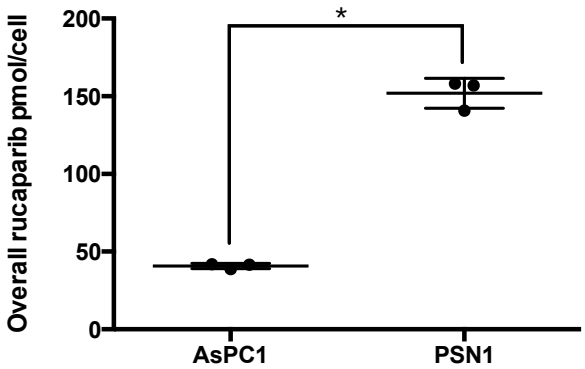

Figure 2.1: Rucaparib uptake in AsPC1 and PSN1 cells. Asterisks indicate levels of significance: *, $P < 0.05$. $n = 3$; error bars represent standard deviation.

The binding selectivity of [^{18}F]rucaparib was assessed by blocking studies using non-radiolabelled PARP inhibitors, olaparib and rucaparib. Their binding specificity has been

investigated by Reiner and co-workers; both inhibitors showed similar inhibitory profile across 12 PARP enzymes and at 100 nM, > 90% of PARP1 and PARP2 was inhibited (Figure 2.2).[143]

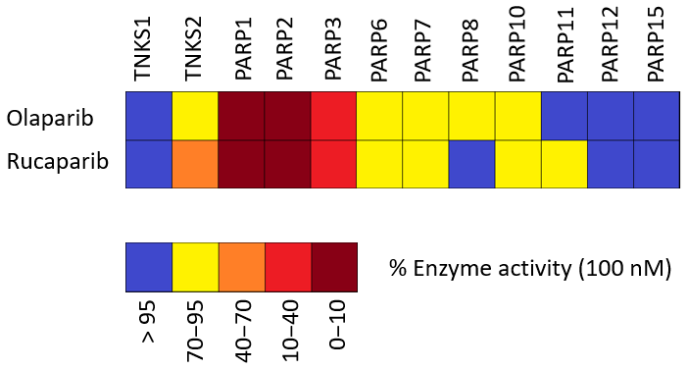

Figure 2.2: Enzymatic activity screening of olaparib and rucaparib against 12 PARP enzymes.[5]

Exposure of excessive unlabelled olaparib or rucaparib (100 μM, >1000 fold) could reduce the uptake of [^{18}F]rucaparib (> 50%) in PSN1 cells (Figure 2.3), showing the binding selectivity of [^{18}F]rucaparib towards PARP enzymes, especially PARP1 and 2, where the PARP inhibitors bound to the catalytic binding site of PARP enzymes and blocked the binding of the [^{18}F]rucaparib to PARP enzymes.

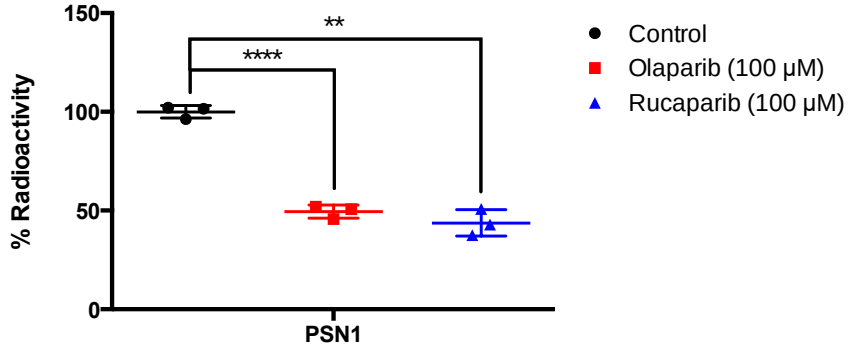

Figure 2.3: Blocking of [^{18}F]rucaparib uptake in PSN1 cells by addition of an excess of non-labelled olaparib or rucaparib. Asterisks indicate levels of significance: **, P < 0.01; and ****, P < 0.0001. *n* = 3; error bars represent standard deviation.

2.5.2 *In vivo* imaging of [^{18}F]Rucaparib in PSN1 Xenograft-Bearing Mice

In vivo, 1 h dynamic PET imaging was obtained of PSN1 xenograft-bearing mice injected intravenously with [^{18}F]rucaparib (0.87-11.38 MBq in 100 μL of PBS, A_m = 1.5-30.9 GBq/μmol), revealing that [^{18}F]rucaparib was clear through hepatobiliary and renal pathways with high uptake in liver, small and large intestines (Figure 2.4a). Region of interest (ROI) with

standardised uptake value (SUV) from PET images 1 h post injection showed rapid blood clearance with half-life of 3.8 ± 1.3, and a tumour-to-muscle ratio of 1.48, indicating [^{18}F]rucaparib avidity in PSN1 tumours (Figure 2.4b). *Ex vivo* biodistribution at 1 h post-intravenous injection showed PSN1 tumour xenograft uptake with a tumour-to-blood ratio of 1.53, which was verified the image-based quantification results, and 2 h post-injection with a tumour-to-blood ratio of 3.4, showing better tumour-to-background ratio (Figure 2.4c).

In vivo blocking studies, the PSN1 xenograft-bearing mice were co-injected with therapeutic amount (0.5 mg) of non-radiolabelled olaparib or rucaparib showed significant reduction of [^{18}F]rucaparib uptake at 2 h post-injection in tumour and those high PARP expressing organs, demonstrating the binding selectivity of [^{18}F]rucaparib (Figure 2.5).

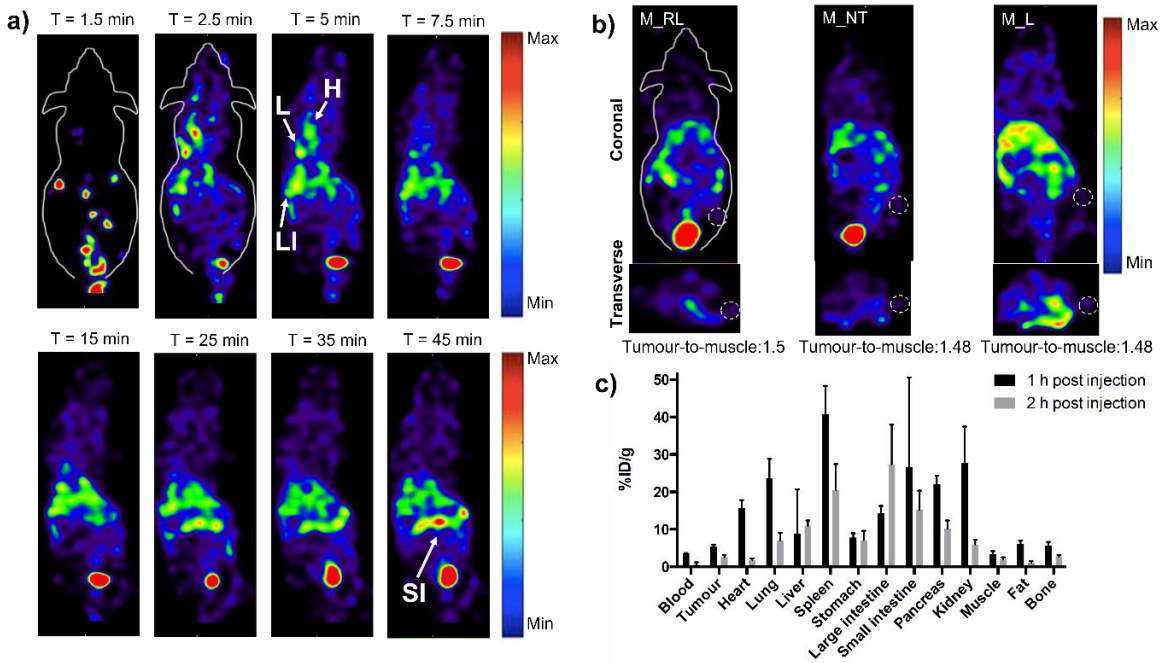

Figure 2.4: a) Representative dynamic PET images after intravenous injection of [^{18}F]rucaparib (2.38 MBq, 30.9 GBq/μmol). *In vivo* dynamic PET imaging of PSN1 xenograft-bearing mice. L = lung; H = heart; LI = large intestine; SI = small intestine. b) Representative MIP images of PSN1 xenograft-bearing mice, 1 h post injection of [^{18}F]rucaparib. c) Biodistribution of [^{18}F]rucaparib in selected tissues in PSN1 xenograft-bearing mice, 1 or 2 h after intravenous administration of [^{18}F]rucaparib ((0.87-11.38 MBq, 1.5-30.9 GBq/μmol).); error bars represent standard deviation.

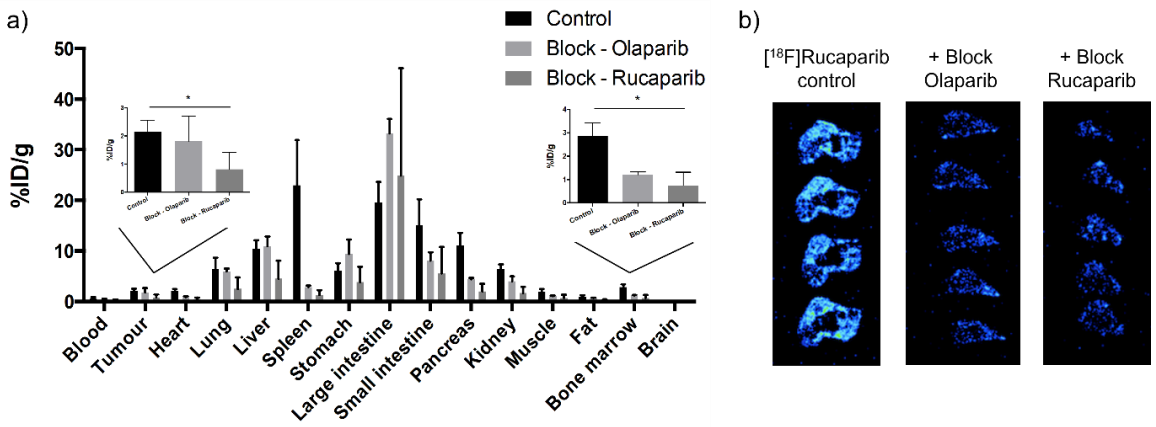

Figure 2.5: a) Biodistribution in selected tissues in PSN1 xenograft-bearing mice 2 h after intravenous injection of [^{18}F]rucaparib (0.87-2.47 MBq, A_m = 5.5 GBq/μmol) (n=3/group), with or without an excess of cold, unlabeled olaparib or rucaparib (0.5 mg). b) Autoradiography of PSN1 tumour sections showing ^{18}F localisation and the PARP1 occupancy by unlabelled PARP inhibitors (olaparib and rucaparib). Asterisks indicate levels of significance: *, $P < 0.05$; error bars represent standard deviation.

2.6 Conclusion and Future Work

This work demonstrated the development of a viable radiotracer, [^{18}F]rucaparib, using Cu(II)-mediated ^{18}F-fluorination of aryl boronic ester precursors. Two radiosynthesis precursors were compared and the aldehydic precursor with higher RCY was selected for further semiautomated radiosynthesis.

Both *in vitro* and *in vivo* evaluations confirmed the correlation between PARP1 expression and uptake of [^{18}F]rucaparib, boding well for the potential use of [^{18}F]rucaparib as a PARP-targeting diagnostic radiotracer for cancer imaging, and for treatment monitoring of patients with pancreatic cancer.

Future aims of this project are: 1) to translate the radiosynthesis of [^{18}F]rucaparib to a fully-automated platform under GMP conditions and 2) to pursue [^{18}F]rucaparib through clinical trials, eventually developed as a commercial radiotracer for patient stratification.

2.7 Reference

[1] Miller, P. W.; Long, N. J.; Vilar, R.; Gee, A. D., Synthesis of ^{11}C, ^{18}F, ^{15}O, and ^{13}N Radiolabels for Positron Emission Tomography. *Angew. Chem. Int. Ed.* **2008**, *47* (47), 8998−9033.

[2] Ametamey, S. M.; Honer, M.; Schubiger, P. A., Molecular Imaging with PET. *Chem. Rev.* **2008**, *108* (5), 1501−1516.

[3] Gambhir, S. S., Molecular Imaging of Cancer with Positron Emission Tomography. *Nat. Rev. Cancer* **2002,** *2* (9), 683−693.

[4] Phelps, M. E., Positron Emission Tomography Provides Molecular Imaging of Biological Processes. *Proc. Natl. Acad. Sci.* **2000,** *97* (16), 9226−9233.

[5] Petroni, D.; Menichetti, L.; Poli, M., Historical and Radiopharmaceutical Relevance of [^{18}F]FDG. *J. Radioanal. Nucl. Chem.* **2020,** *323* (3), 1017−1031.

[6] Kuhl, D. E.; Phelps, M. E.; Hoffman, E. J.; Robinson, G. D., Jr.; MacDonald, N. S., Initial Clinical Experience with ^{18}F-2-Fluoro-2-deoxy-$_D$-glucose for Determination of Local Cerebral Glucose Utilization by Emission Computed Tomography. *Acta. Neurol. Scand. Suppl.* **1977,** *64*, 192−3.

[7] Rich, D. A., A Brief History of Positron Emission Tomography. *J. Nucl. Med. Technol.* **1997,** *25* (1), 4−11.

[8] Kapoor, V.; McCook, B. M.; Torok, F. S., An Introduction to PET-CT Imaging. *RadioGraphics* **2004,** *24* (2), 523−543.

[9] Strijckmans, K., The Isochronous Cyclotron: Principles and Recent Developments. *Comput. Med. Imaging Graph.* **2001,** *25* (2), 69−78.

[10] Dash, A.; Chakravarty, R., Radionuclide Generators: The Prospect of Availing PET Radiotracers to Meet Current Clinical Needs and Future Research Demands. *Am. J. Nucl. Med. Mol. Imaging* **2019,** *9* (1), 30−66.

[11] Shukla, A. K.; Kumar, U., Positron Emission Tomography: An overview. *J. Med. Phys.* **2006,** *31* (1), 13−21.

[12] Tong, S.; Alessio, A. M.; Kinahan, P. E., Image Reconstruction for PET/CT Scanners: Past Achievements and Future Challenges. *Imaging Med.* **2010,** *2* (5), 529−545.

[13] Moses, W. W., Fundamental Limits of Spatial Resolution in PET. *Nucl. Instrum. Methods Phys. Res. A.* **2011,** *648* (Supplement 1*)*, S236−S240.

[14] Levin, C. S.; Hoffman, E. J., Calculation of Positron Range and Its Effect on the Fundamental Limit of Positron Emission Tomography System Spatial Resolution. *Phys. Med. Biol.* **1999,** *44* (3), 781−799.

[15] Cho, Z. H.; Chan, J. K.; Ericksson, L.; Singh, M.; Graham, S.; MacDonald, N. S.; Yano, Y., Positron Ranges Obtained from Biomedically Important Positron-Emitting Radionuclides. *J. Nucl. Med.* **1975,** *16* (12), 1174−1176.

[16] Derenzo, S. E., Mathematical Removal of Positron Range Blurring in High Resolution Tomography. *IEEE Trans. Nucl. Sci.* **1986,** *33* (1), 565−569.

[17] Surti, S.; Scheuermann, R.; Werner, M. E.; Karp, J. S., Improved Spatial Resolution in PET Scanners Using Sampling Techniques. *IEEE trans. Nucl. Sci.* **2009,** *56* (3), 596−601.

[18] (a) Snyder, S. E.; Kilbourn, M. R., Chemistry of Fluorine-18 Radiopharmaceuticals. In *Handbook of Radiopharmaceuticals*, John Wiley & Sons, 2002; pp 195−227. (b) Palmer, A. J.; Clark, J. C.; Goulding, R. W., The Preparation of Fluorine-18 Labelled Radiopharmaceuticals. *Int. J. Appl. Radiat. Isot.* **1977,** *28* (1), 53−65.

[19] Jacobson, O.; Chen, X., PET Designated Flouride-18 Production and Chemistry. *Curr. Top. Med. Chem.* **2010,** *10* (11), 1048−1059.

[20] Jacobson, O.; Kiesewetter, D. O.; Chen, X., Fluorine-18 Radiochemistry, Labeling Strategies and Synthetic Routes. *Bioconjug. Chem.* **2015,** *26* (1), 1−18.

[21] Wang, J.; Sánchez-Roselló, M.; Aceña, J. L.; del Pozo, C.; Sorochinsky, A. E.; Fustero, S.; Soloshonok, V. A.; Liu, H., Fluorine in Pharmaceutical Industry: Fluorine-Containing Drugs Introduced to the Market in the Last Decade (2001–2011). *Chem. Rev.* **2014,** *114* (4), 2432−2506.

[22] Purser, S.; Moore, P. R.; Swallow, S.; Gouverneur, V., Fluorine in Medicinal Chemistry. *Chem. Soc. Rev.* **2008,** *37* (2), 320−330.

[23] Inoue, M.; Sumii, Y.; Shibata, N., Contribution of Organofluorine Compounds to Pharmaceuticals. *ACS Omega* **2020,** *5* (19), 10633−10640.

[24] Haynes, W. M.; Lide, D. R.; Bruno, T. J., Section 9 Molecular Structure and Spectroscopy. In *CRC Handbook of Chemistry and Physics: A Ready-reference Book of Chemical and Physical Data*, CRC Press, 2016; pp 9-i−9-112.

[25] Bondi, A., van der Waals Volumes and Radii. *J. Phys. Chem.* **1964,** *68* (3), 441−451.

[26] Biffinger, J. C.; Kim, H. W.; DiMagno, S. G., The Polar Hydrophobicity of Fluorinated Compounds. *ChemBioChem* **2004,** *5* (5), 622−627.

[27] Müller, K.; Faeh, C.; Diederich, F., Fluorine in Pharmaceuticals: Looking Beyond Intuition. *Science* **2007,** *317* (5846), 1881−1886.

[28] Schweizer, E.; Hoffmann-Röder, A.; Schärer, K.; Olsen, J. A.; Fäh, C.; Seiler, P.; Obst-Sander, U.; Wagner, B.; Kansy, M.; Diederich, F., A Fluorine Scan at the Catalytic Center of Thrombin: C-F, C-OH, and C-OMe Bioisosterism and Fluorine Effects on pKa and log D Values. *ChemMedChem* **2006,** *1* (6), 611−621.

[29] Furge, L. L.; Guengerich, F. P., Cytochrome P450 Enzymes in Drug Metabolism and Chemical Toxicology: An Introduction. *Biochem. Mol. Biol. Educ.* **2006,** *34* (2), 66−74.

[30] Butler, M. A.; Iwasaki, M.; Guengerich, F. P.; Kadlubar, F. F., Human cytochrome P-450PA (P-450IA2), the phenacetin O-deethylase, is primarily responsible for the hepatic 3-

demethylation of caffeine and N-oxidation of carcinogenic arylamines. *Proc. Natl. Acad. Sci.* **1989,** *86* (20), 7696.

[31] Böhm, H.-J.; Banner, D.; Bendels, S.; Kansy, M.; Kuhn, B.; Müller, K.; Obst-Sander, U.; Stahl, M., Fluorine in Medicinal Chemistry. *ChemBioChem* **2004,** *5* (5), 637−643.

[32] Park, B. K.; Kitteringham, N. R., Effects of Fluorine Substitution on Drug Metabolism: Pharmacological and Toxicological Implications. *Drug Metab. Rev.* **1994,** *26* (3), 605−643.

[33] Barnes-Seeman, D.; Beck, J.; Springer, C., Fluorinated Compounds in Medicinal Chemistry: Recent Applications, Synthetic Advances and Matched-Pair Analyses. *Curr. Top. Med. Chem.* **2014,** *14* (7), 855−864.

[34] Nickles, R. J.; Daube, M. E.; Ruth, T. J., An $^{18}O_2$ Target for the Production of [^{18}F]F_2. *Int. J. Appl. Radiat. Isot.* **1984,** *35* (2), 117−122.

[35] O'Neil, J. P.; Van Brocklin, H. F., New Solid and Gas Phase Targets for the CTI RDS 111 Cyclotron. *AIP Conf. Proc* **1999,** *475* (1), 936−939.

[36] Roberts, A. D.; Oakes, T. R.; Nickles, R. J., Development of an Improved Target for [^{18}F]F_2 Production. *Appl. Radiat. Isot.* **1995,** *46* (2), 87−91.

[37] Bishop, A.; Satyamurthy, N.; Bida, G.; Phelps, M.; Barrio, J. R., Identification and Quantitation of Gaseous Compounds of Fluorine Generated in [^{18}F]F_2 Target Systems. *Nucl. Med. Biol.* **1996,** *23* (4), 391−405.

[38] Hess, E.; Blessing, G.; Coenen, H. H.; Qaim, S. M., Improved Target System for Production of High Purity [^{18}F]Fluorine via the ^{18}O(p,n)^{18}F Reaction. *Appl. Radiat. Isot.* **2000,** *52* (6), 1431−1440.

[39] Casella, V.; Ido, T.; Wolf, A. P.; Fowler, J. S.; MacGegor, R. R.; Ruth, T. J., Anhydrous F-18 Labeled Elemental Fluorine for Radiopharmaceutical Preparation. *J. Nucl. Med.* **1980,** *21* (8), 750.

[40] Bishop, A.; Satyamurthy, N.; Bida, G.; Phelps, M.; Barrio, J. R., Identification and Quantitation of Gaseous Compounds of Fluorine Generated in [^{18}F]F_2 Target Systems. *Nucl. Med. Biol* **1996,** *23* (4), 391−405.

[41] Berridge, M. S.; Tewson, T. J., Chemistry of Fluorine-18 Radiopharmaceuticals. *Int. J. Rad. Appl. Instrum. A* **1986,** *37* (8), 685−693.

[42] Thomas, C. C.; Sondel, J. A.; Kerns, R. C., Production of Carrier-Free Fluorine-18. *Int. J. Appl. Radiat. Isot.* **1965,** *16* (2), 71−74.

[43] Clark, J. C.; Silvester, D. J., A Cyclotron Method for the Production of Fluorine-18. *Int. J. Appl. Radiat. Isot.* **1966,** *17* (3), 151−154.

[44] Kilbourn, M. R.; Jerabek, P. A.; Welch, M. J., An Improved [^{18}O]Water Target for [^{18}F]Fluoride Production. *Int. J. Appl. Radiat. Isot.* **1985,** *36* (4), 327−328.

[45] Guillaume, M.; Luxen, A.; Nebeling, B.; Argentini, M.; Clark, J. C.; Pike, V. W., Recommendations for Fluorine-18 Production. . *Int. J. Rad. Appl. Instrum. A* **1991,** *42* (8), 749−762.

[46] Kilbourn, M. R.; Hood, J. T.; Welch, M. J., A Simple ^{18}O Water Target for ^{18}F Production. *Int. J. Appl. Radiat. Isot.* **1984,** *35* (7), 599−602.

[47] Wieland, B. W.; Hendry, G. O.; Schmidt, D. G.; Bida, G.; Ruth, T. J., Efficient Small-Volume O-18 Water Targets for Producing F-18 Fluoride with Low Energy Protons. *J. Labelled Comp. Radiopharm.* **1986,** *23* (10-12), 1205−1207.

[48] Metzger, R. L.; Lasche, G. P.; Eckerman, K. F.; Leggett, R. W., Long-Lived Contaminants in Cyclotron-Produced Radiopharmaceuticals: Measurement and Dosimetry. *J. Radioanal. Nucl. Chem.* **2018,** *318* (1), 7−10.

[49] Gagnon, K.; Wilson, J. S.; Sant, E.; Backhouse, C. J.; McQuarrie, S. A., Assessing the Performance and Longevity of Nb, Pt, Ta, Ti, Zr, and ZrO_2-Sputtered Havar Foils for the High-

Power Production of Reactive [^{18}F]F by Proton Irradiation of [^{18}O]H_2O. *Appl. Radiat. Isot.* **2011,** *69* (10), 1330−1336.

[50] Eberl, S.; Eriksson, T.; Svedberg, O.; Norling, J.; Henderson, D.; Lam, P.; Fulham, M., High Beam Current Operation of a PETtrace™ Cyclotron for 18F$^-$ Production. *Appl. Radiat. Isot.* **2012,** *70* (6), 922−930.

[51] Füchtner, F.; Preusche, S.; Mäding, P.; Zessin, J.; Steinbach, J., Factors Affecting the Specific Activity of [^{18}F]Fluoride from a [^{18}O]water Target. *Nuklearmedizin* **2008,** *47* (3), 116−119.

[52] Berridge, M. S.; Apana, S. M.; Hersh, J. M., Teflon Radiolysis as the Major Source of Carrier in Fluorine-18. *J. Labelled Comp. Radiopharm.* **2009,** *52* (13), 543−548.

[53] Savisto, N.; Bergman, J.; Aromaa, J.; Forsback, S.; Eskola, O.; Viljanen, T.; Rajander, J.; Johansson, S.; Grigg, J.; Luthra, S.; Solin, O., Influence of Transport Line Material on the Molar Activity of Cyclotron Produced [^{18}F]Fluoride. *Nucl. Med. Biol.* **2018,** *64−65*, 8−15.

[54] Adam, M. J.; Jivan, S., Synthesis and Purification of l-6-[^{18}F]fluorodopa. . *Int. J. Rad. Appl. Instrum. A* **1988,** *39* (12), 1203−1206.

[55] Namavari, M.; Bishop, A.; Satyamurthy, N.; Bida, G.; Barrio, J. R., Regioselective Radiofluorodestannylation with [^{18}F]F_2 and [^{18}F]CH_3COOF: A High Yield Synthesis of 6-[^{18}F]Fluoro-L-dopa. *Int. J. Rad. Appl. Instrum. A* **1992,** *43* (8), 989−996.

[56] Coenen, H. H.; Franken, K.; Kling, P.; Stoecklin, G., Direct Electrophilic Radiofluorination of Phenylalanine, Tyrosine and Dopa. *Appl. Radiat. Isot.* **1988,** *39* (12), 1243−1250.

[57] Murakami, M.; Takahashi, K.; Kondo, Y., 2-^{18}F-Phenylalanine and 3-^{18}F-Tyrosine Synthesis Preliminary Data of Tracer Kinetics. *J. Labelled Comp. Radiopharm.* **1988,** *25* (7), 773−782.

[58] Babich, J. W.; Rubin, R. H.; Graham, W. A.; Wilkinson, R. A.; Vincent, J.; Fischman, A. J., ^{18}F-Labeling and Biodistribution of the Novel Fluoro-Quinolone Antimicrobial Agent, Trovafloxacin (CP 99,219). *Nucl. Med. Biol.* **1996,** *23* (8), 995−998.

[59] Ogawa, M.; Hatano, K.; Oishi, S.; Kawasumi, Y.; Fujii, N.; Kawaguchi, M.; Doi, R.; Imamura, M.; Yamamoto, M.; Ajito, K.; Mukai, T.; Saji, H.; Ito, K., Direct Electrophilic Radiofluorination of a Cyclic RGD Peptide for In Vivo $\alpha_v\beta_3$ Integrin Related Tumor Imaging. *Nucl. Med. Biol.* **2003,** *30* (1), 1−9.

[60] Preshlock, S.; Tredwell, M.; Gouverneur, V., ^{18}F-Labeling of Arenes and Heteroarenes for Applications in Positron Emission Tomography. *Chem. Rev.* **2016,** *116* (2), 719−766.

[61] Chirakal, R.; Firnau, G.; Schrobilgen, G. J.; McKay, J.; Garnett, E. S., The Synthesis of [^{18}F]Xenon Difluoride from [^{18}F]Fluoride Gas. *Int. J. Appl. Radiat. Isot.* **1984,** *35* (5), 401−404.

[62] Firnau, G. S. G.; Chirakal, R.; Garnett, E. S., Synthesis of [^{18}F]XeF_2, a Novel Agent for the Preparation of ^{18}F-Radiopharmaceuticals. *J. Chem. Soc., Chem. Commun.* **1981,** (4), 198−199.

[63] Neirinckx, R. D.; Lambrecht, R. M.; Wolf, A. P., Cyclotron Isotopes and Radiopharmaceuticals— XXV An Anhydrous ^{18}F-Fluorinating Intermediate: Trifluoromethyl Hypofluorite. *Int. J. Appl. Radiat. Isot.* **1978,** *29* (4), 323−327.

[64] Ehrenkaufer, R. E.; MacGregor, R. R., Synthesis of [18F]Perchloryl Fluoride and Its Reactions with Functionalized Aryl Lithiums. *Int. J. Appl. Radiat. Isot.* **1983,** *34* (3), 613−615.

[65] Hiller, A.; Fischer, C.; Jordanova, A.; Patt, J. T.; Steinbach, J., Investigations to the Synthesis of n.c.a. [^{18}F]$FClO_3$ as Electrophilic Fluorinating Agent. *Appl. Radiat. Isot.* **2008,** *66* (2), 152−157.

[66] Satyamurthy, N.; Bida, G. T.; Phelps, M. E.; Barrio, J. R., *N*-[^{18}F]Fluoro-*N*-alkylsulfonamides: Novel Reagents for Mild and Regioselective Radiofluorination. *Int. J. Radiat. Appl. Instrum. A* **1990,** *41* (8), 733−738.

[67] Oberdorfer, F.; Hofmann, E.; Maier-Borst, W., Preparation of a New ^{18}F-Labelled Precursor: 1-[^{18}F]Fluoro-2-pyridone. *Int. J. Radiat. Appl. Instrum. A* **1988,** *39* (7), 685−688.

[68] Oberdorfer, F.; Hofmann, E.; Maier-Borst, W., Preparation of ^{18}F-Labelled *N*-Fluoropyridinium Triflate. *J. Labelled Comp. Radiopharm.* **1988,** *25* (9), 999−1005.

[69] Teare, H.; Robins, E. G.; Kirjavainen, A.; Forsback, S.; Sandford, G.; Solin, O.; Luthra, S. K.; Gouverneur, V., Radiosynthesis and Evaluation of [^{18}F]Selectfluor bis(triflate). *Angew. Chem. Int. Ed.* **2010,** *49* (38), 6821−6824.

[70] Teare, H.; Robins, E. G.; Årstad, E.; Luthra, S. K.; Gouverneur, V., Synthesis and Reactivity of [^{18}F]-*N*-Fluorobenzenesulfonimide. *Chem. Commun.* **2007,** (23), 2330−2332.

[71] Lal, G. S.; Pez, G. P.; Syvret, R. G., Electrophilic NF Fluorinating Agents. *Chem. Rev.* **1996,** *96* (5), 1737−1756.

[72] Firnau, G.; Chirakal, R.; Sood, S.; Garnett, S., Aromatic Fluorination with Xenon Difluoride: L-3,4-Dihydroxy-6-fluoro-phenylalanine. *Can. J. Chem.* **1980,** *58* (14), 1449−1450.

[73] Firnau, G.; Chirakal, R.; Garnett, E. S., Aromatic Radiofluorination with [^{18}F]Fluorine Gas: 6-[^{18}F]Fluoro-$_{L}$-Dopa. *J. Nucl. Med.* **1984,** *25* (11), 1228−1233.

[74] Adam, M. J.; Ruth, T. J.; Grierson, J. R.; Abeysekera, B.; Pate, B. D., Routine Synthesis of $_{L}$-[^{18}F]6-Fluorodopa with Fluorine-18 Acetyl Hypofluorite. *J. Nucl. Med.* **1986,** *27* (9), 1462−1466.

[75] Adam, M. J.; Grierson, J. R.; Ruth, T. J.; Jivan, S., Reaction of ^{18}F Acetyl Hypofluorite with Derivatives of Dihydroxyphenylalanine: Synthesis of $_{L}$-[^{18}F]-6-Fluorodopa. *Appl. Radiat. Isot.* **1986,** *37* (8), 877−882.

[76] Adam, M. J.; Jivan, S., Synthesis and Purification of $_{L}$-6-[^{18}F]Fluorodopa. *Int. J. Radiat. Appl. Instrum. A.* **1988,** *39* (12), 1203−1206.

[77] Luxen, A.; Perlmutter, M.; Bida, G. T.; Moffaert, G. V.; Cook, J. S.; Satyamurthy, N.; Phelps, M. E.; Barrio, J. R., Remote, Semiautomated Production of 6-[^{18}F]Fluoro-$_{L}$-dopa for Human Studies with PET. *Int. J. Radiat. Appl. Instrum. A.* **1990,** *41* (3), 275−281.

[78] de Vries, E. F. J.; Luurtsema, G.; Brüssermann, M.; Elsinga, P. H.; Vaalburg, W., Fully Automated Synthesis Module for the High Yield One-pot Preparation of 6-[^{18}F]Fluoro-$_{L}$-DOPA. *Appl. Radiat. Isot.* **1999,** *51* (4), 389−394.

[79] Furuya, T.; Strom, A. E.; Ritter, T., Silver-Mediated Fluorination of Functionalized Aryl Stannanes. *J. Am. Chem. Soc.* **2009,** *131* (5), 1662−1663.

[80] Furuya, T.; Ritter, T., Fluorination of Boronic Acids Mediated by Silver(I) Triflate. *Org. Lett.* **2009,** *11* (13), 2860−2863.

[81] Bergman, J.; Solin, O., Fluorine-18-Labeled Fluorine Gas for Synthesis of Tracer Molecules. *Nucl. Med. Biol.* **1997,** *24* (7), 677−683.

[82] Stenhagen, I. S. R.; Kirjavainen, A. K.; Forsback, S. J.; Jørgensen, C. G.; Robins, E. G.; Luthra, S. K.; Solin, O.; Gouverneur, V., [^{18}F]Fluorination of an Arylboronic Ester Using [^{18}F]Selectfluor bis(triflate): Application to 6-[^{18}F]Fluoro-l-DOPA. *Chem. Commun.* **2013,** *49* (14), 1386−1388.

[83] Krzyczmonik, A.; Keller, T.; López-Picón, F. R.; Forsback, S.; Kirjavainen, A. K.; Takkinen, J. S.; Wasilewska, A.; Scheinin, M.; Haaparanta-Solin, M.; Sączewski, F.; Solin, O., Radiosynthesis and Preclinical Evaluation of an α_{2A}-Adrenoceptor Tracer Candidate, 6-[^{18}F]Fluoro-marsanidine. *Mol. Imaging Biol.* **2019,** *21* (5), 879−887.

[84] Irie, T.; Fukushi, K.; Inoue, O.; Yamasaki, T.; Ido, T.; Nozaki, T., Preparation of ^{18}F-Labeled 6- and 2-Fluoro-9-benzylpurine as a Potential Brain-Scanning Agent. *Int. J. Appl. Radiat. Isot.* **1982,** *33* (8), 633−636.

[85] Lemaire, C.; Guillaume, M.; Christiaens, L.; Palmer, A. J.; Cantineau, R., A New Route for the Synthesis of [^{18}F]Fluoroaromatic Substituted Amino Acids: No Carrier Added $_{L}$-*p*-[^{18}F]Fluorophenylalanine. *Int. J. Radiat. Appl. Instrum. A* **1987,** *38* (12), 1033−1038.

[86] Seimbille, Y.; Phelps, M. E.; Czernin, J.; Silverman, D. H. S., Fluorine-18 Labeling of 6,7-Disubstituted Anilinoquinazoline Derivatives for Positron Emission Tomography (PET) Imaging of Tyrosine Kinase Receptors: Synthesis of ^{18}F-Iressa and Related Molecular Probes. *J Labelled Comp. Radiopharm.* **2005,** *48* (11), 829−843.

[87] Hashizume, K.; Tamakawa, H.; Hashimoto, N.; Miyake, Y., Single-Step Synthesis of [^{18}F]Haloperidol from the Chloro-precursor and Its Applications in PET Imaging of a Cat's Brain. *Appl. Radiat. Isot.* **1997,** *48* (9), 1179−1185.

[88] Nozaki, T.; Tanaka, Y., The Preparation of F18-Labelled Aryl Fluorides. *Int. J. Appl. Radiat. Isot.* **1967,** *18* (2), 111−119.

[89] Knöchel, A.; Zwernemann, O., Aromatic n.c.a. Labelling with ^{18}F- by Modified Balz-Schiemann-Decomposition. *Int. J. Radiat. Appl. Instrum. A* **1991,** *42* (11), 1077−1080.

[90] Knöchel, A.; Zwernemann, O., Development of a No-Carrier-Added Method for ^{18}F-Labelling of Aromatic Compounds by Fluorodediazonation. *J. Labelled Comp. Radiopharm.* **1996,** *38* (4), 325−336.

[91] Tewson, T. J.; Welch, M. J., Preparation of Fluorine-18 Aryl Fluorides: Piperidyl Triazenes as a Source of Diazonium Salts. *J. Chem. Soc., Chem. Commun.* **1979,** (24), 1149−1150.

[92] Pages, T.; Langlois, B. R., Fluorination of Aromatic Compounds from 1-Aryl-3,3-dimethyltriazenes and Fluoride Anions in Acidic Medium: 1. A Model for ^{18}F Labelling. *J. Fluor. Chem.* **2001,** *107* (2), 321−327.

[93] (a) Mu, L.; Fischer, C. R.; Holland, J. P.; Becaud, J.; Schubiger, P. A.; Schibli, R.; Ametamey, S. M.; Graham, K.; Stellfeld, T.; Dinkelborg, L. M.; Lehmann, L., ^{18}F-

Radiolabeling of Aromatic Compounds Using Triarylsulfonium Salts. *Eur. J. Org. Chem.* **2012,** *2012* (5), 889−892. (b) Sander, K.; Gendron, T.; Yiannaki, E.; Cybulska, K.; Kalber, T. L.; Lythgoe, M. F.; Årstad, E., Sulfonium Salts as Leaving Groups for Aromatic Labelling of Drug-like Small Molecules with Fluorine-18. *Sci. Rep.* **2015,** *5* (1), 9941.

[94] Narayanam, M. K.; Ma, G.; Champagne, P. A.; Houk, K. N.; Murphy, J. M., Nucleophilic ^{18}F-Fluorination of Anilines via N-Arylsydnone Intermediates. *Synlett* **2018,** *29* (9), 1131−1135.

[95] Pike, V. W.; Aigbirhio, F. I., Reactions of Cyclotron-Produced [^{18}F]Fluoride with Diaryliodonium Salts—a Novel Single-Step Route to No-Carrier-Added [^{18}F]Fluoroarenes. *J. Chem. Soc., Chem. Commun.* **1995,** (21), 2215−2216.

[96] Shah, A.; W. Pike, V.; A. Widdowson, D., The Synthesis of [^{18}F]Fluoroarenes from the Reaction of Cyclotron-Produced [^{18}F]Fluoride Ion with Diaryliodonium Salts. *J. Chem. Soc., Perkin Trans. 1* **1998,** (13), 2043−2046.

[97] Cardinale, J.; Ermert, J.; Humpert, S.; Coenen, H. H., Iodonium Ylides for One-Step, No-Carrier-Added Radiofluorination of Electron Rich Arenes, Exemplified with 4-(([^{18}F]Fluorophenoxy)-phenylmethyl)piperidine NET and SERT Ligands. *RSC Adv.* **2014,** *4* (33), 17293−17299.

[98] Kwon, Y.-D.; Son, J.; Chun, J.-H., Catalyst-Free Aromatic Radiofluorination via Oxidized Iodoarene Precursors. *Org. Lett.* **2018,** *20* (24), 7902−7906.

[99] Ross, T. L.; Ermert, J.; Hocke, C.; Coenen, H. H., Nucleophilic 18F-Fluorination of Heteroaromatic Iodonium Salts with No-Carrier-Added [^{18}F]Fluoride. *J. Am. Chem. Soc.* **2007,** *129* (25), 8018−8025.

[100] Ichiishi, N.; Brooks, A. F.; Topczewski, J. J.; Rodnick, M. E.; Sanford, M. S.; Scott, P. J. H., Copper-Catalyzed [18F]Fluorination of (Mesityl)(aryl)iodonium Salts. *Org. Lett.* **2014,** *16* (12), 3224−3227.

[101] McCammant, M. S.; Thompson, S.; Brooks, A. F.; Krska, S. W.; Scott, P. J. H.; Sanford, M. S., Cu-Mediated C–H 18F-Fluorination of Electron-Rich (Hetero)arenes. *Org. Lett.* **2017,** *19* (14), 3939−3942.

[102] Rotstein, B. H.; Stephenson, N. A.; Vasdev, N.; Liang, S. H., Spirocyclic hypervalent iodine(III)-mediated radiofluorination of non-activated and hindered aromatics. *Nat. Commun.* **2014,** *5* (1), 4365.

[103] Neumann, C. N.; Hooker, J. M.; Ritter, T., Concerted Nucleophilic Aromatic Substitution with $^{19}F^-$ and $^{18}F^-$. *Nature* **2016,** *534* (7607), 369−373.

[104] Lyons, T. W.; Sanford, M. S., Palladium-catalyzed ligand-directed C-H functionalization reactions. *Chem. Rev.* **2010,** *110* (2), 1147−1169.

[105] Lee, E.; Kamlet, A. S.; Powers, D. C.; Neumann, C. N.; Boursalian, G. B.; Furuya, T.; Choi, D. C.; Hooker, J. M.; Ritter, T., A Fluoride-Derived Electrophilic Late-Stage Fluorination Reagent for PET Imaging. *Science* **2011,** *334* (6056), 639−642.

[106] Lee, E.; Hooker, J. M.; Ritter, T., Nickel-Mediated Oxidative Fluorination for PET with Aqueous [^{18}F] Fluoride. *J. Am. Chem. Soc.* **2012,** *134* (42), 17456−17458.

[107] Kamlet, A. S.; Neumann, C. N.; Lee, E.; Carlin, S. M.; Moseley, C. K.; Stephenson, N.; Hooker, J. M.; Ritter, T., Application of Palladium-Mediated 18F-Fluorination to PET Radiotracer Development: Overcoming Hurdles to Translation. *PLOS ONE* **2013,** *8* (3), e59187.

[108] Hoover, A. J.; Lazari, M.; Ren, H.; Narayanam, M. K.; Murphy, J. M.; van Dam, R. M.; Hooker, J. M.; Ritter, T., A Transmetalation Reaction Enables the Synthesis of [^{18}F]5-Fluorouracil from [^{18}F]Fluoride for Human PET Imaging. *Organometallics* **2016,** *35* (7), 1008−1014.

[109] Casitas, A.; Canta, M.; Solà, M.; Costas, M.; Ribas, X., Nucleophilic Aryl Fluorination and Aryl Halide Exchange Mediated by a Cu^{I}/Cu^{III} Catalytic Cycle. *J. Am. Chem. Soc.* **2011,** *133* (48), 19386−19392.

[110] Yao, B.; Wang, Z.-L.; Zhang, H.; Wang, D.-X.; Zhao, L.; Wang, M.-X., Cu(ClO4)2-Mediated Arene C–H Bond Halogenations of Azacalixaromatics Using Alkali Metal Halides as Halogen Sources. *J. Org. Chem.* **2012,** *77* (7), 3336−3340.

[111] Fier, P. S.; Luo, J.; Hartwig, J. F., Copper-Mediated Fluorination of Arylboronate Esters. Identification of a Copper(III) Fluoride Complex. *J. Am. Chem. Soc.* **2013,** *135* (7), 2552−2559.

[112] Ye, Y.; Schimler, S. D.; Hanley, P. S.; Sanford, M. S., $Cu(OTf)_2$-Mediated Fluorination of Aryltrifluoroborates with Potassium Fluoride. *J. Am. Chem. Soc.* **2013,** *135* (44), 16292−16295.

[113] Taylor, N. J. Copper-Mediated Nucleophilic ^{18}F-Radiolabelling of (Hetero)Arenes for Applications in Positron Emission Tomography. University of Oxford, 2017.

[114] Tredwell, M.; Preshlock, S. M.; Taylor, N. J.; Gruber, S.; Huiban, M.; Passchier, J.; Mercier, J.; Génicot, C.; Gouverneur, V., A general copper-mediated nucleophilic 18F fluorination of arenes. *Angew. Chem. Int. Ed.* **2014,** *53* (30), 7751−7755.

[115] Mossine, A. V.; Brooks, A. F.; Makaravage, K. J.; Miller, J. M.; Ichiishi, N.; Sanford, M. S.; Scott, P. J. H., Synthesis of [^{18}F]Arenes via the Copper-Mediated [^{18}F]Fluorination of Boronic Acids. *Org. Lett*, **2015,** *17* (23), 5780−5783.

[116] Makaravage, K. J.; Brooks, A. F.; Mossine, A. V.; Sanford, M. S.; Scott, P. J. H., Copper-Mediated Radiofluorination of Arylstannanes with [^{18}F]KF. *Org. Lett.* **2016,** *18* (20), 5440−5443.

[117] Taylor, N. J.; Emer, E.; Preshlock, S.; Schedler, M.; Tredwell, M.; Verhoog, S.; Mercier, J.; Genicot, C.; Gouverneur, V., Derisking the Cu-Mediated 18F-Fluorination of

Heterocyclic Positron Emission Tomography Radioligands. *J. Am. Chem. Soc.* **2017,** *139* (24), 8267−8276.

[118] Chen, W.; Huang, Z.; Tay Nicholas, E. S.; Giglio, B.; Wang, M.; Wang, H.; Wu, Z.; Nicewicz David, A.; Li, Z., Direct arene C–H fluorination with $^{18}F^-$ via organic photoredox catalysis. *Science* **2019,** *364* (6446), 1170−1174.

[119] Tay, N. E. S.; Chen, W.; Levens, A.; Pistritto, V. A.; Huang, Z.; Wu, Z.; Li, Z.; Nicewicz, D. A., 19F- and 18F-arene deoxyfluorination via organic photoredox-catalysed polarity-reversed nucleophilic aromatic substitution. *Nat. Catal.* **2020,** *3* (9), 734−742.

[120] Wilson, T. C.; Xavier, M.-A.; Knight, J.; Verhoog, S.; Torres, J. B.; Mosley, M.; Hopkins, S. L.; Wallington, S.; Allen, P. D.; Kersemans, V.; Hueting, R.; Smart, S.; Gouverneur, V.; Cornelissen, B., PET Imaging of PARP Expression Using [^{18}F]Olaparib. *J. Nucl. Med.* **2019**, *60* (4), 504–510.

[121] Guibbal, F.; Isenegger, P. G.; Wilson, T. C.; Pacelli, A.; Mahaut, D.; Sap, J. B. I.; Taylor, N. J.; Verhoog, S.; Preshlock, S.; Hueting, R.; Cornelissen, B.; Gouverneur, V., Manual and Automated Cu-Mediated Radiosynthesis of the PARP Inhibitor [^{18}F]Olaparib. *Nat. Protoc.* **2020**, *15* (4), 1525–1541.

[122] Bowden, G. D.; Stotz, S.; Kinzler, J.; Geibel, C.; Laemmerhofer, M.; Pichler, B. J.; Maurer, A. DoE Optimization Empowers the Automated Preparation of Enantiomerically Pure [^{18}F]Talazoparib and Its In Vivo Evaluation as a PARP Radiotracer. *ChemRxiv* **2021**. This content is a preprint and has not been peer-reviewed.

[123] Zhou, D.; Chen, H.; Mpoy, C.; Afrin, S.; Rogers, B. E.; Garbow, J. R.; Katzenellenbogen, J. A.; Xu, J., Radiosynthesis and Evaluation of Talazoparib and Its Derivatives as PARP-1-Targeting Agents. *Biomedicines* **2021,** *9* (5), 565.

[124] Shroff, R. T.; Hendifar, A.; McWilliams, R. R.; Geva, R.; Epelbaum, R.; Rolfe, L.; Goble, S.; Lin, K. K.; Biankin, A. V.; Giordano, H.; Vonderheide, R. H.; Domchek, S. M.,

Rucaparib Monotherapy in Patients With Pancreatic Cancer and a Known Deleterious BRCA Mutation. *JCO Precis. Oncol.* **2018**, *2*, 1–15.

[125] Zhou, D.; Xu, J.; Mpoy, C.; Chu, W.; Kim, S. H.; Li, H.; Rogers, B. E.; Katzenellenbogen, J. A., Preliminary Evaluation of a Novel ^{18}F-Labeled PARP-1 Ligand for PET Imaging of PARP-1 Expression in Prostate Cancer. *Nucl. Med. Biol.* **2018**, *66*, 26–31.

[126] (a) Zhou, D.; Chu, W.; Xu, J.; Jones, L. A.; Peng, X.; Li, S.; Chen, D. L.; Mach, R. H., Synthesis, [^{18}F]Radiolabeling, and Evaluation of Poly(ADP-ribose) Polymerase-1 (PARP-1) Inhibitors for *In Vivo* Imaging of PARP-1 Using Positron Emission Tomography. *Bioorg. Med. Chem.* **2014**, *22* (5), 1700–1707. (b) Edmonds, C. E.; Makvandi, M.; Lieberman, B. P.; Xu, K.; Zeng, C.; Li, S.; Hou, C.; Lee, H.; Greenberg, R. A.; Mankoff, D. A.; Mach, R. H., [^{18}F]FluorThanatrace Uptake as a Marker of PARP1 Expression and Activity in Breast Cancer. *Am. J. Nucl. Med. Mol. Imaging* **2016**, *6* (1), 94–101. (c) Chen, D.; Dyroff, S.; Michel, L.; Wang-Gillam, A.; Tan, B.; Phillips, S.; Bognar, C.; Chu, W.; Zhou, D.; Mach, R.; Brooks, F.; Laforest, R., First-in-human Studies Characterizing a Poly(ADP-ribose) Polymerase (PARP) Targeted Tracer, ^{18}F-FluorThanatrace (^{18}F-FTT) for Cancer Imaging. *J. Nucl. Med.* **2016**, *57* (supplement 2), 582. (d) Pantel, A.; MaKvandi, M.; Doot, R.; Schwartz, L.; Greenberg, R.; Simpkins, F.; Mankoff, D.; Lin, L.; Mach, R., A Pilot Study of a Novel Poly(ADP-ribose) Polymerase-1 (PARP) PET Tracer ([^{18}F]FluorThanatrace) in Patients with Ovarian Carcinoma. *J. Nucl. Med.* **2017**, *58* (supplement 1), 386. (e) Makvandi, M.; Pantel, A.; Schwartz, L.; Schubert, E.; Xu, K.; Hsieh, C.-J.; Hou, C.; Kim, H.; Weng, C.-C.; Winters, H.; Doot, R.; Farwell, M. D.; Pryma, D. A.; Greenberg, R. A.; Mankoff, D. A.; Simpkins, F.; Mach, R. H.; Lin, L. L., A PET Imaging Agent for Evaluating PARP-1 Expression in Ovarian Cancer. *J. Clin. Invest.* **2018**, *128* (5), 2116–2126.

[127] (a) Makvandi, M.; Xu, K.; Lieberman, B. P.; Anderson, R.-C.; Effron, S. S.; Winters, H. D.; Zeng, C.; McDonald, E. S.; Pryma, D. A.; Greenberg, R. A.; Mach, R. H., A Radiotracer

Strategy to Quantify PARP-1 Expression *In Vivo* Provides a Biomarker That Can Enable Patient Selection for PARP Inhibitor Therapy. *Cancer Res.* **2016**, *76* (15),1–9. (b) Riad, A.; Gitto, S. B.; Lee, H.; Winters, H. D.; Martorano, P. M.; Hsieh, C.-J.; Xu, K.; Omran, D. K.; Powell, D. J.; Mach, R. H.; Makvandi, M., PARP Theragnostic Auger Emitters Are Cytotoxic in BRCA Mutant Ovarian Cancer and Viable Tumors from Ovarian Cancer Patients Enable Ex-Vivo Screening of Tumor Response. *Molecules* **2020**, *25* (24), 6029. (c) For radiolabeled rucaparib solely used for therapeutic purpose, see [^{211}At]MM4: Makvandi, M.; Lee, H.; Puentes, L. N.; Reilly, S. W.; Rathi, K. S.; Weng, C.-C.; Chan, H. S.; Hou, C.; Raman, P.; Martinez, D.; Xu, K.; Carlin, S. D.; Greenberg, R. A.; Pawel, B. R.; Mach, R. H.; Maris, J. M.; Pryma, D. A., Targeting PARP-1 with Alpha-Particles Is Potently Cytotoxic to Human Neuroblastoma in Preclinical Models. *Mol. Cancer Ther.* **2019**, *18* (7), 1195–1204.

[128] Chan, C. Y.; Tan, K. V.; Cornelissen, B., PARP Inhibitors in Cancer Diagnosis and Therapy. *Clin. Cancer Res.* **2021**, *27* (6), 1585–1594.

[129] Alluri, S. R.; Riss, P. J., Poly(ADP-ribose) Polymerase in Neurodegeneration: Radiosynthesis and Radioligand Binding in ARC-SWE tg Mice. *ACS Chem. Neurosci.* **2018**, *9* (6), 1259–1263.

[130] Liao, M.; Watkins, S.; Nash, E.; Isaacson, J.; Etter, J.; Beltman, J.; Fan, R.; Shen, L.; Mutlib, A.; Kemeny, V.; Pápai, Z.; van Tilburg, P.; Xiao, J. J., Evaluation of Absorption, Distribution, Metabolism, and Excretion of [^{14}C]Rucaparib, a Poly(ADP-ribose) Polymerase Inhibitor, in Patients with Advanced Solid Tumors. *Invest. New Drugs* **2020**, *38* (3), 765–775.

[131] Webber S. E.; Canan-Koch S. S.; Tikhe J. G.; Thoresen L. H., Tricyclic Inhibitors of Poly(ADP-ribose) Polymerases. U. S. Patent WO 2000042040A1, July 20, 2000.

[132] Canan Koch, S. S.; Thoresen, L. H.; Tikhe, J. G.; Maegley, K. A.; Almassy, R. J.; Li, J.; Yu, X.-H.; Zook, S. E.; Kumpf, R. A.; Zhang, C.; Boritzki, T. J.; Mansour, R. N.; Zhang, K. E.; Ekker, A.; Calabrese, C. R.; Curtin, N. J.; Kyle, S.; Thomas, H. D.; Wang, L.-Z.; Calvert,

A. H.; Golding, B. T.; Griffin, R. J.; Newell, D. R.; Webber, S. E.; Hostomsky, Z., Novel Tricyclic Poly(ADP-ribose) Polymerase-1 Inhibitors with Potent Anticancer Chemopotentiating Activity: Design, Synthesis, and X-ray Cocrystal Structure. *J. Med. Chem.* **2002**, *45* (23), 4961–4974.

[133] (a) Negash, K.; Morton, T.; VanBrocklin, H., [^{18}F] Fluorobenzyltrozamicol: An Efficient Synthetic Approach. *J. Labelled Comp. Radiopharm.* **1997,** *40*, 40–42.

[134] Wilson, A. A.; Dannals, R. F.; Ravert, H. T.; Wagner Jr., H. N., Reductive amination of [^{18}F]fluorobenzaldehydes: Radiosyntheses of [2-^{18}F]- and [4-^{18}F]fluorodexetimides. *J. Labelled Comp. Radiopharm.* **1990,** *28* (10), 1189–1199.

[135] Mishani, E.; McCarthy, T.; Brodbeck, R.; Dence, C.; Krause, J.; Welch, M., Synthesis and evaluation of a fluorine-18 labeled NK-1 antagonist. *J. Labelled Comp. Radiopharm.* **1997,** *40*, 653–655.

[136] Ryu, E. K.; Choe, Y. S.; Park, E. Y.; Paik, J. Y.; Kim, Y. R.; Lee, K. H.; Choi, Y.; Kim, S. E.; Kim, B. T., Synthesis and evaluation of 2-[^{18}F]fluoro-CP-118,954 for the in vivo mapping of acetylcholinesterase. *Nucl. Med. Biol.* **2005,** *32* (2), 185–191.

[137] Feng, Y.; Holte, D.; Zoller, J.; Umemiya, S.; Simke, L. R.; Baran, P. S., Total Synthesis of Verruculogen and Fumitremorgin A Enabled by Ligand-Controlled C–H Borylation. *J. Am. Chem. Soc.* **2015,** *137* (32), 10160–10163.

[138] Almond-Thynne, J.; Blakemore, D. C.; Pryde, D. C.; Spivey, A. C., Site-selective Suzuki–Miyaura coupling of heteroaryl halides – understanding the trends for pharmaceutically important classes. *Chem. Sci.* **2017,** *8* (1), 40–62.

[139] Bailey, P.; Chang, D. K.; Nones, K.; Johns, A. L.; Patch, A.-M.; Gingras, M.-C.; Miller, D. K.; Christ, A. N.; Bruxner, T. J. C.; Quinn, M. C.; Nourse, C.; Murtaugh, L. C.; Harliwong, I.; Idrisoglu, S.; Manning, S.; Nourbakhsh, E.; Wani, S.; Fink, L.; Holmes, O.; Chin, V.; Anderson, M. J.; Kazakoff, S.; Leonard, C.; Newell, F.; Waddell, N.; Wood, S.;

Xu, Q.; Wilson, P. J.; Cloonan, N.; Kassahn, K. S.; Taylor, D.; Quek, K.; Robertson, A.; Pantano, L.; Mincarelli, L.; Sanchez, L. N.; Evers, L.; Wu, J.; Pinese, M.; Cowley, M. J.; Jones, M. D.; Colvin, E. K.; Nagrial, A. M.; Humphrey, E. S.; Chantrill, L. A.; Mawson, A.; Humphris, J.; Chou, A.; Pajic, M.; Scarlett, C. J.; Pinho, A. V.; Giry-Laterriere, M.; Rooman, I.; Samra, J. S.; Kench, J. G.; Lovell, J. A.; Merrett, N. D.; Toon, C. W.; Epari, K.; Nguyen, N. Q.; Barbour, A.; Zeps, N.; Moran-Jones, K.; Jamieson, N. B.; Graham, J. S.; Duthie, F.; Oien, K.; Hair, J.; Grützmann, R.; Maitra, A.; Iacobuzio-Donahue, C. A.; Wolfgang, C. L.; Morgan, R. A.; Lawlor, R. T.; Corbo, V.; Bassi, C.; Rusev, B.; Capelli, P.; Salvia, R.; Tortora, G.; Mukhopadhyay, D.; Petersen, G. M.; Munzy, D. M.; Fisher, W. E.; Karim, S. A.; Eshleman, J. R.; Hruban, R. H.; Pilarsky, C.; Morton, J. P.; Sansom, O. J.; Scarpa, A.; Musgrove, E. A.; Bailey, U.-M. H.; Hofmann, O.; Sutherland, R. L.; Wheeler, D. A.; Gill, A. J.; Gibbs, R. A.; Pearson, J. V.; Waddell, N.; Biankin, A. V.; Grimmond, S. M.; Australian Pancreatic Cancer Genome, I., Genomic Analyses Identify Molecular Subtypes of Pancreatic Cancer. *Nature* **2016,** *531* (7592), 47−52.

[140] Pilarski, R., The Role of BRCA Testing in Hereditary Pancreatic and Prostate Cancer Families. *Am. Soc. Clin. Oncol. Educ. Book* **2019,** (39), 79−86.

[141] Shroff, R. T.; Hendifar, A.; McWilliams, R. R.; Geva, R.; Epelbaum, R.; Rolfe, L.; Goble, S.; Lin, K. K.; Biankin, A. V.; Giordano, H.; Vonderheide, R. H.; Domchek, S. M., Rucaparib Monotherapy in Patients With Pancreatic Cancer and a Known Deleterious BRCA Mutation. *JCO Precis. Oncol.* **2018,** (2), 1−15.

[142] Guibbal, F.; Hopkins, S. L.; Pacelli, A.; Isenegger, P. G.; Mosley, M.; Torres, J. B.; Dias, G. M.; Mahaut, D.; Hueting, R.; Gouverneur, V.; Cornelissen, B., [^{18}F]AZD2461, an Insight on Difference in PARP Binding Profiles for DNA Damage Response PET Imaging. *Mol. Imaging Biol.* **2020**, *22* (5), 1226–1234.

[143] Carney, B.; Kossatz, S.; Lok, B. H.; Schneeberger, V.; Gangangari, K. K.; Pillarsetty, N. V. K.; Weber, W. A.; Rudin, C. M.; Poirier, J. T.; Reiner, T., Target Engagement Imaging of PARP Inhibitors in Small-Cell Lung Cancer. *Nat. Commun.* **2018**, *9* (1), 176.

Chapter 3. Radiosynthesis of ^{123}I-Olaparib and ^{123}I-Rucaparib Analogues for Potential Application in Auger Therapy

3.1 Auger Electrons for Cancer Therapy

3.1.1 The Auger Effect

Auger electrons (AEs) are very low energy electrons that are emitted due to an incident X-ray or during the decay of radionuclides, including gallium-67, technetium-99m, indium-111, iodine-123, iodine-125, platinum-191 and thallium-201. The two main decay modes are the electron capture (EC) and the internal conversion (IC).[1]

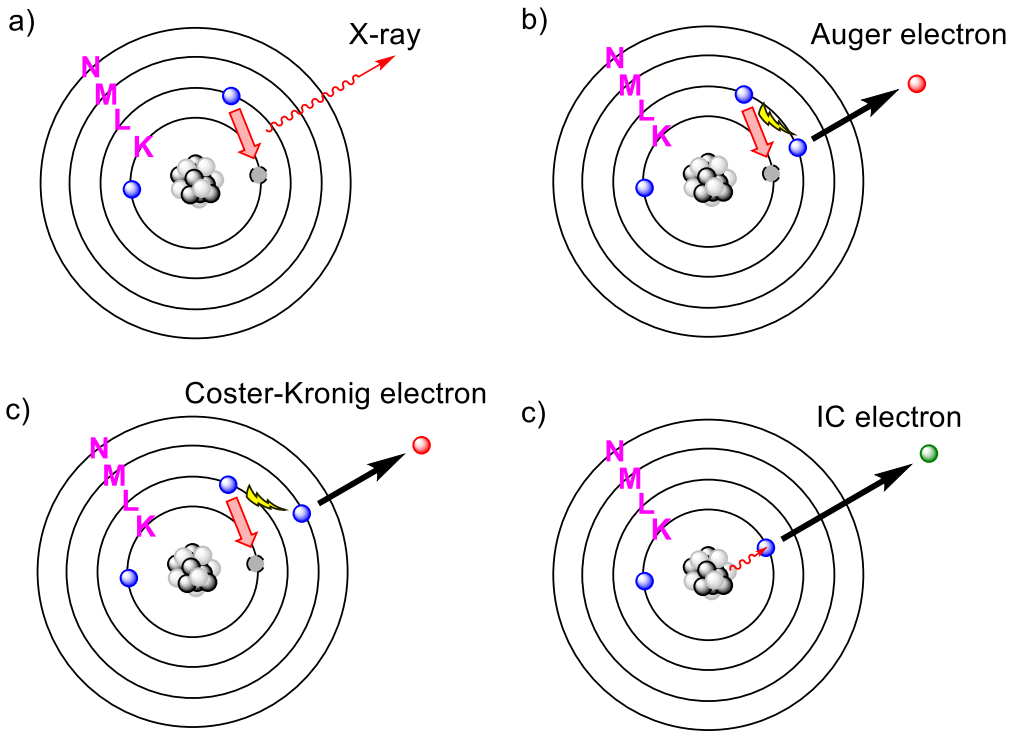

Figure 3.1: a) EC: emission of X-ray due to difference in orbital binding energy. b) EC: emission of an Auger electron: two electron vacancies in the same shell. c) EC: emission of a Coster-Kronig electron: two electron vacancies in different shells. d) IC: emission of an IC electron due to energy transfer during de-excitation of nuclide.

Electron capture occurs when a proton-rich nucleus captures an inner orbital (K) electron to form a neutron, leaving a primary vacancy, which is filled by the downward transition of a higher energy electron from an outer orbital (L).[2] The energy released due to the difference in binding energies between the K and L orbitals results in two possible fates. The first possibility is the emission of an X-ray photon with an energy equal to (E_L – E_K) (Figure 3.1a). The other route is the transfer of energy to another electron with lower binding energy. Upon gaining this energy, the electron will be ejected from the atom. If this ejected electron is from the same

shell (L), it is referred to an Auger Electron (Figure 3.1b). If it originates from an outer shell (M), however, then it is called an Coster-Kronig electron (Figure 3.1c).[3] The resultant outer shell vacancy may trigger further fill-in and ejection of electrons as a cascade process.[4] If this outer vacancy is filled by an electron from the same primary shell and an electron from the same shell is subsequently ejected, the ejected electron is referred to as a Super Coster-Kronig electron.[5] Auger, Coster-Kronig and Super Coster-Kronig electrons are collectively called Auger electrons.

Inner shell vacancies could also be generated from IC where de-excitation of an unstable nuclide transfers sufficient energy to an electron, resulting in its ejection with high kinetic energy from the atom, as a so-called IC electron (Figure 3.1d).[6] The left vacancy may induce a further propagative process.

This whole process, in which elements with high atomic number eject a series of low energy electrons, is referred to as the Auger effect, first described independently by Lise Meitner in 1922 and Pierre Auger in 1923.[7,8]

The majority of AEs (emitted in cascade) have energy lower than 25 keV and travel extremely short distances in tissue (nanometres to micrometres), resulting in high linear energy transfer (LET). This highly localised energy deposition in extremely small volumes, places sensitive cellular targets, such as DNA and cell membranes in immediate vicinity to the decaying radionuclide, thereby providing huge radiotherapeutic potential for the treatment of cancer.

Overall, as the short-range of most AEs leads to very potent clustered damage, efforts have been made to deliver the AE-emitting radionuclide directly to the nucleus, DNA or cell membrane to maximise the cytotoxicity of AEs.

3.1.2 Modes of Cell Death Caused by AEs

DNA is considered the main target of radiation therapy for cancer.[9] AEs can damage DNA both directly and indirectly. The high linear energy transfer radiation delivered by AEs can

directly cause DSBs in DNA or interact with water to generate ROS through radiolysis, inducing DNA damage. The local cross-dose effect of AEs also leads to cell damage. The cross-dose effect is a phenomenon for longer-range particles (up to several millimetres), such as β-particles, where cells distant from the radionuclide may be irradiated. Localised cross-dose effect is observed with AEs. This distant irradiation is mediated by some higher energy AEs and IC electrons.[10] The bystander effect is another common phenomenon in radiation therapy and has been described in various ways, including "indirect effects", "abscopal effects", "clastogenic effects" and more recently "the secretosome".[11] As its name implies, the irradiated cell may release mediators that cause the death of distant non-irradiated cells. It is now known to be communicated in three ways, either by gap-junction intercellular communication,[12] extracellular solubility factors,[13] or through physical signals (i.e., UV photons) from irradiated cells.[14] Lastly, the cell membrane is also an effective target for cytotoxicity from AEs.[15] Pouget and co-workers showed the cytotoxicity of ^{125}I-radiolabelled monoclonal antibodies (^{125}I-mAbs), which target cancer cells, was mainly due to radiation-induced nontargeted effects.[16] Iodine-123 is a radionuclide that emits AEs and has potential to be incorporated into radiopharmaceuticals for cancer treatment. In the next section, we focus on why iodine-123 is favoured, the production of iodine-123 and radioiodination methods to access radiopharmaceuticals.

3.2 Iodine-123

3.2.1 Radioisotopes of Iodine

There are 37 known isotopes of iodine, from iodine-108 to iodine-144; among them iodine-127 is the only stable isotope. Four radioisotopes (iodine-123, iodine-124, iodine-125 and iodine-131) are widely used for medical applications, either for imaging or therapy (Table 3.1). This project focuses on iodine-123, due to its theragnostic application in both SPECT imaging and Auger therapy. Its half-life ($t_{1/2}$ = 13.2 hours) allows for flexible radiosynthesis, delivery

of the radiopharmaceutical from the production facility to the medical facility and also enables the monitoring of longer biological processes. Iodine-123 gradually replaced iodine-131 ($t_{1/2}$ = 8.02 days) for imaging applications, due to its shorter half-life and lower γ-ray energy of 159 keV, which means that patients receive a much lower radiation dose. Although iodine-125 may be "superior" to iodine-123 in the Auger therapy due to its almost double Auger yield (~ 20 electrons) and shorter AE range,[17] the biggest obstacles of iodine-125 is its extremely long half-life of 54.9 days, which renders it unsuitable for clinical exposure and normal tissue dose. In addition, for diagnostic applications, the γ emission for iodine-125 is only 35.5 keV, which is too low for clinical SPECT use.

Radio-isotope	Nuclear reaction	Half-life	Type of decay	Energy (keV)	Imaging application	Therapeutic application
I-123	^{124}Xe(p,pn)^{123}I	13.2 h	Gamma EC/Auger	159 <5	SPECT	Auger electrons
I-124	^{124}Te(p,n)^{124}I	4.2 days	Positron Annihilation radiation	819 β+ (mean) 511 γ	PET	/
I-125	^{124}Xe(n,γ)^{125}I	54.9 days	Gamma EC/Auger	35.5 <5	Preclinical SPECT	Auger electrons
I-131	^{130}Te(n,γ)^{131}I	8.0 days	Gamma β-partical	364 192 (mean)	SPECT	β-particles

Table 3.1: Radioisotopes of iodine used for medical applications.

3.2.1 Production of Iodine-123

Iodine-123, a cyclotron produced radionuclide, is most commonly generated by proton bombardment of enriched xenon-124 (> 99.8%). The intermediate is a short-lived cesium-123 ($t_{1/2}$ = 5.9 minutes) which decays to the next short-lived radionuclide, xenon-123 ($t_{1/2}$ = 2.1 hours), before finally generates iodine-123 (^{124}Xe(p,2n)^{123}Cs:^{123}Xe:^{123}I). The isolation of iodine-123 is achieved by the facile extraction of the very unreactive xenon-123 from the target matrix, which is then allowed to decay to iodine-123 in a separate vessel. Iodine-123 is prepared as iodide, most commonly sodium iodide in solutions of sodium hydroxide (0.01–0.1 M).[18] Iodine-123 has been widely incorporated into radiopharmaceuticals, including *o*-

iodohippurate for renal function imaging, *N*-isopropyl-*p*-iodoamphetamine for cerebral blood-flow imaging, iododeoxyuridine for cancer imaging, and *p*-iodophenylalanine for glioma imaging and therapy.[19]

The iodine-123 incorporated radiopharmaceuticals have been increasingly demanded. Thereby, novel methods have been developed for efficient radioiodination since the early 1980s.

3.2 Radioiodination of (Hetero)arenes

3.2.1 Nucleophilic Aromatic Substitution

Radioiodination via Isotopic/Halogen Exchange

Since all radioiodine isotopes are produced as nucleophilic iodide, nucleophilic substitution of aryl halides was first explored, but under harsh conditions. For instance, *meta*-[^{125}I]iodobenzylguanidine ([^{125}I]MIBG) was prepared via solid state isotopic exchange at high temperature in 1982 (Scheme 3.1).[20]

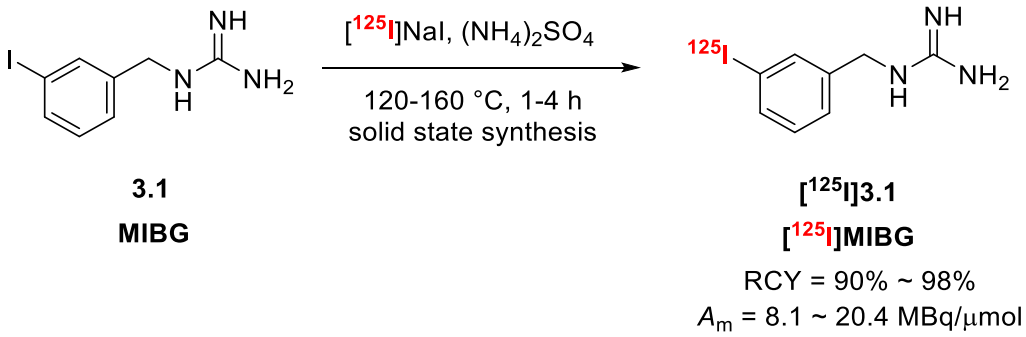

3.1
MIBG

[^{125}I]3.1
[^{125}I]MIBG
RCY = 90% ~ 98%
A_m = 8.1 ~ 20.4 MBq/µmol

Scheme 3.1: Radiosynthesis of [^{125}I]MIBG via isotopic exchange.

The radiolabelled product could not be separated from the unlabelled precursor and therefore, isotopic exchange could not reach A_m in the range of GBq/µmol. In 2014, Brownell reported a halogen exchange (Br/^{123}I) in the presence of $CuSO_4$ and $SnSO_4$, that drastically improved the A_m to 182.8 GBq/ µmol (Scheme 3.2).[21]

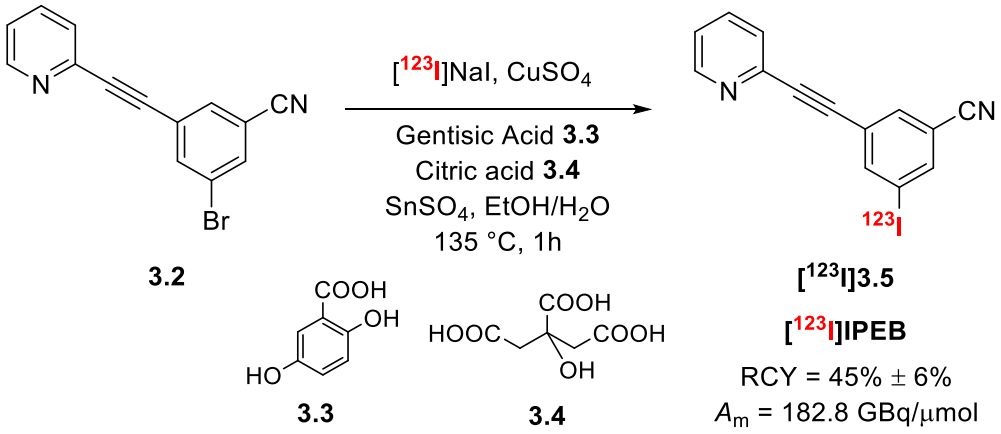

Scheme 3.2: Radiosynthesis of [^{125}I]MIBG via halogen exchange.

Other Leaving Groups

Other common leaving groups that are suitable for S_NAr and enable the incorporation of radiolabelled iodine include triazene derivatives,[22] diazonium salts (which are generally more reactive than their corresponding triazene analogues), as well as iodonium salts.[23-25]

In 2017, Sutherland and co-workers reported a one-pot ^{125}I-iodination of aryl amines, using polymer-supported nitrite to access stable diazonium salts, followed by Sandmeyer reaction under mild conditions.[26] [^{125}I]Iomazenil **[^{125}I]3.8** was synthesised in good RCY and A_m via this method (Scheme 3.3).

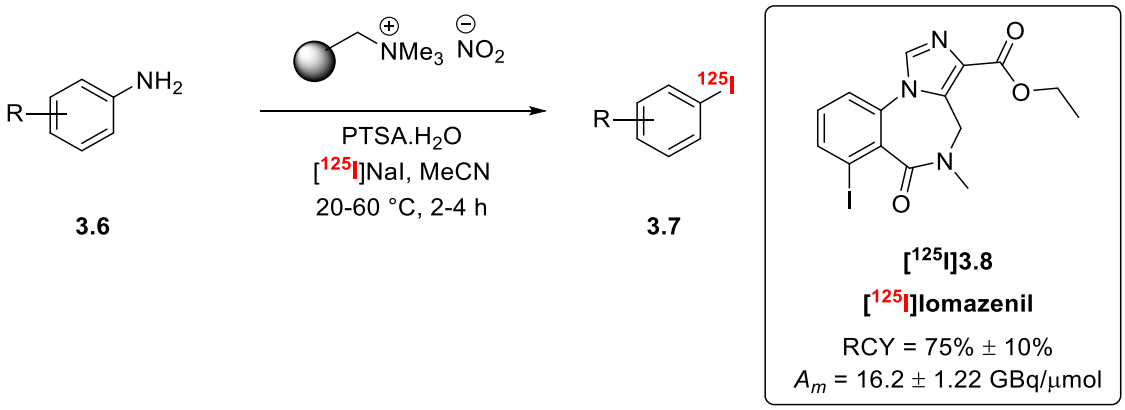

Scheme 3.3: One-pot ^{125}I-iodination of aryl amines.

3.2.2 Electrophilic Aromatic Substitution

Electrophilic aromatic substitution is a popular strategy but requires generation of electrophilic radioactive "I^+" species. It is typically prepared from radiolabelled NaI and strong oxidants, such as hydrogen peroxide and halogenated succinimides.

Direct S_EAr

Direct S_EAr is a common strategy for radioiodination but generally exhibits poor regioselectivity. Nevertheless, with careful choice of starting material, radiopharmaceuticals can be accessible in high RCY and A_m, e.g., [^{125}I]5-HT$_4$R ligand, a serotonin receptor ligand (Scheme 3.3).[27]

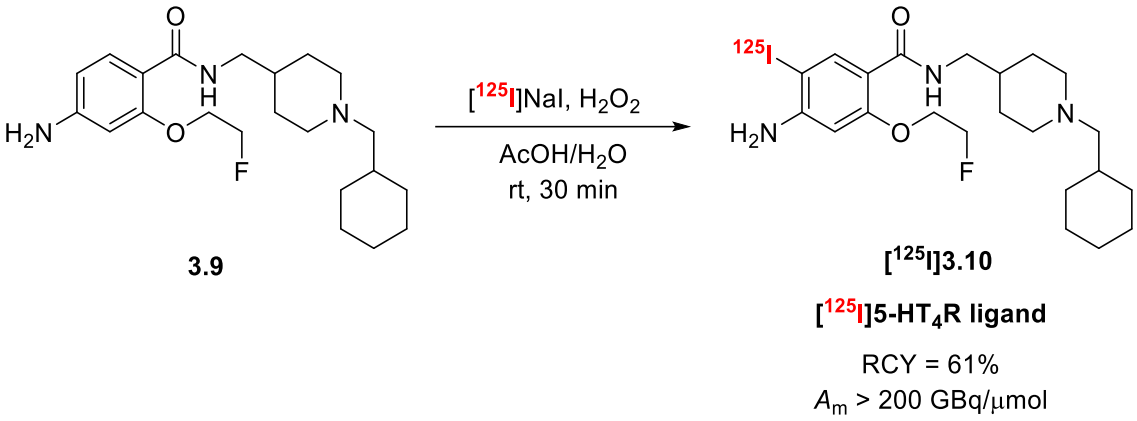

Scheme 3.4: Radiosynthesis of [^{125}I]5-HT$_4$R ligand by direct S_EAr.

***Ipso*-S_EAr**

To overcome the limitation in regioselectivity, silylated,[28] stannylated,[29] and boronated precursors have been developed.[30] [^{131}I]MIBG could be accessed via iododesilylation, with *N*-chlorosuccinimide (NCS) as the oxidant (Scheme 3.4).[28] Compared to the low A_m obtained from isotopic exchange, A_m via this method was much improved, surpassing 37 GBq/μmol (1000 Ci/mmol).

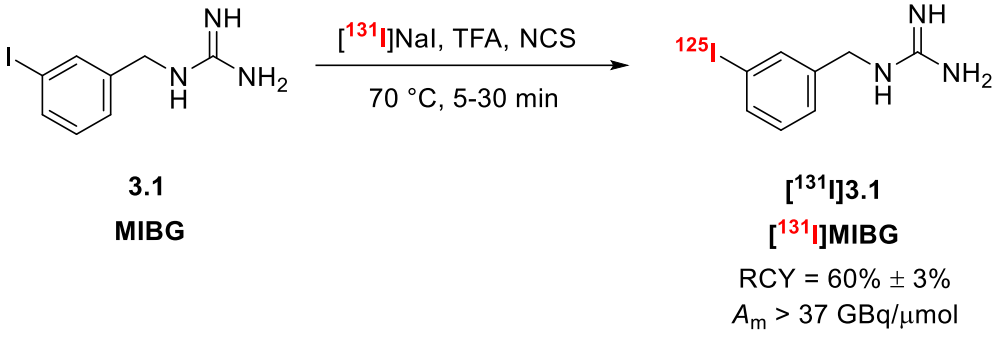

Scheme 3.5: Radiosynthesis of [^{131}I]MIBG via iododesilylation.

3.2.3 Transition-Metal-Mediated Methodologies

Nickel(0)-Mediated Halogen Exchange

One of the main advantages of metal-mediated methodologies is the efficient removal of inorganic metal complexes during purification compared to methods that use stannylated precursors, which present potential toxicity concerns for clinical applications. In 2013, Sutherland et al. reported a nickel(0)-mediated halogen exchange approach to incorporate [$^{123/125}$I]iodide into (hetero)arenes (Scheme 3.6).[31]

The electron-rich Ni(cod)$_2$ underwent oxidative addition with aryl bromide resulting in an Ar-Ni(II)-Br intermediate, followed by a halogen exchange in the presence of [$^{123/125}$I]NaI. Reductive elimination yielded the desired radioiodinated products, including [^{125}I]Iniparib, the non-radioactive isotopologue of which was believed to act as a PARP inhibitor.[32,33] Radioiodination followed by TFA deprotection was performed to deliver isolated 5-[^{123}I]iodo-A-85380, a radioligand used for *in vivo* imaging of neuronal nicotinic acetylcholine receptors, with an AY of 46% and A_m of 37.0 GBq/μmol.[34]

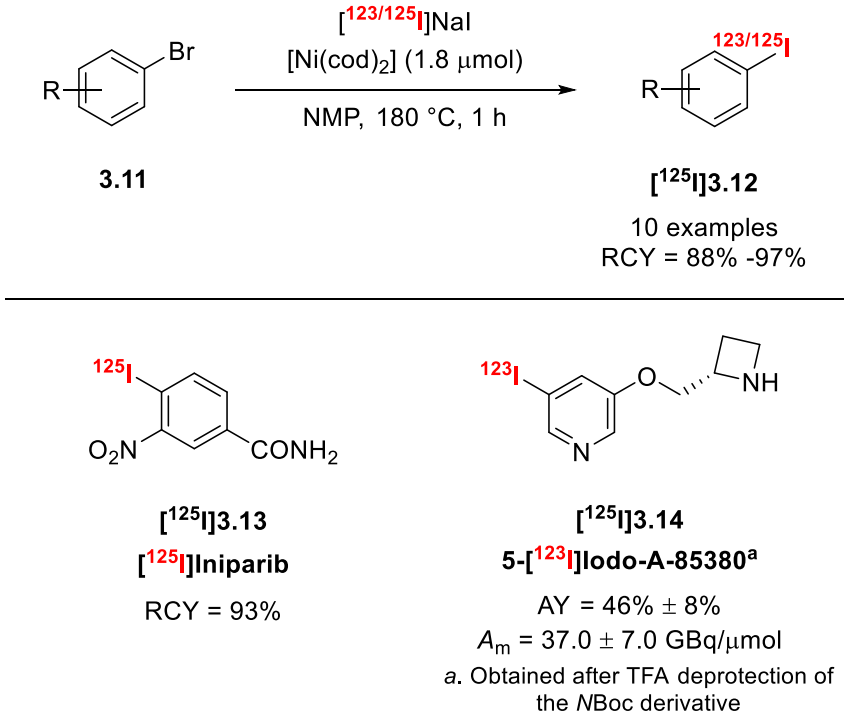

Scheme 3.6: Ni(0)-mediated radioiodination via halogen exchange.

Copper(II)-Mediated Iododeboronation

In 2016, the Gouverneur group reported the first copper(II)-mediated nucleophilic radioiodination of aryl boronic esters and acids, suggested to proceed via a Chan-Lam mechanism. In the presence of catalytic amount of 1,10-phenanthroline and $Cu(OCOCF_3)_2$, iodine-123 was incorporated efficiently with a wide range of substrates, including electron-deficient and electron-rich (hetero)arenes (Scheme 3.7).[35]

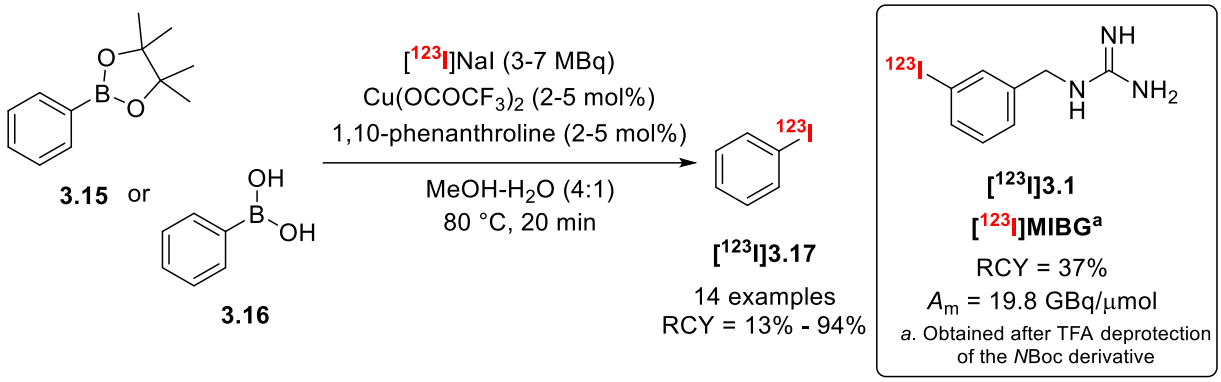

Scheme 3.7: Cu(II)-mediated ^{123}I-iododeboronation of (hetero)arenes.

MIBG was successfully radiolabelled with an RCY of 37% and A_m of 19.8 GBq/μmol. Aligned with the previous work on the Cu(II)-mediated radiofluorination discussed in Chapter 2,[36] this facile transformation demonstrated that diverse radionuclides could be incorporated using the same bench-stable boronic ester precursors and Cu(II) complexes.

Similar approaches were developed by Zhang *et al.* in 2016 and Mach *et al.* in 2018. In the presence of a Cu(I) catalyst, Cu_2O and I-131 the Zhang group demonstrated that the reaction proceeded smoothly at room temperature (Scheme 3.8),[37]

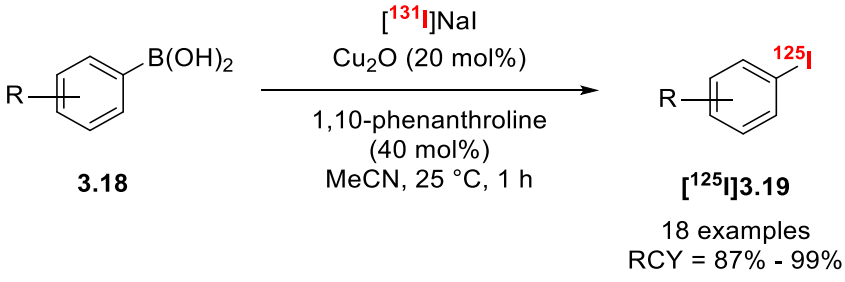

Scheme 3.8: Copper-mediated ^{123}I-iododeboronation by Zhang *et al.*

The Mach group successfully incorporated iodine-125 into two analogues of PARP inhibitors using $Cu(OTf)_2(py)_4$ as the catalyst (Scheme 3.9).[38]

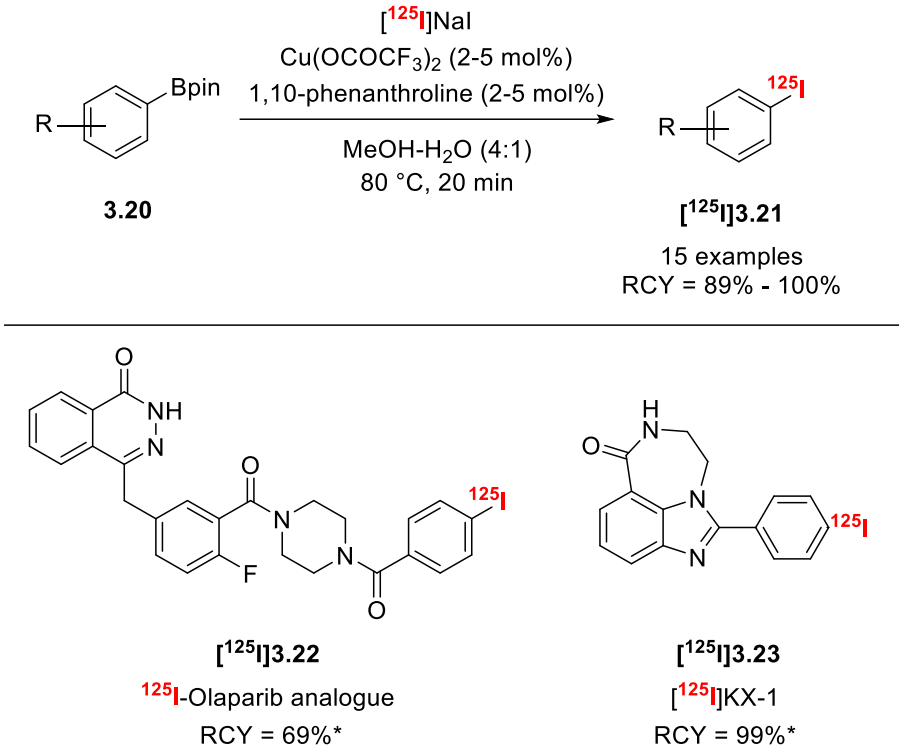

*3,4,7,8-Tetramethyl-1,10-phenanthroline (5 mol %) was added to the reaction.

Scheme 3.9: Copper-mediated ^{123}I-iododeboronation by Mach *et al.*

Gold(I)-Mediated Iododeboronation

In 2018, Sutherland and Lee reported the first gold-catalysed iododeboronation reaction, with the olaparib analogue **3.22** and MIBG **3.1** successfully radiolabelled in 41% RCY and 28% AY respectively (Scheme 3.10).[39] This reaction was performed with the gold(I) catalyst and an electrophilic species of iodine-125, generateed from [^{125}I]NaI and the oxidant *N*-chlorosuccinimide.

Palladium(II)-Mediated C-H Radioiodination

Transition-metal catalysed C-H activation has emerged in the early 2000s, allowing site-selective functionalisation of aromatic C(sp^2)-H bonds in the presence of a directing group.[40,41] In 2018, the Cailly group applied this concept to the field of radioiodination, using *N*-acylsulfonamide as the directing group. The palladacycle **3.27** was formed from stoichiometric

amount of palladium acetate, followed by mixing with *N*-[^{125}I]iodosuccinimide ([^{125}I]NIS) preformed from [^{125}I]NaI and NCS, in the presence of TFA (Scheme 3.11).[42] The pharmaceutical *N*-acylsulfonamide, LY32262 was radiolabelled with an RCY of 42% and A_m of 32.9 GBq/μmol.

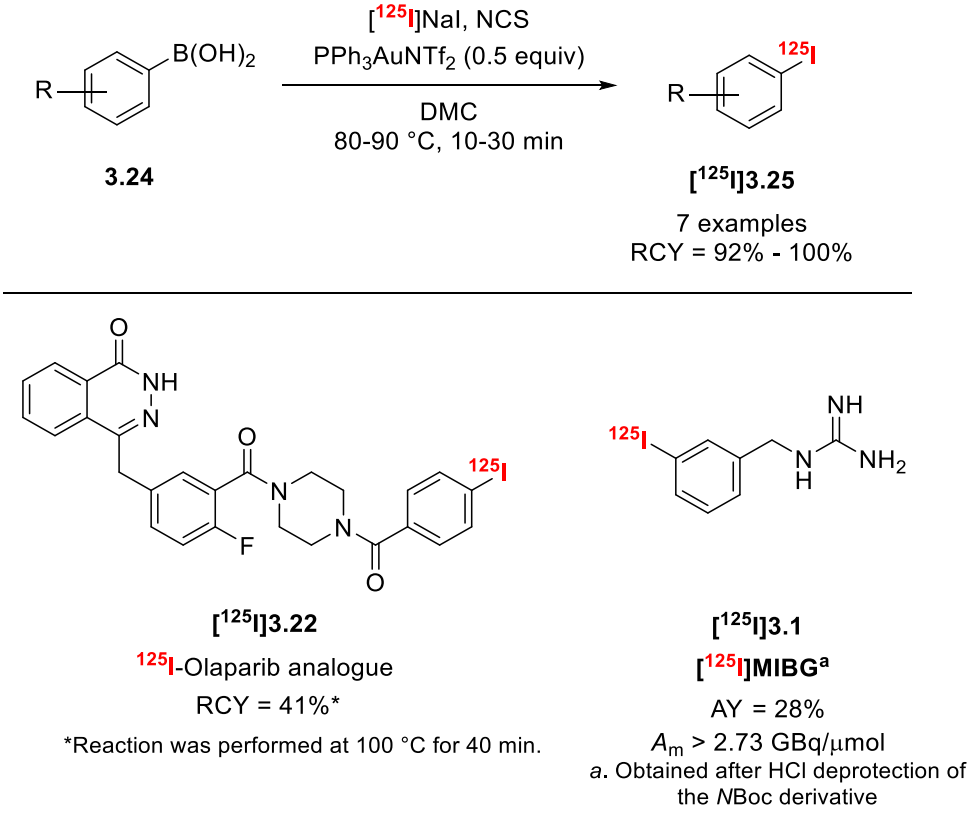

Scheme 3.10: Au(I)-mediated ^{123}I-iododeboronation of arenes.

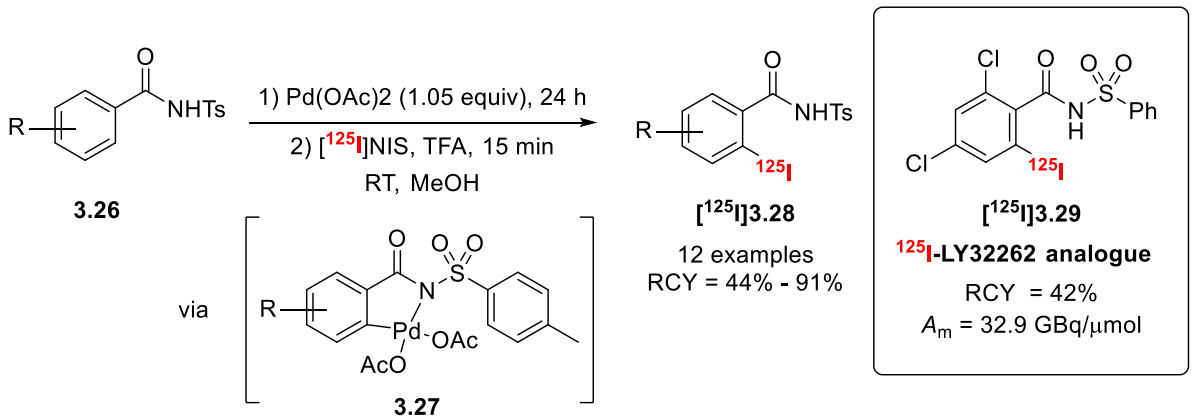

Scheme 3.11: Pd(II)-mediated site-selective C-H radioiodination.

3.3 Synthesis of ^{123}I-Radiolabelled PARP Inhibitors

3.3.1 Radiolabelled PARP Inhibitors for Radionuclide Therapy

PARP inhibitors is a novel class of cancer drugs that bind to PARP enzymes. Roles of PARP enzymes in DNA repair and mechanisms of PARP inhibitors were reviewed in Chapter 1. PARP inhibitors stand out not only as effective treatments for *BRCA1/2*-mutated cancers, but also as potential delivery tools for therapeutic radionuclides which emit high energy particles, including iodine-123 (AEs),[43,44] iodine-125 (AEs),[44] iodine-131 (β-particles),[45] and astatine-131 (α-particles).[46]

Upregulation of PARP1 expression was observed after exposure of PARP inhibitors, suggesting treatment of PARP inhibitors may alter or upregulate DNA damage repair proteins, such as PARP1, thereby increasing uptake of PARP inhibitors.[52] Thus, PARP inhibitor-derived theragnostics may be more selective towards tumour cells. To date, several analogues of the PARP inhibitor-derived therapeutic agents, olaparib and rucaparib, have been radiolabelled, showing efficacy towards brain,[43,45] ovarian,[44] lung,[47] and colon cancer models,[48] and neuroblastoma models,[46] with little off-site toxicity (Figure 3.2).

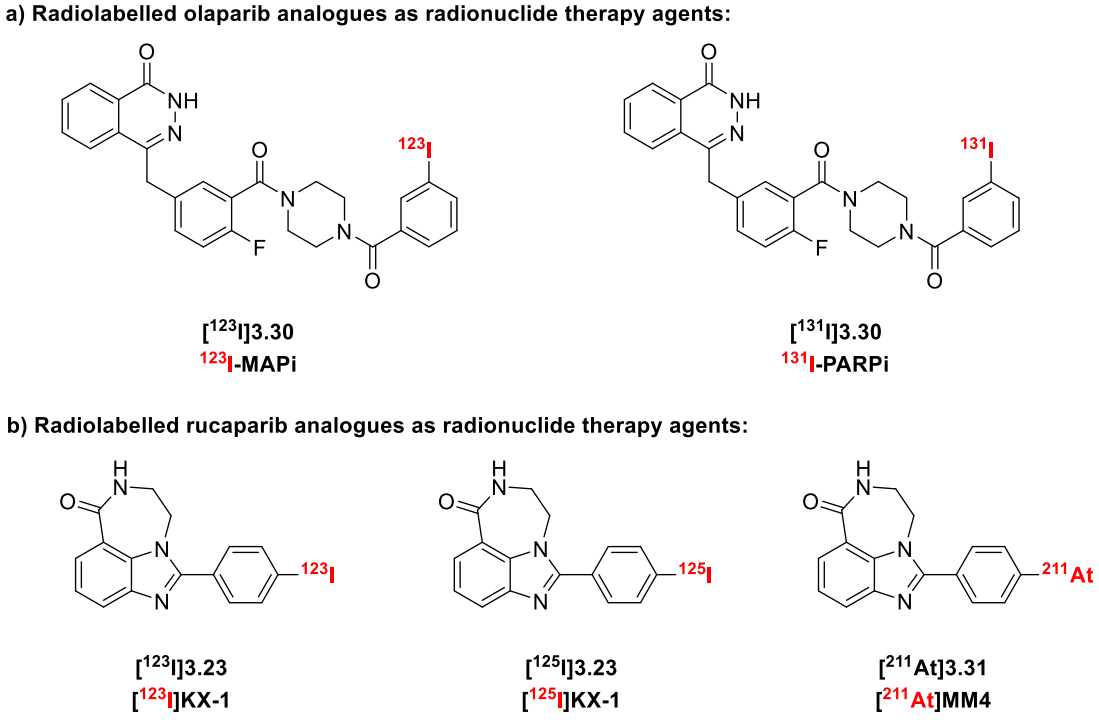

Figure 3.2: Radiolabelled a) olaparib and b) rucaparib analogues in radionuclide therapy.

In particular, iodine-123-containing theragnostic agents, ^{123}I-MAPi and [^{123}I]KX-1 have shown to be promising in the "two-hit" strategy, showing both anti-tumour effects and potential application in PARP1 diagnosis. Given that small structure variations may lead to differences in the IC_{50} of PARP, trapping ability and selective tissue uptake, this project aims to explore the theragnostic potential of two ^{123}I-labelled PARP inhibitors, **[^{123}I]3.31** and **[^{123}I]3.33** derived from olaparib and rucaparib respectively (Scheme 3.12). The iodinated olaparib analogue **3.33** showed similar IC_{50} values toward PARP1 and PARP2 compared to olaparib **3.32** (Table 3.2). This might provide positive evidence of ^{123}I-olaparib analogue **[^{123}I]3.33** acting as a potential theragnostic agent.

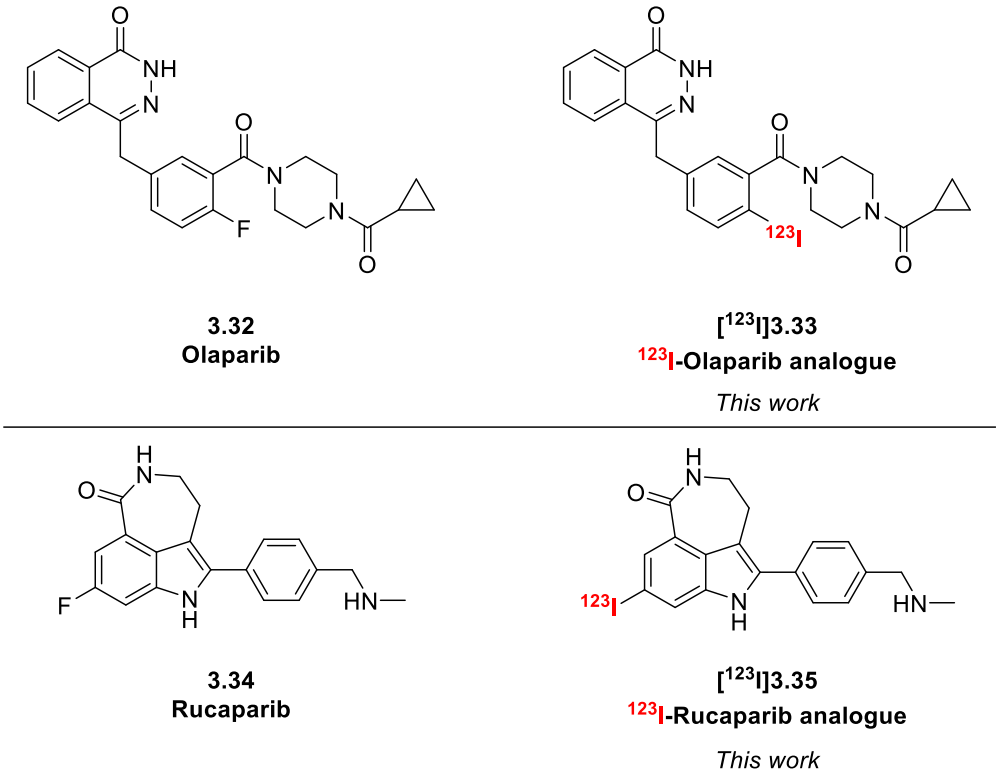

Scheme 3.12: Structures of olaparib and rucaparib and their ^{123}I-labelled analogues in this work.

Compound	PARP1 IC_{50} [nM]	PARP2 IC_{50} [nM]	PARP3 IC_{50} [nM]
Olaparib **3.32**	2.0	0.5	6.0
I-Olaparib analogue **3.33**	2.9	0.6	67.8

Table 3.2: IC_{50} values of olaparib and I-olaparib analogue toward PARP1-3. Experiments were performed with the BPS Bioscience PARP Chemiluminescent Assay Kit 80551-3 (PARP-mediated polyADP-ribosylation of histone). *n* = 3. Data were provided by Dr Florian Guibbal and Dr. Chung Ying Chan (Department of Oncology, University of Oxford).

3.3.2 Project Overview

The Gouverneur group has demonstrated the chemodivergent radiohalogenation of a common aryl boronic ester precursor with either [^{18}F]fluoride or [^{123}I]iodide.[35,36] After developing the radiosynthesis of [^{18}F]olaparib,[49] and [^{18}F]rucaparib in our group,[50] this project aims to employ the same boronic ester precursors to access both iodine-123 labelled olaparib and rucaparib analogues as potential Auger theragnostic agents (Scheme 3.13 and 3.14).

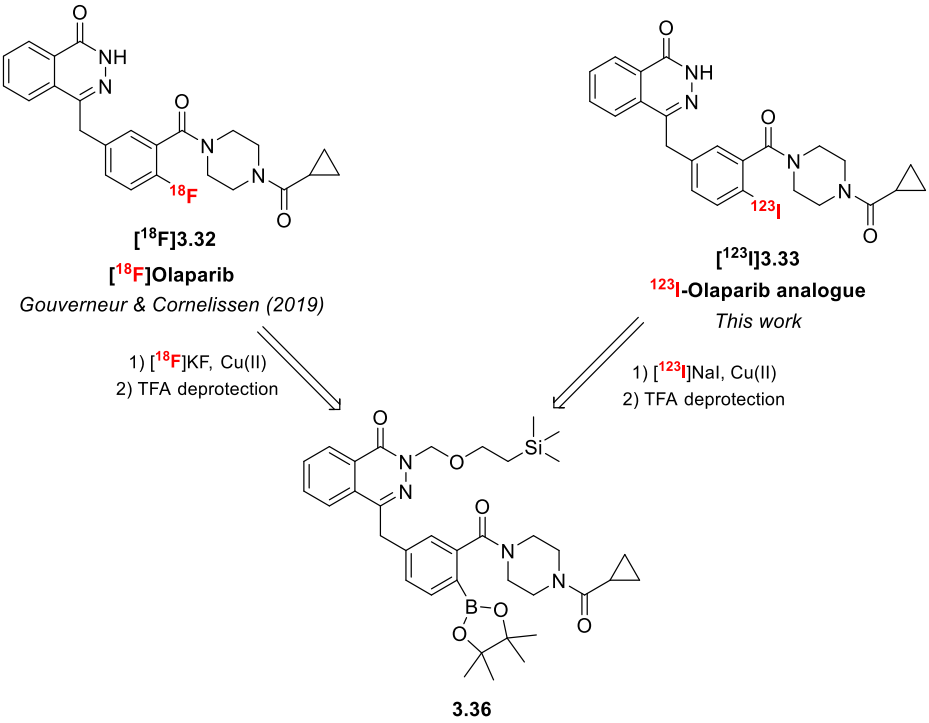

Scheme 3.13: Retro-radiosynthesis of [^{18}F]olaparib and ^{123}I-olaparib analogue **[^{123}I]3.33**.

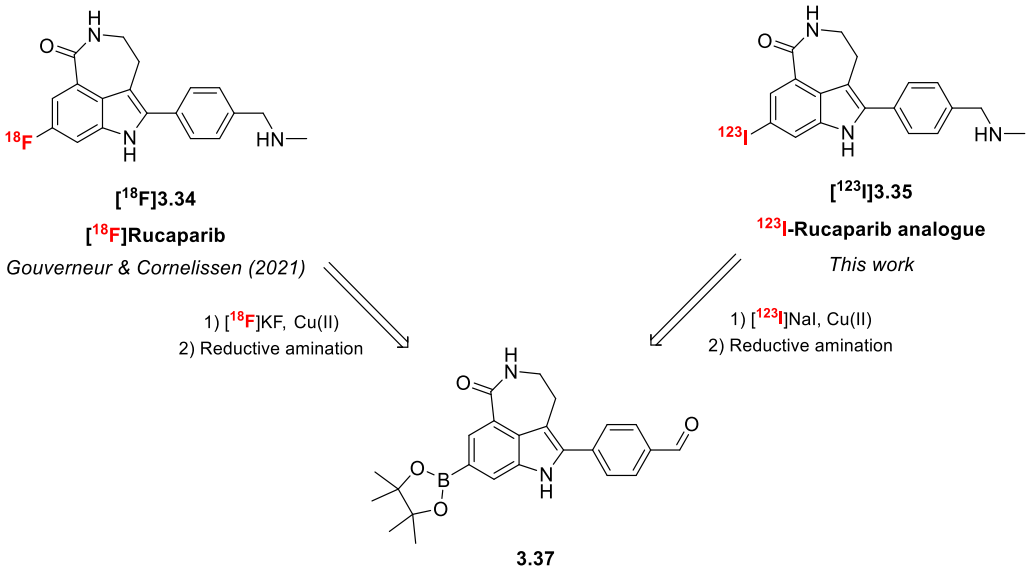

Scheme 3.14: Retro-radiosynthesis of [^{18}F]rucaparib and ^{123}I-rucaparib analogue **[^{123}I]3.35**.

3.3.3 Screening Experiments for ^{123}I-Olaparib Analogue

The unprotected phthalazinone was reported to be problematic when subjected to additive screening experiments of ^{18}F-fluorination with the model aryl boronic ester **3.38** by the Gouverneur group (Scheme 3.15).[51]

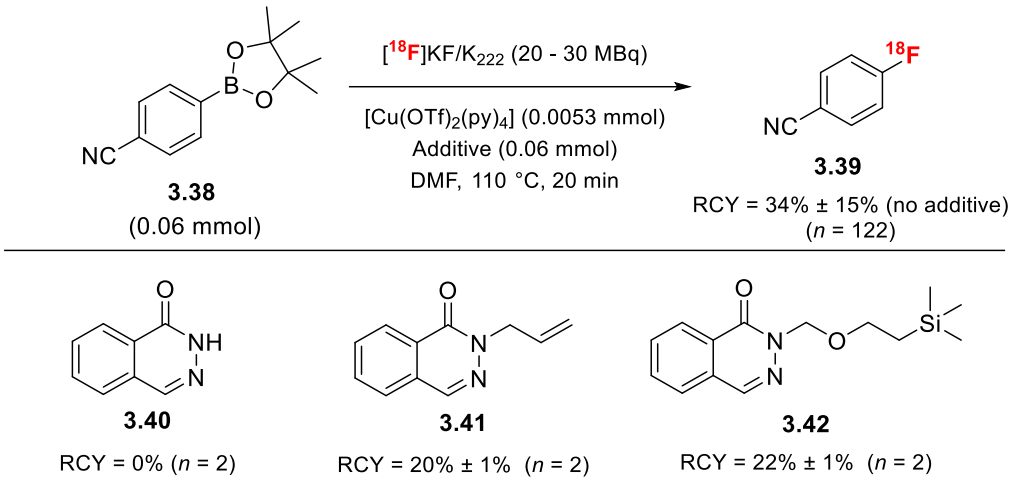

Scheme 3.15: Additive screening experiments of ^{18}F-fluorination for [^{18}F]olaparib.

The unsuccessful ^{18}F-incorporation in the presence of phthalazinone may be due to its role as a potential nucleophile or a ligand that binds with the copper complex. Whilst a free N-H in acyl hydrazide was detrimental, the allyl-protected **3.41** and 2-(trimethylsilyl)ethoxymethyl acetal (SEM)-protected **3.42** were tolerated.

Given that various examples have demonstrated the effective cleavage of the SEM group under acidic conditions, aryl boronic ester **3.36** was chosen and synthesised as the precursor for ^{18}F-fluorination followed by a TFA deprotection to access [^{18}F]olaparib (Scheme 3.16).[49]

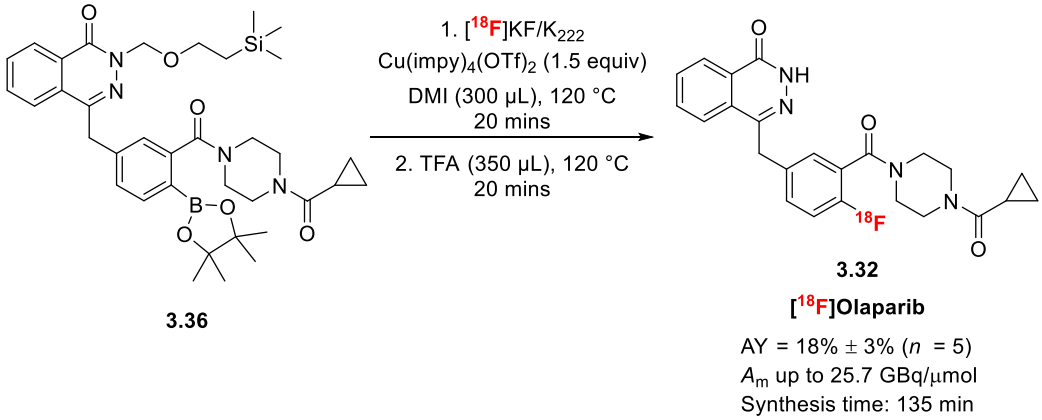

Scheme 3.16: Synthesis of [^{18}F]olaparib from *N*-silanyl–protected boronic pinacol ester precursor.

Additive screening experiments were performed for Cu(II)-mediated ^{123}I-iodination with a model substrate, 2-(4-methoxyphenyl)-4,4,5,5-tetramethyl-1,3,2-dioxaborolane **3.43** (Scheme 3.17).[35] The benchmarking reaction proceeded efficiently via Cu(II)-mediation, with almost quantitive ^{123}I-incorporation (RCY > 95%). The RCY values of **[^{123}I]3.44** were not affected upon spiking with 1 equivalent of phthalazinone **3.40** (RCY = 89% ± 0%), alkylated phthalazinone **3.41** (RCY = 92% ± 2%) or silylated phthalazinone **3.42** (RCY > 95%), contrasting with the results of ^{18}F-fluorination. The tolerance of the free N-H phthalazinone toward radioiodination might due to multiple reasons. Firstly, [^{123}I]NaI is much more soluble in MeOH/H_2O compared with [^{18}F]KF/K_{222}/K_2CO_3 in DMF. Secondly, [^{123}I]iodide is a more competent nucleophile in this specific solvent system. Thirdly, the binding between the copper complex and phthalazinone might affect the reactivity. However, the strength of binding would be expected to depend on the copper oxidation state. The exact mechanism of this transformation is so far unknown with Cu(I), Cu(II) and Cu(III) all possibly involved.

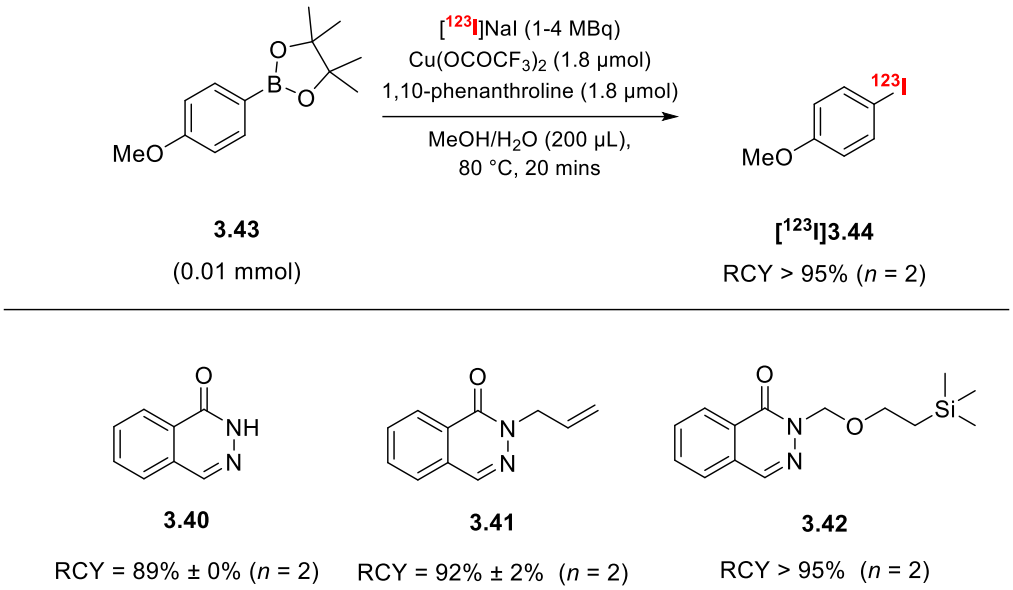

Scheme 3.17: Additive screening experiments informing direct ^{123}I-iodination of unprotected olaparib-motif may be viable.

The success of ^{123}I-iodination with phthalazinone as an additive boded well for a direct ^{123}I-iodination of the olaparib motif **3.45** without the necessity of a post-labelling *N*-deprotection step (Scheme 3.18).

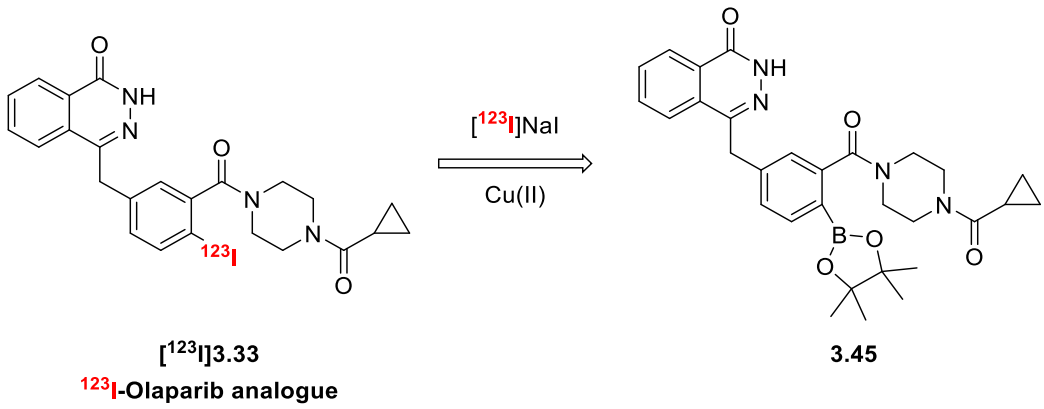

Scheme 3.18: Proposed retro-radiosynthesis for ^{123}I-olaparib analogue.

3.3.4 Synthesis of the Boronic Ester Precursor for ^{123}I-Olaparib Analogue

The synthesis of the boronic ester precursor **3.53** was adapted from a robust protocol developed by the Gouverneur group, starting with a lithium-halogen exchange of commercially available 2-amino-5-bromobenzonitrile **3.46** with *n*-BuLi, quenched by DMF to access the aldehyde **3.47**.[49] A conventional Sandmeyer reaction afforded the bromide **3.48** in 56%, which was then coupled with the commercially available phosphonate **3.49** under Horner-Wadsworth-Emmons conditions, yielding quantitively the alkene **3.50** in an isomeric ratio of 10:1 (E:Z). Hydrolysis under basic conditions converted the pendant nitrile to a carboxylic acid, which was directly reacted with hydrazine *in situ* to furnish phthalazinone **3.51**. The carboxylic acid group in phthalazinone **3.51** was activated by HBTU, followed by coupling with commercially available piperazine **3.52** to afford bromide **3.53**. Miyaura borylation led to the desired boronic ester precursor **3.45** in under 50% due to steric hindrance of the *ortho*-amide. After preparative HPLC purification, **3.45** required for ^{123}I-iodination was obtained with an overall yield of 10% (chemical purity > 95%) over 6 steps from commercially available bromide **3.46** (Scheme 3.19).

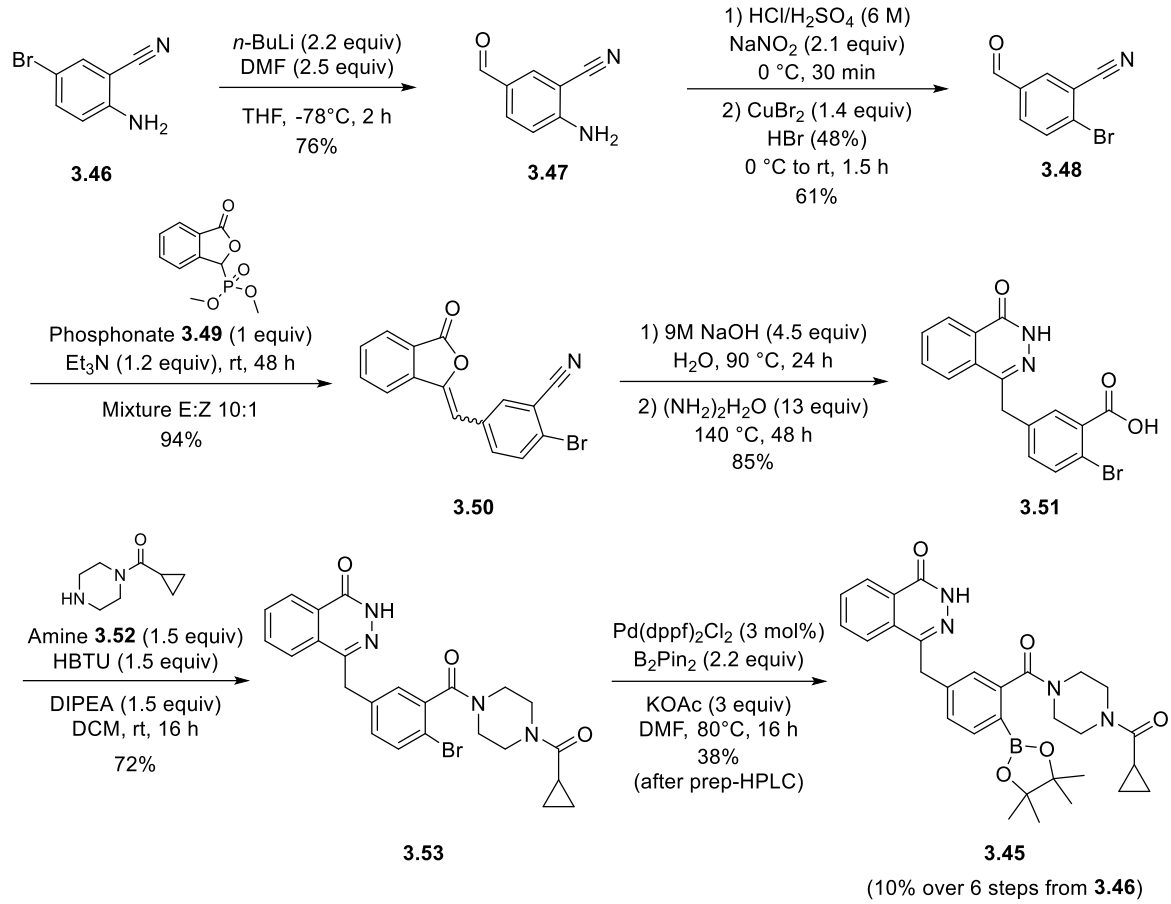

Scheme 3.19: Synthesis of olaparib precursor for ^{123}I-iodination precursor.

The non-radiolabelled iodo-olaparib analogue **3.33** was accessed via Cu(II)-mediated iododeboronation with stoichiometric amount of NaI in 87% yield (see Section 2.4.4). This compound was subsequently used as a reference for the radiolabelling experiments (Scheme 3.20).

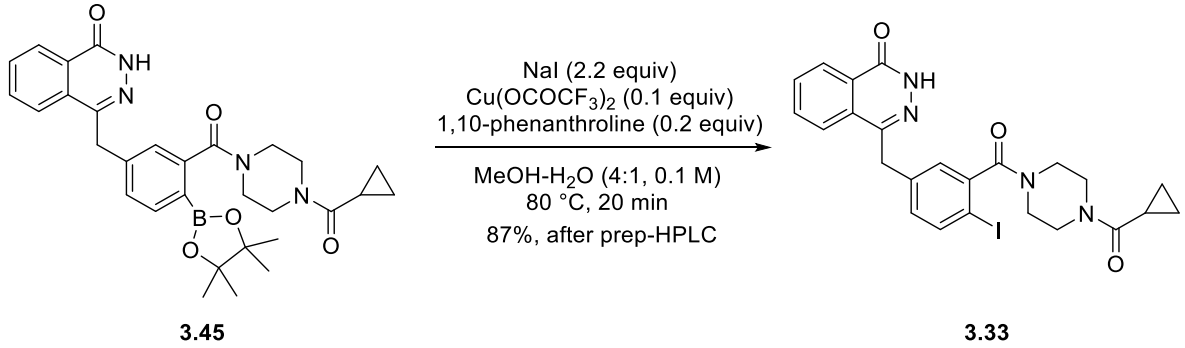

Scheme 3.20: Synthesis of olaparib reference **3.33** via Cu(II)-mediated iododeboronation.

3.3.5 Radiosynthesis of ^{123}I-Olaparib Analogue

Boronic ester precursor **3.45** was next subjected to radioiodination. [^{123}I]NaI in 0.05 M NaOH dissolved in a solution of copper(II) trifluoroacetate and 1,10-phenanthroline in MeOH/H_2O was added to the precursor **3.45**. The reaction was performed at 80 °C for 25 minutes affording [^{123}I]**3.33** with almost quantitative ^{123}I-incorporation (RCY > 95%).

Without further optimisation, starting from approximately 100 MBq of [^{123}I]NaI, the desired ^{123}I-olaparib analogue was isolated and reformulated in 10% DMSO/PBS solution within 1.5 hours with a non-decay corrected AY of 67% ± 10% (n = 4), an RCP above 95%, and A_m up to 342 GBq/μmol (Scheme 3.21, and Figure 3.3).

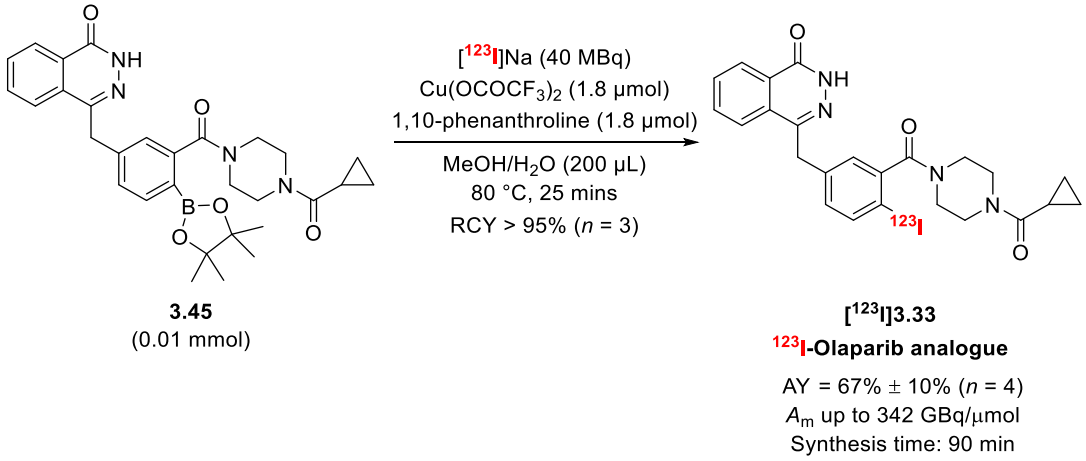

Scheme 3.21: Radiosynthesis of ^{123}I-olaparib analogue **[^{123}I]3.33**.

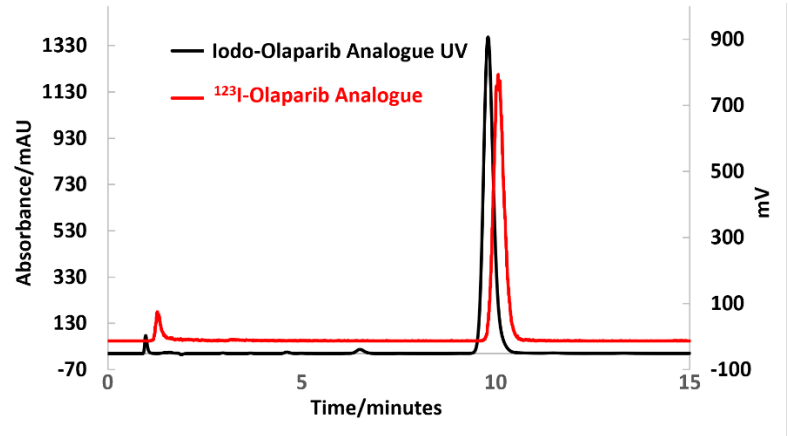

Figure 3.3: Radiochromatogram obtained during the HPLC analysis of ^{123}I-olaparib analogue (red) overlayed with UV chromatogram of non-radiolabelled reference standard iodo-olaparib analogue **3.33** (λ = 220 nm, black).

3.3.6 Radiosynthesis of ^{123}I-Rucaparib Analogue from Aldehydic Precursor **3.37**

With the successful labelling of ^{123}I-olaparib in hand, we next turned our attention to the radiosynthesis of the ^{123}I-rucaparib analogue. A iodo-rucaparib analogue reference compound **3.54** was synthesised in a two-step sequence, via Cu(II)-mediated iododeboronation, followed by reductive amination (Scheme 3.22). Iododeboronation proceeded smoothly in 86% yield. When aldehyde **3.54** was subjected to reductive amination, poor solubility of reactants was observed when using MeOH as solvent. The mixture was solubilised by addition of DMI as co-solvent. The iodinated rucaparib analogue **3.35** was isolated as a single product.

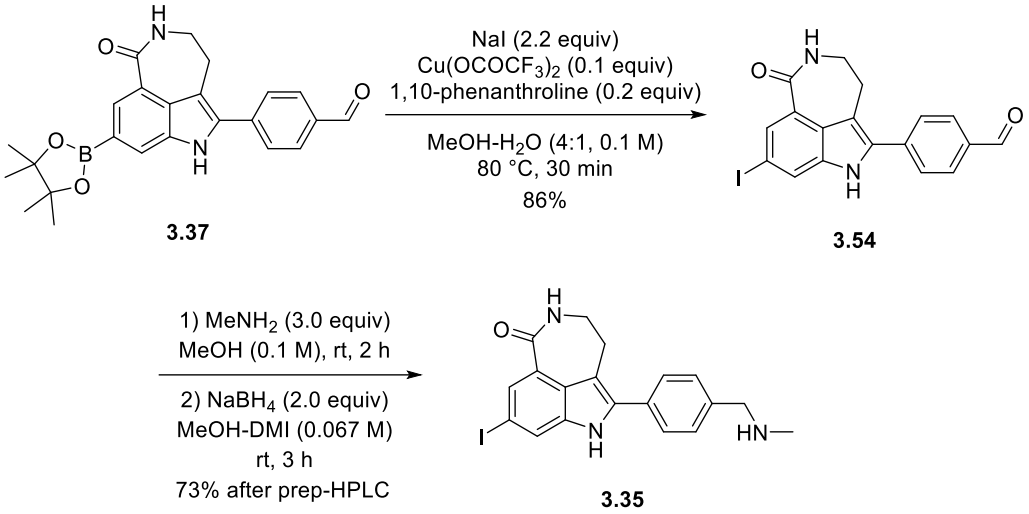

Scheme 3.22: Synthesis of iodo-rucaparib analogue reference **3.35**.

Subsequently, with the precursor **3.37** in hand (see Chapter 2 for synthesis), Cu(II)-mediated radioiodination was performed with the same protocol described for ^{123}I-olaparib analogue in Section 3.3.5 with an RCY of 81% ± 10%. The identity of this radiolabelled aldehyde intermediate **[^{123}I]3.54** was confirmed by radio-HPLC (Scheme 3.23 and Figure 3.4).

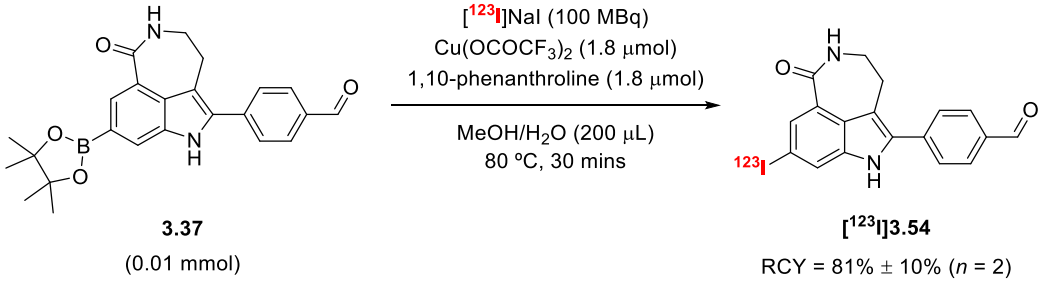

Scheme 3.23: Radiosynthesis of ^{123}I-aldehyde **[^{123}I]3.54**.

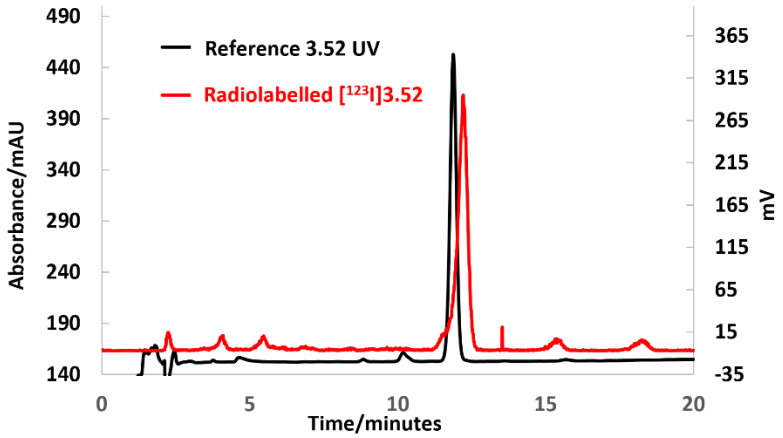

Figure 3.4: Radiochromatogram obtained during the HPLC analysis of ^{123}I-Aldehyde **[^{123}I]3.54** (red) overlayed with UV chromatogram of non-radiolabelled reference aldehyde **3.54** (λ = 220 nm, black).

The Cu(II) complex was then removed via a C-18 cartridge purification to prevent potential coupling reactivity between iodide and the secondary amine formed from reductive amination. Initial attempts of a one-pot reductive amination using methylamine and sodium cyanoborohydride did not yield radiolabelled product **[^{123}I]3.35** (Scheme 3.24). The conversion was quantitative with its corresponding fluorinated analogue. By increasing temperature and reaction time, aldehyde **[^{123}I]3.54** underwent proto-deiodination and formation of [^{123}I]iodide was observed by radio-HPLC (Figure 3.5). Varying the reaction sequence, temperature, adding a DMI co-solvent or the use of alternative reductants, such as silane, borane and Hantzsch ester did not provide a solution, either the imine did not react, or underwent deiodination. These observations alluded not only to the different reactivity of C_{sp}^2-F and C_{sp}^2-I, but also the sub-stoichoimetric quantities of radionuclide present in these reactions.

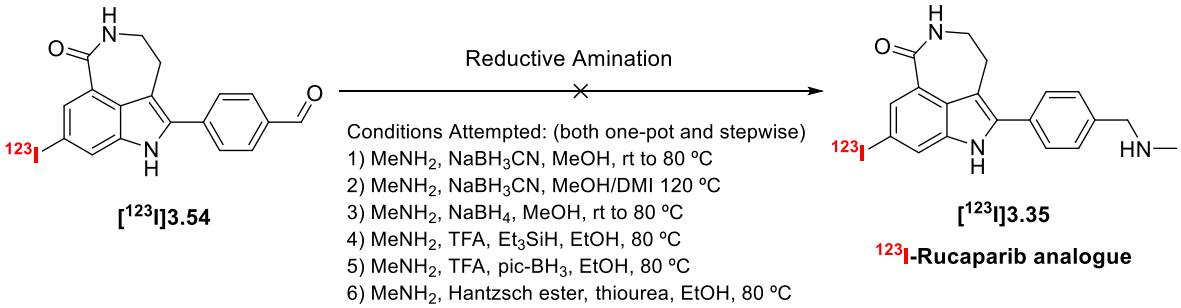

Scheme 3.24: Attempted reductive amination of aldehyde **[^{123}I]3.54**.

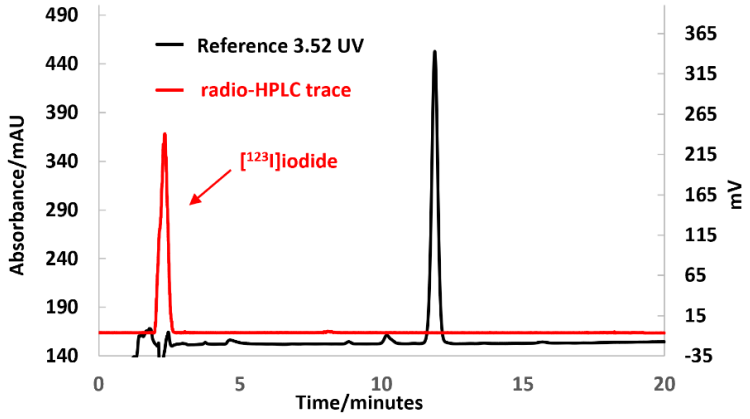

Figure 3.5: Radiochromatogram obtained after reductive amination radio-HPLC trace (red) and UV chromatogram of non-radiolabelled reference aldehyde **3.54** (λ = 220 nm, black). Aldehyde **[^{123}I]3.54** underwent protodeboronation and formation of [^{123}I]iodide (red) was observed.

3.3.7 Radiosynthesis of ^{123}I-Rucaparib Analogue from *N*Boc-Protected Precursor **3.55**

We then investigated an alternative approach to the ^{123}I-rucaparib analogue using an *N*Boc-protected boronic ester **3.55**. **[^{123}I]3.56** was afforded in over 95% RCY, which was then directly subjected to a post-labelling deprotection with TFA in quantitative conversion to generate the desired ^{123}I-rucaparib analogue. Attempts to reformulate in 10% DMSO/PBS were unsuccessful and the ^{123}I-rucaparib analogue was insoluble in this solvent system. Upon heating in 100 µL of 1 M HCl prior to reformulation, an ammonium salt of ^{123}I-rucaparib analogue, **[^{123}I]3.35·HCl** was obtained (Scheme 3.25).

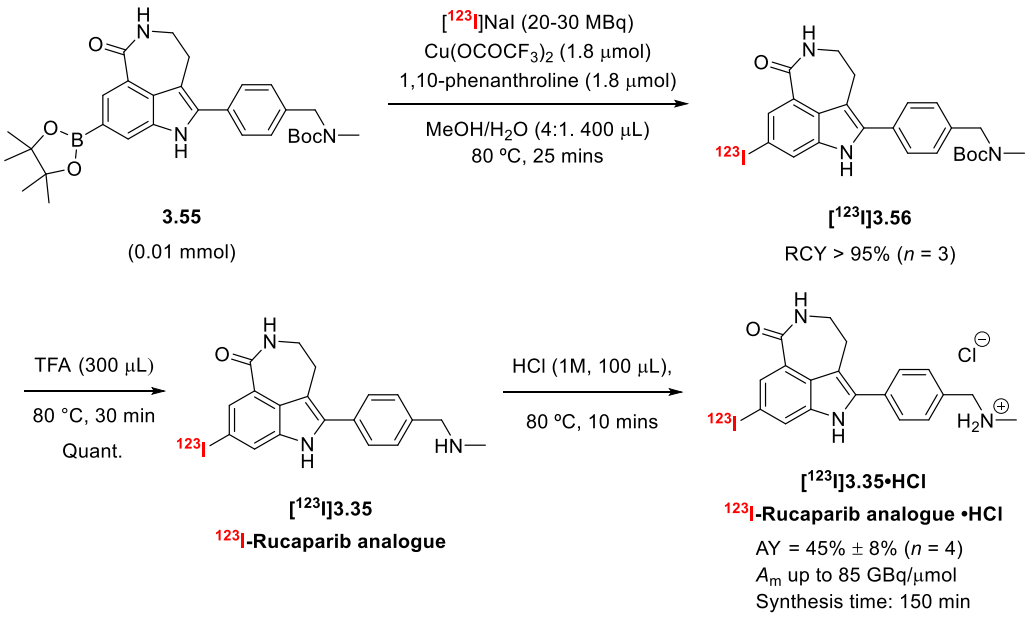

Scheme 3.23: Radiosynthesis of ^{123}I-rucaparib analogue **[^{123}I]3.35**

The *N*Boc boronic ester precursor **3.55** was subjected to radioiodination, starting from 100-150 MBq of [^{123}I]NaI. The crude mixture after deprotection was loaded onto a semi-preparative HPLC in reverse phase for separation. The ^{123}I-rucaparib analogue **[^{123}I]3.35** was collected from the HPLC and trapped onto a C18 cartridge. It was then released with 3 mL of EtOH and reformulated as an ammonium salt with a non-decay corrected AY of 45% ± 8% (n = 4), a radiochemical purity (RCP) higher than 95%, and A_m up to 85 GBq/μmol, in a total synthesis time of 2.5 hours (Figure 3.6).

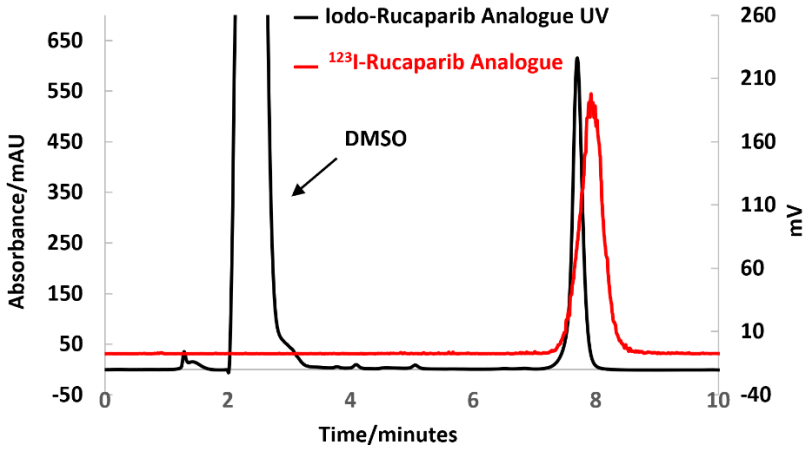

Figure 3.6: Radiochromatogram obtained during the HPLC analysis of ^{123}I-rucaparib analogue (red) overlayed with UV chromatogram of non-radiolabelled reference standard iodo-rucaparib analogue **3.33** (λ = 220 nm, black).

3.4 Conclusion and Future Work

This work demonstrated the radiosynthesis of both ^{123}I-olaparib and ^{123}I-rucaparib analogues, using Cu(II)-mediated ^{123}I-iodination of the identical or slightly modified aryl boronic ester precursors for [^{18}F]olaparib and [^{18}F]rucaparib, exemplifying the divergence of radiohalogenation.

In vitro and *in vivo* evaluations of both radiotracers are ongoing. Specificity of cell uptake of both ^{123}I-labelled radiopharmaceuticals will be evaluated by addition of non-radiolabelled PARP inhibitors. Their ability to reduce clonogenic survival will be determined with human

pancreatic adenocarcinoma and glioblastoma cells. *Ex vivo* biodistribution will be performed in PSN1 xenograft-bearing mice.

Future aims of this project are: 1) to explore the potential of both tracers as theragnostic agents and 2) to translate the radiosynthesis of both ^{123}I-olaparib and ^{123}I-rucaparib analogues to a fully-automated platform under GMP conditions.

The recent introduction of many biologically-targeted therapies for cancer such as PARP enzyme provides opportunities to design novel auger electron emitting agents for theragnostic use. If *in vitro and in vivo* experiments demonstrate promising results, Both ^{123}I-olaparib and ^{123}I-rucaparib analogues will be tested in clinical trials, as a novel tool for cancer treatment.

3.5 Reference

[1] Ku, A.; Facca, V. J.; Cai, Z.; Reilly, R. M., Auger Electrons for Cancer Therapy – A Review. *EJNMMI Radiopharm. Chem.* **2019,** *4* (1), 27.

[2] Intemann, R. L.; Pollock, F., K-Electron Ejection Accompanying Nuclear K Capture. *Phys. Rev.* **1967**, *157* (1), 41.

[3] McGuire, E., Auger and Coster-Kronig Transitions. *Atomic Inner-Shell Processes* **1975,** *1*, 293–330.

[4] Auger, P., Sur L'effet Photoélectrique Composé. *Journal de Physique et le Radium* **1925,** *6* (6), 205–208.

[5] Howell, R. W., Radiation Spectra for Auger-Electron Emitting Radionuclides: Report No. 2 of AAPM Nuclear Medicine Task Group No. 6. *Med. Phys.* **1992**, *19* (6), 1371–1383

[6] Choppin, G.; Liljenzin, J.; Rydberg, J.; Ekberg, C., Chapter 4: Unstable Nuclei and Radioactive Decay. In *Radiochemistry and Nuclear Chemistry*, 3rd ed.; Butterworth-Heinemann, 2002; pp 58–93.

[7] Meitner, L., Über Die Entstehung Der β-Strahl-Spektren Radioaktiver Substanzen. *Zeitschrift für Physik* **1922,** *9* (1), 131–144.

[8] Auger, P., Sur Les Rayons β Secondaires Produits Dans Un Gaz Par Des Rayons X. *CR Acad. Sci.(F)* **1923,** *177,* 169.

[9] Chan, P. C.; Lisco, E.; Lisco, H.; Adelstein, S. J., The Radiotoxicity of Iodine-125 in Mammalian Cells: II. A Comparative Study on Cell Survival and Cytogenetic Responses to ^{125}IUdR, ^{131}IUdR, and ^{3}HTdR. *Radiat. Res.* **1976,** *67* (2), 332–343.

[10] Cai, Z.; Pignol, J.-P.; Chan, C.; Reilly, R. M., Cellular Dosimetry of ^{111}In Using Monte Carlo N-particle Computer Code: Comparison with Analytic Methods and Correlation with In Vitro Cytotoxicity. *J. Nucl Med.* **2010,** *51* (3), 462–470.

[11] Mothersill, C.; Rusin, A.; Fernandez-Palomo, C.; Seymour, C., History of Bystander Effects Research 1905-Present; What Is in a Name? *Int. J. Radiat. Biol.* **2018,** *94* (8), 696–707.

[12] Azzam, E. I.; de Toledo, S. M.; Gooding, T.; Little, J. B., Intercellular Communication Is Involved in the Bystander Regulation of Gene Expression in Human Cells Exposed to Very Low Fluences of Alpha Particles. *Radiat. Res.* **1998,** *150* (5), 497–504.

[13] Mothersill, C.; Seymour, C., Medium from Irradiated Human Epithelial Cells but Not Human Fibroblasts Reduces the Clonogenic Survival of Unirradiated Cells. *Int. J. Radiat. Biol.* **1997**, *71* (4), 421–427.

[14] Mosse, I.; Marozik, P.; Seymour, C.; Mothersill, C., The Effect of Melanin on the Bystander Effect in Human Keratinocytes. *Mutat. Res.* **2006**, *597* (1-2), 133–137.

[15] Pouget, J. P.; Santoro, L.; Raymond, L.; Chouin, N.; Bardiès, M.; Bascoul-Mollevi, C.; Huguet, H.; Azria, D.; Kotzki, P. O.; Pèlegrin, M.; Vivès, E.; Pèlegrin, A., Cell Membrane is a More Sensitive Target Than Cytoplasm to Dense Ionization Produced by Auger Electrons. *Radiat. Res.* **2008**, *170* (2), 192–200.

[16] Paillas, S.; Ladjohounlou, R.; Lozza, C.; Pichard, A.; Boudousq, V.; Jarlier, M.; Sevestre, S.; Le Blay, M.; Deshayes, E.; Sosabowski, J.; Chardès, T.; Navarro-Teulon, I.; Mairs, R. J.; Pouget, J. P., Localized Irradiation of Cell Membrane by Auger Electrons Is Cytotoxic Through Oxidative Stress-Mediated Nontargeted Effects. *Antioxid. Redox Signal* **2016,** *25* (8), 467–484.

[17] Kassis, A. I., Molecular and Cellular Radiobiological Effects of Auger Emitting Radionuclides. *Radiat. Prot. Dosimetry* **2011**, *143* (2-4), 241–247.

[18] Sutherland, A., Radiohalogenation of Organic Compounds: Practical Considerations and Challenges for Molecular Imaging. *Synthesis* **2019,** *51* (23), 4368–4373.

[19] Medicine, I. o.; Council, N. R., *Advancing Nuclear Medicine Through Innovation*. The National Academies Press: Washington, DC, 2007; p 173.

[20] Mangner, T. J.; Wu, J. L.; Wieland, D. M., Solid-Phase Exchange Radioiodination of Aryl Iodides. Facilitation by Ammonium Sulfate. *J. Org. Chem.* **1982,** *47* (8), 1484–1488.

[21] Kil, K.-E.; Zhu, A.; Zhang, Z.; Choi, J.-K.; Kura, S.; Gong, C.; Brownell, A.-L., Development of [^{123}I]IPEB and [^{123}I]IMPEB as SPECT Radioligands for Metabotropic Glutamate Receptor Subtype 5. *ACS Med. Chem. Lett.* **2014,** *5* (6), 652–656.

[22] Vivier, M.; Rapp, M.; Papon, J.; Labarre, P.; Galmier, M.-J.; Sauzière, J.; Madelmont, J.-C., Synthesis, Radiosynthesis, and Biological Evaluation of New Proteasome Inhibitors in a Tumor Targeting Approach. *J. Med. Chem.* **2008,** *51* (4), 1043–1047.

[23] Navarro, L.; Berdal, M.; Chérel, M.; Pecorari, F.; Gestin, J. F.; Guérard, F., Prosthetic Groups for Radioiodination and Astatination of Peptides and Proteins: A Comparative Study of Five Potential Bioorthogonal Labeling Strategies. *Bioorg. Med. Chem.* **2019,** *27* (1), 167–174.

[24] Guérard, F.; Lee, Y. S.; Baidoo, K.; Gestin, J. F.; Brechbiel, M. W., Unexpected Behavior of the Heaviest Halogen Astatine in the Nucleophilic Substitution of Aryliodonium Salts. *Chemistry* **2016,** *22* (35), 12332–12339.

[25] Guérard, F.; Navarro, L.; Lee, Y. S.; Roumesy, A.; Alliot, C.; Chérel, M.; Brechbiel, M. W.; Gestin, J. F., Bifunctional Aryliodonium Salts for Highly Efficient Radioiodination and Astatination of Antibodies. *Bioorg. Med. Chem.* **2017,** *25* (21), 5975–5980.

[26] Sloan, N. L.; Luthra, S. K.; McRobbie, G.; Pimlott, S. L.; Sutherland, A., A One-Pot Radioiodination of Aryl Amines via Stable Diazonium Salts: Preparation of ^{125}I-imaging Agents. *Chem. Commun.* **2017,** *53* (80), 11008–11011.

[27] Lalut, J.; Tournier, B. B.; Cailly, T.; Lecoutey, C.; Corvaisier, S.; Davis, A.; Ballandonne, C.; Since, M.; Millet, P.; Fabis, F.; Dallemagne, P.; Rochais, C., Synthesis and Evaluation of Novel Serotonin 4 Receptor Radiotracers for Single Photon Emission Computed Tomography. *Eur. J. Med. Chem.* **2016,** *116*, 90–101.

[28] Vaidyanathan, G.; Zalutsky, M. R., No-Carrier-Added Synthesis of *meta*-[^{131}I]Iodobenzylguanidine. *Appl. Radiat. Isot.* **1993,** *44* (3), 621–628.

[29] Chitneni, S. K.; Reitman, Z. J.; Spicehandler, R.; Gooden, D. M.; Yan, H.; Zalutsky, M. R., Synthesis and Evaluation of Radiolabeled AGI-5198 Analogues as Candidate Radiotracers for Imaging Mutant IDH1 Expression in Tumors. *Bioorg. Med. Chem. Lett.* **2018,** *28* (4), 694–699.

[30] Molloy, J. J.; O'Rourke, K. M.; Frias, C. P.; Sloan, N. L.; West, M. J.; Pimlott, S. L.; Sutherland, A.; Watson, A. J. B., Mechanism of Cu-Catalyzed Aryl Boronic Acid Halodeboronation Using Electrophilic Halogen: Development of a Base-Catalyzed Iododeboronation for Radiolabeling Applications. *Org. Lett.* **2019,** *21* (7), 2488–2492.

[31] Cant, A. A.; Champion, S.; Bhalla, R.; Pimlott, S. L.; Sutherland, A., Nickel-Mediated Radioiodination of Aryl and Heteroaryl Bromides: Rapid Synthesis of Tracers for SPECT Imaging. *Angew. Chem. Int. Ed.* **2013,** *52* (30), 7829–7832.

[32] Liu, X.; Shi, Y.; Maag, D. X.; Palma, J. P.; Patterson, M. J.; Ellis, P. A.; Surber, B. W.; Ready, D. B.; Soni, N. B.; Ladror, U. S.; Xu, A. J.; Iyer, R.; Harlan, J. E.; Solomon, L. R.; Donawho, C. K.; Penning, T. D.; Johnson, E. F.; Shoemaker, A. R., Iniparib Nonselectively Modifies Cysteine-Containing Proteins in Tumor Cells and Is Not a *Bona Fide* PARP Inhibitor. *Clin. Cancer Res.* **2012,** *18* (2), 510–523.

[33] Patel, A. G.; De Lorenzo, S. B.; Flatten, K. S.; Poirier, G. G.; Kaufmann, S. H., Failure of Iniparib to Inhibit Poly(ADP-Ribose) Polymerase *In Vitro*. *Clin. Cancer Res.* **2012,** *18* (6), 1655–1662.

[34] Mukhin, A. G.; Gündisch, D.; Horti, A. G.; Koren, A. O.; Tamagnan, G.; Kimes, A. S.; Chambers, J.; Vaupel, D. B.; King, S. L.; Picciotto, M. R.; Innis, R. B.; London, E. D., 5-Iodo-A-85380, an α4β2 Subtype-Selective Ligand for Nicotinic Acetylcholine Receptors. *Mol. Pharmacol.* **2000,** *57* (3), 642–649.

[35] Wilson, T. C.; McSweeney, G.; Preshlock, S.; Verhoog, S.; Tredwell, M.; Cailly, T.; Gouverneur, V., Radiosynthesis of SPECT Tracers via a Copper-Mediated ^{123}I-Iodination of (Hetero)aryl Boron Reagents. *Chem. Commun.* **2016,** *52* (90), 13277–13280.

[36] Tredwell, M.; Preshlock, S. M.; Taylor, N. J.; Gruber, S.; Huiban, M.; Passchier, J.; Mercier, J.; Génicot, C.; Gouverneur, V., A General Copper-Mediated Nucleophilic ^{18}F-Fluorination of Arenes. *Angew. Chem. Int. Ed.* **2014,** *53* (30), 7751–7755.

[37] Zhang, P.; Zhuang, R.; Guo, Z.; Su, X.; Chen, X.; Zhang, X., A Highly Efficient Copper-Mediated Radioiodination Approach Using Aryl Boronic Acids. *Chemistry* **2016,** *22* (47), 16783–16786.

[38] Reilly, S. W.; Makvandi, M.; Xu, K.; Mach, R. H., Rapid Cu-Catalyzed [^{211}At]Astatination and [^{125}I]Iodination of Boronic Esters at Room Temperature. *Org. Lett.* **2018,** *20* (7), 1752–1755.

[39] Webster, S.; O'Rourke, K. M.; Fletcher, C.; Pimlott, S. L.; Sutherland, A.; Lee, A.-L., Rapid Iododeboronation with and without Gold Catalysis: Application to Radiolabelling of Arenes. *Chem. Eur. J.* **2018,** *24* (4), 937–943.

[40] Cernak, T.; Dykstra, K. D.; Tyagarajan, S.; Vachal, P.; Krska, S. W., The Medicinal Chemist's Toolbox for Late Stage Functionalization of Drug-Like Molecules. *Chem. Soc. Rev.* **2016,** *45* (3), 546–576.

[41] Gensch, T.; Hopkinson, M. N.; Glorius, F.; Wencel-Delord, J., Mild Metal-Catalyzed C–H Activation: Examples and Concepts. *Chem. Soc. Rev.* **2016,** *45* (10), 2900–2936.

[42] Dubost, E.; Babin, V.; Benoist, F.; Hébert, A.; Barbey, P.; Chollet, C.; Bouillon, J.-P.; Manrique, A.; Pieters, G.; Fabis, F.; Cailly, T., Palladium-Mediated Site-Selective C–H Radio-iodination. *Org. Lett.* **2018,** *20* (19), 6302–6305.

[43] Pirovano, G.; Jannetti, S. A.; Carter, L. M.; Sadique, A.; Kossatz, S.; Guru, N.; Demétrio De Souza França, P.; Maeda, M.; Zeglis, B. M.; Lewis, J. S.; Humm, J. L.; Reiner, T., Targeted Brain Tumor Radiotherapy Using an Auger Emitter. *Clin. Cancer Res.* **2020,** *26* (12), 2871–2881.

[44] Riad, A.; Gitto, S. B.; Lee, H.; Winters, H. D.; Martorano, P. M.; Hsieh, C.-J.; Xu, K.; Omran, D. K.; Powell, D. J.; Mach, R. H.; Makvandi, M., PARP Theragnostic Auger Emitters Are Cytotoxic in BRCA Mutant Ovarian Cancer and Viable Tumors from Ovarian Cancer Patients Enable Ex-Vivo Screening of Tumor Response. *Molecules* **2020**, *25* (24), 6029

[45] Jannetti, S. A.; Carlucci, G.; Carney, B.; Kossatz, S.; Shenker, L.; Carter, L. M.; Salinas, B.; Brand, C.; Sadique, A.; Donabedian, P. L.; Cunanan, K. M.; Gönen, M.; Ponomarev, V.; Zeglis, B. M.; Souweidane, M. M.; Lewis, J. S.; Weber, W. A.; Humm, J. L.; Reiner,

T., PARP-1-Targeted Radiotherapy in Mouse Models of Glioblastoma. *J. Nucl. Med.* **2018,** *59* (8), 1225–1233.

[46] Makvandi, M.; Lee, H.; Puentes, L. N.; Reilly, S. W.; Rathi, K. S.; Weng, C.-C.; Chan, H. S.; Hou, C.; Raman, P.; Martinez, D.; Xu, K.; Carlin, S. D.; Greenberg, R. A.; Pawel, B. R.; Mach, R. H.; Maris, J. M.; Pryma, D. A., Targeting PARP-1 with Alpha-Particles Is Potently Cytotoxic to Human Neuroblastoma in Preclinical Models. *Mol. Cancer Ther.* **2019**, *18* (7), 1195–1204.

[47] Wilson, T. C.; Jannetti, S. A.; Guru, N.; Pillarsetty, N.; Reiner, T.; Pirovano, G., Improved Radiosynthesis of ^{123}I-MAPi, an Auger Theragnostic Agent. *Int. J. Radiat. Biol.* **2020**, 1–7.

[48] Wilson, T.; Pirovano, G.; Xiao, G.; Samuels, Z.; Roberts, S.; Viray, T.; Guru, N.; Zanzonico, P.; Gollub, M.; Pillarsetty, N. V. K.; Reiner, T.; Bargonetti, J., PARP-Targeted Auger Therapy in p53 Mutant Colon Cancer Xenograft Mouse Models. *Mol. Pharm.* **2021,** *18* (9), 3418–3428.

[49] Wilson, T. C.; Xavier, M.-A.; Knight, J.; Verhoog, S.; Torres, J. B.; Mosley, M.; Hopkins, S. L.; Wallington, S.; Allen, P. D.; Kersemans, V.; Hueting, R.; Smart, S.; Gouverneur, V.; Cornelissen, B., PET Imaging of PARP Expression Using [^{18}F]Olaparib. *J. Nucl. Med.* **2019,** *60* (4), 504–510.

[50] Chen, Z.; Destro, G.; Guibbal, F.; Chan, C. Y.; Cornelissen, B.; Gouverneur, V., Copper-Mediated Radiosynthesis of [^{18}F]Rucaparib. *Org. Lett.* **2021,** *23* (18), 7290–7294.

[51] Wilson, T. C. Late Stage ^{18}F-Fluorination and ^{123}I-Iodination for PET and SPECT Imaging. University of Oxford, 2018.

[52] Chan, C. Y., Chen Z., Destro G., Veal M., Lau D., O'Neill E., Dias G., Mosley M., Kersemans V., Guibbal F., Gouverneur V., Cornelissen B. Imaging PARP with [^{18}F]rucaparib in pancreatic cancer models. *EJNMMI*. In press

Chapter 4. Experimental

4.1 General Information

All reagents were purchased from commercial suppliers (Sigma-Aldrich, Alfa Aesar, Fluorochem and Apollo Scientific) and used without further purification. Moisture sensitive reactions were carried out using solvents obtained from the MBRAUN-SPS solvent purification system (CH_2Cl_2, THF, DMF, Et_2O). Reactions were monitored by thin layer chromatography (TLC) on silica gel pre-coated aluminium sheets (Merck Kieselgel 60 F_{254} plates). Visualization was accomplished by irradiation with UV light at 254 nm. Flash column chromatography (FCC) was performed on Merck silica gel (60, particle size 0.040-0.063 mm). All NMR spectra were recorded on Bruker AVIIIHD 400, AVIIIHD 500 or VII 500. ^{1}H and ^{13}C NMR spectral data are reported as chemical shifts (δ) in parts per million (ppm) relative to the solvent peak using the Bruker internal referencing procedure (edlock). ^{19}F NMR spectra are referenced relative to $CFCl_3$. Data are reported as follows: chemical shift, multiplicity (s = singlet, d = doublet, t= triplet, q = quartet, pent = pentet, sept = septet, br = broad, m = multiplet), coupling constants (Hz) and integration. NMR spectra were processed with MestReNova 11.0 or higher. High resolution mass spectra (HRMS, m/z) were recorded on a Thermo Exactive mass spectrometer (Thermo Exactive High-Resolution Orbitrap FTMS) equipped with Waters Acquity liquid chromatography system using the heated electrospray (HESI-II) probe for positive electrospray ionization (ESI+). Infrared spectra were recorded as the neat compound or in solution using a Bruker tensor 27 FT-IR spectrometer. Absorptions are reported in wavenumber (cm^{-1}). Melting points of solids were measured on a Griffin apparatus and were uncorrected. Some isolated compounds might contain trace amount of impurities, which didn't affect the sequential steps and were labeled in the NMR spectra.

4.2 Preparation and Characterisation Data for Chapter II

2-Nitroethyl acetate (**2.153**)

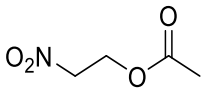

2-nitroethanol (1.27 g, 13.9 mmol), pyridine (1.12 mL, 13.9 mmol) and acetic anhydride (1.31 mL, 13.9 mmol) were dissolved in CH_2Cl_2 (80 mL) in a round-bottom flask. The mixture was stirred at room temperature in the dark for 7 hours. 1N HCl was added upon completion. The organic solvent was removed under reduced pressure. The aqueous phase was extracted with Et_2O (3 x 80 mL). The organic phases were combined, dried over Na_2SO_4 and concentrated in vacuo to afford 2-nitroethylacetate as yellow oil (1.40 g, 10.5 mmol, 76%). Data is in accordance with known literature.[1] **^{1}H NMR** (400 MHz, $CDCl_3$) δ 4.65 – 4.52 (m, 4H), 2.04 (s, 3H); **^{13}C NMR** (101 MHz, $CDCl_3$) δ 170.4, 73.7, 59.5, 20.5.

Methyl 6-bromo-3-(2-nitroethyl)-1*H*-indole-4-carboxylate (**2.174**)

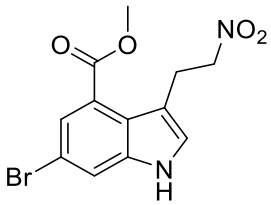

Methyl 6-bromo-1*H*-indole-4-carboxylate (2.00 g, 7.87 mmol) and 4-tert-butylcatechol (13.1 mg, 0.08 mmol) were dissolved in *p*-xylene (10 mL). 2-nitroethyl acetate (1.26 g, 9.44 mmol) was added, and the mixture was heated at 145 °C in an oil bath for 3.5 hours. After cooled down to room temperature, the solvent was removed under reduced pressure. The crude was purified by flash column chromatography (20% EtOAc in pentane, Rf: 0.30) to yield methyl 6-bromo-3-(2-nitroethyl)-1*H*-indole-4-carboxylate (1.88 g, 5.74 mmol, 73%) as a pale-yellow solid. **^{1}H NMR** (400 MHz, $CDCl_3$) δ 8.35 (s, 1H), 7.91 (d, *J* = 1.8 Hz, 1H), 7.68 (d, *J* = 1.8 Hz, 1H),

7.16 (d, *J* = 2.5 Hz, 1H), 4.70 (t, *J* = 6.5 Hz, 2H), 3.95 (s, 3H), 3.63 (t, *J* = 6.6 Hz, 2H); **^{13}C NMR** (101 MHz, $CDCl_3$) δ 167.10, 138.60, 127.30, 126.83, 124.27, 123.53, 118.70, 114.41, 111.47, 77.36, 52.38, 26.00; **IR** (cm^{-1}): 3412, 1708, 1556, 1537, 1254, 1224, 1063, 1934, 785, 622; **HRMS** (ESI+) m/z: $[M+Na]^+$ Calcd for $C_{12}H_{11}O_4N_2Br_1Na_1$ 348.9794 ; Found 348.9794; **M.P.** 128-130 °C.

8-Bromo-2,3,4,6-tetrahydro-1*H*-azepino[5,4,3-*cd*]indol-1-one (**2.171**)

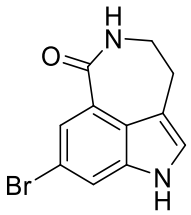

Methyl 6-bromo-3-(2-nitroethyl)-1*H*-indole-4-carboxylate (1.69 g, 5.16 mmol) was dissolved in MeOH (80 mL). 2M HCl (80 mL) was added, followed by addition of zinc dust (7.96 g, 122 mmol) portion wise. The mixture was heated under reflux in an oil bath for 30 minutes and filtered directly. The filtrate was basified with 2M NaOH (100 mL) and the resultant mixture was filtered through a Büchner funnel. The filter cake was washed with MeOH (2 x 100 mL). MeOH was removed under reduced pressure. The aqueous phase was extracted with EtOAc (3 x 100 mL). The organic phases were combined, dried over Na_2SO_4 and concentrated *in vacuo*. The crude was purified by flash column chromatography (4% MeOH in CH_2Cl_2, Rf: 0.25) to yield 8-bromo-2,3,4,6-tetrahydro-1*H*-azepino[5,4,3-*cd*]indol-1-one (974 mg, 3.67 mmol, 71%) as a white solid. **^{1}H NMR** (400 MHz, DMSO) δ 11.27 (s, 1H), 8.16 (t, *J* = 5.8 Hz, 1H), 7.74 – 7.68 (m, 2H), 7.33 – 7.28 (m, 1H), 3.44 – 3.37 (m, 2H), 2.94 – 2.87 (m, 2H); **^{13}C NMR** (101 MHz, DMSO) δ 168.4, 137.6, 126.0, 124.4, 124.1, 123.9, 116.9, 114.7, 113.3, 42.1, 27.9; **IR**

(cm^{-1}): 3190, 1655, 1608, 1458, 1316, 1127, 1068, 782, 642; **HRMS** (ESI+) m/z: $[M+H]^+$ Calcd for $C_{11}H_{10}O_1N_2Br_1$ 264.9971; Found 264.9973; **M.P.** 186-188 °C.

2d. 8-Bromo-5-iodo-2,3,4,6-tetrahydro-1*H*-azepino[5,4,3-*cd*]indol-1-one (**2.170**)

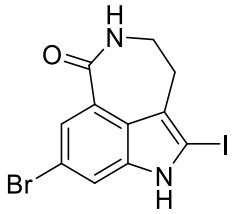

8-Bromo-2,3,4,6-tetrahydro-1*H*-azepino[5,4,3-*cd*]indol-1-one (640 mg, 2.41 mmol) was dissolved in 58 mL of THF/CH_2Cl_2 (1:1) and cooled to 0 °C in an ice bath. Bis(trifluoroacetoxy)iodobenzene (1.25 g, 2.90 mmol) and iodine (359 mg, 2.41 mmol) were added. The reaction mixture was stirred at 0 °C for 30 minutes followed by another 30 minute stirring at room temperature. The reaction was quenched by a mixture of saturated sodium sulfite (40 mL) and saturated sodium thiosulfate (40 mL). The aqueous phase was extracted with EtOAc (3 x 80 mL). The organic phases were combined, dried over Na_2SO_4 and concentrated *in vacuo*. The crude was purified by flash column chromatography (4% MeOH in CH_2Cl_2, Rf: 0.25) to yield 8-bromo-5-iodo-2,3,4,6-tetrahydro-1*H*-azepino[5,4,3-*cd*]indol-1-one (437 mg, 1.12 mmol, 46%) as an off-white solid. **^{1}H NMR** (500 MHz, DMSO) δ 11.98 (s, 1H), 8.22 (t, *J* = 5.8 Hz, 1H), 7.70 (d, *J* = 1.8 Hz, 1H), 7.61 (d, *J* = 1.8 Hz, 1H), 3.47 – 3.38 (m, 2H), 2.80 – 2.73 (m, 2H); **^{13}C NMR** (126 MHz, DMSO) δ 167.9, 140.0, 124.6, 124.4, 123.8, 120.3, 115.9, 113.8, 84.0, 41.3, 29.8; **IR** (cm^{-1}): 3590, 3176, 1630, 1601, 1423, 1350, 1312, 1086, 995, 859, 780, 645; **HRMS** (ESI+) m/z: $[M+H]^+$ Calcd for $C_{11}H_9O_1N_2Br_1I_1$ 390.8937; Found 390.8940; **M.P.** 228-230 °C.

4-(1-Oxo-8-(4,4,5,5-tetramethyl-1,3,2-dioxaborolan-2-yl)-2,3,4,6-tetrahydro-1*H*-azepino[5,4,3-*cd*]indol-5-yl)benzaldehyde (**2.163**)

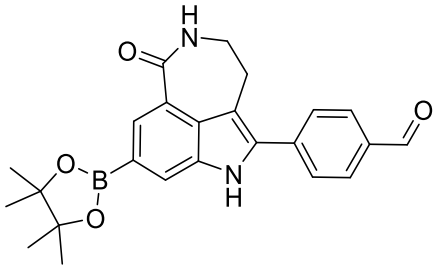

A two-necked round bottom flask, purged with nitrogen gas, was charged 8-bromo-5-iodo-2,3,4,6-tetrahydro-1*H*-azepino[5,4,3-*cd*]indol-1-one (260 mg, 0.67 mmol). 4-Formylphenylboronic acid (99.7 mg, 0.67 mmol), Na_2CO_3 (141 mg, 1.33 mmol) and $Pd(PPh_3)_4$ (154 mg, 0.13 mmol) was added. The flask was flushed with nitrogen three times. Degassed 1,4-dioxane (7.2 mL) and water (1.8 mL) were added. The mixture was stirred at 85 °C in an oil bath for 16 hours and cooled to room temperature. The mixture was diluted with H_2O (10 mL) and extracted with EtOAc (3 x 10 mL). The combined organic phases were dried over Na_2SO_4 and concentrated *in vacuo*. The crude material was used for the consecutive step without further purification. Isolation of 4-(8-bromo-1-oxo-2,3,4,6-tetrahydro-1*H*-azepino[5,4,3-*cd*]indol-5-yl)benzaldehyde was proved to be challenging. The best result was obtained by directly using this crude intermediate in the next step. To a two-necked round bottom flask under nitrogen atmosphere, the crude material, Bis(pinacolato)diboron (169 mg, 0.67 mmol), $Pd(dppf)Cl_2$ (15.0 mg ,0.02 mmol) and potassium acetate (196 mg, 2.00 mmol) were added. The reaction flask was then backfilled with nitrogen and degassed DMF (3.3 mL) was added. The reaction was heated to 80 °C in an oil bath and stirred for 16 hours. Upon completion, the reaction mixture was cooled to room temperature, passed through a plug of Celite and concentrated *in vacuo*. The crude was isolated by column chromatography (4% MeOH in DCM, Rf: 0.35) before purification by reverse phase HPLC to afford 4-(1-oxo-8-

(4,4,5,5-tetramethyl-1,3,2-dioxaborolan-2-yl)-2,3,4,6-tetrahydro-1*H*-azepino[5,4,3-*cd*]indol-5-yl)benzaldehyde as a bright yellow solid (80 mg, 0.192 mmol, 29%). **^{1}H NMR** (500 MHz, DMSO) δ 11.86 (s, 1H), 10.07 (s, 1H), 8.13 (t, *J* = 5.8 Hz, 1H), 8.10 – 8.02 (m, 3H), 7.92 – 7.87 (m, 3H), 3.40 (t, *J* = 6.3 Hz, 2H), 3.11 (t, *J* = 4.6 Hz, 2H), 1.33 (s, 12H); **^{13}C NMR** (126 MHz, DMSO) δ 192.6, 169.5, 137.3, 136.5, 135.0, 134.8, 129.9, 128.8, 128.5, 128.4, 127.9, 124.5, 120.9, 114.4, 83.6, 41.8, 29.1, 24.8; **IR** (cm^{-1}): 3207, 2883, 1691, 1639, 1604, 1370, 1326, 1214, 1142, 965, 831, 789, 669; **HRMS** (ESI+) m/z: $[M+H]^+$ Calcd for $C_{24}H_{26}O_4N_2B_1$ 417.1982; Found 417.1980; **M.P.** 275-277 °C.

Tert-butyl (4-bromobenzyl)(methyl)carbamate

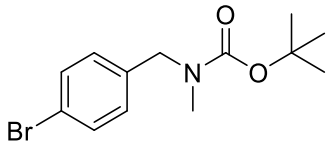

4-Bromobenzaldehyde (1.85 g, 10.0 mmol) was dissolved in MeOH (50 mL). Methylamine (33% wt. in EtOH, 3.74 mL, 30.0 mmol) was added. The mixture was stirred at room temperature for 3 hours and cooled to 0 °C in an ice bath. $NaBH_4$ (1.13 g, 30.0 mmol) was added in one portion. The mixture was stirred at 0 °C in an ice bath for 3 hours and quenched with 1 M HCl (50 mL) slowly at 0 °C. $NaHCO_3$ (50 mL) and NaOH (50 mL) was added and the aqueous phase was extracted with Et2O (3 x 150 mL). The combined organic phases were dried over Na_2SO_4 and the solvent was removed under reduced pressure. The crude was dissolved in anhydrous THF (33 mL) and cooled to 0 °C in an ice bath. DMAP (1.47 g, 12.0 mmol) was added to the solution, followed by addition of Boc_2O (2.62 g, 12.0 mmol). The mixture was stirred for 30 minutes and warmed to room temperature. After stirred for 15 hours, the solvent was removed under reduced pressure. The crude was purified by column chromatography (4% EtOAc in pentane, Rf: 0.30) to yield tert-butyl (4-

bromobenzyl)(methyl)carbamate as a light yellow oil (2.81 g, 9.36 mmol, 94 %) over two steps. Data is in accordance with known literature.[4] **^{1}H NMR** (400 MHz, DMSO) δ 7.54 (d, *J* = 8.1 Hz, 2H), 7.17 (d, *J* = 8.2 Hz, 2H), 4.33 (s, 2H), 2.75 (s, 3H), 1.39 (s, 9H); **^{13}C NMR** (101 MHz, DMSO) δ 154.9, 137.6, 131.3, 129.4, 120.1, 78.9, 50.8, 33.8, 28.0.

Tert-butyl methyl(4-(4,4,5,5-tetramethyl-1,3,2-dioxaborolan-2-yl)benzyl)carbamate (**2.175**)

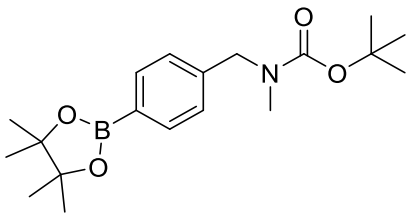

A two-necked round bottom flask, purged with nitrogen gas, was charged with tert-butyl (4-iodobenzyl)(methyl)carbamate (3.06 g, 8.80 mmol). B_2pin_2 (2.24 g, 8.80 mmol), KOAc (2.59 g, 26.4 mmol) and Pd(dppf)Cl_2 (193 mg, 0.264 mmol) was added to the flask under nitrogen atmosphere. Degassed and anhydrous 1,4-dioxane (35 mL) was added and the mixture was heated to 80 °C in an oil bath under nitrogen atmosphere. After stirred for 14 hours, the mixture was cooled to room temperature and flushed through a Celite plug with DCM. Solvent was removed under reduced pressure. The crude was purified by column chromatography (8 % EtOAc in pentane, Rf: 0.55) to yield tert-butyl methyl(4-(4,4,5,5-tetramethyl-1,3,2-dioxaborolan-2-yl)benzyl)carbamate as a white solid (2.87 g, 8.26 mmol, 94 %). Data is in accordance with known literature.[5] **^{1}H NMR** (400 MHz, $CDCl_3$) δ 7.77 (d, *J* = 8.0 Hz, 2H), 7.22 (d, *J* = 7.4 Hz, 2H), 4.43 (s, 2H), 2.98– 2.61 (m, 3H), 1.46 (s, 9H), 1.34 (s, 12H); **^{13}C NMR** (101 MHz, $CDCl_3$) δ 156.0, 141.4, 135.1, 134.8, 126.8, 83.8, 79.7, 52.5, 34.1, 28.5, 24.9.

Tert-butyl methyl(4-(1-oxo-8-(4,4,5,5-tetramethyl-1,3,2-dioxaborolan-2-yl)-2,3,4,6-tetrahydro-1H-azepino[5,4,3-cd]indol-5-yl)benzyl)carbamate (**2.161**)

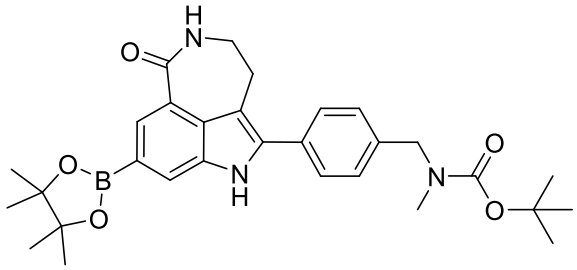

A two-necked round bottom flask, purged with nitrogen gas, was charged 8-bromo-5-iodo-2,3,4,6-tetrahydro-1*H*-azepino[5,4,3-*cd*]indol-1-one (196 mg, 0.50 mmol). Tert-butyl methyl(4-(4,4,5,5-tetramethyl-1,3,2-dioxaborolan-2-yl)benzyl)carbamate (174 mg, 0.50 mmol), Na_2CO_3 (106 mg, 1.00 mmol) and $Pd(PPh_3)_4$ (116 mg, 0.1 mmol) was added. The flask was flushed with nitrogen three times. Degassed 1,4-dioxane (5.0 mL) and water (1.3 mL) were added. The mixture was stirred at 85 °C in an oil bath for 16 hours and cooled to room temperature. The mixture was diluted with H_2O (10 mL) and extracted with EtOAc (3 x 10 mL). The combined organic phases were dried over Na_2SO_4 and concentrated *in vacuo*. The crude material was used for the consecutive step without further purification. Isolation of tert-butyl (4-(8-bromo-1-oxo-2,3,4,6-tetrahydro-1H-azepino[5,4,3-cd]indol-5-yl)benzyl)(methyl)carbamate was proved to be challenging. The best result was obtained by directly using this crude intermediate in the next step. To a two-necked round bottom flask under nitrogen atmosphere, the crude material, Bis(pinacolato)diboron (127 mg, 0.50 mmol), $Pd(dppf)Cl_2$ (18.3 mg ,0.03 mmol) and potassium acetate (147 mg, 1.50 mmol) were added. The reaction flask was then backfilled with nitrogen and degassed DMF (2.5 mL) was added. The reaction was heated to 80 °C in an oil bath and stirred for 16 hours. Upon completion, the reaction mixture was cooled to room temperature, passed through a plug of Celite and concentrated *in vacuo*. The crude was isolated by column chromatography (4% MeOH in DCM, Rf: 0.32) before purification by reverse phase HPLC to afford 4-(1-oxo-8-(4,4,5,5-

tetramethyl-1,3,2-dioxaborolan-2-yl)-2,3,4,6-tetrahydro-1*H*-azepino[5,4,3-*cd*]indol-5-yl)benzaldehyde as a light yellow solid (93 mg, 0.175 mmol, 35%). **^{1}H NMR** (500 MHz, MeOD) δ 8.24 (s, 1H), 8.01 (s, 1H), 7.62 (d, *J* = 7.8 Hz, 2H), 7.36 (d, *J* = 8.0 Hz, 2H), 4.48 (s, 2H), 3.56 – 3.51 (m, 2H), 3.14 (t, *J* = 4.9 Hz, 2H), 2.86 (s, 3H), 1.49* (s, br, 9H), 1.37 (s, 12H); **^{13}C NMR** ^{13}C NMR (126 MHz, MeOD) δ 174.1, 158.0, 139.2, 138.2, 137.9, 132.5, 130.4, 130.0, 129.6, 129.1, 124.1, 122.7, 122.0, 113.4, 85.0, 81.4, 53.3 (52.5*), 43.9, 34.6, 30.2, 28.7, 25.3; **IR** (cm^{-1}):2980, 1673, 1632, 1601, 1468, 1392, 1365, 1303, 1252, 1143, 870, 784; **HRMS** (ESI+) m/z: $[M+H]^+$ Calcd for $C_{30}H_{39}N_3O_5B$ 532.2981; Found 532.2979. **M.P.** 243-244 °C. Peaks in ^{1}H-NMR spectrum broad and split due to the presence of N-Boc rotamers (labelled with asterisks). Peaks in ^{13}C-NMR spectrum broad and split due to the presence of N-Boc rotamers (labelled with asterisks).

Methyl 6-fluoro-3-(2-nitroethyl)-1H-indole-4-carboxylate (**2.179**)

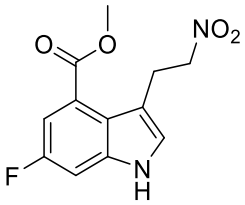

Methyl 6-fluoro-1*H*-indole-4-carboxylate (200 mg, 1.04 mmol) and 4-tert-butylcatechol (1.7 mg, 0.01 mmol) were dissolved in *p*-xylene (1.3 mL). 2-nitroethyl acetate (165 mg, 1.24 mmol) was added, and the mixture was heated at 145 °C in an oil bath for 3.5 hours. After cooled down to room temperature, the solvent was removed under reduced pressure. The crude was purified by flash column chromatography (20% EtOAc in pentane, Rf: 0.25) to yield methyl 6-fluoro-3-(2-nitroethyl)-1*H*-indole-4-carboxylate (154 mg, 0.58 mmol, 56%) as a pale-yellow solid. Data is in accordance with known literature.[2] **^{1}H NMR** (400 MHz, DMSO) δ 11.48 (s, 1H), 7.48 – 7.36 (m, 3H), 4.74 (t, *J* = 7.0 Hz, 2H), 3.89 (s, 3H); **^{13}C NMR** (126 MHz, DMSO) δ 167.0 (d, J_{CF} = 3.1 Hz), 157.0 (d, J_{CF} = 235.3 Hz), 137.9 (d, J_{CF} = 12.1 Hz), 128.3 (d, J_{CF} =

3.3 Hz), 123.2 (d, J_{CF} = 8.9 Hz), 120.8, 110.0 (d, J_{CF} = 26.2 Hz), 109.3, 102.3 (d, J_{CF} = 24.8 Hz), 76.7, 52.3, 25.2; **^{19}F NMR** (377 MHz, DMSO) δ -122.57 (dd, *J* = 10.2, 9.2 Hz).

8-Fluoro-2,3,4,6-tetrahydro-1*H*-azepino[5,4,3-*cd*]indol-1-one (**2.180**)

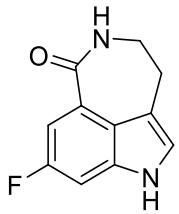

Methyl 6-fluoro-3-(2-nitroethyl)-1*H*-indole-4-carboxylate (150 mg, 0.56 mmol) was dissolved in MeOH (8.7 mL). 2M HCl (8.7 mL) was added, followed by addition of zinc dust (870 mg, 13.3 mmol) portionwise. The mixture was heated under reflux in an oil bath for 30 minutes and filtered directly. The filtrate was basified with 2M NaOH (10.5 mL) and the resultant mixture was filtered through a Büchner funnel. The filter cake was washed with MeOH (2 x 15 mL). MeOH was removed under reduced pressure. The aqueous phase was extracted with EtOAc (3 x 15 mL). The organic phases were combined, dried over Na_2SO_4 and concentrated *in vacuo*. The crude was purified by flash column chromatography (4% MeOH in CH_2Cl_2, Rf: 0.25) to yield 8-fluoro-2,3,4,6-tetrahydro-1*H*-azepino[5,4,3-*cd*]indol-1-one (107 mg, 0.52 mmol, 93%) as an white solid. Data is in accordance with known literature.[3] **^{1}H NMR** (500 MHz, DMSO) δ 11.19 (s, 1H), 8.17 (t, *J* = 5.8 Hz, 1H), 7.40 (dd, *J* = 11.0, 2.4 Hz, 1H), 7.33 (dd, *J* = 9.4, 2.4 Hz, 1H), 7.29 – 7.25 (m, 1H), 3.43 – 3.36 (m, 2H), 2.93 – 2.88 (m, 2H); **^{13}C NMR** (126 MHz, DMSO) δ 168.5 (d, J_{CF} = 2.7 Hz), 158.3 (d, J_{CF} = 233.8 Hz), 136.8 (d, J_{CF} = 12.2 Hz), 125.5 (d, J_{CF} = 9.0 Hz), 123.8 (d, J_{CF} = 3.2 Hz), 121.9, 114.5, 109.2 (d, J_{CF} = 25.9 Hz), 100.9 (d, J_{CF} = 26.1 Hz), 42.1, 28.0; **^{19}F NMR** (470 MHz, DMSO) δ -122.20 (dd, *J* = 11.0, 9.4 Hz).

5-Bromo-8-fluoro-2,3,4,6-tetrahydro-1*H*-azepino[5,4,3-*cd*]indol-1-one (**2.181**)

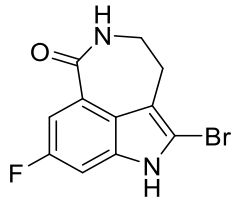

8-Fluoro-2,3,4,6-tetrahydro-1*H*-azepino[5,4,3-*cd*]indol-1-one (312 mg, 1.53 mmol) was dissolved in THF-DCM (1:1, 22 mL) and cooled to 0 °C in an ice bath. Pyridinium tribromide (538 mg, 1.68 mmol) was added in one portion. The mixture was stirred at 0 °C for 10 minutes and warmed to room temperature. After stirred at room temperature for 1 hour, the reaction was quenched with $NaHCO_3$ (20 mL) and extracted with EtOAc (3 x 20 mL). The combined organic phases were dried over Na_2SO_4 and the solvent was removed under reduced pressure. The crude was purified by column chromatography (3% MeOH in DCM, Rf: 0.28) to yield 5-bromo-8-fluoro-2,3,4,6-tetrahydro-1*H*-azepino[5,4,3-*cd*]indol-1-one as a off-white solid (373 mg, 1.32 mmol, 86 %). Data is in accordance with known literature.[3] **^{1}H NMR** (500 MHz, DMSO) δ 12.13 (s, 1H), 8.25 (d, *J* = 5.7 Hz, 1H), 7.42 (dd, *J* = 11.0, 2.4 Hz, 1H), 7.29 (dd, *J* = 9.1, 2.6 Hz, 1H), 3.41 (d, *J* = 4.1 Hz, 2H), 2.81 – 2.76 (m, 2H); **^{13}C NMR** (126 MHz, DMSO) δ 168.0 d, J_{CF} = 2.4 Hz, 158.4 (d, J_{CF} = 236.0 Hz), 136.6 (d, J_{CF} = 12.4 Hz), 124.9 (d, J_{CF} = 8.7 Hz), 121.9, 114.10, 109.9 (d, J_{CF} = 25.6 Hz), 109.2 (d, J_{CF} = 2.6 Hz) 100.6 (d, J_{CF} = 26.25 Hz), 41.3, 27.8; **^{19}F NMR** (377 MHz, DMSO) δ -120.91 (dd, *J* = 11.0, 9.1 Hz).

4-(8-Fluoro-1-oxo-2,3,4,6-tetrahydro-1*H*-azepino[5,4,3-*cd*]indol-5-yl)benzaldehyde (**2.162**)

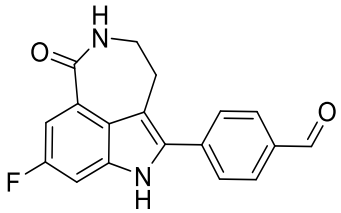

A two-necked round bottom flask, purged with nitrogen gas, was charged 5-bromo-8-fluoro-2,3,4,6-tetrahydro-1*H*-azepino[5,4,3-*cd*]indol-1-one (357 mg, 1.26 mmol). 4-Formylphenylboronic acid (439 mg, 1.89 mmol), Na_2CO_3 (267 mg, 2.52 mmol) and $Pd(PPh_3)_4$ (291 mg, 0.25 mmol) was added. The flask was flushed with nitrogen for three time. Degassed 1,4-dioxane (14 mL) and water (3.5 mL) were added. The mixture was stirred at 85 °C in an oil bath for 16 hours and cooled to room temperature. The organic solvent was removed *in vacuo*. The resultant mixture was diluted with H_2O (10 mL) and extracted with EtOAc (3 x 15 mL). The combined organic phases were dried over Na_2SO_4 and concentrated *in vacuo*. The crude was isolated by column chromatography (4% MeOH in DCM, Rf: 0.30) to afford 4-(8-fluoro-1-oxo-2,3,4,6-tetrahydro-1*H*-azepino[5,4,3-*cd*]indol-5-yl)benzaldehyde as a bright yellow solid (314 mg, 1.02 mmol, 81%). Data is in accordance with known literature.[3] **^{1}H NMR** (400 MHz, DMSO) δ 11.90 (s, 1H), 10.06 (s, 1H), 8.30 (t, *J* = 5.8 Hz, 1H), 8.09 – 8.01 (m, 2H), 7.90 – 7.82 (m, 2H), 7.46 (dd, *J* = 11.0, 2.4 Hz, 1H), 7.37 (dd, *J* = 9.1, 2.4 Hz, 1H) , 3.44 – 3.39 (m, 2H), 3.10 (bt, *J* = 3.5 Hz, 2H); **^{13}C NMR** (101 MHz, DMSO) δ 192.6, 168.1, 158.9 (d, J_{CF} = 236.1 Hz), 137.2, 134.8, 133.9 (d, J_{CF} = 3.5 Hz), 129.9, 128.7 (d, J_{CF} = 11.9 Hz), 128.2, 126.6 (d, J_{CF} = 8.7 Hz), 123.0, 114.3, 110.2 (d, J_{CF} = 25.8 Hz), 100.8 (d, J_{CF} = 25.7 Hz), 41.7, 28.9; **^{19}F NMR** (377 MHz, DMSO) δ -119.85 (dd, *J* = 11.0, 9.1 Hz).

8-Fluoro-5-(4-((methylamino)methyl)phenyl)-2,3,4,6-tetrahydro-1*H*-azepino[5,4,3-*cd*]indol-1-one (**2.147**)

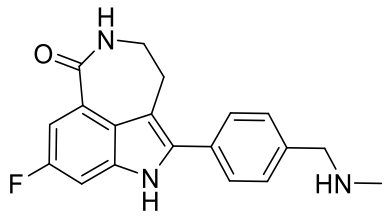

4-(8-Fluoro-1-oxo-2,3,4,6-tetrahydro-1*H*-azepino[5,4,3-*cd*]indol-5-yl)benzaldehyde (50.0 mg, 0.162 mmol) was suspended in MeOH (0.8 mL), followed by addition of methylamine (0.24 mL, 2M in THF). The mixture was stirred at room temperature for 2 hours and cooled to 0 °C in an ice bath. Sodium borohydride (30.6 mg, 0.810 mmol) was added slowly. The reaction was stirred at 0 °C for 1 hour. After gradually warmed to room temperature, the mixture was stirred for another hour. Upon completion, 1 M HCl was added to quench the reaction, which was then basified with 1 M NaOH. Organic solvent was removed *in vacuo*. The aqueous phase was extracted with EtOAc (3 x 10 mL). The combined organic phases were dried over Na_2SO_4 and concentrated *in vacuo*. The crude was isolated by column chromatography (NH_3/MeOH/DCM 1/4/95, Rf: 0.15) to afford 8-fluoro-5-(4-((methylamino)methyl)phenyl)-2,3,4,6-tetrahydro-1*H*-azepino[5,4,3-*cd*]indol-1-one as a light yellow solid (38.2 mg, 0.12 mmol, 73 %). Data is in accordance with known literature.[3] **^{1}H NMR** (400 MHz, DMSO) δ 11.66 (s, 1H), 8.24 (t, *J* = 5.8 Hz, 1H), 7.58 (d, *J* = 8.4, 2H), 7.46 (d, *J* = 8.1 Hz, 2H), 7.42 (d, *J* = 11.0, 2.4 Hz, 1H), 7.32 (dd, *J* = 9.2, 2.4 Hz, 1H), 3.70 (s, 2H), 3.43 – 3.35 (m, 2H), 3.07 – 3.00 (m, 2H), 2.29 (s, 3H); **^{13}C NMR** (101 MHz, DMSO) δ 168.4 (d, J_{CF} = 2.3 Hz), 158.3 (d, J_{CF} = 234.5 Hz), 140.5, 136.7 (d, J_{CF} = 12.2 Hz), 135.4 (d, J_{CF} = 3.3 Hz), 129.9, 128.3, 127.6, 125.8 (d, J_{CF} = 8.8 Hz), 123.2, 111.5, 109.5 (d, J_{CF} = 25.5 Hz), 100.5 (d, J_{CF} = 25.9 Hz), 54.7 (d, J_{CF} = 5.3 Hz), 41.9, 35.6, 28.8; **^{19}F NMR** (376 MHz, DMSO) δ -121.39 (dd, *J* = 11.0, 9.2 Hz).

Tert-butyl (4-(8-fluoro-1-oxo-2,3,4,6-tetrahydro-1H-azepino[5,4,3-cd]indol-5-yl)benzyl)(methyl)carbamate (**2.160**)

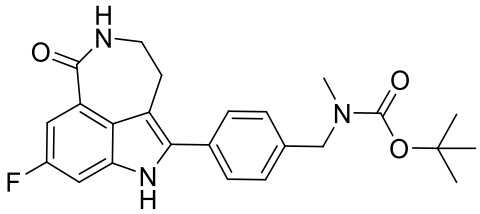

A two-necked round bottom flask, purged with nitrogen gas, was charged 5-bromo-8-fluoro-2,3,4,6-tetrahydro-1*H*-azepino[5,4,3-*cd*]indol-1-one (142 mg, 0.50 mmol). Tert-butyl methyl(4-(4,4,5,5-tetramethyl-1,3,2-dioxaborolan-2-yl)benzyl)carbamate (174 mg, 0.50 mmol), Na_2CO_3 (106 mg, 1.00 mmol) and $Pd(PPh_3)_4$ (116 mg, 0.1 mmol) was added. The flask was flushed with nitrogen for three time. Degassed 1,4-dioxane (14 mL) and water (3.5 mL) were added. The mixture was stirred at 85 °C in an oil bath for 16 hours and cooled to room temperature. The organic solvent was removed *in vacuo*. The resultant mixture was diluted with H_2O (10 mL) and extracted with EtOAc (3 x 15 mL). The combined organic phases were dried over Na_2SO_4 and concentrated *in vacuo*. The crude was isolated by column chromatography (4% MeOH in DCM, Rf: 0.30) to afford tert-butyl (4-(8-fluoro-1-oxo-2,3,4,6-tetrahydro-1*H*-azepino[5,4,3-*cd*]indol-5-yl)benzyl)(methyl)carbamate as a light yellow solid (154 mg, 0.36 mmol, 73%). **^{1}H NMR** (500 MHz, MeOD) δ 7.60 (d, *J* = 7.9 Hz, 2H), 7.52 (dd, *J* = 10.8, 2.4 Hz, 1H), 7.38 (d, *J* = 7.9 Hz, 2H), 7.30 (dd, *J* = 9.0, 2.4 Hz, 1H), 4.50 (s, 2H), 3.56 – 3.52 (m, 2H), 3.17 – 3.12 (m, 2H), 2.88 (s, 3H), 1.50* (s, br, 9H); **^{13}C NMR** (126 MHz, DMSO) δ 168.4 (d, *J* = 2.4 Hz), 158.4 (d, *J* = 234.6 Hz), 155.3 (154.8*), 137.8, 136.8 (d, *J* = 12.2 Hz), 135.1 (d, *J* = 3.4 Hz), 130.6, 128.0, 127.6, 125.9 (d, *J* = 8.6 Hz), 123.2, 111.8, 109.6 (d, *J* = 25.6 Hz), 100.6 (d, *J* = 25.8 Hz), 78.9, 51.6 (50.9*), 41.9, 34.0, 28.8, 28.1; **^{19}F NMR** (470 MHz, MeOD) δ -123.33 (dd, *J* = 9.9, 9.9 Hz); **IR** (cm^{-1}):3258, 1650, 1618, 1453, 1408, 1366, 1319, 1155, 1127, 881, 815; **HRMS** (ESI+) m/z: $[M+H]^+$ Calcd for $C_{24}H_{27}N_3O_3F$ 424.2031; Found 424.2030; **M.P.** 242-243 °C. Peaks in ^{1}H-NMR spectrum broad and split due

to the presence of N-Boc rotamers (labelled with asterisks). Peaks in ^{13}C-NMR spectrum broad and split due to the presence of N-Boc rotamers (labelled with asterisks).

Methyl 3-(2-nitroethyl)-1*H*-indole-4-carboxylate (**2.154**)

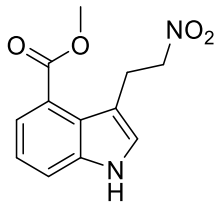

Methyl 1*H*-indole-4-carboxylate (182 mg, 1.04 mmol) and 4-tert-butylcatechol (1.7 mg, 0.01 mmol) were dissolved in *p*-xylene (1.3 mL). 2-nitroethyl acetate (165 mg, 1.24 mmol) was added, and the mixture was heated at 145 °C in an oil bath for 3.5 hours. After cooled down to room temperature, the solvent was removed under reduced pressure. The crude was purified by flash column chromatography (20% EtOAc in pentane, Rf: 0.30) to yield methyl methyl 3-(2-nitroethyl)-1*H*-indole-4-carboxylate (160 mg, 0.64 mmol, 62%) as a pale-yellow solid. Data is in accordance with known literature.[9] **^{1}H NMR** (400 MHz, DMSO) δ 11.43 (s, 1H), 7.63 (dd, *J* = 8.1, 1.1 Hz, 1H), 7.59 (dd, *J* = 7.4, 1.1 Hz, 1H), 7.38 (d, *J* = 2.6 Hz, 1H), 7.17 (dd, *J* = 8.1, 7.4 Hz, 1H), 4.74 (t, *J* = 7.0 Hz, 2H), 3.88 (s, 3H), 3.49 (d, *J* = 6.9 Hz, 2H); **^{13}C NMR** (101 MHz, DMSO) δ 168.1, 137.8, 127.6, 123.6, 122.4, 122.4, 120.2, 116.5, 109.1, 76.9, 51.9, 25.4.

2,3,4,6-Tetrahydro-1*H*-azepino[5,4,3-*cd*]indol-1-one (**2.155**)

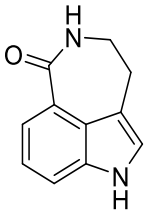

Methyl 3-(2-nitroethyl)-1*H*-indole-4-carboxylate (140 mg, 0.56 mmol) was dissolved in MeOH (8.7 mL). 2M HCl (8.7 mL) was added, followed by addition of zinc dust (870 mg, 13.3 mmol) portionwise. The mixture was heated under reflux in an oil bath for 30 minutes and filtered directly. The filtrate was basified with 2M NaOH (10.5 mL) and the resultant mixture was filtered through a Büchner funnel. The filter cake was washed with MeOH (2 x 15 mL). MeOH was removed under reduced pressure. The aqueous phase was extracted with EtOAc (3 x 15 mL). The organic phases were combined, dried over Na_2SO_4 and concentrated *in vacuo*. The crude was purified by flash column chromatography (4% MeOH in CH_2Cl_2, Rf: 0.28) to yield 2,3,4,6-tetrahydro-1*H*-azepino[5,4,3-*cd*]indol-1-one (70 mg, 0.38 mmol, 67%) as an white solid. Data is in accordance with known literature.[8] **^{1}H NMR** (400 MHz, DMSO) δ 11.11 (s, 1H), 7.99 (t, *J* = 5.8 Hz, 1H), 7.66 (dd, *J* = 7.5, 1.0 Hz, 1H), 7.52 (dd, *J* = 8.0, 1.0 Hz, 1H), 7.27 – 7.24 (m, 1H), 7.17 (t, *J* = 7.7 Hz, 1H), 3.44 – 3.36 (m, 2H), 2.96 – 2.86 (m, 1H); **^{13}C NMR** (101 MHz, DMSO) δ 169.8, 136.6, 124.8, 124.5, 123.1, 121.9, 120.6, 114.7, 114.3, 42.2, 28.3.

6-(triisopropylsilyl)-2,3,4,6-tetrahydro-1H-azepino[5,4,3-cd]indol-1-one (**2.165**)

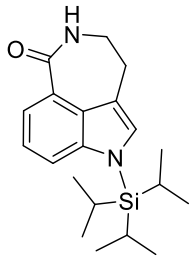

2,3,4,6-Tetrahydro-1*H*-azepino[5,4,3-*cd*]indol-1-one (0.350 g, 1.88 mmol) was dissolved in anhydrous THF (9.5 mL) and cooled to -78 °C. LiHMDS (1 M in THF, 2.26 mL, 2.26 mmol) was added dropwise. The mixture was stirred at -78 °C for 1 hour. TIPSCl (0.402 mL, 1.88 mmol) was added dropwise. After stirred for 1 hour at -78 °C, the mixture was warm to room

temperature. The reaction was quenched with water (10 mL) and extracted with EtOAc (3 x 10 mL). The combined organic phases were dried over Na_2SO_4 and the solvent was removed under reduced pressure. The crude was purified by column chromatography (4 % MeOH in DCM, Rf: 0.40) to yield 6-(triisopropylsilyl)-2,3,4,6-tetrahydro-1H-azepino[5,4,3-cd]indol-1-one as a white solid (0.490 g, 1.43 mmol, 76.1 %).

^{1}H NMR (400 MHz, $CDCl_3$) δ 7.99 (dd, *J* = 7.6, 0.8 Hz, 1H), 7.62 (dd, *J* = 8.3, 0.9 Hz, 1H), 7.40 (t, *J* = 6.0 Hz, 1H), 7.24 (t, *J* = 8.1 Hz, 1H), 7.08 (s, 1H), 3.66 – 3.56 (m, 2H), 3.10 – 3.03 (m, 2H), 1.68 (hept, *J* = 7.5 Hz, 3H), 1.13 (d, *J* = 7.5 Hz, 18H); **^{13}C NMR** (101 MHz, $CDCl_3$) δ 171.9, 141.6, 128.9, 124.6, 123.7, 121.4, 117.7, 117.5, 43.1, 28.7, 18.2 (6C), 12.9 (3C); **HRMS** (ESI+) m/z: $[M+H]^+$ Calcd for $C_{20}H_{31}N_2OSi$ 343.2200; Found 343.2201; **M.P.**: 192 – 194 ˚C

8-(4,4,5,5-tetramethyl-1,3,2-dioxaborolan-2-yl)-6-(triisopropylsilyl)-2,3,4,6-tetrahydro-1H-azepino[5,4,3-cd]indol-1-one (**2.164**)

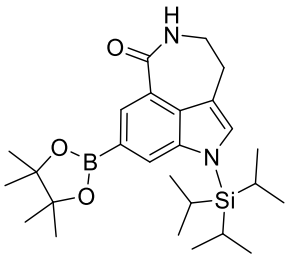

A flame-dried pressure tube under nitrogen was charged with 6-(triisopropylsilyl)-2,3,4,6-tetrahydro-1H-azepino[5,4,3-cd]indol-1-one (343 mg, 1.00 mmol), $[Ir(cod)OMe]_2$ (33.1 mg, 0.050 mmol), 1,10-phenanthroline (18.0 mg, 0.100 mmol) and B_2pin_2 (1.02 g, 4.00 mmol). The tube was purged with nitrogen gas. Hexane (6 mL) was added followed by immediate addition of HBpin (0.036 mL, 0.250 mmol). The cap was screwed tightly and the mixture was heated at 80 °C for 24 hours. The mixture was then allowed to cool to room temperature. The reaction

was quenched with $NaHCO_3$ (10 mL) and extracted with EtOAc (3 x 10 mL). The combined organic phases were dried over Na_2SO_4 and the solvent was removed under reduced pressure. The crude was purified by column chromatography (4 % MeOH in $CHCl_3$, Rf: 0.40) to yield 8-(4,4,5,5-tetramethyl-1,3,2-dioxaborolan-2-yl)-6-(triisopropylsilyl)-2,3,4,6-tetrahydro-1H-azepino[5,4,3-cd]indol-1-one as a white solid (302 mg, 0.644 mmol, 64.4 %).

^{1}H NMR (400 MHz, $CDCl_3$) δ 8.42 (d, *J* = 0.7 Hz, 1H), 8.03 (d, *J* = 0.8 Hz, 1H), 7.14 (s, 1H), 6.45 (t, *J* = 6.0 Hz, 1H), 3.63 – 3.53 (m, 2H), 3.12 – 2.98 (m, 2H), 1.69 (hept, *J* = 7.5 Hz, 3H), 1.33 (s, 12H), 1.14 (d, *J* = 7.5 Hz, 18H); **^{13}C NMR** (101 MHz, $CDCl_3$) δ 171.7, 141.4, 130.8, 130.3, 130.2, 124.0, 123.7, 117.7, 83.7, 43.2, 28.8, 25.1, 18.3, 13.0; **HRMS** (ESI+) m/z: $[M+H]^+$ Calcd for $C_{26}H_{42}BN_2O_3Si$ 469.3052; Found 469.3054.

8-(4,4,5,5-tetramethyl-1,3,2-dioxaborolan-2-yl)-2,3,4,6-tetrahydro-1H-azepino[5,4,3-cd]indol-1-one (**2.163**)

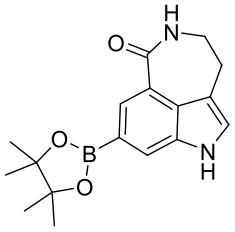

One-pot procedure:

A flame-dried pressure tube under nitrogen was charged with 6-(triisopropylsilyl)-2,3,4,6-tetrahydro-1H-azepino[5,4,3-cd]indol-1-one (343 mg, 1.00 mmol), $[Ir(cod)OMe]_2$ (33.1 mg, 0.050 mmol), 1,10-phenanthroline (18.0 mg, 0.100 mmol) and B_2pin_2 (1.02 g, 4.00 mmol). The tube was purged with nitrogen gas. Hexane (6 mL) was added followed by immediate addition of HBpin (0.036 mL, 0.250 mmol). The cap was screwed tightly and the mixture was heated at 80 °C for 24 hours. The mixture was then allowed to cool to room temperature. THF (6 mL) was added, followed by TBAF (2.8 mL, 1 M in THF, 2.8 mmol). The mixture was stirred at

room temperature for 8 hours. The reaction was quenched with $NaHCO_3$ (10 mL) and extracted with EtOAc (3 x 10 mL). The combined organic phases were dried over Na_2SO_4 and the solvent was removed under reduced pressure. The crude was purified by column chromatography (4 % MeOH in DCM, Rf: 0.35) to yield 8-(4,4,5,5-tetramethyl-1,3,2-dioxaborolan-2-yl)-2,3,4,6-tetrahydro-1H-azepino[5,4,3-cd]indol-1-one as a yellow solid (312 mg, 0.700 mmol, 70.0 %). **^{1}H NMR** (400 MHz, $CDCl_3$) δ 8.45 (d, *J* = 0.9 Hz, 1H), 8.22 (s, 1H), 7.99 (d, *J* = 0.9 Hz, 1H), 7.13 (dt, *J* = 2.3, 1.1 Hz, 1H), 6.38 (t, *J* = 5.8 Hz, 1H), 3.65 – 3.56 (m, 2H), 3.10 – 3.03 (m, 2H), 1.35 (s, 12H); **IR** (cm^{-1}): 2977, 2930, 1636, 1607, 1507, 1473, 1455, 1372, 1342, 1321, 1253, 1143, 1166, 995, 852, 693; **HRMS** (ESI+) m/z: $[M+H]^+$ Calcd for $C_{17}H_{22}N_2O_3{}^{10}B$ 313.1718; Found 313.1718.

5,8-bis(4,4,5,5-tetramethyl-1,3,2-dioxaborolan-2-yl)-2,3,4,6-tetrahydro-1H-azepino[5,4,3-cd]indol-1-one (**2.162**)

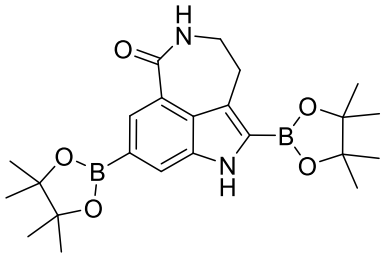

A flame-dried pressure tube under nitrogen was charged with 8-(4,4,5,5-tetramethyl-1,3,2-dioxaborolan-2-yl)-2,3,4,6-tetrahydro-1H-azepino[5,4,3-cd]indol-1-one (156 mg, 0.35 mmol), $[Ir(cod)OMe]_2$ (12.0 mg, 0.018 mmol), 1,10-phenanthroline (6.3 mg, 0.035 mmol) and B_2pin_2 (357 mg, 1.40 mmol). The tube was purged with nitrogen gas. Hexane-THF (2:1, 3 mL) was added. The cap was screwed tightly and the mixture was heated at 80 °C for 24 hours. The mixture was then allowed to cool to room temperature. Solvent was removed under nitrogen flow. The crude was purified by column chromatography (4 % MeOH in DCM, Rf: 0.38) to

yield 5,8-bis(4,4,5,5-tetramethyl-1,3,2-dioxaborolan-2-yl)-2,3,4,6-tetrahydro-1H-azepino[5,4,3-cd]indol-1-one as a yellow solid (58.2 mg, 0.133 mmol, 38.1 %) and the unreacted starting material was recovered.

^{1}H NMR (400 MHz, $CDCl_3$) δ 8.94 (s, 1H), 8.37 (d, 1H), 7.95 (d, *J* = 0.8 Hz, 1H), 6.97 (t, *J* = 5.9 Hz, 1H), 3.61 – 3.52 (m, 2H), 3.27 (s, 2H), 1.33 (s, 12H), 1.33 (s, 12H); **^{13}C NMR** (101 MHz, $CDCl_3$) δ 173.4, 140.4, 128.8, 127.9, 127.0, 123.7, 122.9, 117.9, 83.7, 85.2 43.2, 28.8, 19.3 16.2; **IR** (cm^{-1}): 2978, 1634, 1506, 1474, 1372, 1327, 1142, 1009, 981, 951, 851, 673; **HRMS** (ESI+) m/z: $[M+H]^+$ Calcd for $C_{23}H_{33}N_2O_5{}^{10}B_2$ 439.2574; Found 439.2572.

5-Bromo-2,3,4,6-tetrahydro-1*H*-azepino[5,4,3-*cd*]indol-1-one (**2.156**)

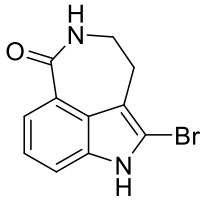

2,3,4,6-Tetrahydro-1*H*-azepino[5,4,3-*cd*]indol-1-one (285 mg, 1.53 mmol) was dissolved in THF-DCM (1:1, 22 mL) and cooled to 0 °C in an ice bath. Pyridinium tribromide (538 mg, 1.68 mmol) was added in one portion. The mixture was stirred at 0 °C for 10 minutes and warmed to room temperature. After stirred at room temperature for 1 hour, the reaction was quenched with $NaHCO_3$ (20 mL) and extracted with EtOAc (3 x 20 mL). The combined organic phases were dried over Na_2SO_4 and the solvent was removed under reduced pressure. The crude was purified by column chromatography (3% MeOH in DCM, Rf: 0.28) to yield 5-bromo-2,3,4,6-tetrahydro-1*H*-azepino[5,4,3-*cd*]indol-1-one as a off-white solid (306 mg, 1.16 mmol, 76%). Data is in accordance with known literature.[8] **^{1}H NMR** (400 MHz, DMSO) δ 12.00 (s, 1H), 8.10 (t, J = 5.7 Hz, 1H), 7.70 (dd, J = 7.6, 1.0 Hz, 1H), 7.48 (dd, J = 8.1, 1.0 Hz,

1H), 7.20 (t, J = 7.8 Hz, 1H), 3.47 – 3.33 (m, 2H), 2.86 – 2.74 (m, 2H); **^{13}C NMR** (101 MHz, DMSO) δ 169.3, 136.5, 124.7, 123.7, 122.6, 121.2, 114.1, 113.9, 109.2, 41.4, 28.1.

4-(1-Oxo-2,3,4,6-tetrahydro-1*H*-azepino[5,4,3-*cd*]indol-5-yl)benzaldehyde (**2.157**)

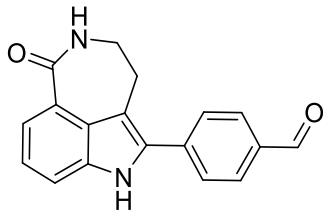

A two-necked round bottom flask, purged with nitrogen gas, was charged 5-bromo-2,3,4,6-tetrahydro-1*H*-azepino[5,4,3-*cd*]indol-1-one (167 mg, 0.63 mmol). 4-Formylphenylboronic acid (220 mg, 0.95 mmol), Na_2CO_3 (134 mg, 1.26 mmol) and $Pd(PPh_3)_4$ (146 mg, 0.13 mmol) was added. The flask was flushed with nitrogen for three time. Degassed 1,4-dioxane (7 mL) and water (1.8 mL) were added. The mixture was stirred at 85 °C in an oil bath for 16 hours and cooled to room temperature. The organic solvent was removed *in vacuo*. The resultant mixture was diluted with H_2O (10 mL) and extracted with EtOAc (3 x 15 mL). The combined organic phases were dried over Na_2SO_4 and concentrated *in vacuo*. The crude was isolated by column chromatography (4% MeOH in DCM, Rf: 0.32) to afford 4-(1-oxo-2,3,4,6-tetrahydro-1*H*-azepino[5,4,3-*cd*]indol-5-yl)benzaldehyde as a bright yellow solid (133 mg, 0.46 mmol, 73%). Data is in accordance with known literature.[8] **^{1}H NMR** (400 MHz, MeOD) δ 10.03 (s, 1H), 8.04 (d, *J* = 8.5, 2H), 7.87 – 7.79 (m, 3H), 7.64 (dd, *J* = 8.1, 1.0 Hz, 1H), 7.30 (dd, *J* = 7.8, 7.8 Hz, 1H), 3.62 – 3.53 (m, 2H), 3.28 – 3.13 (m, 2H); **^{13}C NMR** (101 MHz, MeOD) δ 193.6, 173.8, 139.5, 138.7, 136.7, 135.3, 131.1, 129.6, 128.9, 125.4, 124.4, 123.4, 116.6, 115.3, 43.8, 30.4.

Tert-butyl methyl(4-(1-oxo-2,3,4,6-tetrahydro-1*H*-azepino[5,4,3-*cd*]indol-5-yl)benzyl)carbamate (**2.159**)

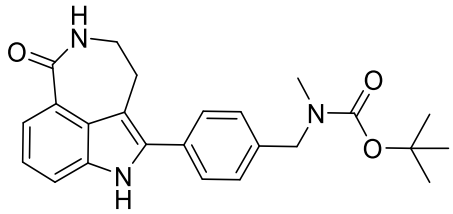

A two-necked round bottom flask, purged with nitrogen gas, was charged 5-bromo-2,3,4,6-tetrahydro-1*H*-azepino[5,4,3-*cd*]indol-1-one (66.3 mg, 0.25 mmol). Tert-butyl methyl(4-(4,4,5,5-tetramethyl-1,3,2-dioxaborolan-2-yl)benzyl)carbamate (87.2 mg, 0.25 mmol), Na_2CO_3 (53.0 mg, 1.00 mmol) and $Pd(PPh_3)_4$ (57.8 mg, 0.05 mmol) was added. The flask was flushed with nitrogen for three time. Degassed 1,4-dioxane (7 mL) and water (1.8 mL) were added. The mixture was stirred at 85 °C in an oil bath for 16 hours and cooled to room temperature. The organic solvent was removed *in vacuo*. The resultant mixture was diluted with H_2O (10 mL) and extracted with EtOAc (3 x 10 mL). The combined organic phases were dried over Na_2SO_4 and concentrated *in vacuo*. The crude was isolated by column chromatography (4% MeOH in DCM, Rf: 0.33) to afford tert-butyl (4-(1-oxo-2,3,4,6-tetrahydro-1*H*-azepino[5,4,3-*cd*]indol-5-yl)benzyl)(methyl)carbamate as a light yellow solid (85.0 mg, 0.21 mmol, 84%). **^{1}H NMR** (500 MHz, MeOD) δ 7.79 (dd, *J* = 7.5, 1.0 Hz, 1H), 7.65 – 7.57 (m, 3H), 7.38 (d, *J* = 8.1 Hz, 2H), 7.25 (dd, *J* = 7.8, 7.8 Hz, 1H), 4.50 (s, 2H), 3.57 – 3.52 (m, 2H), 3.16 (t, *J* = 4.9 Hz, 2H), 2.87 (s, 3H), 1.49* (s, br, 9H); **^{13}C NMR** (126 MHz, MeOD) δ 174.2, 157.6, 139.0, 138.2, 136.6, 132.7, 129.5, 128.8, 128.0, 124.7, 124.0, 122.4, 116.3, 113.0, 81.4, 53.4 (52.5*), 44.0, 34.6, 30.2, 28.7; **IR** (cm^{-1}):3262, 2978, 1666, 1643, 1461, 1406, 1366, 1256, 1151, 881, 817, 747; **HRMS** (ESI+) m/z: $[M+H]^+$ Calcd for $C_{24}H_{28}N_3O_3$ 406.2125; Found 406.2121; **M.P.** 244-245 °C. Peaks in ^{1}H-NMR spectrum broad and split due to the presence of N-Boc rotamers (labelled with asterisks). Peaks in ^{13}C-NMR spectrum broad and split due to the presence of N-Boc rotamers (labelled with asterisks).

4.3 Radiochemistry for Chapter II

4.3.1 General Information

[^{18}F]Fluoride was produced by Alliance Medical (UK) via the ^{18}O(p,n)^{18}F reaction and delivered as [^{18}F]fluoride in [^{18}O]water. Radiosynthesis and azeotropic drying were performed on a NanoTek® automated microfluidic device (Advion). HPLC analysis was performed with a Dionex Ultimate 3000 dual channel HPLC system equipped with shared autosampler, parallel UV-detectors and LabLogic NaI/PMT-radiodetectors with Flowram analog output. Due to the separation of the modules the radio-signal is offset by 0.1-0.3 min from the UV signal.

All ^{18}F-radiolabelled compounds were characterized by comparing the radio-HPLC trace with the HPLC UV-trace of an authentic reference sample, which was synthesized as described in Sections 2. Radiochemical yields (RCY) were calculated by comparing the integration of the product radio-HPLC peak with the integration of all radio-HPLC peaks. Activity yield (AY) was determined by dividing the isolated activity by the activity of dry [^{18}F]Fluoride after elution from the QMA cartridge and azeotropic drying. All reported AYs are non-decay corrected.

4.3.2 Procedure for preparation of a solution of [^{18}F]KF/K_{222} in MeCN:

A solution of Kryptofix 222 (6.3 mg), $K_2C_2O_4$ (1.0 mg) and K_2CO_3 (0.1 mg) in 1 mL of MeCN/H_2O, 4:1 was freshly prepared. [^{18}F]Fluoride (3.0-4.0 GBq) was separated from ^{18}O-enriched-water using a Sep-Pak Accell Plus QMA Carbonate Plus Light Cartridge (46 mg; quaternary methyl ammonium; Waters, cat. no. 186004540) and subsequently released with 900 µL (in 6 x 150 µL portions) of the K_{222}/ $K_2C_2O_4$/K_2CO_3 solution into a 5 mL V-vial containing a magnetic stir bar in the concentrator. The solution was dried with five cycles of azeotropic drying with MeCN (5 x 200 µl) under a flow of N_2 at 105°C. The dried [^{18}F]KF/K_{222} residue was redissolved in anhydrous MeCN (500 - 1000 µL).

This elution method was optimized in the work of radiosynthesis of [^{18}F]olaparib, both manual and automated.[6,7]

4.3.3 General procedure for small scale screening experiments with 4-(4,4,5,5-tetramethyl1,3,2-dioxaborolan-2-yl)benzonitrile:

A solution of [^{18}F]KF/K_{222} in MeCN (20 - 30 MBq, 10-50 µL) was dispensed into a V-vial containing a magnetic stirrer bar. A solution containing $Cu(OTf)_2(py)_4$ (0.01 mmol), 4-(4,4,5,5-tetramethyl-1,3,2-dioxaborolan-2-yl)benzonitrile (2.3 mg, 0.01 mmol) and the tricyclic indole additive (0.01 mmol) in DMF (300 µL) was added via syringe. Air (20 mL) was flushed through the reaction vial using a syringe. The sealed vial was heated at 110 °C for 20 min. An aliquot was removed for analysis by radio-HPLC for radiochemical conversion and product identity. Analysis was performed using a Synergi 4 µm HydroRP 80Å column, 150 x 4.6 mm, eluted with MeCN/H_2O at a flow rate 1 mL/min, monitoring with UV (220 nm) and radioactive traces.

HPLC gradient for analysis of small scale screening experiments:

MeCN/H_2O, 1 mL/min, Synergi 4 µm HydroRP 80 Å column, 150 x 4.6 mm, 0 - 1 min (5% MeCN) isocratic, 1 - 10 min (5% MeCN to 95% MeCN) linear increase, 10 - 13 min (95% MeCN) isocratic, 13 - 15 min (5% MeCN) isocratic.

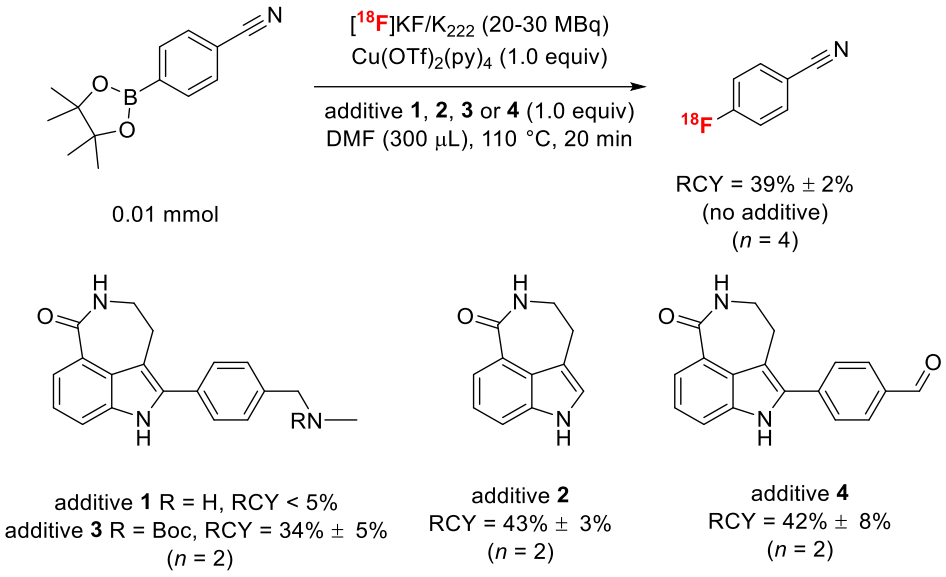

Supplementary Scheme 1. Small scale screening experiments with 4-(4,4,5,5-tetramethyl1,3,2-dioxaborolan-2-yl)benzonitrile

4.3.4 General procedure for small scale optimizing synthesis of [^{18}F] tert-butyl (4-(8-fluoro-1-oxo-2,3,4,6-tetrahydro-1H-azepino[5,4,3-cd]indol-5-yl)benzyl)(methyl)carbamate:

A solution of [^{18}F]KF/K_{222} in MeCN (20 - 30 MBq, 10-50 µL) was dispensed into a V-vial containing a magnetic stirrer bar. A solution containing Cu(II) catalyst, tert-butyl methyl(4-(1-oxo-8-(4,4,5,5-tetramethyl-1,3,2-dioxaborolan-2-yl)-2,3,4,6-tetrahydro-1H-azepino[5,4,3-cd]indol-5-yl)benzyl)carbamate (5.3 mg, 0.01 mmol) in solvent (300 µL) was added *via* syringe. Air (20 mL) was flushed through the reaction vial using a syringe. The sealed vial was heated at 120 °C for 20 min. An aliquot was removed for analysis by radio-HPLC for radiochemical conversion and product identity. Analysis was performed using a Gemini LC column, 150 x 4.6 mm, eluted with MeCN/H_2O buffer at a flow rate 1 mL/min, monitoring with UV (220 nm) and radioactive traces. TFA (300 µL) was added *via* syringe to the mixture. The sealed vial was heated at 120 °C for 20 min. Analysis was performed using a Gemini LC column, 150 x 4.6 mm, eluted with MeCN/H_2O buffer at a flow rate 1 mL/min, monitoring with UV (220 nm) and radioactive traces.

HPLC gradient for analysis of small scale screening experiments:

Preparation of H_2O (buffer) for analytical radio-HPLC: 25 mM aqueous NH_4HCO_2 (pH 9.2 adjusted with 35% aqueous ammonia, 10 mL/L)

MeCN/H_2O, 1 mL/min, Gemini LC column, 150 x 4.6 mm, 0 - 12 min (5-95% MeCN) gradient, 12 - 20 min (95% MeCN) isocratic, 20 - 22 min (5% MeCN) isocratic.

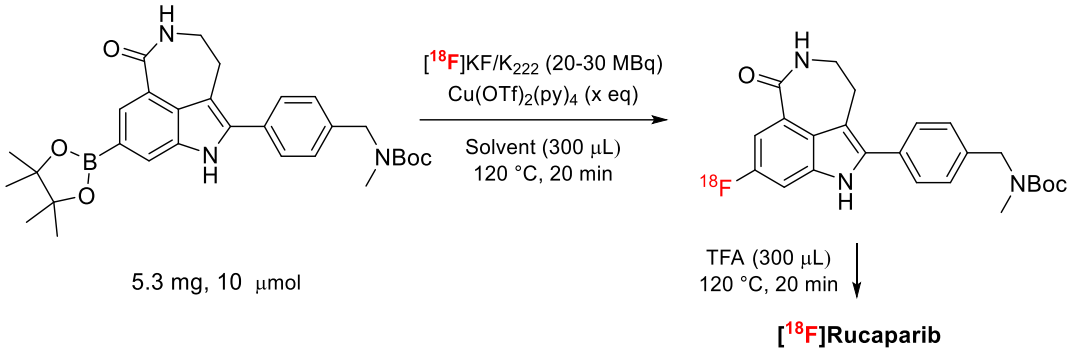

Entry	Solvent	$Cu(OTf)_2(py)_4$	RCY (n = 2)[a]
1	DMI	1 equiv	42% ± 5%
2	DMI	2 equiv	39% ± 1%
3	DMI	3 equiv	25% ± 3%
4	DMA	2 equiv	29% ± 2%
5	DMF	2 equiv	7% ± 0%
6	DMI	2 equiv[b]	1% ± 0%

Supplementary Table 1. Small scale optimizing synthesis of [18F] tert-butyl (4-(8-fluoro-1-oxo-2,3,4,6-tetrahydro-1H-azepino[5,4,3-cd]indol-5-yl)benzyl)(methyl)carbamate. a) RCY = radiochemical yield, determined by integration of the radio-HPLC trace, b) Reaction performed with the copper complex $Cu(OTf)_2(impy)_4$; (impy = imidazo[1,2-*b*]pyridazine). K_{222} = 4,7,13,16,21,24-Hexaoxa-1,10-diazabicyclo[8.8.8]hexacosane (Kryptofix 222). DMI = 1,3-Dimethyl-2-imidazolidinone. DMA = *N*,*N*-Dimethylacetamide. DMF = *N*,*N*-dimethylformamide.

4.3.5 General procedure for small scale optimizing synthesis of [^{18}F]4-(8-fluoro-1-oxo-2,3,4,6-tetrahydro-1H-azepino[5,4,3-cd]indol-5-yl)benzaldehyde:

A solution of [^{18}F]KF/K_{222} in MeCN (20 - 30 MBq, 10-50 µL) was dispensed into a V-vial containing a magnetic stirrer bar. A solution containing Cu(II) catalyst, 4-(1-oxo-8-(4,4,5,5-tetramethyl-1,3,2-dioxaborolan-2-yl)-2,3,4,6-tetrahydro-1*H*-azepino[5,4,3-*cd*]indol-5-yl)benzaldehyde (4.2 mg, 0.01 mmol) in solvent (300 µL) was added *via* syringe. Air (20 mL)

was flushed through the reaction vial using a syringe. The sealed vial was heated at 120 °C for 20 min. An aliquot was removed for analysis by radio-HPLC for radiochemical conversion and product identity. Analysis was performed using a Phenomenex Synergi 4µm Hydro-RP 80 Å LC column, 150 x 4.6 mm, eluted with MeCN/H_2O at a flow rate 1 mL/min, monitoring with UV (220 nm) and radioactive traces.

HPLC gradient for analysis of small scale screening experiments:

MeCN/H_2O, 1 mL/min, Phenomenex Synergi 4µm Hydro-RP 80 Å LC column, 150 x 4.6 mm, 0 - 16 min (34% MeCN) isocratic, 16 - 22 min (95% MeCN) isocratic, 22 - 24 min (34% MeCN) isocratic.

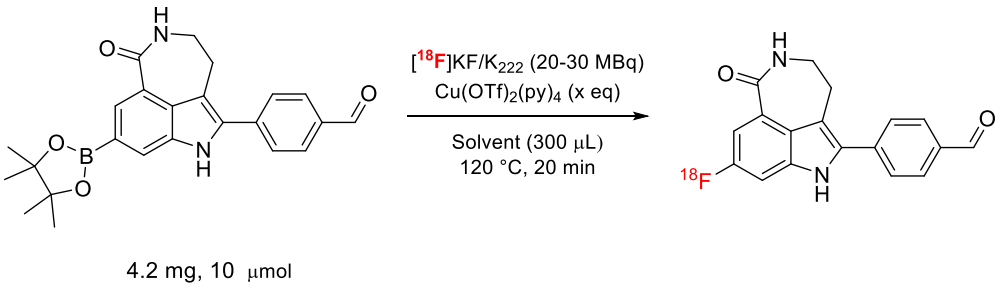

Entry	Solvent	$Cu(OTf)_2(py)_4$	RCY (n = 2)[a]
1	DMI	1 equiv	73% ± 7%
2	DMI	2 equiv	80% ± 3%
3	DMI	3 equiv	56% ± 1%
4	DMA	2 equiv	50% ± 5%
5	DMF	2 equiv	13% ± 3%
6	DMI	2 equiv[b]	14% ± 7%

Supplementary Table 2. Small scale optimizing synthesis of [^{18}F]4-(8-fluoro-1-oxo-2,3,4,6-tetrahydro-1*H*-azepino[5,4,3-*cd*]indol-5-yl)benzaldehyde. a) RCY = radiochemical yield, determined by integration of the radio-HPLC trace, b) Reaction performed with the copper complex $Cu(OTf)_2(impy)_4$; (impy = imidazo[1,2-*b*]pyridazine). K_{222} = 4,7,13,16,21,24-Hexaoxa-1,10-diazabicyclo[8.8.8]hexacosane (Kryptofix 222). DMI = 1,3-Dimethyl-2-imidazolidinone. DMA = *N*,*N*-Dimethylacetamide. DMF = *N*,*N*-dimethylformamide.

4.3.6 Procedure for [^{18}F]rucaparib manual radiosynthesis:

Reagent setup

Elution solutions for [^{18}F]fluoride: Prepare fresh solutions of Kryptofix 222 (6.3 mg) in MeCN (800 µL) in a 1 mL V-Vial, and K_2CO_3(aq) (1 mg/mL) and $K_2C_2O_4$(aq) (10 mg/mL) in two separate 10 mL vials. Add 100 µL each of the K_2CO_3 and $K_2C_2O_4$ aqueous solutions to the previous 1 mL V-Vial.

Buffer for semi-preparative radio-HPLC: Buffer is 71% (vol/vol) 25 mM aqueous NH_4HCO_2 (pH 9.2 adjusted with 35% aqueous ammonia, 10 mL/L) in MeCN. Dissolve 1.12 g of NH_4HCO_2 and 7 mL of 35% aqueous ammonia in 703 mL of H_2O and add 290 mL of MeCN.

Equipment setup

QMA Sep-Pak cartridge (Sep Pak Accell Plus QMA Carbonate Plus Light Cartridge, 46 mg Sorbent per Cartridge, 40 µm particle size, Waters) preconditioning: Use a 10 mL syringe to slowly pass 10 mL of H_2O through the cartridge to ensure a dropwise elution.

C18 Plus cartridge preconditioning: Use a 2 mL syringe to slowly pass 2 mL of EtOH through the cartridge, and then use a 10-mL syringe to pass 10 mL of H_2O through the cartridge to ensure a dropwise elution.

Preparation of vials

● Drying and reaction vial. Place a small stir bar inside a 5-mL V-Vial, seal it with a cap holding a PTFE/silicone septum (silicone layer side facing inside the vial) and install a vent needle.

● Crude mixture filtration vial. Place a small stir bar inside a 5-mL V-Vial, seal it with a cap holding a PTFE/silicone septum (silicone layer side facing inside the vial) and install a vent needle.

● Collection vial for semi-preparative radio-HPLC. Add H_2O (15 mL) to a 35 mL glass vial, seal with a cap holding a PTFE/silicone septum (silicone layer side facing inside the vial) and install a vent needle.

● Waste vial for transfer. Seal a 35-mL glass vial with a septum-holding cap and install a vent needle.

● Rucaparib delivery vial. Seal a 3-mL Wheaton V-Vial with a crimp cap and install a vent needle.

Preparation of the analytical radio-HPLC system for quality control

Condition the 150 × 4.6-mm Gemini LC column with 34% MeCN and 66% H_2O (buffer) (vol/vol), using a flow rate of 1 mL/min for 30 min. Then connect a 5-mL V-Vial to the collection valve for peak collection and molar activity determination. Use the following radio-HPLC method for quality control: isocratic flow of 34% MeCN–66% H_2O (buffer) with a flow rate of 1 mL/min.

H_2O (buffer): 25 mM aqueous NH_4HCO_2 (pH 9.2 adjusted with 35% aqueous ammonia, 10 mL/L) Dissolve 1.58 g of NH_4HCO_2 and 10 mL of 35% aqueous ammonia in 990 mL of H_2O

Preparation of the semi-preparative radio-HPLC system for isolation

Install the 250 × 10-mm Gemini LC column and condition it with buffer, using a flow rate of 1 mL/min for 90 min. Then purge the collection line with the buffer and connect to the [^{18}F]rucaparib collection vial containing 15 mL of H_2O. Use the following radio-HPLC method for isolation: isocratic flow of buffer with a flow rate of 4 mL/min.

Radiosynthesis

1 Place the drying and reaction vial inside the NanoTek concentrator module and connect the N_2 line, as well as the two lines required for azeotropic drying (^{18}F-elution and MeCN).

2 Trap and dry [^{18}F]fluoride using a NanoTek automated microfluidic device syringe pump. Trap the [^{18}F]fluoride delivered in an [^{18}O]H_2O solution on a Sep-Pak QMA cartridge by taking up the solution of [^{18}F]fluoride and passing it through the cartridge (7 × 1 mL, 2 mL/min).

3 Rinse the [^{18}O]H_2O vial with MeCN (2 × 400 μL) and pass the contents through the cartridge (2 mL/min).

4 Elute [^{18}F]fluoride from the cartridge with an elution solution of Kryptofix 222/$K_2C_2O_4$/K_2CO_3 (900 μL, 6 × 150-μL portions) into a 5-mL V-Vial.

5 Rinse the cartridge with MeCN (200 μL). Dry the [^{18}F]fluoride azeotropically at 105 °C with MeCN (1 mL, 5 × 200-μL portions) under a flow of N_2.

6 Charge a 1-mL glass vial with the rucaparib Bpin precursor (8.3 mg, 0.02 mmol) and $Cu(OTf)_2(py)_4$ (27 mg, 0.04 mmol), and add 300 μL of DMI.

7 Use a 1-mL syringe to transfer the solution from Step 6 to the 5-mL V-Vial containing dry [^{18}F]KF.

8 Use a 20-mL syringe to add 20 mL of air to the reaction vial. Air should not be bubbled inside the reaction mixture.

9 Remove the vent needle, place the vial inside the NanoTek concentrator module and stir it for 20 min at 120 °C.

10 Place the reaction vial in a vial holder inside the hot cell, install a vent needle, add through 1-mL syringe $NaBH_3CN$ (12.6 mg, 0.2 mmol) and $MeNH_2$ methanolic (0.25 ml, 2.0 mmol, 33 wt. % in EtOH, 8 M) previously dissolved together. Place the reaction vial inside the NanoTek concentrator module, and stir for 20 min at 120 °C.

11 Remove the reaction vial from the NanoTek concentrator module and cool for 1 min; install a vent needle and connect a let evaporate the remaining $MeNH_2$ in EtOH. After that, add through a 1-mL syringe 200 μL of DMSO and 300 μL of MeCN to solubilise all the reaction mixture.

12 With the help of a 2-mL syringe remove all the reaction mixture and pass it through a filter (VWR syringe filter, PP membrane, 0.45 μm pore size, 25 mm diameter) in a new 5-mL-V-Vial with a stir bar inside.

13 Use 1-mL syringe containing 1 mL of MeCN to rinse the reaction vial and pass the solution through the filter. After that, wash the filter with 0.5 mL of MeCN. Place the reaction vial inside the NanoTek concentrator module, and stir under a N_2 flow at 105 °C (500 μL will remain 300 μL DMI + 200 μL DMSO).

14 Using the NanoTek syringe pump, dilute the crude solution of [^{18}F]rucaparib with 500 μL of buffer and inject 1 mL of the solution onto the HPLC 2 mL loading loop with a flow rate of 1 mL/min.

15 Rinse the V-Vial with 400 μL of buffer, take up 900 μL from the V-Vial (400 μl solution + 500 μl air), and transfer the solution to the HPLC loop with a flow rate of 1 mL/min.

16 Perform semi-preparative radio-HPLC purification using an isocratic flow (4 mL/min) with buffer as described before.

17 Collect the product peak (retention time, $R_t \sim 20$ min) into a vial containing 15 mL of H_2O

18 Shake the vial containing [^{18}F]rucaparib, transfer the solution to an C18 Plus cartridge with the NanoTek syringe pump (3 mL/min).

19 Connect the C18 Plus cartridge to the delivery vial, elute the product with 2.7 mL of EtOH. Place the reaction vial inside the NanoTek concentrator module, and heat under a N_2 flow at 105 °C. When the volume is diminished rinse the C18 cartridge with 1 mL of EtOH and drying the remaining solvent under nitrogen at 105 °C to ensure complete dryness.

20 Reformulate with buffer (10% DMSO in PBS (vol/vol)) to a volume suitable for *in vitro* or *in vivo* studies.

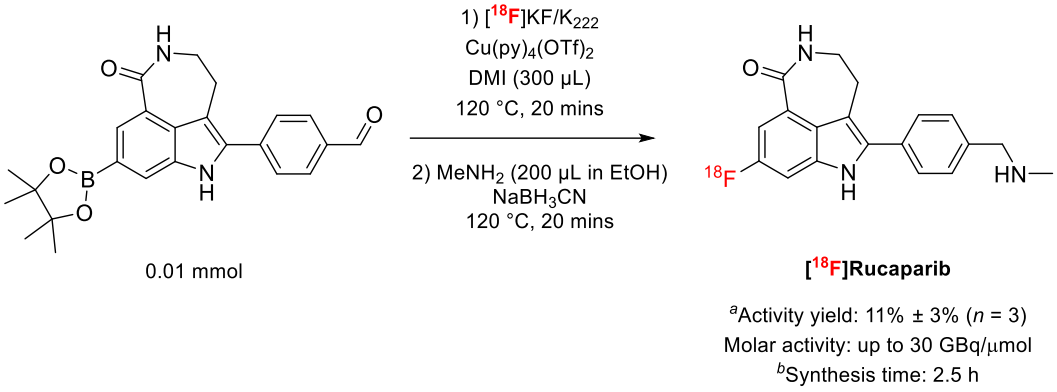

Supplementary Scheme 2. Radiosynthesis of [^{18}F]rucaparib from its aldehydic boronic ester precursor. [a]Non-decay corrected activity yield calculated from dried [^{18}F]fluoride. Total activity afforded up to 330 MBq of the desired tracer. [b]Synthesis time calculated from loading [^{18}F]fluoride onto QMA cartridges to the end of reformulation of [^{18}F]rucaparib.

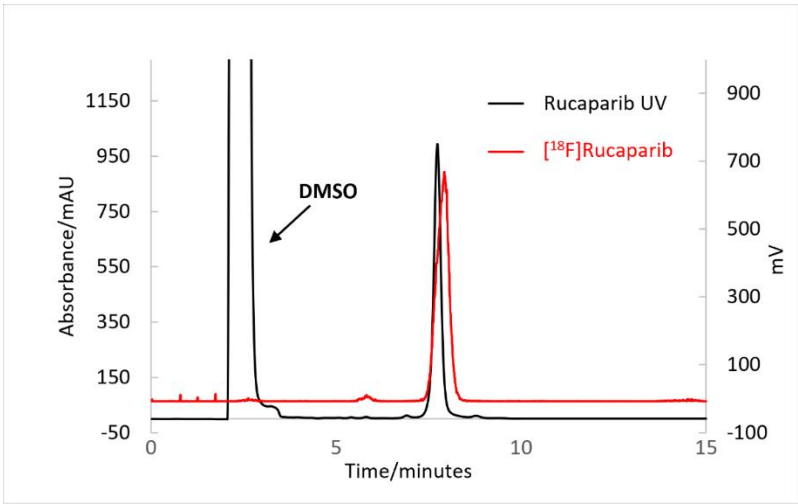

Supplementary Figure 1. Radiochromatogram obtained during the HPLC analysis of [^{18}F]rucaparib (red) overlayed with UV chromatogram of non-radiolabeled reference standard rucaparib (λ = 220 nm, black).

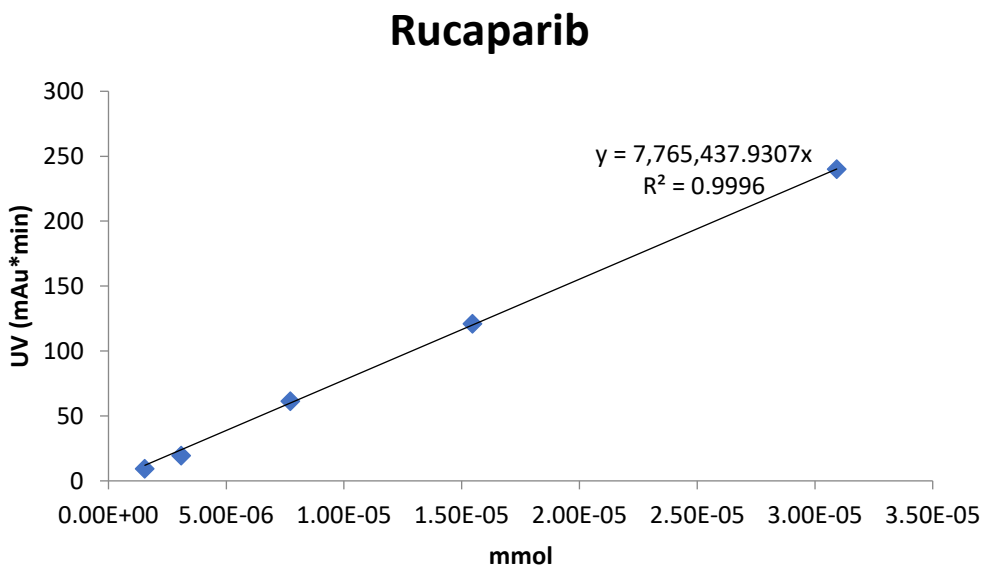

Supplementary Figure 2. Calibration curve for molar activity of [^{18}F]rucaparib.

Injection Number	Activity (MBq)	Area (mAu*min)	Mmol injected (* 10^{-7})	Molar Activity GBq/µmol
1	0.6	0.2319	0.2982	20.1
2	1.7	2.7481	3.5342	4.8
3	3.2	2.8067	3.6096	8.8
4	0.8	0.2013	0.2589	30.9
5	1.0	1.4144	1.8190	5.5

Supplementary Table 3. Molar activity calculations for [^{18}F]rucaparib.

4.4 Biological Procedures and Characterisations for Chapter II (Conducted by C. Y. Chan)

Supplemental Methods:

Unless otherwise noted, all reagents were purchased from Sigma-Aldrich and used without further purification.

Autoradiography

PSN1 xenograft tissues were harvested and immediately flash-frozen using liquid nitrogen, and sectioned (10 µm) using a Leica CM1950 cryostat. Tissue sections were thaw-mounted onto Superfrost PLUS glass microscope slides (Menzel-Glaser, Thermo Scientific) and

allowed to dry briefly at room temperature (RT). The slides were then fixed in 10% NBF for 10 min at RT, dried, and exposed to a storage phosphor screen (PerkinElmer, Super Resolution, 12.5 x 25.2 cm) in a standard X-ray cassette for 15 h at 4°C. The phosphor screen was then imaged using a Cyclone® Plus Storage Phosphor System (PerkinElmer).

For tissues that were not used in autoradiography, selected tissues from mice were fixed in 10% neutral buffered formalin overnight. Tissue was then flash frozen and stored at -80°C overnight. Frozen tissue was sectioned (10 µm) using a Leica CM1950 cryostat. Tissue sections were thaw-mounted onto Superfrost PLUS glass microscope slides (Menzel-Glaser, Thermo Scientific). The slides were then stored at 4°C until used.

Immunohistochemical staining

For immunohistochemical staining, slides were placed at RT for 5-10 mins to thaw. Slide incubation procedures were performed in glass Coplin type jars. The sections were dehydrated and rehydrated by sequential immersion in ethanol at 100% (twice), 70% and 50%, for 3 min at each concentration, with a final 1 min wash in water. The slides were then immersed in citrate buffer (10 mM sodium citrate pH 6.0) with 0.05% tween-20, and antigen retrieval was performed in an antigen-decloaking chamber (Biocare Medical) at 125°C for 2.5 min, then 95°C for 1 min. The slides were allowed to cool, then placed on ice.

The sections were processed using the EnVision FLEX DAB+ Substrate Chromogen System (Dako Omnis; Agilent Stockport UK). Tissue sections were blocked in Peroxidase and Alkaline Phosphatase Blocking Reagent (S2003) for 15 min at RT, then incubated overnight at 4°C in tris-buffered saline buffer (TBS) with 1% bovine serum albumen (BSA) containing the following Atlas Antibodies (Sigma Aldrich, UK) anti-human PARP rabbit polyclonal antibodies at 1:150 dilution: anti-PARP1 antibody (HPA045168), anti-PARP2 antibody (HPA052003), and anti-PARP3 antibody (HPA067657). Following this incubation, the tissues were washed five times (5 min each) in phosphate-buffered saline (PBS), incubated for 30 min

with Envision rabbit/mouse HRP polymer (K4065), and developed for 2.5 min using 1:50 dilution of DAB+ 2-component substrate (K3467). The sections were then washed in water twice (5 min each), and the nuclei counter-stained for 1 min in aqueous haematoxylin. This was followed by a 3 min wash in water, and four separate incubations in 100% ethanol (30 sec each), and two incubations in xylene (30 sec each). Coverslips were then mounted on DPX mounting media, and the slides left to set, and stored at 4°C.

Positive PARP staining in the tissue sections appeared brown, and the nuclei were counter-stained pink by the haematoxylin. Section images were acquired by a brightfield Aperio (Leica biosystem ScanScope CS2, Milton Keynes UK), and image analysis performed using the Leica Aperio ImageScope software.

Transcript Per Million	AsPC1	PSN1
PARP1	109	229
PARP2	22	44
PARP3	30	27
Tankyrase1	9	2
Tankyrase2	40	61
ALDH2	60	41
IMPDH2	244	381

Supplementary Table 4: mRNA expression in AsPC1 and PSN1 cells. www.ebi.ac.uk

%ID/g	1 h			2 h					
Blood	3.51	3.67	3.59	0.92	0.49	0.48	1.57	0.51	0.44
Tumour	5.25	6.05	5.16	2.58	2.10	1.74	2.60	3.45	2.99
Heart	13.27	16.24	17.47	2.44	2.15	1.73	1.73	1.61	1.27
Lung	17.76	25.71	27.51	8.77	6.24	4.58	9.27	5.27	8.24
Liver	--	4.24	22.33	12.22	8.90	10.25	12.44	11.01	11.46
Spleen	32.86	41.87	47.79	32.75	20.87	15.30	23.45	16.14	14.89
Stomach	9.10	6.86	7.46	4.66	5.94	7.68	11.59	5.59	7.44
Large intestine	12.50	16.33	14.08	23.81	19.26	15.83	25.44	36.97	43.06
Small intestine	--	33.79	46.24	16.44	9.50	19.42	22.39	10.51	13.44
Pancreas	19.47	23.54	23.22	13.99	9.45	9.78	11.07	9.35	7.70
Kidney	17.24	30.17	36.00	7.28	6.56	5.54	7.41	4.70	4.13
Muscle	2.63	4.25	3.13	2.51	1.58	1.90	2.77	1.57	1.57
Fat	6.53	4.98	6.82	1.32	0.74	0.84	1.78	1.03	0.86
Bone	4.90	6.79	5.26	3.49	2.71	2.38	3.10	2.18	2.26

Supplementary Table 5: *Ex vivo* biodistribution of [^{18}F]rucaparib (%ID/g) (0.87-11.38 MBq, A_m = 1.5-30.9 GBq/μmol) in PSN1 xenograft-bearing mice at 1 h and 2 h post-injection time points.

%ID/g	Non-treated			Olaparib-blocked			Rucaparib-blocked		
Blood	0.92	0.49	0.48	0.62	0.49	0.38	0.04	0.29	0.36
Tumour	2.58	2.10	1.74	2.83	1.36	1.23	0.11	1.20	1.12
Heart	2.44	2.15	1.73	1.07	0.82	0.83	0.06	0.76	0.51
Lung	8.77	6.24	4.58	5.83	5.49	6.59	0.35	4.77	2.50
Liver	12.22	8.90	10.25	13.15	9.74	9.86	0.62	5.66	7.42
Spleen	32.75	20.87	15.30	3.05	3.03	2.63	0.19	1.85	1.85
Stomach	4.66	5.94	7.68	12.09	9.73	6.47	0.53	6.53	4.49
Large intestine	23.81	19.26	15.83	33.55	35.89	30.25	3.24	45.68	25.75
Small intestine	16.44	9.50	19.42	8.33	9.66	6.32	0.56	11.02	5.09
Pancreas	13.99	9.45	9.78	4.67	4.17	4.43	0.31	3.02	2.76
Kidney	7.28	6.56	5.54	5.09	3.73	3.29	0.24	2.32	2.51
Muscle	2.51	1.58	1.90	1.19	1.07	1.10	0.10	1.36	0.74
Fat	1.32	0.74	0.84	0.73	0.74	0.75	0.04	0.41	0.31
Bone	3.49	2.71	2.38	1.34	1.17	1.13	0.10	1.21	0.90
Brain	0.09	0.06	0.06	0.06	0.06	0.04	0.00	0.06	0.06

Supplementary Table 6: *Ex vivo* biodistribution of [^{18}F]rucaparib (%ID/g) (0.87-2.47 MBq, A_m = 5.5 GBq/μmol) in PSN1 xenograft-bearing mice with or without the co-injection of olaparib or rucaparib (0.5 mg) as blocking agent.

Supplemental data:

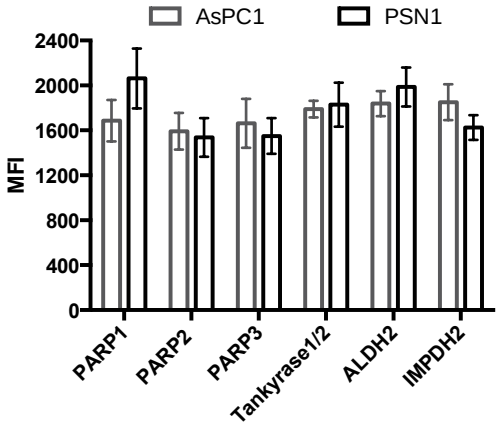

Supplemental Figure 3: Mean fluorescence intensity (MFI) for the staining of PARP1, 2 and 3, Tankyrase 1/2, ALDH2 and IMPDH2 enzymes in AsPC1 and PSN1 cells assessed by flow cytometry analysis.

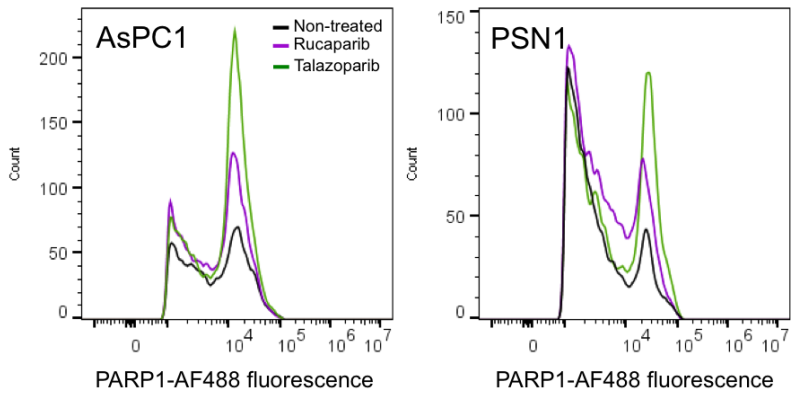

Supplemental Figure 4: Representative frequency histograms probing for PARP1 expressions in AsPC1 and PSN1 cells after exposed to PARP inhibitors (10 μM) for 3 h.

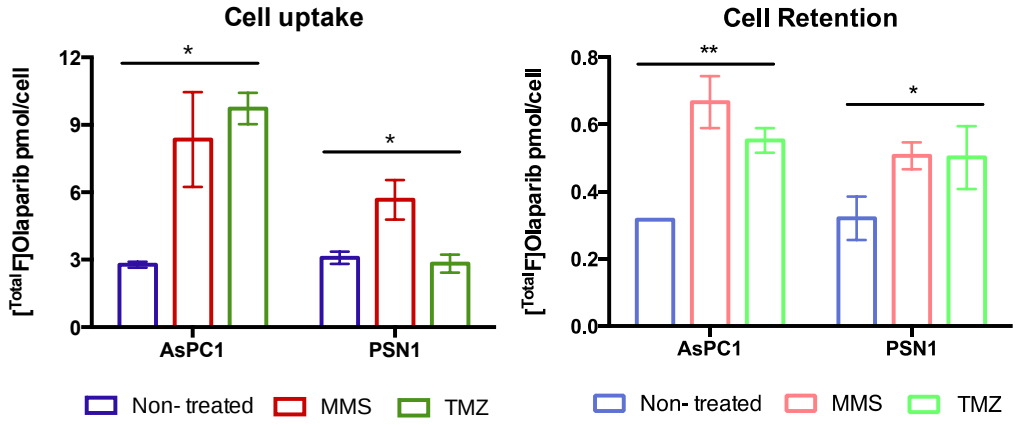

Supplemental Figure 5: Uptake and retention (at 3 h) of [$^{18+19}$F]olaparib (300 nM, [^{18}F]olaparib: 400 kBq, 8.5 GBq/μmol) in cells (AsPC1 and PSN1) treated with DNA damaging reagents (MMS and TMZ). Asterisks indicate levels of significance: *, $P < 0.05$; **, $P < 0.01$.

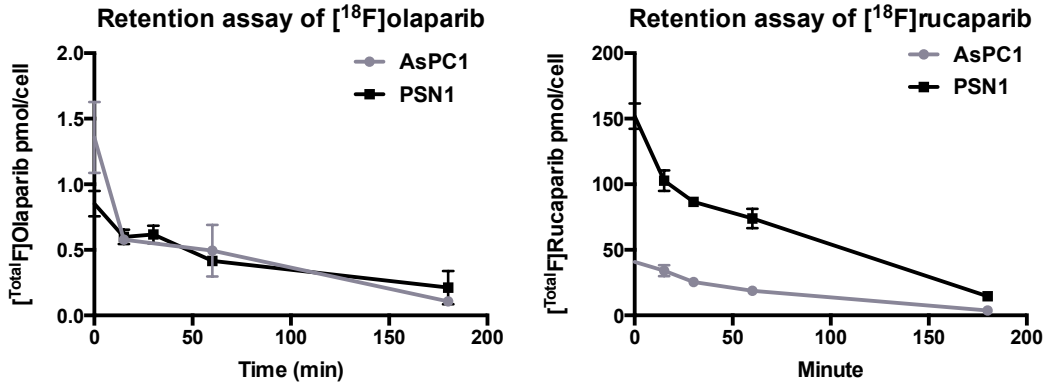

Supplemental Figure 6: Cell retention of [^{Total}F]olaparib (left, 75.6 μM, molar activity: 2.8 GBq/μmol) and [^{Total}F]rucaparib (right, 77.4 μM, molar activity: 4.8 GBq/μmol) in AsPC1 and PSN1 cells.

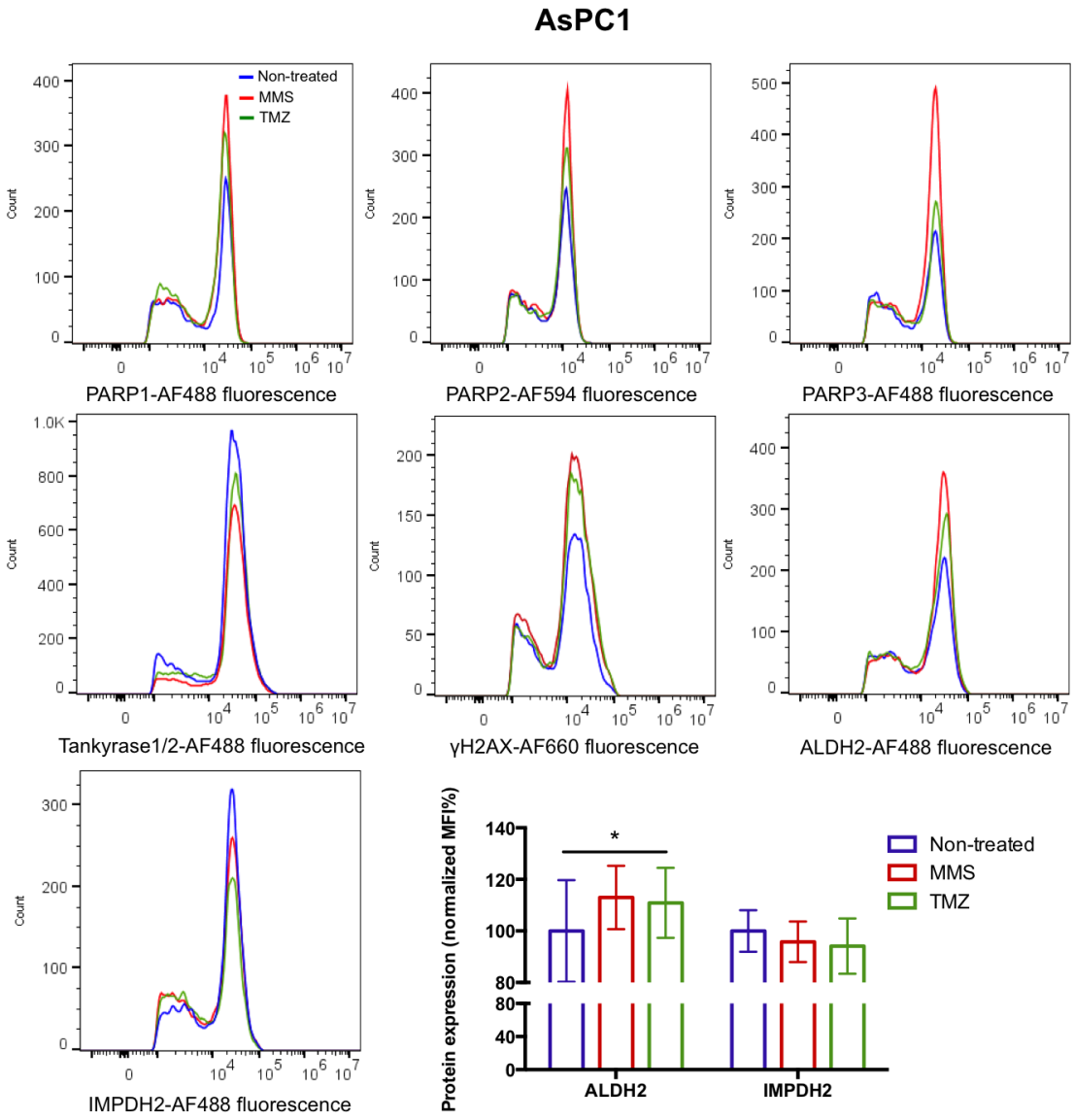

Supplemental Figure 7: Representative frequency histograms probing for protein expressions in AsPC1 cells after exposed to MMS or TMZ (100 μM) for 3 h, and mean fluorescence intensity (MFI) for ALDH2 and IMPDH2 assessed by flow cytometry analysis. Asterisks indicate levels of significance: *, $P < 0.05$.

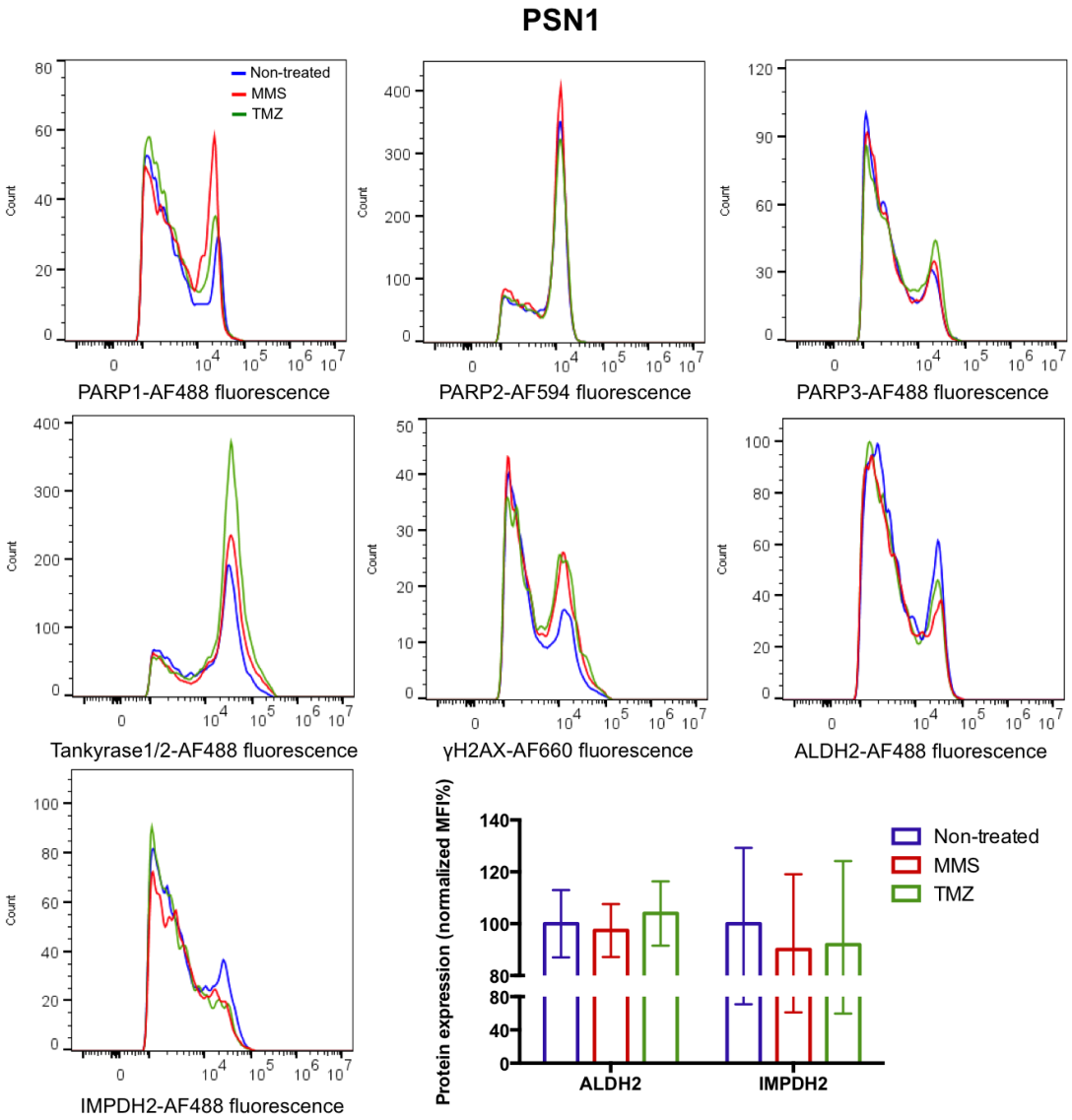

Supplemental Figure 8: Representative frequency histograms probing for protein expressions in PSN1 cells after exposed to MMS or TMZ (100 μM) for 3 h, and mean fluorescence intensity (MFI) for ALDH2 and IMPDH2 assessed by flow cytometry analysis.

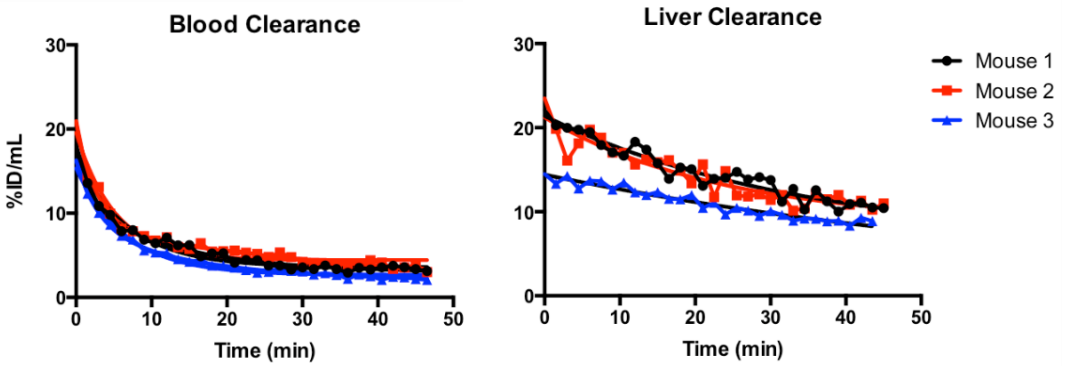

Supplemental Figure 9: [^{18}F]rucaparib clearance in blood and liver of mice bearing PNS1 xenografts (n=3).

4.5 Preparation and Characterisation Data for Chapter III

2-Amino-5-formylbenzonitrile (**3.47**)*

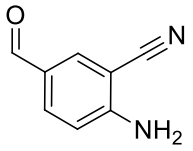

To a flame-dried round bottom flask was added 2-amino-5-bromo-benzonitrile (6.00 g, 30.5 mmol) and THF (180 mL). The solution was cooled to -78°C before *n*-BuLi in THF (2.5 M, 26.4 mL, 67 mmol) was added dropwise. The reaction was left to stir at -78°C for 2 h before quenching with DMF (6 mL, 77 mmol) and allowed to warm to room temperature. The solution was then extracted with DCM (3 x 100 mL) and washed with $NaHCO_3$ (300 mL). The organic layers were collected, dried with $MgSO_4$, and the excess solvent removed *in vacuo*. The crude material was then purified *via* flash column chromatography (*n*-Pent:EtOAc 8:2, R_f = 0.29) affording 2-amino-5-formylbenzonitrile (2.96 g, 66%) as a pale yellow solid.

^{1}H NMR (400 MHz, $CDCl_3$) δ = 9.75 (s, 1H), 7.92 (d, *J* = 1.8 Hz, 1H), 7.88 (dd, *J* = 8.6, 1.8 Hz, 1H), 6.83 (d, *J* = 8.6 Hz, 1H), 5.01 (bs, 2H). **^{13}C NMR** (126 MHz, $CDCl_3$) δ 188.8, 162.7, 153.9, 136.7, 134.5, 127.4, 116.4, 115.2. Data is in accordance with known literature.[6]

2-Bromo-5-formylbenzonitrile (**3.48**)*

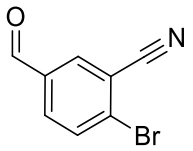

To a round bottom flask containing 2-Amino-5-formylbenzonitrile (2.00 g, 13.7 mmol) at 0°C was added 6M HCl (13 mL) and fuming H_2SO_4 (13 mL). After being allowed to cool, a solution of sodium nitrite (1.98 g, 28.7 mmol) in H_2O (5 mL) was added dropwise before allowing the reaction to stir for 30 minutes. The reaction mixture was then added dropwise to a solution of

* Data provided by Dr. Florian Guibbal (Department of Chemistry, University of Oxford).

copper(II) bromide (4.28 g, 19.2 mmol) in 48% HBr (13 mL) at 0°C. The reaction was then stirred at 0°C for 60 min before being allowed to warm to room temperature and being stirred for another hour. Upon completion, the reaction was poured into an ice/water mixture before the organic layer was extracted with DCM (3 x 20 mL). The organic layer was then dried with $MgSO_4$ and the excess solvent removed *in vacuo*. The crude material was purified by flash column chromatography (*n*-Pent:EtOAc 9:1, R_f = 0.35) to afford 2-bromo-5-formylbenzonitrile as a pale yellow solid (2.22 g, 77%).

^{1}H NMR (400 MHz, $CDCl_3$) δ = 10.00 (s, 1H), 8.15 (s, 1H), 7.95 (d, 8.4, 1H), 7.90 (d, *J* = 8.3 Hz, 1H). **^{13}C NMR** (126 MHz, $CDCl_3$) δ 189.0, 135.6, 135.3, 134.4, 133.7, 132.1, 117.4, 116.2. Data is in accordance with known literature.[6]

2-Bromo-5-((3-oxoisobenzofuran-1(*3H*)-ylidene)methyl)benzonitrile (**3.50**)*

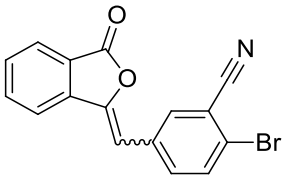

A solution of dimethyl-(3-oxo-1,3-dihydrobenzofuran-1-yl)phosphonate (3.10 g, 12.7 mmol) and 2-bromo-5-formylbenzonitrile (2.22 g, 10.6 mmol) in THF (60 mL) was prepared at room temperature. The solution was cooled to 0°C followed by the addition of Et_3N (2.94 mL, 21.1 mmol). The reaction mixture was warmed to room temperature and was stirred for 48 h, followed by concentration *in vacuo* to produce a white solid. The solid was suspended in water, collected by vacuum filtration and washed with hexane (2 × 30 mL) and Et_2O (3 × 30 mL) affording 2-Bromo-5-((3-oxoisobenzofuran-1(*3H*)-ylidene)methyl)benzonitrile (3.32 g, 96%) as a white solid in an mixture of *e:z* stereoisomers (10:1) and a purity of 90% (water present). NMR spectra showed a 10:1 mixture of E and Z isomers.

^{1}H NMR (400 MHz, DMSO-d_6) δ = 8.20 – 8.07 (m, 2H, 2H*), 8.03 – 7.90 (m, 3H, 3H*), 7.84 – 7.49 (m, 2H, 2H*), 6.98 (s, 1H*), 6.97 (s, 1H) (where possible, shifts are assigned to each respective isomer). **^{13}C NMR** (101 MHz, DMSO) δ 165.9, 146.2, 135.5, 135.4, 135.0, 133.9, 133.7, 131.6, 131.2, 125.4, 123.5, 121.1, 117.1, 115.1, 103.5 (Only peaks corresponding to the major isomers are reported). Data is in accordance with known literature.[6] (E isomer: B; Z isomer: A)

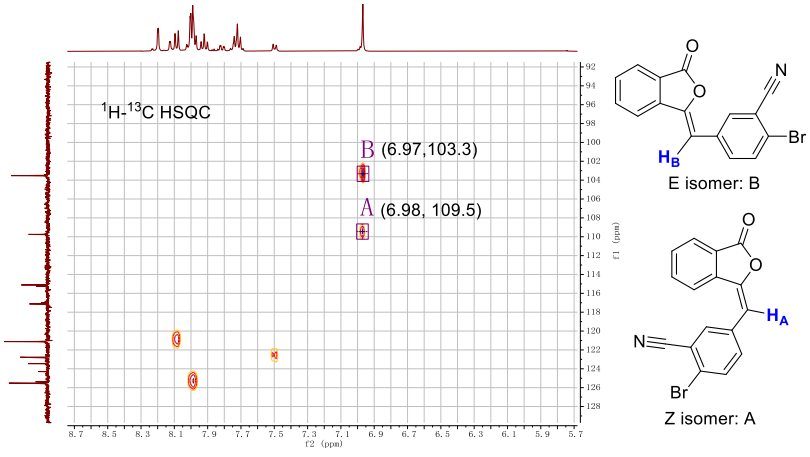

2-Bromo-5-((4-oxo-3,4-dihydrophthalazin-1-yl)methyl)benzoic acid (**3.51**)*

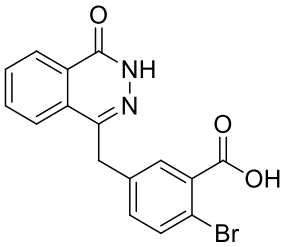

2-Bromo-5-[(3'-oxo-2'- benzofuran-1'-ylidene)methyl]benzonitrile (3.30 g, 10.1 mmol) was suspended in water (33 mL) and 9 M NaOH was added (6 mL, 90 mmol). The mixture was heated to 90°C and stirred for 24 h, after which it was warmed to reflux (140°C), followed by the addition of hydrazine monohydrate (6.2 mL, 200 mmol) and a further 48 h of stirring. The mixture was then cooled to room temperature and acidified with 6 M HCl to an approximate pH of 2. The solid precipitate was collected by vacuum filtration and washed with water (40

mL) and Et_2O (3 × 20 mL) affording 2-Bromo-5-((4-oxo3,4-dihydrophthalazin-1-yl)methyl)benzoic acid (3.25 g, 91%) as a light yellow powder after drying under vacuum. **^{1}H NMR** (400 MHz, DMSO-d_6) δ = 12.60 (s, 1H), 8.26 (dd, *J* = 7.7, 1.4 Hz, 1H), 7.98 – 7.95 (m, 1H), 7.90 (td, *J* = 7.9, 1.5 Hz, 1H), 7.83 (m, 1H), 7.71 (d, *J* = 2.3 Hz, 1H), 7.62 (d, *J* = 8.2 Hz, 1H), 7.36 (dd, *J* = 8.2, 2.3 Hz, 1H), 4.34 (s, 2H). **^{13}C NMR** (126 MHz, DMSO) δ 167.3, 159.4, 144.7, 138.0, 135.0, 133.9, 133.6 132.9, 131.6, 130.9, 129.8, 129.1, 127.8, 125.4, 117.9, 36.5, Data is in accordance with known literature.[6]

4-(3-(4-(cyclopropanecarbonyl)piperazine-1-carbonyl)-4-(4,4,5,5-tetramethyl-1,3,2-dioxaborolan-2-yl)benzyl)phthalazin-1(2H)-one **(3.45)**

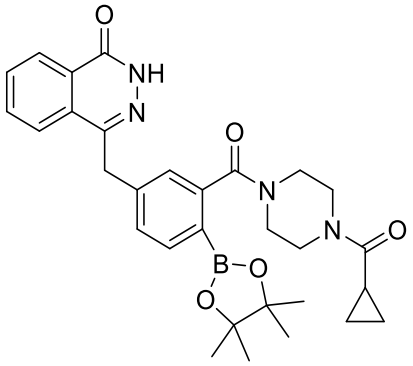

To a Schlenk tube charged with nitrogen, 4-(4-bromo-3-(4-(cyclopropanecarbonyl)-piperazine-1-carbonyl)benzyl)phthalazin-1(2H)-one (166 mg, 0.266 mmol), bis(pinacolato)diboron (149 mg, 0.585 mmol), Pd(dppf)Cl_2 (5.9 mg, 0.008 mmol) and potassium acetate (78.3 mg, 0.798 mmol) were added. Degassed anhydrous DMF (1.3 mL) was added. The reaction was heated to 85 °C and stirred for 16 hours, before cooled down and passed through a Celite plug with EtOAc. The excess solvent was removed under reduced pressure and the crude material was isolated by flash column chromatography (100% EtOAc, Rf 0.2) to afford borylated 4-(3-(4-(cyclopropanecarbonyl)piperazine-1-carbonyl)-4-(4,4,5,5-

tetramethyl-1,3,2-dioxaborolan-2-yl)benzyl)phthalazin-1(2H)-one (63.4 mg, 0.117 mmol, 44%)

^{1}H NMR (400 MHz, $CDCl_3$) δ 8.48 – 8.41 (m, 1H), 7.81 – 7.54 (m, 4H), 7.32 – 7.25 (m, 1H), 7.14 (s, 1H), 4.32 (s, 2H), 3.89 – 2.95 (m, 8H), 1.77 (s, 1H), 1.27 (s, 12H), 1.04 – 0.94 (m, 2H), 0.79 (s, 2H); **^{13}C NMR** (101 MHz, $CDCl_3$) δ 174.9, 173.4, 162.3, 147.6, 143.7, 143.3, 137.1, 134.9, 132.9, 131.0, 130.0, 129.2,127.7, 127.5, 126.9, 85.5 , 39.3, 25.3, 25.2, 11.8, 8.1; **IR** (cm^{-1}): 3216, 1601, 1433, 1351, 1062, 962, 855, 774; **HRMS** (ESI+) m/z: $[M+H]^+$ Calcd for $C_{30}H_{36}N_4O5B$ 543.2770; Found 543.2777

4-(3-(4-(cyclopropanecarbonyl)piperazine-1-carbonyl)-4-iodobenzyl)phthalazin-1(2*H*)-one **(3.33)**

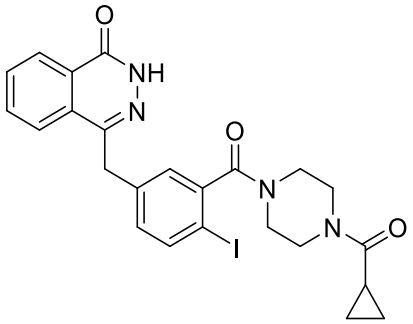

4-(3-(4-(cyclopropanecarbonyl)piperazine-1-carbonyl)-4-(4,4,5,5-tetramethyl-1,3,2-dioxaborolan-2-yl)benzyl)phthalazin-1(2*H*)-one (5.4 mg, 10 μmol), $Cu(OCOCF_3)_2$ (0.60 μmol), 1,10-phenanthroline (0.60 μmol) in MeOH:H2O (4:1, 200 μL). The reaction was stirred at 80 °C for 25 minutes. The excess solvent was removed under reduced pressure and the crude material was isolated by flash column chromatography (100% EtOAc, Rf 0.3) to afford 4-(3-(4-(cyclopropanecarbonyl)piperazine-1-carbonyl)-4-iodobenzyl)phthalazin-1(2*H*)-one (5.0 mg, 0.9 μmol, 92%)

^{1}H NMR (400 MHz, $CDCl_3$) δ 10.58 (s, 1H), 8.46 (dd, *J* = 5.7, 3.6 Hz, 1H), 7.90 – 7.70 (m, 3H), 7.66 (br, 1H), 7.12 (br, 1H), 7.04 (dd, J = 8.2, 2.2 Hz, 1H), 4.26 (s, 2H), 4.08 – 2.92 (m, 8H), 1.71 (br, 1H), 1.00 (m, 2H), 0.80 (br, 2H); **^{13}C NMR** (101 MHz, CDCl3) δ 174.8, 171.5, 162.2, 147.3, 143.1, 141.7, 140.8, 140.7, 135.0, 132.9, 132.4, 130.9, 129.2, 128.7, 127.5, 126.7, 90.7, 38.5, 25.0, 11.8, 8.1.; **IR** (cm^{-1}): 3185, 1630, 1431, 1286, 1227, 1020, 1005, 772; **HRMS** (ESI+) m/z: $[M+Na]^+$ Calcd for $C_{24}H_{23}N_4O_3INa$ 565.0707; Found 565.0705.

4-(8-iodo-1-oxo-2,3,4,6-tetrahydro-1H-azepino[5,4,3-cd]indol-5-yl)benzaldehyde (**3.54**)

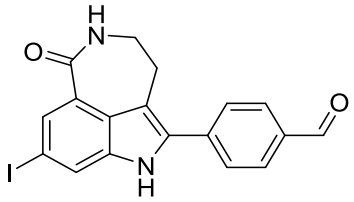

4-(1-Oxo-8-(4,4,5,5-tetramethyl-1,3,2-dioxaborolan-2-yl)-2,3,4,6-tetrahydro-1*H*-azepino[5,4,3-*cd*]indol-5-yl)benzaldehyde (8.4 mg, 20 μmol), $Cu(OCOCF_3)_2$ (1.2 μmol), 1,10-phenanthroline (1.2 μmol) in MeOH:H2O (4:1, 400 μL). The reaction was stirred at 80 °C for 25 minutes. The excess solvent was removed under reduced pressure and the crude material was isolated by flash column chromatography (100% EtOAc, Rf 0.3) to afford 4-(3-(4-(cyclopropanecarbonyl)piperazine-1-carbonyl)-4-iodobenzyl)phthalazin-1(2*H*)-one (6.2 mg, 14 μmol, 74%)

^{1}H NMR (400 MHz, MeOD) δ 10.05 (s, 1H), 8.05 (s, 1H), 7.86 (s, 1H), 7.70 – 7.59 (m, 2H), 7.60 – 7.51 (m, 2H), 3.52 – 3.44 (m, 2H), 3.13 (m, 2H); **^{13}C NMR** (126 MHz, MeOD) δ 193.1, 169.6, 136.8, 136.6, 135.8, 135.0, 131.2, 129.2, 128.2, 128.0, 127.6, 124.8, 121.3, 114.1, 83.5, 41.2, 29.9, 25.4 **HRMS** (ESI-) m/z: $[M-H]^-$ Calcd for $C_{18}H_{12}N_2O_2I$ 414.9949; Found 414.9946.

8-iodo-5-(4-((methylamino)methyl)phenyl)-2,3,4,6-tetrahydro-1H-azepino[5,4,3-cd]indol-1-one (**3.35**)

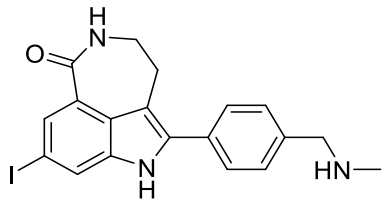

4-(8-iodo-1-oxo-2,3,4,6-tetrahydro-1H-azepino[5,4,3-cd]indol-5-yl)benzaldehyde (5.0 mg) was suspended in MeOH (0.1 mL), followed by addition of methylamine (0.01 mL, 2M in THF). The mixture was stirred at room temperature for 2 hours and cooled to 0 °C in an ice bath. Sodium borohydride (3 mg, 0.08 mmol) was added slowly. The reaction was stirred at 0 °C for 1 hour. After gradually warmed to room temperature, the mixture was stirred for another hour. Upon completion, 1 M HCl was added to quench the reaction, which was then basified with 1 M NaOH. Organic solvent was removed *in vacuo*. The aqueous phase was extracted with EtOAc (3 x 5 mL). The combined organic phases were dried over Na_2SO_4 and concentrated *in vacuo*. The crude was isolated by column chromatography (NH_3/MeOH/DCM 1/4/95, Rf: 0.15) to afford 8-fluoro-5-(4-((methylamino)methyl)phenyl)-2,3,4,6-tetrahydro-1*H*-azepino[5,4,3-*cd*]indol-1-one as a light yellow solid (2 mg, 5 μmol, 41 %).

^{1}H NMR (400 MHz, MeOD) δ 8.51 (s, 1H), 8.06 (d, *J* = 1.5 Hz, 1H), 7.95 (d, *J* = 1.5 Hz, 1H), 7.77 – 7.69 (d, *J* = 8.3, 2H), 7.63 (d, *J* = 8.3 Hz, 2H), 4.23 (s, 2H), 3.54 (m, 2H), 3.15 (m, 2H), 2.74 (s, 3H); **^{13}C NMR** (126 MHz, MeOD) δ 172.2, 139.6, 136.4, 134.4, 132.5, 131.4, 130.0, 129.9, 127.2, 126.7, 124.7, 114.1, 85.4, 53.3, 43.7, 30.0.; **IR** (cm^{-1}): 3271, 1668, 1644, 1466, 1363, 1296, 1144, 881, 821; **HRMS** (ESI+) m/z: $[M+H]^+$ Calcd for $C_{19}H_{19}N_3OI$ 432.0567; Found 432.0569.

4.6 Radiochemistry for Chapter III

4.6.1 General procedure for small scale screening experiments with 2-(4-methoxyphenyl)-4,4,5,5-tetramethyl-1,3,2-dioxaborolane:

To a V-vial containing a magnetic stirrer bar, 2-(4-methoxyphenyl)-4,4,5,5-tetramethyl-1,3,2-dioxaborolane (10 µmol) and [^{123}I]NaI (5-10 MBq, 5 µL MeOH approx.) was added $Cu(OCOCF_3)_2$ (0.20 µmol), 1,10-phenanthroline (0.20 µmol) in MeOH:H2O (4:1, 200 µL) from a stock solution. The reaction vial was then heated to 80 °C for 20 minutes. An aliquot was removed for analysis by radio- HPLC to calculate the RCY.

HPLC gradient for analysis of small scale screening experiments:

MeCN/H_2O, 1 mL/min, Synergi 4 µm HydroRP 80 Å column, 150 x 4.6 mm, 0 - 1 min (5% MeCN) isocratic, 1 - 10 min (5% MeCN to 95% MeCN) linear increase, 10 - 13 min (95% MeCN) isocratic, 13 - 15 min (5% MeCN) isocratic.

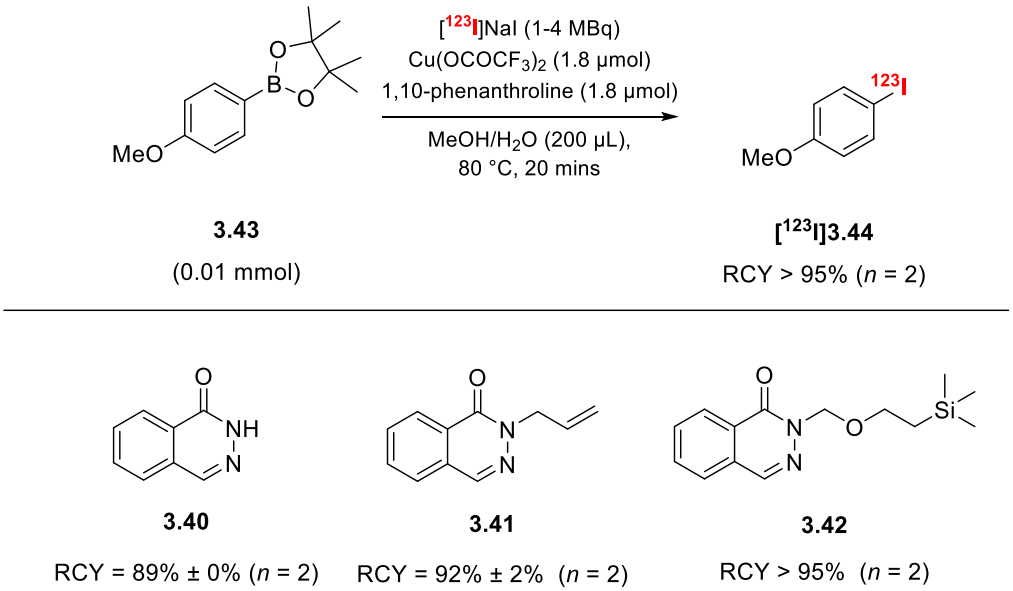

Supplementary Scheme 3. Small scale screening experiments with 2-(4-methoxyphenyl)-4,4,5,5-tetramethyl-1,3,2-dioxaborolane

4.6.3 Procedure for radiosynthesis of ^{123}I-olaparib analogue **[^{123}I]3.33**:

[^{123}I]NaI was produced by GE Healthcare as none carrier added [^{123}I]NaI in 0.05 M NaOH, which was diluted in 200 µL MeOH and transferred to a V-vial containing 4-(3-(4-

(cyclopropanecarbonyl)piperazine-1-carbonyl)-4-(4,4,5,5-tetramethyl-1,3,2-dioxaborolan-2-yl)benzyl)phthalazin-1(2H)-one (5.4 mg, 10 µmol), $Cu(OCOCF_3)_2$ (0.60 µmol), 1,10-phenanthroline (0.60 µmol) in MeOH:H2O (4:1, 200 µL). The reaction was stirred at 80 °C for 25 minutes. The reaction mixture was then diluted in with 33% MeCN/ 67% 25 mM NH_4HCO_2 in H_2O and loaded directly onto a 2 mL HPLC loop and injected on a semi-Prep HPLC column (Synergi 4µm Hydro-RP 250x10mm) and eluted into a collection vial with 33% MeCN/ 67% 25 mM NH_4HCO_2 in H_2O monitoring with UV (220 nm) and radioactive traces.

The ^{123}I-olaparib was collected in 25 mL of H_2O and eluted over an Oasis HLB Plus cartridge (preconditioned with 2 mL MeOH and 10 mL H_2O). The product was eluted with EtOH (2.0 mL). Ethanol was evaporated under a flow of N_2 while heating at 105°C. The dry residue was then re-dissolved in 10% DMSO/PBS (pH = 7.4).

The Molar Activity of ^{123}I-olaparib was assessed by radio-HPLC, using an analytical Synergi 4 µm Hydro-RP 80A column, 150 x 4.6 mm eluted with 40% MeCN/60% H_2O (isocratic 1 mL/min), monitoring with UV (220 nm) and radioactive traces.

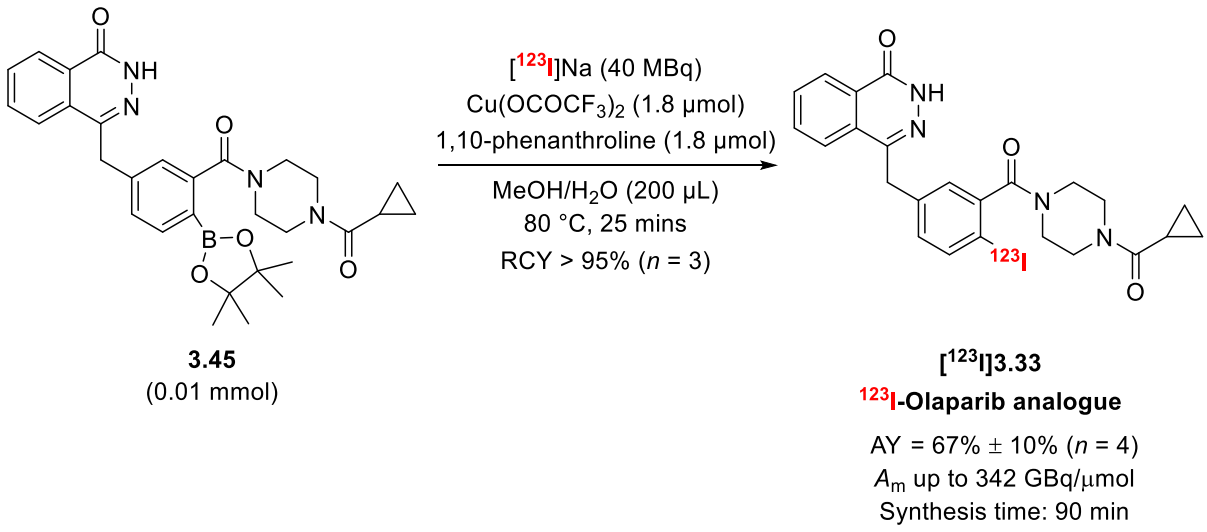

Supplementary Scheme 4: Radiosynthesis of ^{123}I-olaparib analogue **[^{123}I]3.33**.

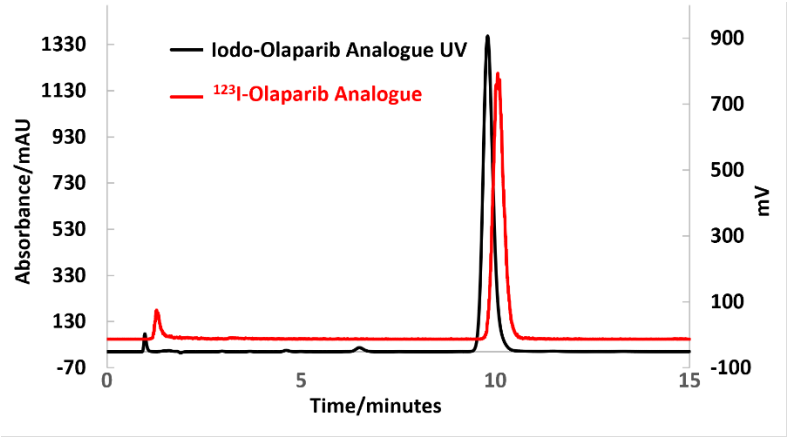

Supplementary Figure 10: Radiochromatogram obtained during the HPLC analysis of ^{123}I-olaparib analogue (red) overlayed with UV chromatogram of non-radiolabelled reference standard iodo-olaparib analogue **3.33** (λ = 220 nm, black).

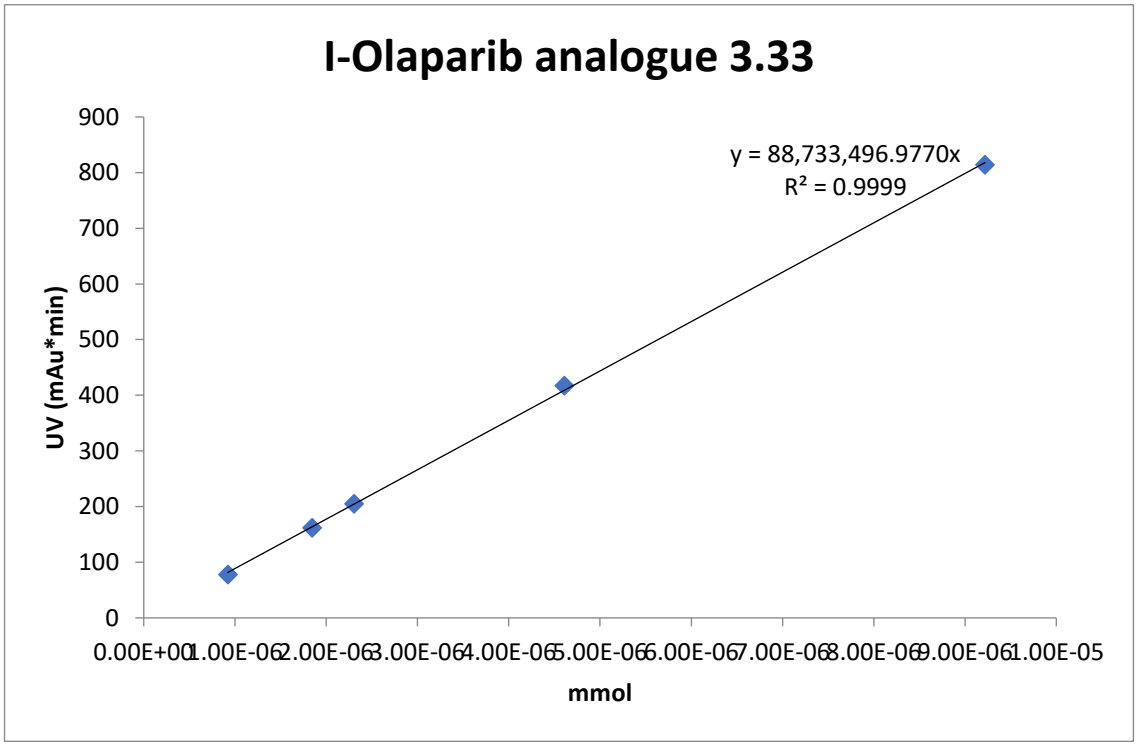

Supplementary Figure 10. Calibration curve for molar activity of 123I-olaparib analogue **[^{123}I]3.33**.

Injection Number	Activity (MBq)	Area (mAu*min)	Mmol injected (* 10^{-8})	Molar Activity GBq/µmol
1	0.1	0.0348	0.03921	255.0
2	0.7	1.8979	2.13888	32.7
3	1.45	1.2740	1.43576	101.0
4	0.63	3.6671	4.13271	15.2
5	1.42	6.9961	7.88440	18.0
6	0.2	0.6630	0.747181	26.9

Supplementary Table 7. Molar activity calculations for 123I-olaparib analogue **[^{123}I]3.33**.

4.6.3 Procedure for radiosynthesis of ^{123}I-rucaparib analogue **[^{123}I]3.35**:

Buffer for semi-preparative radio-HPLC: Buffer is 71% (vol/vol) 25 mM aqueous NH_4HCO_2 (pH 9.2 adjusted with 35% aqueous ammonia, 10 mL/L) in MeCN. Dissolve 1.12 g of NH_4HCO_2 and 7 mL of 35% aqueous ammonia in 703 mL of H_2O and add 290 mL of MeCN.

[^{123}I]NaI was produced by GE Healthcare as none carrier added [^{123}I]NaI in 0.05 M NaOH, which was diluted in 200 µL MeOH and transferred to a V-vial containing Tert-butyl methyl(4-(1-oxo-8-(4,4,5,5-tetramethyl-1,3,2-dioxaborolan-2-yl)-2,3,4,6-tetrahydro-1H-azepino[5,4,3-cd]indol-5-yl)benzyl)carbamate (5.2 mg, 10 µmol), $Cu(OCOCF_3)_2$ (0.60 µmol), 1,10-phenanthroline (0.60 µmol) in MeOH:H2O (4:1, 200 µL). The reaction was stirred at 80 °C for 25 minutes, followed by addition TFA (300 µL). The reaction mixture was stirred at 80 °C for 30 minutes. Solvent was removed at 100 °C under nitrogen flow. After drying, the crude reaction mixture was dissolved in the pre-made buffer and loaded directly onto a 2 mL HPLC loop and injected on a semi-Prep HPLC column (Gemini LC column, 4µm, 250x10mm) and eluted into a collection vial with 45% MeCN/ 55% 25 mM NH_4HCO_2 in H_2O/NH_3 monitoring with UV (220 nm) and radioactive traces.

The ^{123}I-rucaparib analogue was collected in 25 mL of H_2O and eluted over an C18 cartridge (preconditioned with 2 mL MeOH and 10 mL H_2O). The product was eluted with EtOH (2.0 mL). 1 M HCl (100 µL) was added. Solvent was evaporated under a flow of N_2 while heating at 105°C. The dry residue was then re-dissolved in 10% DMSO/PBS (pH = 7.4).

The Molar Activity of ^{123}I-rucaparib was assessed by radio-HPLC, using a Gemini LC column, 150 x 4.6 mm, eluted with MeCN/H_2O/NH_3 buffer at a flow rate 1 mL/min, monitoring with UV (220 nm) and radioactive traces.

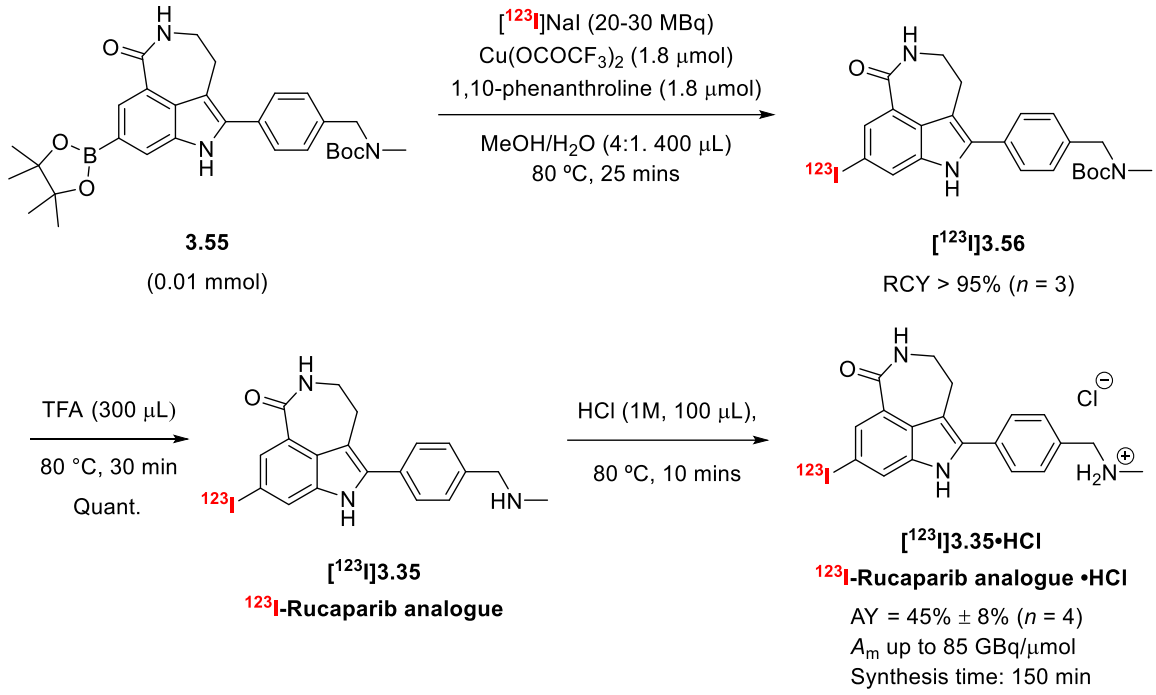

Supplementary Scheme 5: Radiosynthesis of ^{123}I-rucaparib analogue **[^{123}I]3.35**

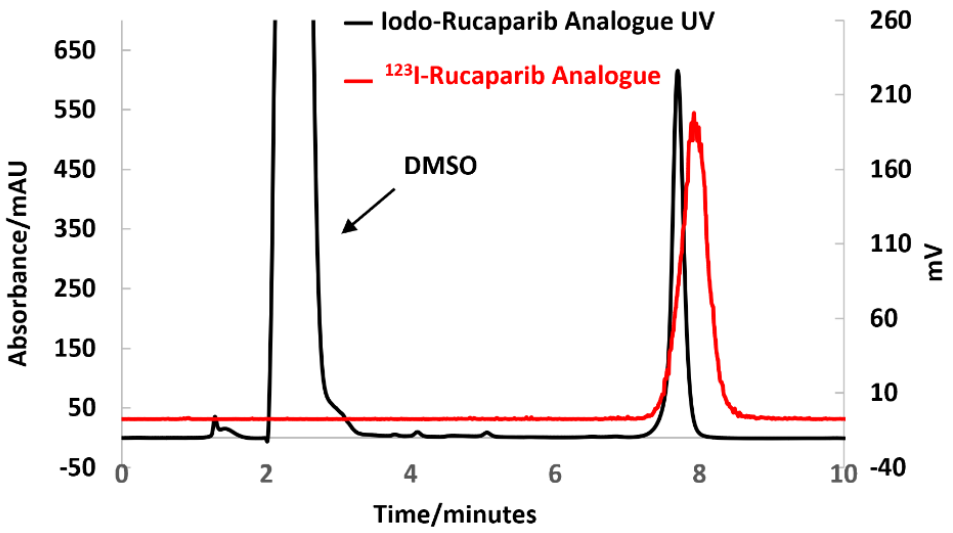

Supplementary Figure 10: Radiochromatogram obtained during the HPLC analysis of ^{123}I-rucaparib analogue (red) overlayed with UV chromatogram of non-radiolabelled reference standard iodo-rucaparib analogue **3.33** (λ = 220 nm, black).

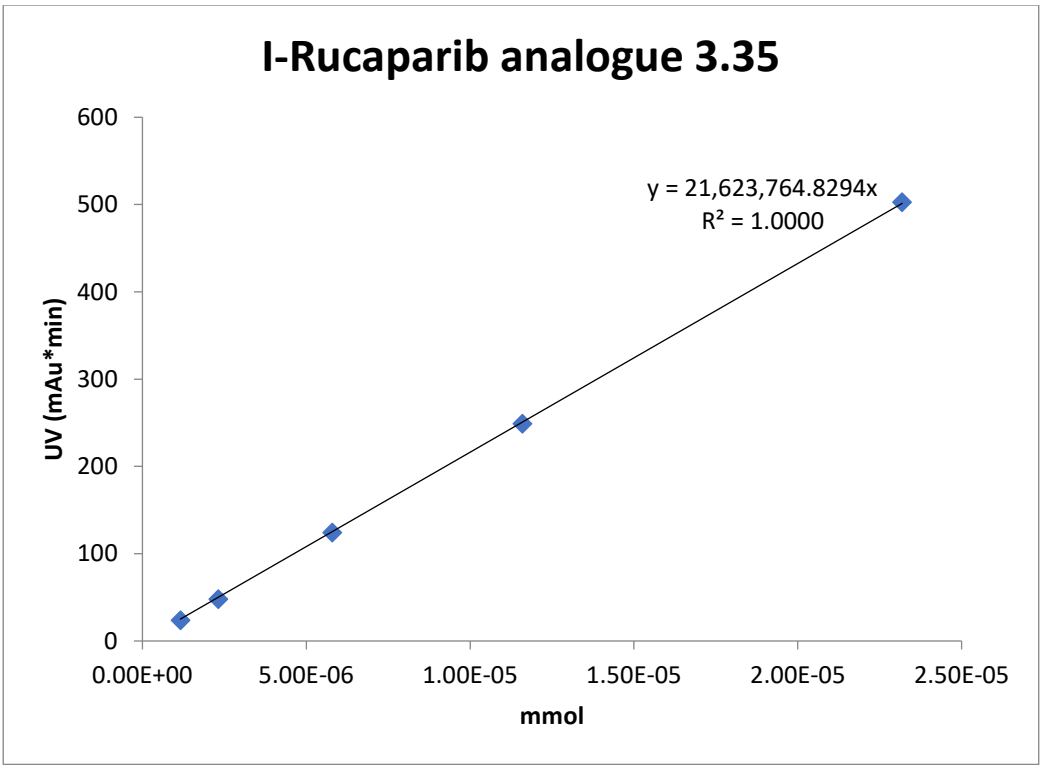

Supplementary Figure 11. Calibration curve for molar activity of 123I-rucaparib analogue **[^{123}I]3.35**.

Injection Number	Activity (MBq)	Area (mAu*min)	Mmol injected (* 10^{-8})	Molar Activity GBq/µmol
1	0.39	1.0305	4.76559	8.2
2	0.8	0.2047	0.94644	84.5
3	0.53	1.1857	1.43576	9.7
4	0.3	0.3216	4.13271	20.0
5	1.65	1.4204	7.88440	25.1

Supplementary Table 8. Molar activity calculations for 123I-rucaparib analogue **[^{123}I]3.35**.

4.7 References

[1] Gelat, F.; Jayashankaran, J.; Lohier, J.-F.; Gaumont, A.-C.; Perrio, S., Organocatalytic Asymmetric Synthesis of Sulfoxides from Sulfenic Acid Anions Mediated by a Cinchona-Derived Phase-Transfer Reagent. *Org. Lett.* **2011,** *13* (12), 3170-3173.

[2] Geng, Y.; Hu, P.; Wang, X.; Liu, C.; Li, Z., Synthesis of Rucaparib-a Poly(ADP-ribose) Polymerase Inhibitor. *Jingxi Huagong Zhongjianti* **2012**, *42*(5), 48-52

[3] Gillmore, A. T.; Badland, M.; Crook, C. L.; Castro, N. M.; Critcher, D. J.; Fussell, S. J.; Jones, K. J.; Jones, M. C.; Kougoulos, E.; Mathew, J. S.; McMillan, L.; Pearce, J. E.; Rawlinson, F. L.; Sherlock, A. E.; Walton, R., Multkilogram Scale-Up of a Reductive Alkylation Route to a Novel PARP Inhibitor. *Org. Process Res. Dev.* **2012,** *16* (12), 1897-1904.

[4] Hadida-Ruah, S.; Hamilton, M.; Miller, M.; Grootenhuis, P.; Bear B.; McCartney, J.; Zhou, J.; Van Goor, F., Modulators of ATP-binding Cassette Transporters. US 20080019915A1, January 24, 2008.

[5] O'dowd, C.; Harrison, T.; Hewitt, P; Rountree, S.; Hugues, M; Burkamp, F.; Jordan, L.; Helm, M.; Broccatelli, F.; Crawford, J. J.; Gazzard, L.; Wertz, I.; Lee, W., Piperidine Derivatives as Inhibitors of Ubiquitin Specific Protease 7. WO 2018073602A1, April 26, 2018.

[6] Wilson, T. C.; Xavier, M.-A.; Knight, J.; Verhoog, S.; Torres, J. B.; Mosley, M.; Hopkins, S. L.; Wallington, S.; Al-len, P. D.; Kersemans, V.; Hueting, R.; Smart, S.; Gouver-neur, V.; Cornelissen, B., PET Imaging of PARP Expression Using (18)F-Olaparib. *J. Nucl. Med.* **2019**, *60* (4), 504-510.

[7] Guibbal, F.; Isenegger, P. G.; Wilson, T. C.; Pacelli, A.; Ma-haut, D.; Sap, J. B. I.; Taylor, N. J.; Verhoog, S.; Preshlock, S.; Hueting, R.; Cornelissen, B.; Gouverneur, V., Manual and automated Cu-mediated radiosynthesis of the PARP in-hibitor [^{18}F]olaparib. *Nat. Protoc.* **2020**, *15* (4), 1525-1541.

[8] Alluri, S. R.; Riss, P. J., Poly(ADP-ribose) Polymerase in Neurodegeneration: Radiosynthesis and Radioligand Binding in ARC-SWE tg Mice. *ACS Chem. Neurosci.* **2018**, *9* (6), 1259–1263.

[9] Webber S. E.; Canan-Koch S. S.; Tikhe J. G.; Thoresen L. H., Tricyclic Inhibitors of Poly(ADP-ribose) Polymerases. U. S. Patent WO 2000042040A1, July 20, 2000.